Zeolitic Imidazolate Frameworks (ZIFs) Derived Metal Sulphides/Carbon Nanocomposites: Synthesis and Electrochemical Applications

Submitted by

Zheng Huang

to the University of Exeter as a thesis for the degree of

Doctor of Philosophy in Engineering

August 2022

I certify that all material in this thesis which is not my own work has been identified and that any material that has previously been submitted and approved for the award of a degree by this or any other University has been acknowledged.

Abstract

In the past decade, Zeolitic imidazolate frameworks (ZIFs) as precursors towards functional materials have attracted enormous attention. The easy modification of the ZIF structure itself, as well as the easy incorporation of various materials by different manners to form ZIF-based composites, have resulted in a great kingdom of functionalised ZIFs. Moreover, functional ZIFs derived nanocomposites of desired compositions and sophisticated structures can be obtained under suitable pyrolysis conditions and show great potential in various catalytic applications. Built on a pertinent literature review with special emphasis on the application in electrocatalytic water splitting, this thesis focuses on the rational design, synthesis, characterisation and electrochemical evaluation of ZIF-based composites and their nanocomposite derivatives.

First, a facile and cost-effective one-pot in situ encapsulation method was applied for the synthesis of phosphotungstic acid (PTA) encapsulated ZIF-67, and the bimetallic $WS_2/Co_{1-x}S$/N, S co-doped porous carbon nanocomposites were derived from one-step sulphurization/carbonisation of the PTA@ZIF-67 composites. Significant improvement in electrocatalytic activity towards both oxygen evolution reaction (OER) and hydrogen evolution reaction (HER) was observed.

Then, a different post-synthetic strategy to introduce PTA into ZIF-67 is utilised. Moreover, phosphomolybdic acid (PMA), which is unable to be introduced into ZIF-67 with the previous in situ encapsulation method, has been successfully encapsulated into modified ZIF-67 with this new synthesis approach. The HER and OER active, defect-rich ultra-fine Co-Mo-S/N, S-doped porous carbon nanocomposites and $WS_2/Co_{1-x}S$/N, S co-doped porous carbon nanocomposites were derived from the modified ZIFs. This new synthesis strategy to modify acid-sensitive ZIFs with selected compounds offers an alternative approach to develop novel transition metal sulphide/carbon composites for various applications.

Finally, the in situ encapsulation method is extended to a metal organic framework (MOF)-based composites (PMA@MIL-100), which demonstrates the universal applicability of the method. Bimetallic Fe-Mo sulphide/S-doped carbon nanocomposite was derived from the PMA@MIL-100 composite through chemical vapour sulphurization at high temperatures and showed a dramatic improvement in the HER performance.

Publications & Presentations

Peer-reviewed publications from this thesis

- **Z. Huang**, Z. Yang, M. Z. Hussain, B. Chen, Q. Jia, Y. Zhu, Y. Xia, Polyoxometallates@ zeolitic-imidazolate-framework derived bimetallic tungsten-cobalt sulphide/porous carbon nanocomposites as efficient bifunctional electrocatalysts for hydrogen and oxygen evolution, Electrochimica Acta, 330, 2020, 135335.
- **Z. Huang**, Z. Yang, M. Z. Hussain, Q. Jia, Y. Zhu, Y. Xia, Bimetallic Fe-Mo sulphide/carbon nanocomposites derived from phosphomolybdic acid encapsulated in MOF for efficient hydrogen generation, Journal of Materials Science and Technology, 84, 2021, 76-85.
- **Z. Huang**, Z. Yang, Q. Jia, N. Wang, Y. Zhu, Y. Xia, Bimetallic Co–Mo sulfide/carbon composites derived from polyoxometalate encapsulated polydopamine-decorated ZIF nanocubes for efficient hydrogen and oxygen evolution, Nanoscale, 14, 2022, 4726-4739.

Peer-reviewed publications outside the scope of this thesis

- M. Z. Hussain, G.S. Pawar, **Z. Huang**, A. A. Tahir, R. A. Fischer, Y. Zhu, Y. Xia, Porous ZnO/Carbon nanocomposites derived from metal-organic frameworks for highly efficient photocatalytic applications: A correlational study, Carbon, 146, 2019, 348-363.
- M. Z. Hussain, Z. Yang, B. van der Linden, **Z. Huang**, Q. Jia, E. Cerrato, R. A. Fischer, F. Kapteijn, Y. Zhu, Y. Xia, Surface functionalised N-C-TiO2/C nanocomposites derived from metal-organic framework in water vapour for enhanced photocatalytic H2 generation, Journal of Energy Chemistry, 57, 2021, 485-495.
- M. Z. Hussain, Z. Yang, **Z. Huang**, Q. Jia, Y. Zhu and Y. Xia, Recent Advances in Metal–Organic Frameworks Derived Nanocomposites for Photocatalytic Applications in Energy and Environment, Advance Science, 8, 2021, 2100625.

Conference presentations

- Bifunctional W,Co sulfide-based carbon nanocomposite for overall water splitting. Great western Electrochemistry Conference, Bath, U.K. July 2018.

Acknowledgments

I would like to express my deepest gratitude to my supervisor, Dr Yongde Xia, for his meticulous guidance, continuous support and constant encouragement during my PhD studies. His immense knowledge and working attitude have encouraged me in all the time of my academic research and daily life. I would also like to extend my sincere thanks to Prof. Yanqiu Zhu for his insightful comments and suggestions, which always inspire me to stay optimistic and think outside the box.

I would like to offer my special thanks to the fallows of our functional materials group: Dr. Zhuxian Yang, Dr. Binling Chen, Dr. Nannan Wang, Dr.Kunyapat Thummavichai, Dr. Mian Zahid Hussain, Dr. Yu Chen and many others. It is their kind help and support that have made my study and life in the UK a wonderful time.

I would like to thank Dr. Hong Chang, Dr Lesley Wears from Harrison Image Suit, Dr Ellen Green from Physics department, and Dr. David Morgan from Harwell XPS EPSRC National Facility for their technical support on material characterisation. And I would like to thank the technical teams from Harrison workshop and Harrison store for their support.

Thank should also go to the University of Exeter for the provision of scholarship.

Last, I am deeply indebted to my parents for their unconditional love, caring, understanding and support.

Table of Contents

List of Figures

List of Tables

List of abbreviations

AF	4-aminophenol and formaldehyde	**BET**	Brunauer-Emmett-Teller
CNTs	carbon nanotubes	**CPB**	Cetylpyridinium Bromide
CTAB	Cetyltrimethylammonium bromide	**CV**	cyclic voltammetry
CVD	chemical vapour deposition	**CVI**	chemical vapour infiltration
DFT	Density Functional Theory	**DMF**	Dimethylformamide
EDX	Energy-dispersive X-ray spectroscopy	**EIS**	electrochemical impedance spectroscopy
FA	furfuryl alcohol	**FT-IR**	Fourier-transform infrared
GC	glassy carbon	**GO**	graphene oxides
HER	hydrogen evolution reaction	**HRTEM**	high-resolution Transmission electron microscopy
ICP-MS	Inductively coupled plasma mass spectrometry	**ICP-OES**	inductively coupled plasma-optical emission spectrometry
Im	imidazolate	**LDHs**	Layered double hydroxides
LSV	linear sweep voltammograms	**MeIM**	2-mitroimidazolate
M-N	metal-nitrogen bond	**MOFs**	Metal organic frameworks
NPs	nanoparticles	**OER**	oxygen evolution reaction
ORR	oxygen reduction reaction	**PDA**	polydopamine
PhIM	4-phenyl imidazole	**PLA**	polylactic acid
PMA	phosphomolybdic acid	**POMs**	polyoxometalates
PTA	phosphotungstic acid	**PVA**	polyvinyl alcohol
PVP	polyvinylpyrrolidone	**PXRD**	Powder X-ray Diffraction
rGO	reduced GO	**RHE**	reversible hydrogen electrode
SAED	selected area electron diffraction	**SALE**	solvent-assisted linker exchange
SAs	single atoms	**SDS**	Sodium dodecyl sulfate

SEM	Scanning electron microscopy	**TEM**	Transmission electron microscopy
TGA	Thermogravimetric analysis	**TTAB**	Tetradecyltrimethylammonium (bromide)
XPS	X-ray photoelectron spectroscopy	**XRD**	X-ray diffraction
ZIFs	Zeolitic imidazolate frameworks		

Chapter 1 Introduction

1.1 Introduction and motivation

As the global population increases, the energy demand has boosted explosively, and energy sustainability is in dire need. Much effort has been invested in the high energy density, zero-pollution, non-toxicity and renewable energy source, hydrogen (H_2), to tackle this problem. Electrochemical water splitting driven by renewable electricity is the cleanest and most sustainable way to generate H_2.[1] However, one of the bottlenecks toward large-scale practical application of this method is its production efficiency.[2] As a result, efficient electrocatalysts for water splitting (i.e. cathodic hydrogen evolution reaction (HER) and anodic oxygen evolution reaction (OER)) are highly demanded. Moreover, current benchmark catalysts for HER in both acidic and alkaline environments, and OER in acidic environments, contain precious metals such as Pt, Ir and Ru, which are expensive and undesirable for commercial use. Efforts have been invested in the searching of efficient non-precious metal catalysts as substitutions.[1, 3, 4] For instance, transitional metal-based catalysts show better catalytic activity for OER in alkaline environments (i.e. in traditional alkaline water electrolysers); yet, many recent studies still use Ir and Ru base oxide as benchmark materials in alkaline electrolytes.

Recently, zeolitic imidazolate frameworks (ZIFs), a special subclass of metal-organic frameworks (MOFs) which assembled from tetrahedral-coordinated transition metal ions and imidazolate organic linkers, have attract great interest as the precursor and self-sacrificial template to develop heterogeneous electrocatalysts for HER and OER. [5, 6] This is owing to the intrinsic porosity characteristics, chemical and thermal stability, and high freedom in choosing the organic/inorganic assembly parts. Their unrivalled design possibilities can lead to inorganic functional materials such as carbons, metal-based compounds with high surface area, hierarchical pores, complex nanostructure and designable functionalities. Therefore, to designing and producing novel nanostructured materials from ZIFs and evaluating their performance as electrocatalysts are the primary aims of this PhD project.

1.2 Challenges

Despite the advantages of ZIFs as precursors for electrocatalysts, challenges remain: metal ions and organic linkers need to have a suitable coordination configuration in order to achieve a feasible and stable ZIFs structure, which means the tailorability on the

chemical constitution via backbone modification has been limited, and the intended design on the electrocatalysts may be unable to realise. Nonetheless, thanks to the robust structures, wide synthesis windows and cage-like porous structures, incorporating selected chemical components into ZIFs to form a composite can overcome the drawback of the backbone modification and lead to desired derivatives. However, the acid instability of ZIFs and the affinity between composite constituents need to be considered for the design of the precursor composites. Moreover, the dispersion of the guest species within the ZIFs-based composites is vital for the structure of the derivatives and can affect the electrocatalytic performance of the derivatives, but the rational control remains challenging.

1.3 Aims and objectives

Therefore, the aims and objectives of this thesis are as follows:

- To explore simple and effective ways to synthesise ZIFs-based composites with conventionally unachievable compositions and achieve a homogeneous dispersion of the compositions.
- To investigate facile way to derive carbon-based porous composites from the ZIFs-based composites with desired composition and controllable morphology.
- To evaluate the electrochemistry performance of the obtained ZIF-derived carbon-based heterogeneous nanocomposites.
- To insight into the relationship between synthesis, structures and electrocatalytic performance of ZIF-derived nanocomposites.

1.4 Organization of the thesis

This thesis is presented with 7 chapters. In Chapter 1, the motivation, challenge, objective and structure of this thesis are introduced. Chapter 2 presents and discusses the broad research background, the literature review on the development and recent progress in modification strategies of precursor ZIFs and ZIF-derivatives, as well as the recent electrochemistry applications of the ZIF-derivatives. In Chapter 3, the materials and synthesis method for ZIFs and ZIF-derivatives is provided. The characterisation techniques used in this thesis are also presented. Followed that, in Chapter 4 we present a facile and cost-effective one-pot in situ method for the synthesis of phosphotungstic acid (PTA) encapsulated ZIF-67, and the bimetallic $WS_2/Co_{1-x}S$/N, S co-doped porous carbon nanocomposites derived from one-step sulphurization/carbonisation of the modified ZIF-67. The HER and OER performance of the derivatives have been

investigated. Chapter 5 presents the post-synthetic modification of ZIF-67 with phosphotungstic acid (PTA) and phosphomolybdic acid (PMA) with the help of polydopamine (PDA). The HER and OER activities of the Co-Mo-S/N, S-doped porous carbon nanocomposites and $WS_2/Co_{1-x}S$/N, S co-doped porous carbon nanocomposites have been evaluated. Chapter 6 extend the in situ encapsulation strategy to a cages-structured MOF, MIL-100. The HER activities of the derived bimetallic Fe-Mo sulphide/S-doped carbon nanocomposites in acidic and alkaline media have been investigated. Conclusions of this thesis are summarised in Chapter 7 with suggestions for future works briefly provided.

Chapter 2 Literature review

2.1 Introduction

Metal organic frameworks (MOFs), also known as porous coordination polymers (PCPs), are crystalline solids comprised of metal nodes and organic ligands to form a periodic coordination network via coordinate bonds. The nature of the molecular structure allows MOFs to garner a series of intrinsic properties such as exceptional large surface area [7] and ordered and interconnected porosity [8]. Also, the substitutable organic linkers and metal ions enable easy functionalisation of the MOFs [9], as well as the tailorability of the pore structure and size [10]. As a result, the high level of freedom on modification, robust structure and wide synthesis window has led MOFs to be one of the most studied porous materials in the past 20 years.

Among MOFs, there is a special subfamily which composed of tetrahedral-coordinated transition metal ions and imidazolate organic linkers. Although the first crystalline polymeric structure built from imidazolate (*Im*) and Zn^{2+} was synthesised in 1980 with a dense *zni* topology network [11], the concept of zeolitic imidazolate frameworks (ZIFs) and a group of stable structures composed with imidazolate linkers and tetrahedral metal atoms were established by Yaghi and co-workers in 2006 [12]. With similar structure to aluminosilicate zeolites, the tetrahedral-coordinated transition metal ions in ZIFs play the role of Si, bringing by the imidazolate anions which mimic the role of O in zeolite frameworks. The M-Im-M (metal-imidazolate-metal) bond within the structure has bond angle of 145° which is similar to the Si-O-Si bond in zeolites (see **Fig. 2.1**), therefore these kinds of porous materials were so-called zeolitic imidazolate frameworks.

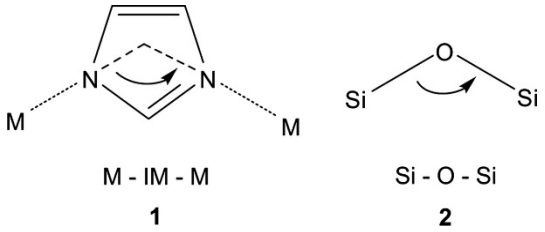

Fig. 2.1 The bridging angles in ZIFs (1) and zeolites (2) [2].

In the past decade, ZIFs as precursors towards functional materials have attracted enormous attention. The easy modification of the ZIF structure itself, as well as the easy incorporation of various materials by different manners to form ZIF-based composites, have resulted in a great kingdom of functionalised ZIFs and ZIF-based composites. These highly ordered porous structures constructed with both organic species and metallic

species could lead to functional ZIF-derivatives with desired compositions and sophisticated structures under suitable pyrolysis conditions, which show great potential in various catalytic applications [13].

The limited reserves of non-renewable fossil fuels has led to the global energy crisis. Renewable hydrogen (H_2) has emerged as a promising alternative to tackle this problem. The most sustainable way to produce H_2 is via renewable energy-driven electrochemical water splitting [14], which involve two half-reactions, hydrogen evolution reaction (HER) and oxygen evolution reaction (OER). The production cost and production efficiency could be optimised by developing novel non-precious-metal-based catalysts for these two reactions. In this context, ZIF-derivatives have been intensively investigated as efficient and cost-effective electrocatalysts for water splitting.

Therefore, this chapter aims to summarise the research developments on the synthesis of precursor ZIFs and ZIF-derivatives, and to discuss the recent progression on ZIF-derivatives as electrocatalysts for HER and OER.

2.2 Synthesis of precursor ZIFs

To date, various strategies have been explored to synthesise complex structures by modifying ZIFs. Roughly speaking, it can be realised by either modifying the backbone of ZIFs or incorporating ZIFs into a composite. The ultimate goal of modifying ZIFs is to form designed derivatives, therefore only the manipulation which cause meaningful changes in the derivatives will be discussed. Different modification approaches for the preparation of the precursor ZIFs are summarised in **Fig. 2.2**.

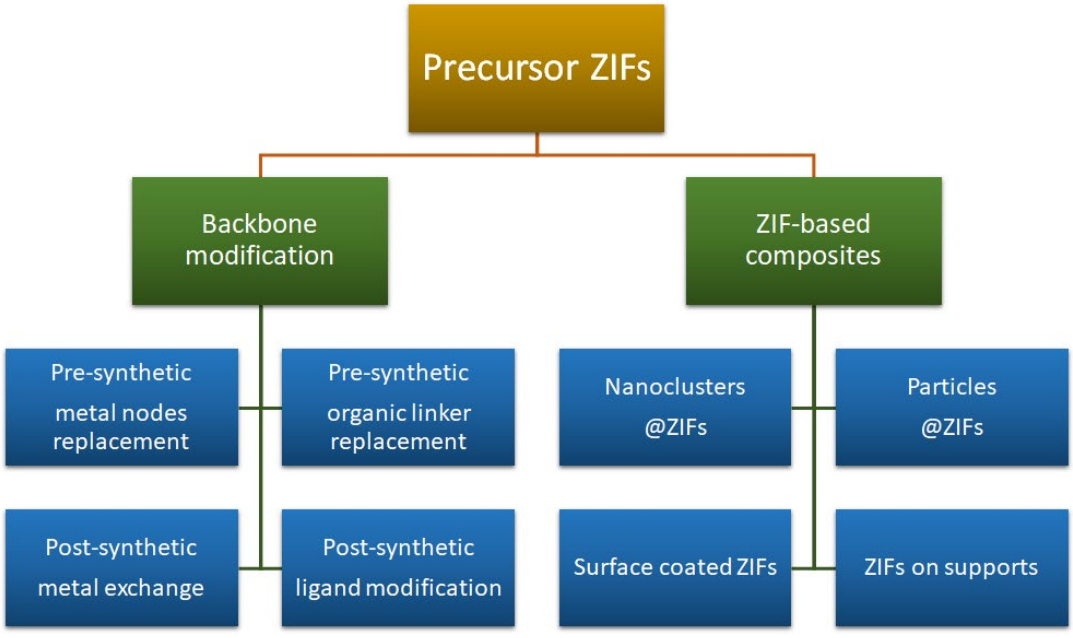

Fig. 2.2 Summary of different modification approaches for the preparation of precursor ZIFs.

2.2.1 Backbone modification

The composition, morphology and porosity of the ZIF-derivatives could be altered by changing the metal nodes or organic linkers of the parental ZIFs, and the replacement of these primary building units could be realized either before or after the formation of ZIFs. It is worth noting that pre-synthetic backbone modification is simply realised by changing the compatible metal nodes or organic linkers at the very beginning of the synthesis, therefore it is also called de novo synthesis or one-pot synthesis. The metal ions and organic linkers need to have certain electronic configuration and steric structure in order to form a ZIFs. On the other hand, post-synthetic modification takes place on the ready formed ZIFs structures, hence it is able to achieve complex and conventionally unachievable ZIFs. This requires an outstanding stability of the parental ZIFs, in order to withstand the harsh modification conditions without compromising the porosity and crystallinity.

Herein, we will discuss the backbone modification in four categories: Pre-synthetic metal nodes replacement, pre-synthetic organic linker replacement, post-synthetic metal exchange and post-synthetic ligand modification.

2.2.1.1 Pre-synthetic metal node replacement

Unlike the vast selection of metal ions available for building general MOFs, conventionally the choice of metal nodes for ZIFs have been limited into two: Zn (II) and Co (II) (except ZIF-5 which involve In (III) and Zn (II) as metal nodes) [12, 15-20], this is probably because M-Im-M bonds composed by other tetrahedral coordinated metal ions are unable to solely form an extended stable framework as Zn (II) and Co (II) did [29, 30-32, 34] Introducing new metal centres would open up the opportunity towards a wider range of new ZIF-derived hybrids. The presence of different metals can modulate the electronic structure of the hybrid and its derivatives, thereby lead to different applications [21 22].

Merging two existing ZIFs of different metal nodes is a typical example of pre-synthetic metal nodes replacement. In this case both metal nodes have the same electron configuration and can fit in the ZIF structure with no obstacle. For example, Zn based ZIF-8 and Co based ZIF-67 are isologue to each other, so with the same lattice structure interchanging these two metal ions would be more favourable than other metal ions [23]. A more in-depth research was conducted by Yamauchi et al.. The group not only systematically characterised the as-synthesised Co-Zn-ZIF but also investigated the effect of different metal nanoparticles on the graphitisation of carbon in the carbonised hybrid

[24]. Recently the primary structure as well as the change in physical properties of the dual metal ZIF was addressed [25]. Based on the single crystal analysis, the positions of Zn and Co are completely random, and the percentage of their existence depends on the concentration of the metal precursor used for the synthesis. Despite the same sodalite structure formed, the dual metal ZIF actually has different textural properties and better thermal stabilities. A research also suggested that with different Co to Zn molar ratio, the rate of nucleation may change, resulting in a controllable particle size [26]. Moreover, Lai et al. demonstrated that ZIF-derivatives with different compositions and porosities could be obtained by changing Co/Zn ratio in the bimetallic ZIF (see **Fig. 2.3**) [27].

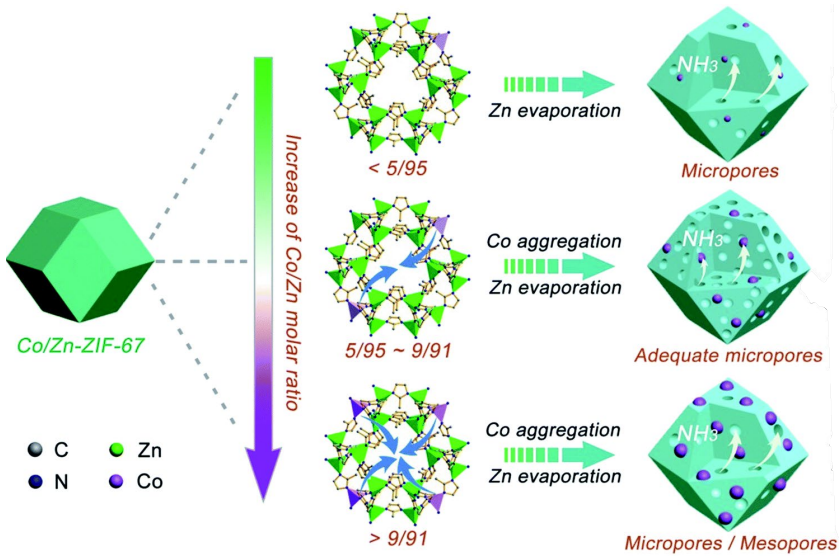

Fig. 2.3 Schematic synthesis process of Co NPs embedded in N-doped porous carbon of different porosity from the bimetallic Co/Zn-ZIF-67 of different Co/Zn ratio [27].

Besides the merging of two different existing ZIFs, many have tried to synthesise bimetallic ZIFs with other isovalent metal ions (such as Cu^{2+}, Ni^{2+} and Fe^{2+}). For example, in 2012 Yang et al. successfully introduced Cu^{2+} into ZIF-67 via one-pot hydrothermal synthesis but with uncontrolled doping percentage and unclear structural details of the Cu-doped ZIF-67 phase [28]. Three years later, Cu-doped ZIF-8 with a Cu doping percentage up to 25% was reported. Experiment suggested that doping level higher than 50% might lead to the complete structural collapse [29]. Examined by the inductively coupled plasma-optical emission spectrometry (ICP-OES), the actual doping level could only go up to 8.7%. This means only part of Zn metal centres are replaced by Cu ions and most Cu ions remain in the grain boundary, which is certainly not ideal for the acquisition of functional derivatives. Ni-doped ZIF-8 [30] and Fe-doped ZIF-8 [31] have later been reported via one-pot hydrothermal method, which also show a low doping level

and meta-stable structure. This is because these metal ions are prone to adopt six-coordinated structure with imidazole, which causes structural distortion and leads to a less stable structure [30, 32].

Nevertheless, polymetallic ZIFs have been achieved by Xu et al. via an entropy-driven room-temperature mechanochemistry method (see **Fig. 2.4**) [33]. This high-entropy ZIF (HE-ZIF) contains five different metal species (Zn^{2+}, Co^{2+}, Cd^{2+}, Ni^{2+} and Cu^{2+}) which were incorporated into the framework with random occupancy via ball milling. However, single Ni or Cu ion ZIF cannot be obtained via ball milling, and Cd-ZIF can only be obtained via solvothermal method. Attempt has also been made on the solvothermal synthesis of the HE-ZIF, but the obtained ZIF only contains Zn and Co ions. Compared with the physical mixture of ZIF-8, ZIF-67 and Cd-ZIF, the HE-ZIF shows better catalytic conversion of CO_2 to carbonate, suggesting the difference is caused by metal node substitution.

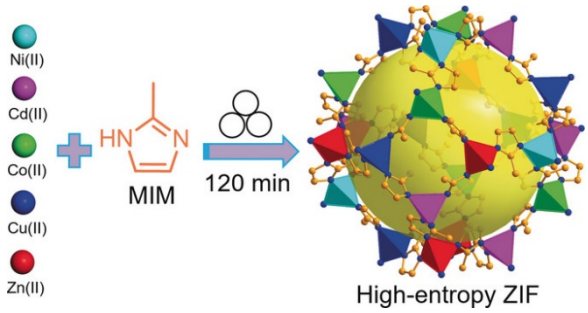

Fig. 2.4 Schematic representation of the synthesis of HE-ZIF via ball milling [33].

The labile metal-nitrogen bond in these metal-doped ZIFs makes it extremely difficult to form a stable framework as pristine ZIFs. The structure will collapse with more substituted metal ions, as a result it is difficult to synthesise phase pure ZIFs with substituted metal ions. However, there are still several successful examples. Horike et al. have successfully synthesised Mg-ZIF-8 with all Zn(II) being replaced by Mg(II) through a solvothermal method [34]. It is challenging to stabilise the tetrahedral Mg^{2+}-N coordination geometry in ZIF due to the variation in X-Mg^{2+}-X angles (range from 105°-115°), and the tetrahedral angle should be ideally 109.5° in order to form an extended structure (note that ZIF-8 has a tetrahedral angle of 109.3°). $Mg(BH_4)_2$ was carefully chosen to be the source of Mg as the authors suggested that the presence of hydride ligand during the reaction would encourage the formation of tetrahedral Mg^{2+}-N core. The synthesis took place in an Ar-filled glove box, and acetone was used as the solvent. It is worth mentioning that the coordinating counter anions such as Cl^- from $MgCl_2$ was avoid as it would interrupt the formation of such geometry. Shortly after that, the same group

reported the synthesis of Mn-ZIF-8 with $[Mn(BH_4)_2 \cdot 3THF] \cdot NaBH_4$ as precursor [35]. The change in metal nodes results in larger pore volume. Lately, the inaccessible iron analogue of ZIF-8, Fe-ZIF-8, was synthesised via a solvent-free method with the use of 4, 4-bipyridine as the template. Although the resulting ZIF is sensitive to humidity in air, it can maintain the structure under inert atmosphere for months [36].

By changing the metal nodes within ZIFs, the pore size as well as the effective aperture sizes can be finely tuned due to the change in M-N bond length, which is vital for gas adsorption and separation applications. Moreover, introducing new metal centre means change in electron configuration of the framework and introduction of new catalytically active sites. With appropriate heat treatment, these metal node modified ZIFs would lead to metal-nitrogen-carbon (M-N-C) system [37, 38] composites with single atomic dispersion [39, 40], bimetallic sulphides [41] and other nanostructures for all kinds of applications. The challenge of metal centre substitution is to construct a non-distorted tetrahedral $M\text{-}N_4$ coordination geometry in order to retain the extended yet stable ZIF structure.

2.2.1.2 Pre-synthetic organic linker replacement

Other than changing the metal centres, substituting the organic linkers can produce ZIFs with various functional groups, pore sizes, pore aperture sizes, heteroatom (e.g. C and N) loadings and hence different functionalities, therefore changing or mixing organic linkers can be seen as an example of pre-synthetic modification.

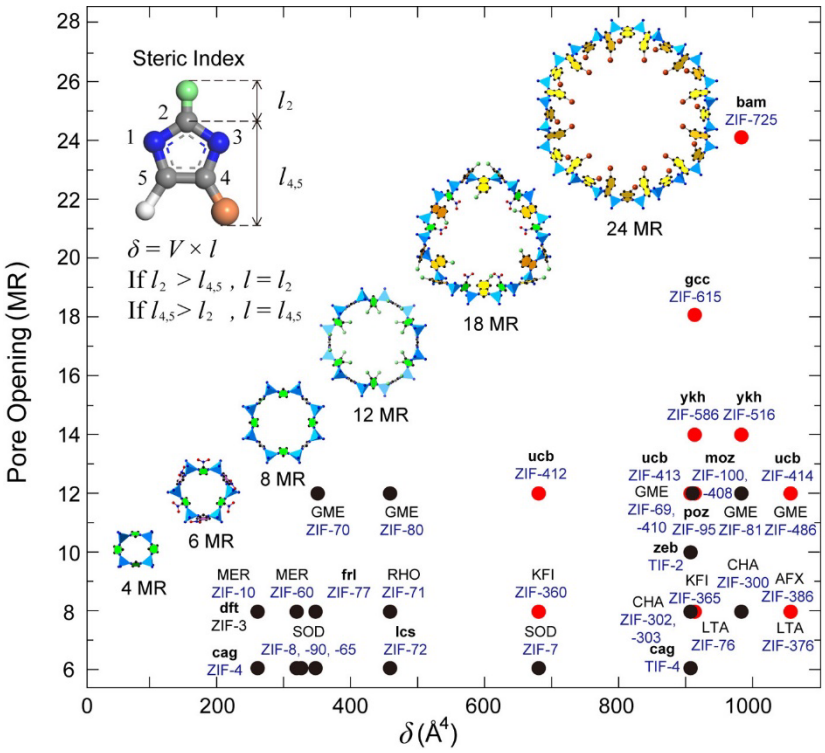

Fig. 2.5 Correlation between the δ values of Im linkers with the largest ring sizes in ZIFs where progressively larger ring sizes (pore opening) are made in ZIFs by increasing Im linkers' size and shape (steric index, δ) [42]. The corresponding x-membered ring (x-MR) are demonstrated in ball-and-stick images. Red dots represent structures reported in the paper and black dots represent those already reported. The 3-letter framework type code assigned by the Structure Commission of the International Zeolite Association (IZA-SC), indicate the unique and confirmed topologies of different ZIF structures. The inset, upper left, shows a schematic of the Im linker including the definition of δ.

In 2009, Yaghi's group reported a group of ZIFs, of which each tetrahedral metal atom is connected to two 2-mitroimidazolate and two other Im with different functional groups [16]. With –Cl, –CN, –Me, –Br and –NO_2 attached on the Im respectively, precise control on matrix and functionality can be achieved. Similar examples include ZIF-7, ZIF-8 and ZIF-90. [43] By changing the linker from phenyl imidazole (PhIM) to 2-methylimidazole (MeIM) and to Imidazole-2-carboxaldehyde (ICA), different pore aperture shapes can be obtained [43]. Later, they further demonstrated a rational design of ZIFs to achieve structures with progressively increased pore opening and cage size (up to 22.5 Å and 45.8 Å) (see **Fig. 2.5**) [42]. By using linkers with different steric index (δ) and combining different linkers, 15 new ZIFs with successive size of rings and cages have been obtained. Three design principles are revealed: (1) the size and shape of the imidazolate linkers determine the pore opening. (2) Combination of different linker with

different δ value is necessary to achieve maximum cage size. (3) For a fixed set of organic linkers, pore topology is determined by different ratios of mixed linkers.

These imparted functionalities may disappear after heat treatment, but may assist further modification to obtain desirable precursor ZIFs. There is yet no systematic research crosswise studies the properties of ZIF-derivatives obtained from pre-synthesis organic linker replacement (i.e. ZIFs with same metal centre but different organic linkers). Nevertheless, researches have shown that the porosity of the carbonaceous materials varies with different parental ZIFs [44, 45]. Moreover, the catalytic activities of ZIF-derivatives are found to be positively correlates to the cavity size and mass-specific pore volume of the parental ZIFs [46, 47].

Although there have been already a bunch of ZIFs with different functionality based on different organic linkers, direct synthesis of ZIFs with new linkers still remains challenging. Some linkers can be inherently incompatible with typical direct synthesis conditions, and some are chemically unstable that they cannot form structure via direct synthesis. To overcome these issues, several indirect post-synthesis methods have emerged, which will be discussed in section 2.2.1.4.

2.2.1.3 Post-synthetic metal exchange

Post-synthetic metal exchange sometimes refers to transmetalation. So far there has been no report on ZIFs prepared by full substitution of other metals. But bi-metallic ZIFs (such as Cu, Fe, Ni, Mn-ZIF-8) have been obtained via post-synthetic metal exchange [48-51].

The pristine metal-nitrogen bonds in ZIFs are generally robust and hard to break whereas the exchanged metal-nitrogen coordination might be less stable [35]. Therefore, compared with pre-synthetic metal nodes replacement, more drastic experiment conditions (such as specific reaction and longer reaction time) are required for post-synthetic metal exchange. For example, Cohen's group presented post-synthetic Mn(II) exchange for ZIF-71 and ZIF-8 for the first time in 2013 (see **Fig 2.6**) [52]. The pristine ZIFs were synthesised beforehand and were consecutively incubated in methanol at 55 °C for 24 hours in the presence of $Mn(acac)_2$. X-ray fluorescence (XRF) analysis has suggested that about 12% and 10% of the Zn^{2+} centres were replaced by Mn^{2+} in ZIF-71 and ZIF-8 respectively. The topology, crystallinity, BET surface area and the thermal stability of the modified ZIFs have been maintained in a similar level of the parental ZIFs, suggesting that the Mn^{2+}has been successfully exchanged into the structure instead of trapped in the pores. Instead of changing the experiment temperature to assist the breaking of the M-N bond, Ban et al. utilized metastable ZIF-108 as parent material to synthesise

dual-metal ZIFs at low temperature, with Mg^{2+}, Cr^{2+}, Mn^{2+}, Fe^{2+}, Co^{2+}, Ni^{2+} and Cu^{2+} as the second metal nodes [53]. In this work, both isostructural and heterostructural ZIFs were obtained, indicating that metal exchange involves partial dissolution of parent ZIF and heterogeneous nucleation of the mixed metal ZIF. Compared with ZIF-8, the longer Zn-N bond makes ZIF-108 more suitable for metal substitution.

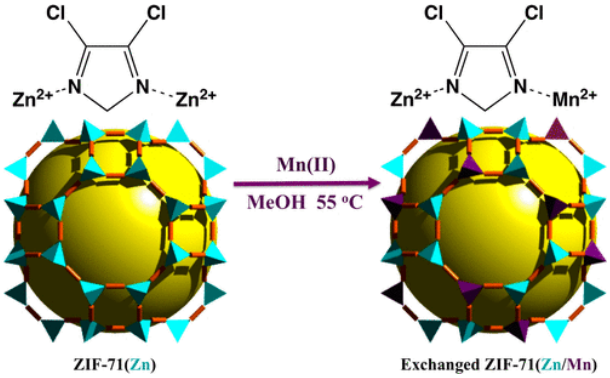

Fig. 2.6 Post-synthetic Mn(II) Exchange of ZIF-71 [52].

There is a lack of open metal sites in the ZIFs crystal, therefore, to replace metal nodes inside the crystal the substitution ions need to penetrate into the frameworks. Usually, long time is needed for reaction to fully take place. Recently, Tang et al. has presented Au^{3+} cation exchange for ZIF-8 in methanol at room temperature (see **Fig. 2.7**) [54]. After 8 hours of vigorous stirring in $NaAuCl_4$ solution, the modified ZIF-8 with hollow structure (named Au/Zn-MOF) was obtained. The longer the reaction time results in the more Zn^{2+} been replaced, and the larger the hollow space within the crystals. The hollow space is believed to be the Kirkendall voids resulted from the non-equilibrium interdiffusion of Zn^{2+} and Au^{3+}. Besides, due to the continual association-dissociation of the ZIF, the shell thickness of the nanostructure can be tuned by controlling the concentration of the Au cation solution. Note that unlike the de novo synthesis, parental metal nodes can hardly be fully replaced by the new metal ions. So far complete exchange of metal ions via post-synthetic metal exchange has not been reported.

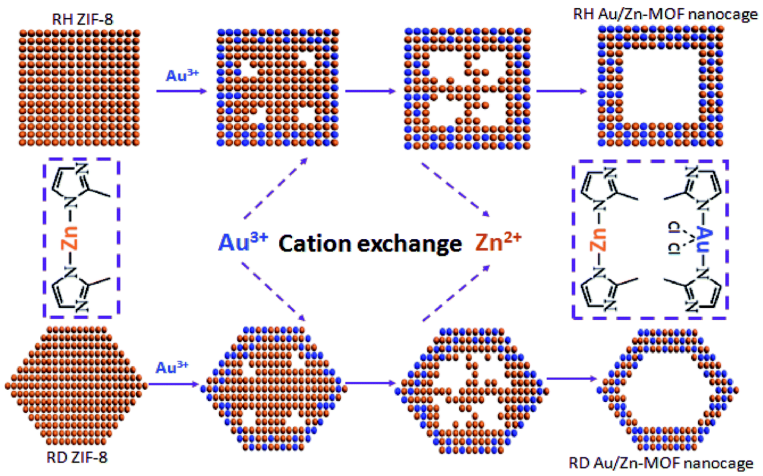

Fig. 2.7 Schematic diagram of the formation process of Au/Zn-MOF nanocages and the cation exchange reaction between either regular hexahedral (RH) or rhombic dodecahedral (RD) ZIF-8 NPs and Au^{3+} ions [54].

Other metal nodes unachievable by de novo substitution have also been reported via post-synthetic metal exchange. For example, recently, doping Lanthanide ion (Ln^{3+} :La^{3+}, Ce^{3+}, Nd^{3+} and Tb^{3+}) into ZIF-8 has been demonstrated by Hao et al. [55]. Typically, ZIF-8 was dispersed in water and then added into $La(NO_3)_3$, $Ce(NO_3)_3$, $Nd(NO_3)_3$ and $Tb(NO_3)_3$ respectively. It is suggested that the confinement of Ln^{3+} as well as ion exchange between Zn^{2+} and Ln^{3+} occurred at the same time. ICP-MS indicates that about 10-13% of Zn^{2+} was released because of the ion exchange, but XRD results show that ZIF-8-Lns tend to lost their crystallinity. In addition, the Mo/W containing mixed metal ZIFs were also reported by Lou's group lately [56]. Instead of the use of solitary metal cations, the exchange takes place between Zn(imidazolate)$_4^{2-}$ units in ZIF-8 and MO_4^{2-} (M=Mo or W) from the inorganic salts Na_2MoO_4 and Na_2WO_4. The reaction becomes possible due to the similar four-connected open structure of both units. The possibility of inclusion of molybdate or tungstate in the framework by adsorption has been ruled out by the absence of sodium element. The nearly identical textural properties of ZIF-8 and ZIF-8-MO_4 indicate that the framework structure is intact and the pores are not blocked by the MO_4^{2-} units. Moreover, Xu et al. have reported a Ti containing bimetallic ZIF [57], which was obtained through Ti^{4+} exchanging with Co^{2+} on the surface of ZIF-67 in DMF solvent.

Although post-synthetic metal exchange modification does not facilitate the completely exchange of all the metal nodes in the parental ZIFs, mixed metal ZIFs could be obtained easily by this method. However, for all the modified ZIFs it is important to thoroughly wash the product to remove excess metal ions in order to avoid surface

clumping of metal NPs and large NPs inside the framework after heat treatment. It is worth noting that an early report revealed that the presence of multivalent metal ions in solution will result in structure collapse of ZIFs, whereas univalent metal cations show no effect on the ZIF structure.[58]

2.2.1.4 Post-synthetic ligand modification

Post-synthetic ligand modification can be realised by modifying the existing organic linkers in the ZIF framework or by replacing existing linkers in the ZIFs with new linkers. To the best of our knowledge, Yaghi and co-workers were the first to demonstrate a post-synthesis covalent functionalization of ZIFs without losing the structure integrity during the organic transformations [17]. In their work, the -CHO groups in organic linker of ZIF-90 were converted to a carboxyl containing linker to form a new structure named ZIF-91. Another structure, ZIF-92, was formed by modifying the original linker under the same reflux condition with different reactants, and show a more obstructed aperture due to the presence of the space-hogging imine group.

Apart from changing functional groups on the existing organic linker, sometimes the whole linker can be replaced, which is commonly referred as solvent-assisted linker exchange (SALE). This method is often used to synthesise the conventionally unachievable ZIF structures. However, the obtained structure may be less stable than conventional ZIFs or even collapse if high substitution ratios applied. For example, Olga et al. reported the exchange of the majority of 2-methylimidazole (MeIM) in ZIF-8 by imidazole (Im) (up to 85%), forming a new isostructural analogue named SALEM-2 [59]. The molar ratio of Him to ZIF-8 during the linker exchange was vital. While lower ratios will not yield observable change, higher ratios can lead to the loss of the SOD topology. Without the obstruction of the methyl group from MeIM, the new framework got a larger pore aperture on the *a* crystallographic axis. The type of solvent will affect the exchange ratio of the ligand. Sanchez-Lainez et al. has incorporated benzimidazole in ZIF-90 via SALE [60]. By changing the solvent used and the reaction time, 7.4-23% of the organic linkers in the framework of ZIF-90 had been exchanged by benzimidazole.

Although the functionalisation via linker exchange is expected to disappear after heat treatment as discussed above, the nitrogen content of the ZIF derivatives can be affected by the use of different organic linkers [61]. The introduced uncoordinated nitrogen atoms provide stronger adsorption for metal ions than the original ZIF due to the improved Lewis acid-base interactions, which would potentially be a new way to introduce metal element into ZIFs and its derivatives. Moreover, the porous structure of

the ZIF-derivative can also be changed via linker exchange. Zhou's group has demonstrated the synthesis of ligand-exchanged ZIF-8 via substituting the MeIM linker with 'explosive' organic linker to produce expanded foam-like porous carbon via pore-expansion strategy [62]. The N-rich 'explosive' organic linker, 1H-1, 2, 3-triazole, can release large amounts of gases (CO_2, NO_2, NO, HCN and N_2) during the pyrolysis process, which would result in higher surface area and pore volume in its derivatives.

Moreover, the presence of abundant organic functional groups in ligand modified ZIFs enable them function as starting materials for further modification. For example, Bhattacharjee et al. demonstrate that large metal complex can be attached to the surface of ZIF crystals by attaching to the modified organic linker [63]. You et al. show that metal ions can be anchored on the hydroxylamine group of the modified ligands [64]. Pastore et al. has synthesised polymer-ZIF hybrids via ligand exchange [65]. The exchanging ligands were first attached to the polymer backbone, followed by surface-selective ligand exchange, the surface of ZIF crystals were covered with polymer chains that can cross-linked with each other to form a ZIF crystals-polymer composites (see **Fig. 2.8**).

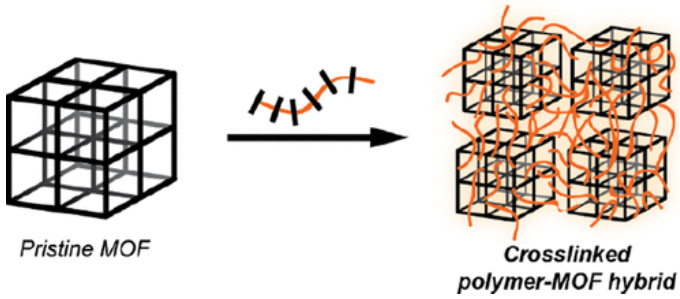

Fig. 2.8 Schematic of direct integration through post-synthetic ligand exchange to form a cross-linked polymer–MOF network with preserved porosity [65].

Remarkably, Tsung and co-workers have reported the post-synthetic decoupling encapsulation of large guest species with molecular size larger than the aperture of ZIF-8 utilizing the SALE method (see **Fig 2.9**) [66]. Instead of introducing new ligand, pre-synthesised ZIF-8 was deliberately mixed with additional original linker in one solution to trigger linker exchange conditions. As a result, a dynamic balance between linker dissociation and association occurred. The size of the aperture would increase when the linker dissociates from the framework, allowing the large guest molecules to enter the pore. After incorporation of the guest, association of the ligands closed the large apertures and trapped the guest molecules in the cage. Leaching experiments proved that leaching is prevented under slow linker exchange conditions.

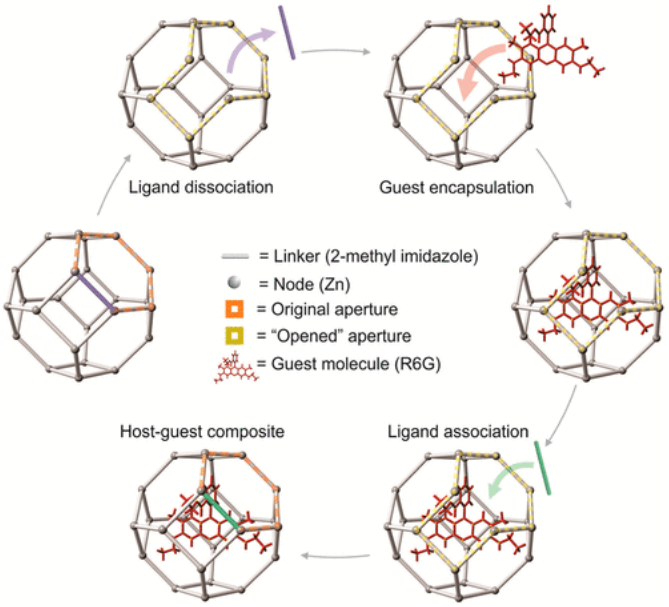

Fig. 2.9 Molecular encapsulation beyond the aperture size limit through dissociative linker exchange [66]. The guest molecule is Rhodamine 6G (R6G).

Besides SALS, post-synthetic linker exchange can also be achieved using vapour-phase linker exchange (VPLE), which is more environmentally friendly due to the solvent-free nature of the method [67]. For instance, Marreiros et al. have demonstrated the VPLE on ZIF for the first time by exposing ZIF-8 to 2-carboxaldehyde imidazole vapour, and the obtained product is identical to the one obtained via direct synthesis or SALE [67]. Moreover, ZIF crystals in the range of 100 nm to 100 μm were used to explore the size-dependent linker exchange kinetics and surprisingly no significant difference was observed, as all crystals end up with 84 ± 6% of linker exchanged in the structure. Compared with SALE, VPLE has faster linker exchange rate, higher precursor utilisation and is easy to scale up [68]. But the process requires to increase the temperature (generally around 50-300˚C) to vaporise the organic linker, therefore the framework may experience certain deformation during the thermal treatment.

In summary, post-synthetic ligand exchange approach usually only requires mild reaction conditions and is reversible when labile metal-ligand bonds are presented. This post-synthetic modification method can avoid the failure of incorporating desired linkers during the assembly of ZIFs, which makes it powerful strategy for ZIF functionalisation. The surface chemistry, the physical structure and the chemical composition of ZIFs could be readily modified. In addition, the modified organic linkers could assist the decoration of guest species which offer more opportunities for further exploration.

2.2.2 Incorporating ZIFs into composites

Other than modifying the backbone of ZIFs, functionalisation of ZIFs can also be achieved by synthesising ZIF-based composites. Herein, we categorise the ZIF-based composites into four different types according to the orientation relationship between the ZIF and the other guest constituents (see **Fig. 2.10**): a) Nanoclusters@ZIFs. Small constituent particles with sizes smaller than the pores of ZIFs are trapped in the pores, b) Particles@ZIFs. Single or multiple particles that are larger than the pores of ZIFs are encapsulated in a single ZIF crystals forming a core-shell structure, c) Surface decorated ZIFs. Other materials are coated on single or multiple ZIF crystals, forming a reverse core-shell structure. The coating material can be a continuous layer or separate particles on the surface of ZIFs, and d) ZIFs on supports. ZIF crystals are grown on supports and the substrates can be partly or fully covered with ZIFs crystals.

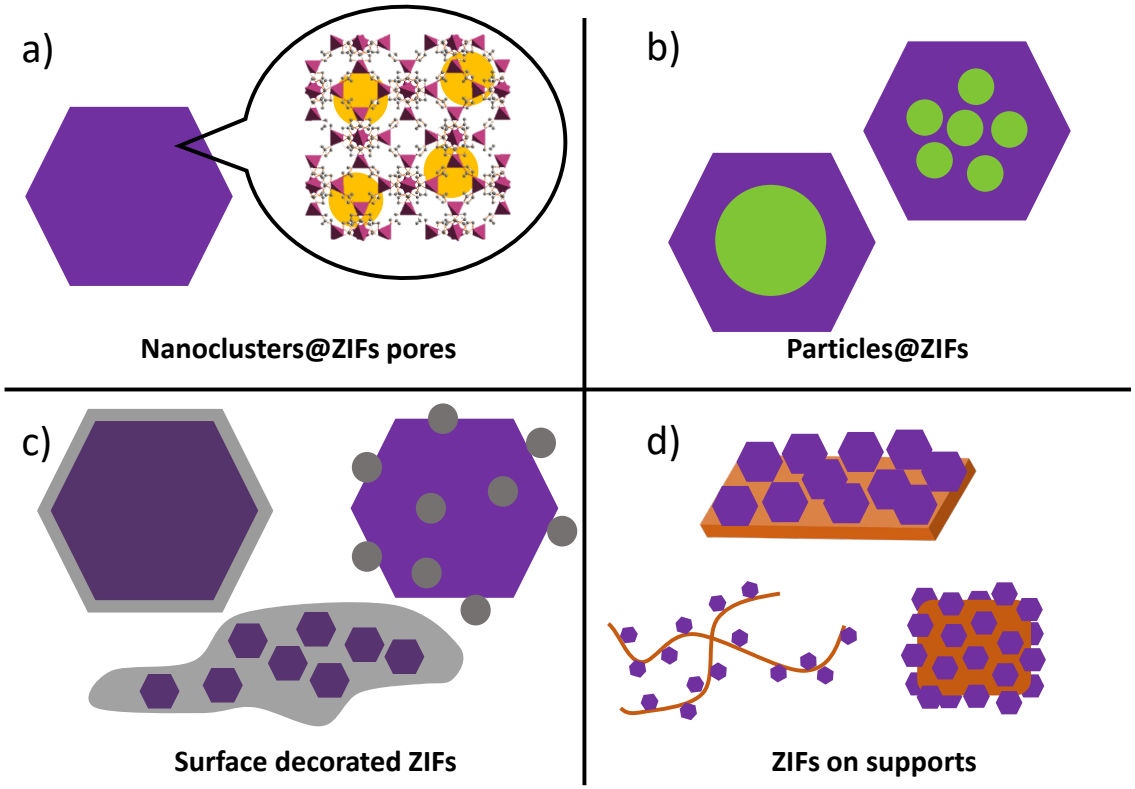

Fig. 2.10 Schematic diagram of four types of ZIFs-based composites based on the orientation relationship between ZIFs and other constituents of the composites

2.2.2.1 Nanoclusters@ZIFs

ZIF-based composites with small components that can be encapsulated in the pores of the hosting ZIFs are referred to Nanoclusters@ZIFs in this review. The encapsulated nanoclusters could be metal ions, metal quantum dots, metal compound particles, complex large molecules and other nanosized species that are smaller than the cage sizes

of ZIFs. This encapsulation of the guest species in ZIF cages can mitigate or avoid the fusion and aggregation of the active centres after heat treatment, leading to desirable functionality, enhanced catalytic actives with increased durability. There are two main approaches to obtain such type of composites: in situ synthesis, in which the encapsulation of exotic species is concurrently with the nucleation and growth of ZIFs, and impregnation synthesis, in which nanoclusters are introduced after the formation of ZIFs. Both synthesis methods are discussed as follows.

2.2.2.1.1 In situ synthesis of Nanoclusters@ZIFs

Nanoclusters@ZIFs can be realised by in situ one-pot synthesis method through bottle-around-a-ship strategy, in which the size of guest species must be smaller than the cavity of ZIFs to realise the encapsulation. For this reason, simple metal cations with the size of 1-2 Å are feasible guest species. However, because the size of the metal cations is far smaller than the aperture size of the ZIF cages, they would stay on the grain boundary of the crystals [31] or easily leak out during the washing steps [52], which eventually leads to different metal contents between batches [28]. The possible surface accumulation of the metal species after calcination could cause unstable performance in the follow-up applications. Although direct evaporation of the solvent could be a good alternative to ensure the number of metal ions introduced [51, 69], the excess amount of organic linker cannot be removed, which is not ideal for rational functionalisation of ZIFs. Moreover, the incorporated metal ions with tetrahedral coordination geometry might either replace some ZIF metal sites or present as free ions within the pores of the framework [52]. This reveals another drawback: metal ion substitution and encapsulation are uncontrolled and they can occur simultaneously.

The above concerns have brought out the second size requirement for in situ encapsulation: the size of the guest particles must also be bigger than the pore aperture for them to be physically trapped in the cage while avoid leaching. Take ZIF-8 as an example, the size of the guest particles must be not only smaller than 1.16 nm (the pore diameter of ZIF-8) to fit into the pores, but also bigger than 0.34 nm (i.e. the aperture diameter of ZIF-8) to be locked in the pores [12]. In this regard, atomically precise nanoclusters (APNCs) have become a better option to meet the precise size requirement. These APNCs are protected by ligands (e.g. thiolate, phosphine, selenolate, alkynyl and etc.), and the size was controlled by factors such as solvent, reactant ratio, reducing agent and temperature [70]. Recently, in situ inclusion of APNCs, such as $Au_{25}(SG)_{12}$@ZIF-8, $Au_{12}Ag_{32}(SR)_{30}$@ZIF-8/67, $Ag_{44}(SR)_{30}$@ZIF-8/67, and $Ag_{12}Cu_{28}(SR)_{30}$@ZIF-8/67 have

been reported [71, 72]. The formation of these APNCs@ZIFs is established either by i) coordination-assisted self-assembly, where the cationic metal nodes of ZIFs coordinate with the carboxyl group in the protecting ligands of the APNCs, initialising surface growth of ZIFs on the pre-synthesised uni-sized metal clusters; or by ii) electrostatic self-assembly, where the anionic APNCs are attracted with cationic metal ions of ZIFs electrostatically, stimulating the growth of ZIFs around the APNCs. Ultra-small APNCs with sizes of ~1.1 and ~1.3 nm [73] and narrow distributions were reported, which suggested that APNCs could be a great candidate for in situ encapsulation of nanoclusters in ZIFs.

Instead of directly encapsulating metal nanoclusters, metal-containing complex molecules are more commonly used as guests in the in situ encapsulation modification of ZIFs, due to their appropriate molecule size and great variety. Taking $Fe(acac)_3$ as an example, the molecular diameter is around 9.7 Å, which is perfectly larger than the pore aperture but smaller than the pore diameter of ZIF-8 [74]. One-pot solvothermal method was applied to synthesise $Fe(acac)_3$@ZIF-8 [75]. XRD result showed that the presence of $Fe(acac)_3$ did not change the crystal structure of ZIF-8, and the in situ encapsulation of the $Fe(acac)_3$ was confirmed by FT-IR, which ruled out the possibility of backbone metal node substitution by iron ions. Depending on the amount of $Fe(acac)_3$ used, single-atom dispersed Fe@carbon and Fe NPs@carbon can be obtained via appropriate heat treatment. Similarly, $Ru(acac)_3$, $Rh(acac)_3$ and $Ir(acac)_3$, with diameters of 9.7, 9.36, and 9.8 Å, respectively, were also incorporated in ZIF-8 via in situ encapsulation [76-78]. Besides metal acetylacetonates, other complex metal compounds such as Iron phenanthroline complex [79], Iron-salen complexes [80], Ammonium ferric citrate [81], Iron (II) Phthalocyanine [82], Lanthanide-pytz complexes [83], and Triruthenium dodecacarbonyl cluster [76] have also been incorporated into the cages of ZIFs by in situ encapsulation. There are still a lot to explore for the synthesis of this great family of large metal-containing molecules based nanoclusters@ZIFs.

Besides metal-containing complex molecules, polyoxometalates (POMs), a family of inorganic anionic metal-oxygen clusters, are also one of the popular guest species which have attracted increased research interest due to their versatile properties [84, 85]. The most common POMs that have been encapsulated into ZIFs are the keggin-type heteropolyanions $[XM_{12}O_{40}]^{n-}$ (where X=P, Si or Co etc. M=Mo, W or V etc.) due to their appropriate molecule size and best chemical stability among all POMs [86]. For instance, phosphomolybdic acid (PMA) and phosphotungstic acid (PTA), which can form keggin

type polyatomic ions with diameters of 13 Å [87] and 10 Å [88] respectively, have been reported to form host-guest structures with ZIFs via hydrothermal in situ encapsulation [89-91]. Zhang et al. have found that the strong acidity of the PMA in some extent, could be buffered by the excess amount of MeIM, so as to protect the acid-vulnerable ZIF-67 and ensure the formation of the PMA@ZIF-67 hybrid (see **Fig. 2.11**) [89]. However, open voids are still observed on the hybrid crystals. With increasing PMA loading in the composites, the hollow interior would gradually enlarge and finally lead to the complete collapse of the crystalline structure even with an excess amount of MeIM. The authors suggest that this unique hollow structure is due to the inside-out Ostwald ripening mechanism, where the competitive coordination and anisotropic etching of PMA occur at the same time during the self-assembly of the ZIF. Interestingly, another report demonstrated that with careful control of the pyrolysis temperature, the ZIF-67 can be carbonised while retaining the POM molecules [91]. Moreover, single metal atom and metal nanocluster anchored nitrogen-doped carbons have also been reported using POM@ZIFs as precursors [92]. The synthesis of many other POM@ZIFs, such as $H_6CoW_{12}O_{40}$@ZIF-8 [93], $H_5PMo_{10}V_2O_{40}$@ZIF-8 [94], $H_4SiW_{12}O_{40}$@ZIF-8 [80, 95], $[SiW_9Co_3(H_2O)_3O_{37}]^{10-}$@ZIF-67 [96] and Al-DTP@ZIF-8 [97] have also been reported. The abundant variety of POM@ZIFs would lead to vast selections of ZIF-derivatives.

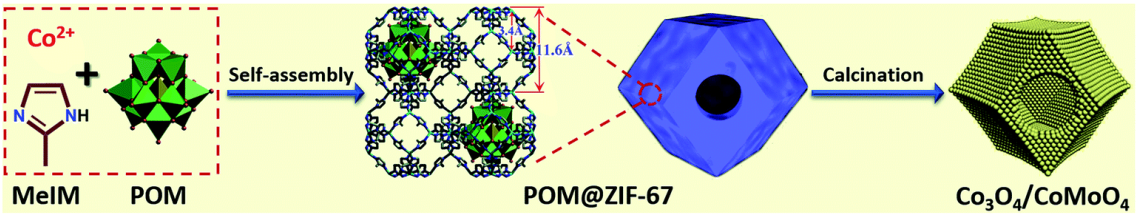

Fig. 2.11 Schematic drawing of the synthesis of hollow POM@MOF hybrids and $Co_3O_4/CoMoO_4$ nanocages [89].

Non-metallic species can also be encapsulated into the pores of ZIFs and assist further functionalisation of ZIF-derivatives. Recently, Lee et al. have reported the sulfurisation of the core-shell ZIF67@ZIF-8 by encapsulating an organic molecule, thiourea**,** during the synthesis process [98]. The planar thiourea molecules with a C=S bond length of 1.71 Å and C-N bond length of 1.33Å [99] remain in the cage of ZIFs even after thorough washing. Lately, Lysozyme (3 x 3 x 4.5 nm), a widely available protein, has been first entrapped in ZIF-8 via in situ hydrothermal inclusion with co-precipitating agent PVP [100]. Later, Ag and Au nanoclusters (1.2 ± 0.3 nm) encapsulated ZIF-8 has been obtained through a biomineralisation approach in metal salts solutions.

In summary, in situ synthesis of nanocluster@ZIFs has set a straight limit on the size of the guest species that the guest must be greater than the aperture size but smaller than the pore size of the host ZIFs. They should also be stable under the synthesis conditions and do not significantly affect the crystallisation of ZIFs. In the in situ synthesized nanocluster@ZIFs composites, with guest components confined in ZIF cage, the evident merits of this type of composite include but not limit to (i) the guest components/elements can be dispersed more evenly within the frameworks of ZIFs and atomic level dispersion can be achieved [81, 82], (ii) more active sites can be exposed, making such structure favourable for high efficient catalytic applications. This enables large number of active sites been preserved for the derivatives by fine control over the following calcination step [78, 82, 101].

2.2.2.1.2 Post-synthetic Impregnation synthesis of nanoclusters@ZIFs

Nanoclusters@ZIFs with filled active guest species in the cages of ZIFs can also be achieved post-synthetically by impregnation method, in which ZIFs are impregnated in a certain amount of guest containing solution, followed by removal of the solvent. It is one of the most widely used methods to synthesise ZIF supported/mixed composite. Generally speaking, factors such as solubility of the guest, viscosity of the solvent, and concentration of the guest solution could affect the amount and the position of the guest in the porous support materials [102]. In contrast to the backbone modification discussed earlier, this process generally does not involve the formation of chemical bonds between the host and the guest.

The post-synthetic nanoclusters@ZIFs have a different size requirement on the guest from the in situ synthesis of nanoclusters@ZIFs. If the size of the precursors is larger than the pore aperture of ZIF, such as metal coordination complex [103-105] or metal nanoparticles [106], impregnation method would only lead to inhomogeneous loading of guest species and result in surface clumping [107], surface coating [108] or physical mixing [109] of the guest species. Therefore, the size of the guest species must be smaller than the pore aperture of ZIFs in order to be infiltrated into the pores of ZIFs. Metal ions are one of the most commonly studied guest species under these constraints.

In a typical wet impregnation process where an excess amount of solution is used, the infiltration of the metal ions is driven by both capillary and diffusion action [110]. The metal ions that infiltrate into the aperture of the ZIF pores can also leak away easily [102], so leaching of the guest species is inevitable during centrifugation/filtration process. Accordingly, the concentration profile of the guest species depends on the mass transfer

conditions within the pores during impregnation and drying process [110]. On this account, direct evaporation of the solvent is used to prevent the guest species leaching and ensure the loading efficiency of the wet impregnation synthesis [69].

In order to control the loading amount and the position of the metal nanocluster precursor more precisely, an incipient wetness impregnation approach is developed. In a typical synthesis, ZIF is impregnated in a small amount of guest-containing solution. Usually, the volume of the solution is the same as the pore volume of the support to ensure the complete infiltration of the metal ion solution, followed by direct drying of the solvent. No washing step is needed, and no leaching occurs during the collection process. Consequently, controlled amount of loading can be achieved [111]. Furthermore, with such a small amount of solution used, all the precursors are diffused to fill in the pores via capillary action, therefore deposition of metal precursors on the surface of the supports can be minimised [112]. The obtained nanoclusters@ZIFs can serve as ideal precursors for the preparation of heterogeneous catalysts by proper heat treatment. Moreover, the efficient loading and the small amount of solvent needed have largely limited the pollution during the synthesis [111]. Composites such as metal salt filled ZIFs [113-115], metal halide filled ZIFs [116], and their use as parental composites towards homogeneous catalysts have been widely reported via incipient wetness impregnation.

The immobilisation of metal precursors via the wet impregnation method has been taken one step further by a ship-in-a-bottle strategy, in which the small metal precursors are first infiltrated into the pores of ZIFs, followed by the in situ reduction/precipitation treatment. The metal precursors can therefore transform into metal nanoclusters within the ZIF pores [117], or metal nanoparticles that are slightly larger than the pores [118]. Both are considered as nanoclusters@ZIFs in this review as the particles are small enough and the majority of the framework remains intact. In this way, the immobilisation of the metal species can therefore be achieved without changing the ZIF structures.

$NaBH_4$ is one of the most commonly used reducing agents in impregnation modification of ZIFs. Metal salt such as chloride [119], sulphate [120], nitrate [121, 122], and halide [116, 118] have been reported as the precursor of the guest metal species. Alloy metal particles could be achieved by introducing multiple metal precursors during synthesis [117, 123]. Interestingly, the core-shell structured metal nanoclusters could be obtained by sequentially immersing and reducing the ZIFs in different metal precursor solutions and reducing agent solutions [124]. Moreover, report shows that the concentration of $NaBH_4$ can affect the metal particle size [112]. At low concentrations, some of the metal ions that have

not been reduced would diffuse out of the pores, leading to agglomeration of metal particles on the outer surface of the crystals.

Besides $NaBH_4$, several other chemicals have also been reported as reducing agents to reduce metal ions. For example, Huang et al. demonstrated the synthesis of $Fe(OH)_3$@ZIF-8 via an in situ precipitation impregnation method using metal hydroxide as the reducing agent [125]. The double-replacement reaction between KOH and metal ions would trigger the in situ precipitation of insoluble $Fe(OH)_3$. Fe_2O_3 encapsulated porous carbon and Fe-doped porous carbon with abundant Fe-N-C sites can be obtained after further appropriate treatment. NaOH is also reported as the reducing agent for the fabrication of nanoclusters@ZIFs composite [126]. Although ZIFs are unstable under acidic conditions, Shaikh et al. have reported the impregnation synthesis of PdNPs@ZIF-8 using formic acid as a mild reducing agent [127]. The results show that the crystal structure of ZIF is intact, but the morphology has changed dramatically, so the balance between the dissolution and formation of ZIFs under acidic conditions is vital to successful production of ZIF-based composites.

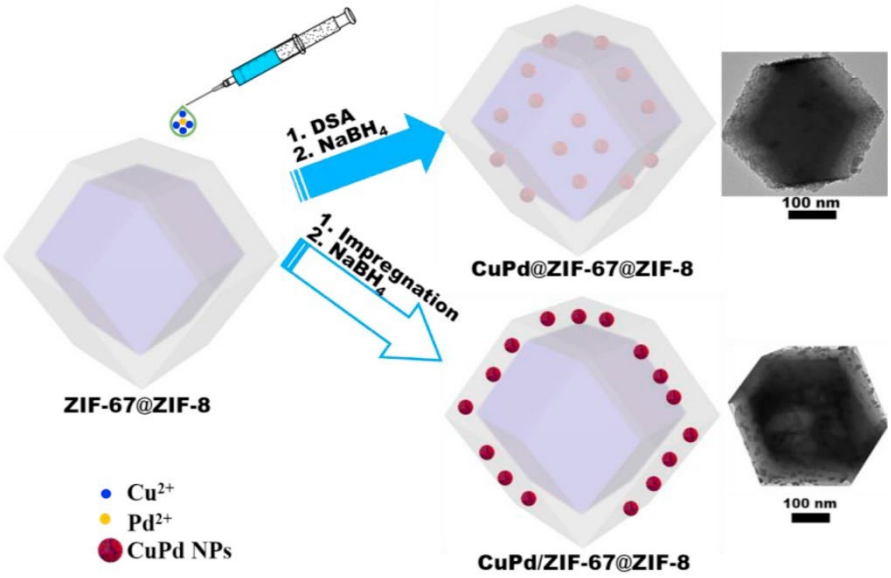

Fig. 2.12 Schematic representation of the synthesis of CuPd@ZIF-67@ZIF-8 and CuPd/ZIF-67@ZIF-8 for catalytic dehydrogenation of ammonia borane [128].

It is worth mentioning that other than simple wet impregnation, which is less controllable over the location of the guest particles, double-solvent impregnation offers an alternative to ensure no guest particles end up at the outer surface of the support substrate. This synthesis approach utilises the hydrophilic properties of the ZIFs to introduce the target metal species into the pores by replacing the apolar solvent with the metal ion containing polar solvent (i.e. water), therefore reducing metal particle migration

[129]. For example, CuPd/ZIF-67@ZIF-8 was synthesised through the wet impregnation approach [128], and the as-obtained CuPd NPs were dispersed on the surface of the core-shell ZIF-67@ZIF-8 instead of within the pores of ZIFs. On the contrary, sample CuPd@ZIF-67@ZIF-8 was synthesised through the double-solvent approach (DSA) (see **Fig. 2.12**), and TEM image showed that the CuPd NPs (with a size of ~3 nm) encapsulated in ZIF-67@ZIF-8 can be achieved. To produce such type of CuPd@ZIF-67@ZIF-8 composite, ZIF-67@ZIF-8 was first suspended in hydrophobic n-hexane, followed by sonication. Then, $PdCl_2$ and $CuCl_2$ aqueous solution was pumped dropwise in the above solution and agitated at ambient temperature to produce purple $Cu^{2+}Pd^{2+}$@ZIF-67@ZIF-8. Followed by the dispersion of dried $Cu^{2+}Pd^{2+}$@ZIF-67@ZIF-8 in methanol, $NaBH_4$ aqueous solution was added into the solution in a dropwise manner to obtain CuPd@ZIF-67@ZIF-8. Other dual metal NPs (ZnPd, FePd, CoPd and NiPd NPs) embedded in ZIF-67@ZIF-8 were also synthesised through this DSA.

Except the encapsulation of the metallic species in ZIFs, organic species have also been reported to form composites with ZIFs. For instance, Jiao et al. reported the construction of polypyrrole (PPy)/ZIFs nanocomposites through a confined polymerisation strategy [130]. Xu and co-workers first reported the introduction of furfuryl alcohol (FA) into ZIF-8, which underwent polymerisation at 80˚C to form PFA/ZIF-8 [131]. The introduced polymerised FA improved the pore texture of the final carbonised product. FA loaded ZIF-68, ZIF-69 and ZIF-70 have also been reported via the impregnation and polymerisation method [132]. Recently, Ma et al. have reported the highly nitrogen-doped porous carbon derived from ZIF-8/urea via a simple wet impregnation process [133]. Externally adsorbed urea was washed away before being subject to heat treatment. Furthermore, ZIF-7/glucose has been reported via a similar method, whereas glucose served as the carbon precursor [134].

In conclusion, impregnation method is a facile and versatile way to synthesise nanoclusters@ZIFs, which can produce both metal and non-metal encapsulated ZIFs in nano level. The fine structures of nanoclusters@ZIFs provide a good foundation for the fabrication of ZIF-derived nanocomposites. Further in situ immobilisation steps, such as polymerisation, chemical reduction/precipitation and hydrolysis reaction, are usually required to anchor the guest components or species inside the pores of ZIF. Moreover, direct pyrolysis can also immobilise the metal particles to obtain ZIF-derivatives [113, 135]. Although the composites will eventually go through heat treatment to obtain ZIF-derivatives, the pre-reduced metallic species are sometimes essential to achieve specific

structure/ZIF-derivatives, as demonstrated by Hu et al. [121]. The surface clumping of the particles could be avoided by using incipient wetness impregnation and double-solvent impregnation, whereas cavity confinement and narrow size distribution of guest particles could be achieved by careful control over the immobilisation conditions after impregnation. It is worth noting that impregnating ZIF in metal salt solutions can sometimes lead to both ion infiltration and metal node exchange [51], which may inevitably complicate the rational design of ZIF-based composites and their derivatives.

2.2.2.2 Particles@ZIFs

With the size of larger composite constituents varying from several nanometres to several hundred nanometres, composites in a larger scale could be formed. Instead of encapsulating small nanoclusters inside the pores, larger particles could act as the seed for the heterogeneous growth of ZIFs, or attach to the surface of the growing ZIF crystals and be confined inside as the crystal growth. Surface chemistry is vital for the successful inclusion of the guest particles. Moreover, single or multiple particles could be included in single or multiple ZIF crystals depending on the experimental conditions. The spatial distribution of the guest particles can be controlled as well. This designability of the Particles@ZIFs composites could lead to abundant derivatives with rich functionalities and structural diversity, suitable for vast applications. Note that these composites can only be achieved by one-pot solvothermal in situ growth of ZIFs on the guest particles. Herein, this method is referred as in situ inclusion of particles to differentiate it from in situ encapsulation of the nanoclusters.

2.2.2.2.1 Guest particle surface modification

Particles with rich surface functional groups, such as polymer and silica spheres, could be the ideal guest particles for the synthesis of Particles@ZIFs composites. For example, Lee et al. have demonstrated the synthesis of polystyrene@ZIF-8 core-shell particles using carboxylate-terminated polystyrene spheres (PSs) with diameter of 0.87 nm [136]. During the synthesis, Zn^{2+} ions interacted with surface carboxylate groups to initiate the growth of ZIF-8 on the surfaces of the spheres. Similar composites were also synthesised using mesoporous silica spheres (MSSs) with diameter of 3 μm [137]. The interaction between Zn^{2+} or Co^{2+} ions and silica hydroxyls promotes the nucleation of ZIF-8 on the surface of the MSSs [138].

However, surface modification is needed for particles that do not contain functional groups on the surface. Although it is possible to grow ZIFs on the bare metal NPs [139], without surface modification, the distribution of guest species in ZIFs is difficult to

control [140]. Research suggests that the uncapped metal NPs will inhibit the crystallisation of ZIF crystal, resulting in smaller crystal size and incomplete inclusion of guest particles [141]. Moreover, without surface modification the metal NPs will not act as nucleation centres for ZIF crystals, and the orientation of NPs within the ZIF crystals will be uncontrollable and individual ZIF crystals will be formed through self-homogenous nucleation [142]. Therefore, the surface affinity of the guest must be modulated in order to ensure the complete inclusion of the guest species and firm bonding at the interface.

Surfactants are widely used to modulate/prepare the particle surface for ZIFs growth. For example, surfactant polyvinylpyrrolidone (PVP), which contains hydrophobic groups that can act as a great stabiliser to prevent the aggregation of NPs [143], can also enhance the affinity between guest particles and ZIFs by the interaction between metal ions and its pyrrolidone rings [144]. Particle encapsulated ZIFs, such as metal NPs [143-148], metal alloy NPs [149-151], metal compounds [152, 153], polystyrene spheres (PSs) [154], and elemental sulphur NPs [155] encapsulated ZIFs have been reported with the assistance of PVP coating. By adjusting the concentration of PVP, the NPs can be tuned from accumulating in the centre of ZIF crystals to evenly dispersed all over the ZIF crystals [156]. Cetyltrimethylammonium bromide (CTAB), an typical ionic surfactant, has also been reported to bridge the interaction between metal NPs and ZIFs [157].

Functional-group-rich coating could also modulate the guest particles as the seed for ZIF growth. A commonly used coating is polydopamine (PDA). It can adhere to almost any surface to form a stable and conformal coating with different thicknesses by adjusting the concentration of the solution during the coating [158]. The metal chelating catechol groups can assist the heterogeneous nucleation and growth of ZIFs on a wide spectrum of NPs to form composites, such as metal NPs, metal nanostars, mesoporous silica, polystyrene nanoparticles, or magnetic iron oxide nanoparticles encapsulated ZIFs (see **Fig. 2.13**) [159]. The PDA layer can assist the growth of ZIFs and endow excellent colloidal stability to NPs, which averts the aggregation of the cores during the formation of particles@ZIFs. Moreover, utilising the redox-active catechol groups of PDA, metal precursors could be reduced locally and form metal nanostructures sandwiched between the guest and the host. Other functional-group-rich coatings such as cellulose [160], lysozyme (LYZ) [161] and polystyrenesulfonate (PSS) [162] have also been reported to assist the formation of particles@ZIFs composites.

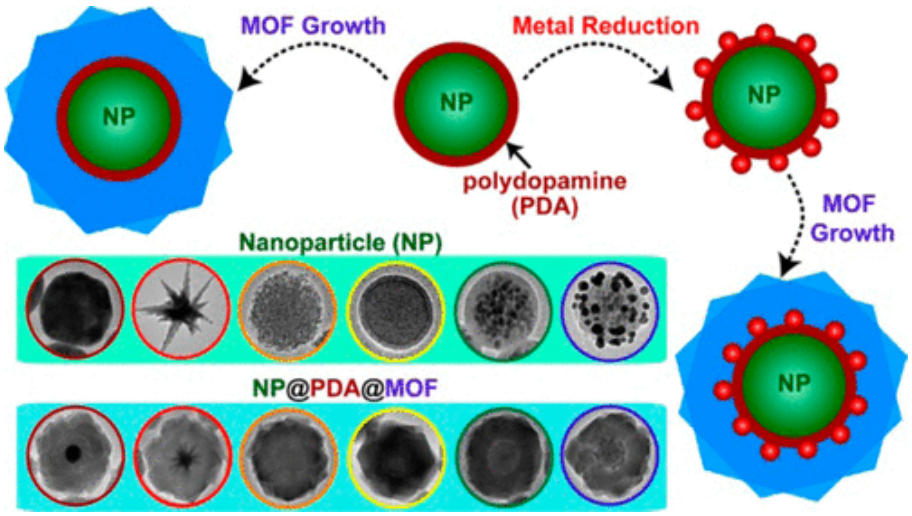

Fig. 2.13 Illustration of the stepwise synthesis of nanoparticle@PDA@MOF and metal nanocatalyst-loaded nanoparticle@PDA@MOF core–shell hybrid nanostructures. TEM images of Au NPs, Au nanostars, mesoporous silica nanoparticles, polystyrene nanoparticles, Polystyrene-trapped magnetic iron oxide nanoparticles (MagNPs), MagNP@PDA@AuNPs, and the correspond nanoparticle@PDA@MOF nanohybrids [159].

Except for the aforementioned metallic and non-metallic particles, ZIFs themselves can also be the guest particles. Reports have demonstrated the confinement of ZIF-8 in ZIF-67 or vice versa [163-165]. With isoreticular structure, similar crystallographic parameters and chemical composition, the ZIFs@ZIFs can be achieved by the epitaxial growth method (EGM), which means the shell is the extension of the core's crystal lattice. The particle shape of the core ZIF and the presence of metal NPs does not disrupt the reconstruction of the standard rhombic dodecahedral crystal shape of the outer ZIFs [166]. Complex structures such as 8-layers interlaced matryoshka structure can be realised [167]. The combination of two ZIFs not only provides two metals for broader applications but also endows the hybrid derivatives with new chemical/physical properties and interfacial functionality [163].

MOFs as the guest species in ZIF-based composites have also been reported. The guest MOFs need to be stable under the growing conditions of ZIFs and have compatible metal nodes or organic linkers to initiate the growth of ZIFs. Feng et al. demonstrate a controlled stepwise synthesis method to fabricate core-shell PCN-222@ZIF-8 with PCN-222 crystals as seed particles [168]. Zn^{2+} can coordinate with the organic linker of PCN-222 to start the growth of ZIF on its surface [169]. However, lattice mismatches between ZIFs and MOFs can lead to increased energy barriers for the heterogeneous nucleation of ZIFs. Liu et al. have developed complex ternary MOF-on-MOF superstructures with ZIF-8,

ZIF-67, Zn/Co-ZIF and MIL-125 [170]. ZIFs are selectively grown on specific facets of bare MIL-125 with minor lattice mismatches at the interface and with other facets uncovered.

With ZIF-incompatible organic linker, metal ions, and lattice structure, epitaxial growth of ZIFs is not possible for most MOFs. A mediator is required to adapt the ZIFs-MOFs interface. Surfactants such as CTAB, PVP, TTAB, CPB and SDS were reported to assist the synthesis of MOFs@ZIFs composites [171-173]. It is worth mentioning that, random copolymer (RCP), which contains multiple functional groups, is a more versatile molecular glue for the in situ growth of ZIF on MOFs demonstrated by Li and co-worker [174]. In this report, ZIF-8 was coated on five different MOFs (Uio-66, MOF-801, MIL-96(Al), MIL-101(Cr), and MIL-53(Cr)) with the help of two homopolymers and four RCPs, respectively. Functional groups of RCPs can coordinate with different MOFs hence mediating the ZIF-MOF interface. A uniform and dense layer of ZIF-8 was obtained with appropriate selections of RCP, reaction time and organic linker to metal nodes ratio. Nucleation on the polymer surface instead of the core surface has eliminated the effect caused by different crystal lattice parameters and coordination modes between ZIF-8 and MOFs.

In conclusion, to effectively form particles@ZIFs composites, the guest particles must be i) stable under the ZIF formation conditions and ii) readily interactive with the metal ions or the organic linker of the ZIFs. The guest particles could be metals, ceramics, polymers, or MOFs as long as the heterogeneous nucleation of ZIFs could happen on their surface or interface.

2.2.2.2.2 Spatial relation of the guest particles

Other than manipulating the surface of the guest particles to achieve successful inclusion, the spatial relationships between the hosting ZIFs and the core guests can be further tailored. The size of the guest species can lead to three different morphologies, I) multiple-core-monocrystalline-shell composite, II) single-core-monocrystalline-shell composite, and III) single-core-polycrystalline-shell composite (see **Fig 2.14**), as proposed by Wang et al. [161]. The author suggests that while smaller NPs can serve as nucleation seeds and lead to the growth of monocrystalline-shell composites (type I and II); ZIF nuclei formed through homogeneous nucleation will randomly attach to the large particles that are introduced before the nucleation of the nuclei, leading to the formation of polycrystalline-shell (type III) composites.

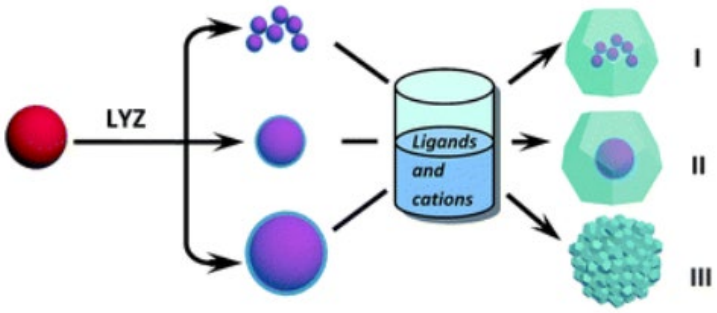

Fig. 2.14 Illustration of the step-wise synthesis of the controlled encapsulation of NPs in MOF crystals to form multiple-(I) or single-core-monocrystalline-shell (II) or single-core-polycrystalline-shell (III) structures [161].

The controllable synthesis of type I and type II particles@ZIFs were also investigated by Chen et al. [145]. The density of ZIF nuclei on Au NPs is the key to the formation of different morphologies. A high density of nuclei can be achieved by low reaction temperature and long incubation time, leading to the coalescence of ZIF-8 nuclei between early-stage single Au NP-ZIF-8 hybrids, resulting in the formation of multi-core-monocrystalline-shell Au@ZIF-8 with further epitaxial growth of ZIF-8. Whereas under high temperature and short reaction time, a low density of nuclei was formed on the Au NPs surface, single-core-monocrystalline-shell Au@ZIF-8 was synthesised via direct epitaxial growth of ZIF-8. These results indicate that particle size, reaction temperature and time will all affect the final morphology of the guest@ZIFs composites. Research also suggests that the number of guest particles within a single ZIF crystal can be rationally controlled by increase in the volume of NP solution added during the synthesis process [175]. However, the amount of NPs encapsulated is limited by the volume of the ZIF crystal, where excess amounts of NPs cannot be completely embedded in the ZIF single crystal. As a result, aggregation is inevitable.

It is worth noting that the spatial distribution of the NPs has also been studied. Huo and co-workers have demonstrated a smart strategy to rationally design the distribution of different NPs with different sizes within the ZIFs crystal [176]. In detail, the spatial distribution of metal NPs can be adjusted by the time of NPs addition during the ZIF formation. Addition at the beginning (T_0) will result in a NPs embedded core. With an additional reaction time, the NPs will be depleted and a NPs free shell will be formed. In contrast, addition after a period of time (T) will result in pure ZIF central areas and shell, but transition layers containing NPs in between. Therefore, sophisticated distribution patterns of different NPs within a single ZIF crystal could be achieved by playing with

the addition sequence of the NPs. The successful inclusion with later introduction of NPs suggests that nanoparticle-induced heterogeneous nucleation is not the dominant mechanism in the inclusion process. Instead, the dominant inclusion mechanism is based on the successive adsorption of NPs on the surface of growing ZIF crystals.

Besides the aforementioned morphologies, the guest species can also be used as a sacrificial template to generate yolk-shell structures [177]. For example, Li et al. have reported the production of yolk-shell Pd@ZIF-8 nanoparticles using core-shell Pd@ZnO NPs as self-template and Zn^{2+} source [178]. It is worth noting that the concentration of the organic linker and the release rate of the metal ions instead of homogeneous nucleation in solution are vital to achieve heterogeneous nucleation on the oxide surface [179]. Thanks to the robust alkali resistant porous structure of ZIFs, sandwich [159], hollow [136], yolk-shell [154, 175, 177, 180], and single-crystal ordered macropore structures [181] can also be realised by the inclusion of specially chosen guest particles, followed by post-synthetic chemical removal of the whole core or the middle layer.

In conclusion, the spatial relationships between the hosting ZIFs and the core guests are controllable by the reaction temperature, reaction time, the size of the guest species, and the time of NPs addition during the ZIF formation. Moreover, sophisticated structured ZIF hybrids could be obtained with carefully chosen guest species. As a result, both new constituents and nanostructures could be introduced to the ZIF derivatives, leading to functional derivatives for various applications [163, 171, 177, 182-184].

2.2.2.3 Surface decorated ZIFs

To form a reverse core-shell structure, single or multiple ZIF crystals could be decorated by discontinuous particle coating or continuous layered coating, which can be realised by in situ growth of the coating, post-synthetic mechanochemical mixing or other physical deposition methods. Surface modification can not only introduce hierarchical pore structure to the composites but also introduce guest metal species, heteroatoms, or even unique morphology and structure to the hybrids. It is also common to produce ZIF-derivatives with complex composition and structure from surface decorated ZIFs. Both organic and inorganic coating will be discussed in this session.

2.2.2.3.1 Organic coating/surface decoration

Thermosetting resin is a kind of organic polymer that can be coated on ZIFs via in situ polymerisation. Composites such as resorcinol and formaldehyde (RF) resin coated ZIF-8 [185] and 3-aminophenol and formaldehyde coated ZIF-8 [186] have recently been reported. Li and co-works have prepared a 4-aminophenol and formaldehyde (AF) coated ZIF-67

via a one-pot synthesis [187]. The resin precursors, 4-aminophenol and formaldehyde, were mixed with the ZIF precursor solutions, $Co(NO_3)_2$ water/ethanol (v/v: 2/1) solution and 2-MeIm aqueous solution, respectively, before mixing the two solutions (see **Fig. 2.15**). The Polymerisation of 4-aminophenol and formaldehyde could be induced by the organic linker of ZIF. Moreover, the fast nucleation of ZIF-67 and the slow polymerisation of AF is the key to the formation of final core-shell structure. The thickness of the coating layer ranged from 11-31 nm and varied with the amount of AF used during the synthesis process. Interestingly, the weak interaction between the O atoms in AF with the Co^{2+} in ZIF-67 could decelerate the growth rate of ZIF, resulting in increasing crystal size. Co/N-doped carbon-based composites were obtained by further heat treatment. AF coating increased the thermal stability of ZIF and prevented the agglomeration of Co NPs during the carbonisation process. It is worth knowing that resin coating can be used to immobilise guest particles on the ZIFs crystals, leading to a core-shell sandwich structure. For example, Liang et al. have synthesised a RF coated ZIF-8 with Pt NPs loaded on the surface of ZIF crystals prior to the RF coating [185]. The organic coating can provide extra protection on the immobilisation of the metal NPs and prevents severe aggregation during pyrolysis. Moreover, by introducing other metal ions into the organic coating (e.g. Co or Ni), PtCo or PtNi alloy NPs embedded in porous carbon could be formed.

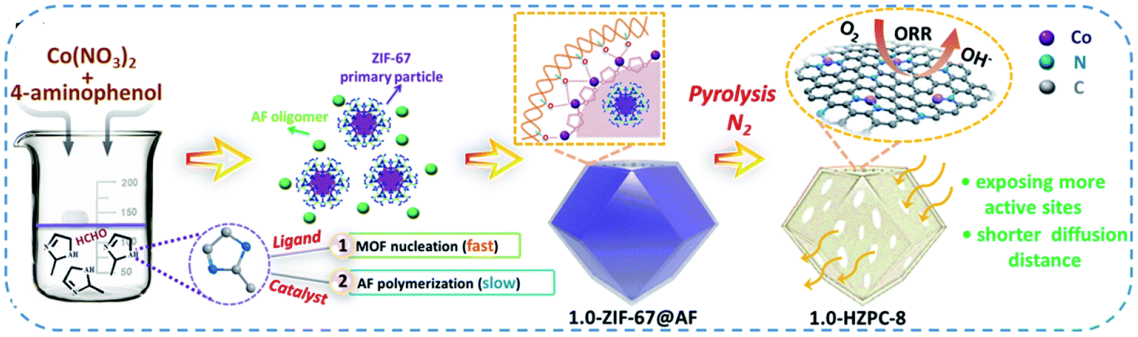

Fig. 2.15 Illustration of the formation of 4-aminophenol and formaldehyde (AF) coated ZIF-67 via a one-pot synthesis [187].

Except serving as a protective layer to immobilise surface loaded guest particles or prevent agglomeration of metal NPs during the carbonisation process, organic coatings can also introduce heteroatoms to the ZIF-based composites and their derivatives. Ma et al. have coated the N, P and S containing poly(cyclotriphosphazene-co-4,4′-sulfonyldiphenol) (PZS) cross-linker polymer on ZIF-67. N, P, S tri-doped hollow carbon shells were obtained with appropriate heat treatment. Moreover, ZIF-8@PZS and their tri-doped hollow carbon derivative have also been reported [188]. It was found that the

existence of the S element in the polymer shell is the key to the formation of the hollow structure. The S element could be removed by substitution of bis(4-hydroxyphenyl) sulfone with bis(4-aminophenyl) during the polymerisation of the cross-linker polymer. Other organic coatings such as N and P-containing cross-linked oligomer, oligo(cyclotriphosphazene-co-hexahydroxytriphenylene) [189] and B-containing 1,4-benzenediboronic acid (BDBA)-Tannic acid (TA) network [190] can also be used to introduce heteroatoms to the ZIF-derived carbon.

Besides the aforementioned polymer and resins, biological compounds have recently become one of the most popular coating materials due to their robustness, easy synthesis and facile functionalisation. For example, polydopamine (PDA) can polymerise on the surface of ZIF particles to form core-shell structures. The N containing functional group structure can not only introduce N element into the ZIF composites [191] but also coordinate with metal ions to form metal-dopamine complexes, hence introducing metal elements to the composites and their derivatives [192]. Recent research shows that the PDA derived N-doped carbon shell can protect the metal-based sites from acid/base attacks [193]. Meanwhile, the abundant N-dopants and graphitic carbon can also provide plentiful active sites for the ZIF-derived electrocatalysts. Interestingly, composites with different morphology and composition could be formed by calcining the ZIF@PDA composites under different temperatures [194].

Tannic acid (TA) can also readily bind with the organic and inorganic surface via covalent and non-covalent bond interactions and is a low-cost alternative to PDA coating [195]. Ge et al. have synthesised TA coated ZIF-67 through a simple hydrothermal process [196]. Due to the instability of ZIF under acidic environment, increased TA concentration will lead to a tendency for structural collapse. With prolonging coating and etching time, the structure of the ZIF-67 crystals can evolve from solid to core/shell and finally to hollow polyhedron structure. A report shows that TA can bind with heteroatom-containing organic molecules [197] as well as the metal ions [198] to further functionalise the ZIF@polymer hybrides and their derivatives. P-rich Phytic acid (PA) shows similar behaviour to TA when coated on the surface of ZIFs [199-201]. Moreover, polysaccharides such as chitosan, sodium alginate, heparin, hyaluronic acid, chondroitin sulfate, dermatan sulfate, glucose, citric acid, pyrrole and β-cyclodextrin have been reported to form coatings on ZIFs [202-204]. They are all functional group-rich biomacromolecules that can be coated on ZIFs via hydrothermal monomers gelation [202], mechanochemical synthesis

[203], or freeze-dry synthesis method [204] to produce functional carbon-based ZIF-derivatives for various applications.

Except for coating on individual ZIF crystals, organic coatings could be coated on multiple ZIFs particles and form cluster structures. For example, Cai et al. have prepared porous phenolic resin coated ZIF-67 films by mixing pre-synthesised ZIF-67, mesoporous soft template F127 and phenolic resin mechanically [205]. The introduction of porous phenolic resin brings more specific surface area and pore volume to the composites and their thermal derivatives, which is favourable for adsorption application. Sankar et al. have demonstrated the fabrication of ZIF embedded polymeric nanofibers through electrospinning using polyacrylonitrile (PAN) as the polymer source [206]. The carbonised sample shows a hierarchical porous structure with large surface area and rich defects. Except PAN, poly(vinyl alcohol) (PVA) [207] and poly (lactic acid) (PLA) [208] have both been reported to serve as organic matrixes for the embedment of ZIFs.

In conclusion, although the organic coating can be readily decomposed during heat treatment, it is still a common way to functionalise ZIFs and their thermal derivatives. It can not only introduce heteroatoms and metal species into the ZIF hybrids but also simultaneously impose the hybrids with macrostructures. Moreover, it can act as a protective layer during the pyrolysis, to immobilise and stabilise the metal NPs during carbonisation process and to prevent the NPs from severe aggregation.

2.2.2.3.2 Inorganic decoration/coating

Metal NPs are one of the most popular surface decorators for ZIF-based composites. Pre-synthesised metal NPs can be anchored on the ZIF surface with the help of functional group rich media such as thermosetting resin [185], water-soluble glutathione (GSH) [71] and PVP [209]. The surface decoration of metal NPs could also be achieved by direct precipitation of the metal NPs via a wet chemical reduction method [210]. In a typical synthesis, metal salts were first added to a homogeneous ZIF containing solution. Then a reducing agent-containing solution was rapidly added to the mixture under vigorous stirring to reduce the metal ions into metal NPs. Direct heat treatment on the precursor salt loaded ZIFs can lead to metal NP reduction and ZIF-derivative formation simultaneously. However, the as-obtained metal NPs show much larger particle size and a wider range of size distribution [211]. Other metal NP decorated ZIFs, such as Ru NP decorated ZIF-67 [212], Pd/Pt/Au NP loaded ZIF-8/67 [213], and CuPd alloy NP coated ZIF-67@ZIF-8 [128] have been reported utilising this deposition-precipitation method, which is

a universal route towards metal NP coated ZIFs and offer a feasible way to obtain abundant ZIF-derivatives.

Except metal NPs, a continuous metal layer can be deposited on ZIF surface via physical vapour deposition (PVD), or more specifically, sputter-coating/sputter deposition method [214]. The thickness of the coating can be controlled by adjusting the applied electric current and the sputter duration, and different metals could be coated on the ZIF particles by simply changing the metal target. Moreover, controllable coating could be realised by masking technique. Maspoch and co-workers have synthesised asymmetric metallic Janus ZIF particles by sputter depositing a layer of metal(s) (Au, Co or Pt) on one side of the ZIF particles' surface. The ZIF was first drop-cast onto a planar surface before sputter-coating to mask one side of the particles [215]. An anisotropic ZIF-metal composite with two chemically distinct regions can be obtained by detaching the half-coated ZIF particles from the surface. In general, this method is feasible for a wide range of metal, metal oxide, polymer coating and more [216], applicable for different types of ZIFs, which offer great opportunities in designing complex surface decorated ZIF based composites and their derivatives.

Besides pure metal, metal sulphides can also be coated on ZIFs and were commonly realised by the hydrothermal in situ transformation method, in which ZIFs act as sacrificial templates. ZIFs-metal sulphides Core-shell and yolk-shell structure could be obtained by fine-tuning the reaction duration and precursor concentration. For example, Li et al. have recently synthesised a ZnS coated rod-like ZIF-L with thioacetamide (TAA) as sulphurization agent [217]. The surface-coating ZnS gradually changed from discontinuous particles to a continuous shell as the reaction time increased. Finally, all ZIF-L would be consumed, and a phase pure tube-like ZnS was obtained. Song et al. have also reported a hydrothermal synthesis of CoS/ZnS coated CoZn-ZIF with TAA as sulphurization agent [218]. The CoS/ZnS coating could protect the inner Co atoms from agglomeration during and after the pyrolysis of the core-shell hybrid. However, using ZIFs as sacrificial templates, the formation of the metal compound coating involves a dissolution-regrowth process, which would eventually lead to the formation of hollow metal compound cages instead of surface coated ZIFs composites [192]. Interestingly, Qiu et al. have shown that it is possible to realise metal compound coating with the ZIF-8 core intact by providing extra Zn precursor [219]. During the synthesis, both Cd and Zn salts were mixed with ZIF-8 suspension. Then a Na_2S solution was added dropwise for the surface precipitation of the $Cd_{0.5}Zn_{0.5}S$ particles.

Layered double hydroxides (LDHs) are a very popular coating for ZIFs. They are a kind of anionic clays with layered structure and chemical formula of $[M^{2+}_{(1-x)}\ N^{3+}_{(x)}\ (OH)_2]^{x+}\ [A^{n-}_{x/n\cdot}\ yH_2O]$, where M^{2+} is a divalent cation (e.g. Mg^{2+}, Ni^{2+}, Fe^{2+}, Co^{2+} and Zn^{2+}), N^{3+} is a trivalent cation (e.g. Al^{3+}, Fe^{3+}, Mn^{3+}, Co^{3+} and Cr^{3+}) and A^{n-} is a charge-balancing interlayer anion (e.g. NO_3^-, SO_4^-, CO_3^-, Cl^-) [220]. The abundant metal cations and the ease of mutual transformation between ZIFs and LDHs [221-224] suggests that large varieties of LDH coated ZIF-based composites can be obtained easily. For example, Saghir et al. have synthesised a NiCo-LDH coated ZIF-67 via a hydrothermal method [225]. The Ni salt was mixed with ZIF-67 in ethanol, and the hydrolysis of $Ni(NO_3)_2$ in ethanol would lead to the dissolution of ZIF-67 and release of Co^{3+} ions [226]; the Co^{3+} ions will then co-precipitate with Ni^{2+} ions to form NiCo-LDH on the surface of ZIF crystals. Similar hybrids were also produced by a one-pot synthesis method, where both LDH precursor and ZIF precursors were mixed in methanol solution and incubated in an autoclave reactor [227]. Core-shelled ZIF-67@Co-Ni LDH polyhedral (C-ZIF@LHD), yolk-shelled ZIF-67@Co–Ni LDH polyhedra (Y-ZIF@LDH) and hollow Co–Ni LDH polyhedra (H-LDH) were obtained with increasing reaction time (see **Fig. 2.16**), which suggested that accurate control over the ZIF template etching and the rates of formation of LDH are vital for the structure control. It is worth noting that no LDH shell would be formed when ZIFs undergo rapid etching. The water-content-dependent etch rate could be reduced by adding ethanol to the solution [228]. LDH coated ZIF hybrids such as ZIF-12/Fe-Cu LDH [229], ZIF-9(III)/Co LDH [230], rGO@ZIF-67@NiAl-LDHs [231] and macro-microporous ZIF-67@NiCo LDH [232]have been reported recently. Moreover, the thermal derivatives of the LDHs/ZIFs hybrids have also been widely reported and show great potential in all kinds of applications [233-235].

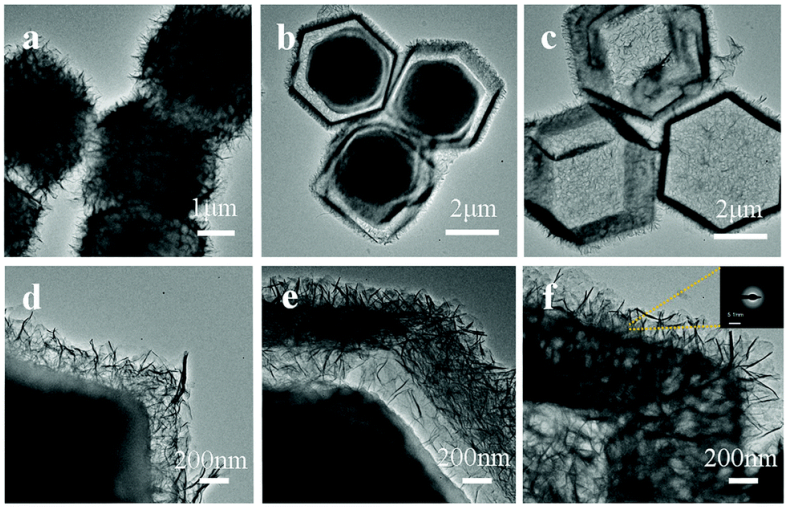

Fig. 2.16 (a–f) TEM images of C-ZIF@LDH (a and d), Y-ZIF@LDH (b and e), and H-LDH (c and f). The inset in (f) shows the SAED pattern of the sheets of Y-ZIF@LDH [227].

In addition, metal oxides coated ZIFs have been widely reported. For example, Yang et al. have synthesised ZnO coated ZIF-8 by simply mixing ZIFs with $AgNO_3$ aqueous solution [236]. The authors proposed that due to the hydroxyl rich environment resulted from the high oxidisability of Ag^+, the chemical reaction, $Zn(MI)_2 + 2Ag^+ + 2NO_3^- + H_2O \rightarrow Zn_2^+ + HAg(MI)_2 + 2OH^- \rightarrow Zn(OH)_2 \rightarrow ZnO + H_2O$, took place. Higher concentration of $AgNO_3$ would lead to smaller and more rounded ZIF-8 particles and deterioration of the total surface area and pore volume. Chang et al. have reported a $Zn(OH)_2$ coated ZIF-8 by directly mixing NaOH solution with $Zn(NO_3)_2$ containing ZIF-8 suspension [237]. The hydroxide coating can be converted to ZnO by a low-temperature thermal treatment in air. Results show that a high concentration of zinc salt is vital to the external deposition of $Zn(OH)_2$, whereas a low concentration would lead to nanoconfinement of the hydroxide in the ZIF cages. Zhang et al. have reported a TiO_2 coated ZIF-67 by in situ hydrolyses of tetrabutyl titanate [238], and the thickness of the TiO_2 shell could be controlled by increasing the amount of tetrabutyl titanate used. Furthermore, Lyu et al. have reported the synthesis of ZIF-67@$CoMoO_4$-$Co(OH)_2$ yolk-shell structure using Na_2MoO_4 as precursor [239]. The released Co^{2+} from the dissolution of ZIF-67 reacts with MoO_4^{2-} to form $CoMoO_4$, whereas the alkaline environment provided by Na_2MoO_4 encourages the formation of $Co(OH)_2$ around the ZIF-67 core. A longer reaction time could lead to the complete dissolution of the ZIF core. CoO-MoO_2 nanocages could be obtained by pyrolysis the synthesized ZIF-67@$CoMoO_4$-$Co(OH)_2$ under H_2/Ar atmosphere. In addition, $CoWO_4$-$Co(OH)_2$ shell could also be obtained by replacing Na_2MoO_4 with Na_2WO_4.

It is worth mentioning that SiO_2 is also a popular surface decorator for ZIFs. The exceptional mechanical properties of SiO_2 coating could significantly enhance the mechanical properties (i.e. toughness and hardness) of the composites [240], resulting in stable core-shell or yolk-shell structure before and after thermal treatment [241, 242]. Moreover, the SiO_2 coating could protect the ZIF core from undesirable fusion and aggregation of individual nanoparticles during the pyrolysis process [243], which ensures the exposure of active sites, high porosity for reaction mass transport and good electrocatalyst dispersibility. Epitaxial growth of SiO_2 coating could be achieved by alkali-catalysed hydrolysis of tetraethoxysilane (TEOS) [241]. The shell thickness could be easily modified by adjusting the amount and the concentration of the precursor used during the hydrolysis process. It was found that thicker shell would lead to larger surface area of the thermal derivative of the ZIF-SiO_2 hybrid, smaller particle size , better particle dispersion, and consequently better catalytic performance of the derivatives [244]. However, a thick SiO_2 shell could hinder reactant diffusion during the catalytic process, resulting in low catalytic efficiency. However, with the addition of CTAB as the pore directing template, a mesoporous SiO_2 shell could be obtained [243]. These mesopores can be used as channels for mass transport during the catalytic reaction. Furthermore, through steric hindrance effects of these pores, the molecular size of the reactant could be selected, which is beneficial to rational design of the catalyst materials [245].

In conclusion, inorganic surface coating/decoration could bring both metallic and inorganic non-metallic materials into the ZIF-based composites. These composite materials can withstand high temperatures and introduce new constituents to the corresponding thermal derivatives.

2.2.2.4 ZIFs on supports

Unlike the coating on small 0D particles, which can be realised by single-crystal confinement, the coverage of ZIFs on the surface of large substrates (1D fibre, 2D plate and 3D foam) is always composed of multiple crystals. Different growth conditions would lead to partly or fully coverage, continuous or discontinuous layer, and intergrown or non-intergrown grains of ZIFs. Synthesis of ZIFs on supports could be achieved by either chemical approaches such as in situ heterogeneous growth or physical approaches such as glue adhesion. Problems such as poor compatibility and weak interaction between ZIFs and substrate could lead to unsatisfactory application properties. Therefore, intermolecular forces such as covalent bonding, ligand bonding, electrostatic interactions and hydrogen bonding are beneficial to the attachment of ZIFs to supports, achieving a

controllable synthesis of different support@ZIFs structures, and provide stable composites that are suitable for further treatments [246]. The synthesis strategies of ZIFs on supports can be catalogued into two main types: ZIFs directly grow on certain kinds of interactive substrates where no additional surface treatment is needed, and ZIFs grow on mediators which have been pre-treated on the surface of substrates.

2.2.2.4.1 Direct growth on substrates

Direct growth of ZIFs can simply be achieved by the seed-and-growth method. Seeding techniques such as dip coating [247], spin coating [248], electrospinning [249] and chemical vapour deposition [250] have been reported for the in situ coating of ZIFs on glass/silicon [249, 251], porous ceramics [248, 252], metal [253] and polymers [254]. The thickness, continuity and uniformity of the ZIF coating could be controlled by epitaxial secondary growth [255] and layer-by-layer method [256]. It has been reported that the structure of the ZIF coating depends on the type of metal salt used [257]. Stronger interaction between the metal ion and the counter anion in the metal salt will lead to slower nucleation rate of the ZIF-8 and fewer nuclei formed on the surface of the support, which consequently results in larger grain sizes and poorer grain boundaries (see **Fig 2.17**.).

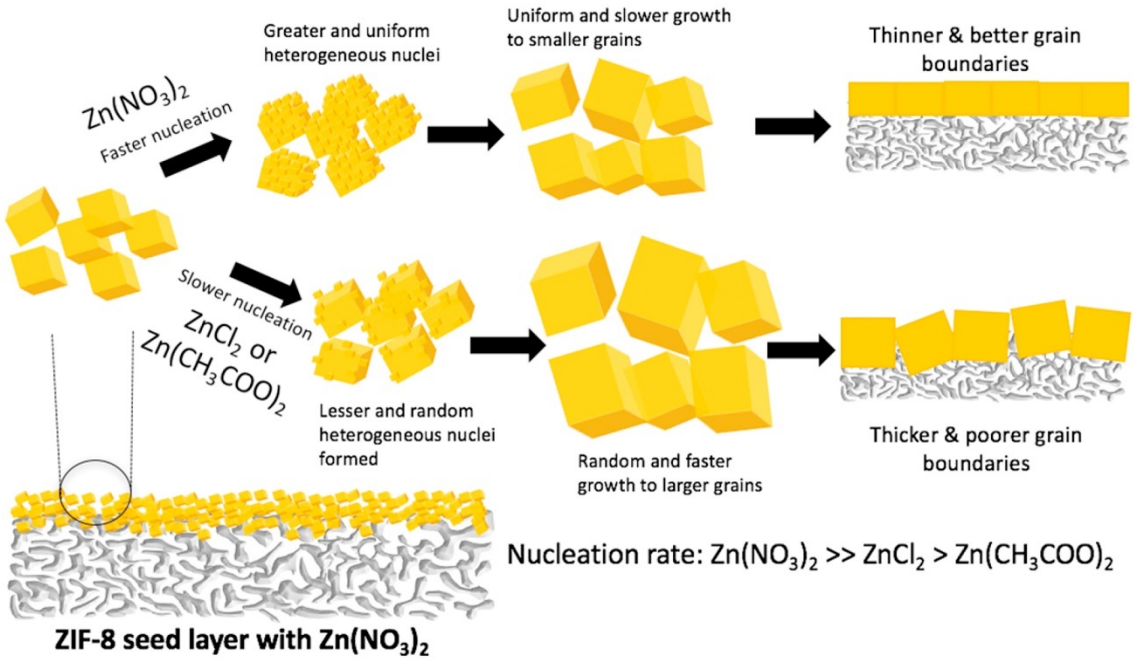

Fig. 2.17 Illustration of the proposed process/hypothesis for secondary growth from a ZN seed layer. Note that fast heterogeneous nucleation with zinc nitrate leads to the uniform growth of the seed crystals, resulting in a thinner membrane with better grain boundary structure [257].

Besides the seed-and-growth method, direct interaction between the ZIF precursor and the substrate can also lead to in situ formation of ZIF coating. Due to the chemical

linkage between the coating and the support, ZIF crystals could be tightly anchored on the support surface producing stable composites for various applications and further treatments. For example, Wang et al. have synthesised ZIF-67 on CeO_2 nanowires [258]. By premixing the nanowires with the organic linker, part of the MeIM would coordinate with Ce ions and allow further nucleation of ZIF-67 on the surface of CeO_2 nanowires.

Based on this principle, Zn and Co containing substrates such as ZnO and CoO are widely used as support for the direct growth of ZIFs. Not only the Zn and Co ions from the substrate can coordinate with MeIM to initiate the heterogeneous nucleation of ZIFs, but the support itself can also serve as a sacrificial template, therefore core-shell structure, layered sandwich structure and hollow nanotube structure with different degrees of sacrificial replacement have been obtained [259-261]. It was found that adding precursors in sequence was the key to successful ZIF coating [262]. By contrast, adding all precursors at once would lead to high precursor concentration, triggering both homogeneous and heterogeneous nucleation. Moreover, without the protective ZIF-8 seed layer, the ZnO substrate would be destroyed by a random etching process, which eventually leads to the formation of 0 D core-shell polyhedral particles. Furthermore, the growth kinetics of ZIF depends on the dissolution kinetics of the substrate [263]. Both the concentration of the organic linker and the exposed faces of ZnO will affect the nucleation of ZIF crystals; And uniform 2D layer or 3D nuclei of ZIF can be obtained by adjusting the synthesis parameters. It is worth noting that a secondary seed-and-growth method was developed based on the sacrificial template method, which allows the coating of ZIFs on a weakly interacted substrate by pre-seeding the metal oxide on the surface of the substrates [264-268]. A densely-packed metal oxide seed layer that is strongly anchored on the support surface is essential for the formation of well intergrown polycrystalline membranes. In addition, the addition of sodium formate is vital for the in situ formation of a continuous well-intergrown ZIF layer without cracks [269].

Layered double hydroxides (LDHs) were found to be a perfect support for the growth of ZIFs, because the surface of LHDs contained plenty of evenly distributed unsaturated metal coordinate sites, which would attract the free organic linker molecules in the reaction solution, leading to in situ heterogeneous nucleation and epitaxial growth of ZIFs [270]. It is found that the ZIF-67 would only grow on CoAl-LDH instead of MgAl-LDH, which indicates the specific interaction between the Co^{2+} in the CoAl-LDH and MeIM is vital to the formation of ZIFs [271]. It was also found that the Co/Al molar ratio of LHD affected the morphology of the coating. With Co/Al=1:2, discrete ZIF-67 crystals

grew, and sparse carbon caves formed after pyrolysis. By increasing the Co/Al molar ratio to 2:1, a dense and uniformly oriented ZIF-67 layer was formed, which could be converted into a well-organised 2D honeycomb-like carbon network. Moreover, ZIF-8 was unable to grow on the CoAl-LDH properly, and ZnAl-LDH would be a better substrate for ZIF-8 [272].

Except for the aforementioned metal ion nucleation sites, substrates which already contain rich functional groups can guide the in situ growth of ZIFs. For example, Jia et al. have reported an in situ growth of ZIF-67 on Alginate fibres (AF), a natural polymer extracted from seaweeds [273], via surface functional group chelating [274]. The AF is composed of polysaccharides with abundant hydroxyl and carboxyl groups which can chelate with metal ions such as Fe^{3+}, Co^{2+} and Ni^{2+} to form an 'egg-box' structure. Co-AFs were simply obtained by soaking the AFs in cobalt salt solution, in which the Co ions in Co-AFs served as growing sites for the formation of Co-based ZIF. Ma et al. have grown ZIF-8 on cellulose fibres with a similar binding mechanism [275]. Both electrostatic and hydrogen interactions between the ZIF and the substrate were found. Other functional group-rich substrates such as chitosan aerogel [276], graphene oxide [277], reduced graphene oxide [278], highly fluorinated graphene oxide [279], and oxidised single-walled carbon nanotubes [280] have also been reported for the growth of ZIFs.

It is worth mentioning that synthesising ZIF-based hydrogels/aerogels with the help of polymer is a feasible way to obtain high dimensional 3D structures on a larger scale. ZIF crystals can be incorporated into the extremely lightweight network by the ex-situ mixing of pre-formed ZIF crystals with intermediate hydrogels or by the in situ growing of ZIFs on the pre-treated ZIFs precursor containing aerogels. Composites include ZIF-8@polylactic acid (PLA) aerogel [281], ZIF-8/polyvinyl alcohol (PVA) hybrid aerogels [282], silica aerogel-ZIF-8 hybrids [283], ZIF-8@cellulose aerogel composites [284], reduced graphene oxide/ZIF-67 aerogel composites [285], hierarchically porous graphene/ZIF-8 hybrid aerogel [286] have been reported. Combining hydrogels/aerogels with ZIFs has entrapped the ZIF crystals in the polymer networks, which not only endows the composites with properties such as open porous structure and large empty spaces that impart extrinsic hierarchical porous structure to the composites, but also enables the easy combination of ZIFs on different substrates. As a result, the composites and their derivatives can offer high accessible surface areas, abundant surface active sites and easy mass transport kinetics. Moreover, the aerogel is mechanically flexible and tolerable to cutting, moulding and patterning, which could render the composites with macroscopic

shapeability and mechanical flexibility, changing ZIFs powder into an easy handling form [287].

Besides, ZIF coatings could also be deposited on substrates by mechanical method. For instance, Cheng et al. have developed a unique but versatile binder-/solvent-free hot-pressing (HoP) method to produce various ZIFs (ZIF-8, Ni-ZIF-8, ZIF-67 and ZIF-9) on different flexible substrates (i.e. anodic aluminium oxide, copper foil, nickel foam, glass/carbon cloth and glass fibres) [288]. ZIF precursor powders were mixed with polyethylene glycol (PEG) and placed on the desired substrates during the fabrication. A piece of aluminium foil was used to pack the sample before being pressed by an electric heating plate at 200 ˚C for 10 min, and a washing step was taken to remove the unreacted ZIF precursors. This HoP method can be scaled up easily and allows facile fabrication of mixed metal ZIF coating and mixed ZIF coating on various substrates.

In conclusion, ZIF coating could be realised by direct physical deposition of pre-synthesised ZIFs, or in situ growth of ZIFs on the substrate. Note that the direct growth of ZIFs on substrates mainly relies on the formation of chemical bonds at the ZIF-substrate interface, therefore the substrate must contain compatible metal ions or functional groups. Using sacrificial substrate, composites with controllable morphologies and structures could also be obtained.

2.2.2.4.2 Growth on pre-treated supports

Surface pre-functionalisation enables more types of substrates to be coated by ZIFs and lead to abundant ZIF-based composites and novel ZIF derivatives. For instance, carbon-based substrates are popular due to their ability to improve the electrical conductivity of the hybrids, as a result, their thermal derivatives could lead to superior performance in energy applications. In order to introduce surface functional groups, carbon substrates need to be chemically oxidised with acids. Using the surface functionalised carbon as substrate, the in situ growth of ZIFs can be initiated at the organic linkers anchored functional group sites [289], or through electric static force between positively charged metal ions and negatively charged substrate surface [290]. In situ growth of ZIFs on 1D CNTs [266, 291], 2D carbon cloths [292], graphene oxides (GO) sheets [293, 294], reduced GO [294], and 3D carbon sponge [246, 295, 296] have all been reported.

Based on the same coordination principle of growing ZIF on acid-treated substrate mentioned earlier, covalent linker grafting could also meditate the substrate and promote local heterogeneous nucleation of ZIFs, but with more precise control on the morphology and structure of the ZIF coating layer. Pokhrel et al. have modified the surface of tubular

porous α-alumina support with 3-(2-imidazolin-1-yl)propyltriethoxysilane (IPTES) (see **Fig. 2.18**) [297]. The IPTES with imidazole end groups could coordinate with Zn^{2+} and act as nucleation sites for the growth of ZIF-8 crystals. The grafting density of IPTES could control the grain size of the polycrystalline ZIF layers that lower graft density would lead to the secondary growth of ZIF-8, resulting in a well-intergrow structure. Lately, Allegretto et al. have synthesised ZIF-8 films on silicon wafers by utilising poly(1-vinylimidazole) (Pvlm) brushes as 3D primers [298]. The Si support was first primed with aminopropyltriethoxysilane (APTES), followed by Br-/*i*BuBr modification to prepare the polymerisation site for the Pvlm. The grafted Pvlm brushes were able to coordinate with imidazole moieties and are capable of preconcentration of Zn^{2+}, which initiated the heterogeneous nucleation of ZIF-8. ZIF-90 and ZIF-22 have also been reported to be covalently grafted onto the Si chip [299] or porous ceramic support [300-302] via condensation of imine with APTES decorated surfaces.

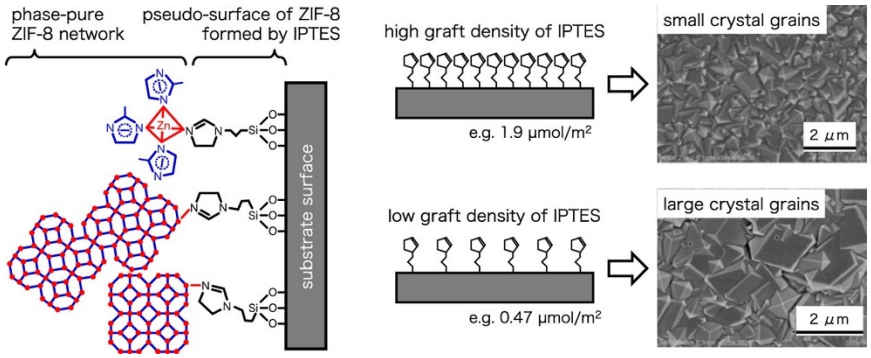

Fig. 2.18 Schematic illustration of the heterogeneous nucleation and crystal growth on the IPTES-grafted surface. The ligand-analogous surface modifier induces preferential heterogeneous nucleation and determines the grain size of polycrystalline ZIF-8 membrane [297].

Not surprisingly, surfactants are also widely used to promote in situ coating of ZIFs [296, 303, 304]. Besides directing the growth of ZIF, it is also found that surfactants can protect the substrate from dissolution during the formation of ZIF [305]. Fu and co-workers have applied non-ionic, anionic and cationic surfactants to synthesise ZIF-8/CNT composites, respectively [306]. SEM images show that different surfactants would affect the size of ZIF crystals attached to the CNTs. Compared with the acid- and surfactant-functionalised CNTs, bare CNTs have fewer nucleation sites and therefore led to larger crystals. Moreover, the use of surfactants could ensure good dispersion of CNTs during the synthesis [304, 306, 307]. Reports also show that the surfactants can act as the template for the in situ nucleation of hierarchical porous ZIFs [308-310], which would bring more dimension to the ZIF-based composites.

Interlayer coatings are widely used to modulate the substrate before the growth of ZIFs. For example, the easily synthesised functional group-rich PDA has been widely reported as modulating layer. It can stick to many kinds of surfaces by forming strong covalent and noncovalent bonds [311], and the abundant functional groups could chelate with metal ions to guide the formation of ZIF layers on the previously incompatible substrates [312]. Substrates such as stainless-steel-nets [313], polypropylene (PP) [314], polysulfone (PS) [315], PEEK [316], melamine sponge [317] and porous Al_2O_3 [158, 318] have been modified by PDA for the in situ growth of ZIFs. Recently, Papurello et al. have reported a simple in situ growth of ZIF-8 onto a common aluminium substrate by pre-treating the substrates in dilute HCl to obtain a surface layer of aluminium hydroxychloride [319]. The acid-induced surface cationic sites of $Al(OH)_nCl_{3-n}$ can then bound with MeIM to facilitate the formation of ZIF-8 nuclei over the Al surface. With subsequent secondary growth, ZIF-8 crystals were firmly anchored on the acid-induced rough substrate surface.

Zhang et al. have used curli nanofibers (CNFs, major protein components of *E. coli* biofilms, also known as adhesive bacterial amyloid nanofibers) as a universal coating to mediate the nucleating and growth of ZIF on various polymeric substrates [320]. The hydrophobic amino acid-rich structure empowered CNFs with strong adhesion towards hydrophobic surfaces, whereas the polar functional groups can provide large numbers of nucleation sites, contributing to the growth of ZIF-8 layers on the mediated substrates. Experiment shows that a complete ZIF-8 layer can grow not only on a flat substrate but also on complex-shaped objects such as tubes, 3D printed pyramid scaffolds and woven fabric with the assistance of CNF coating, which opens up a new route towards complex ZIF-based composites and their derivatives.

Recently Li et al. have shown a scalable route to grow a nanometer-thick ZIF layer on a polymeric substrate [321]. The zinc-ethanolamine gel complex was first coated on the substrate through a sol-gel process. Then the gel layer was transformed into a continuous and uniform ZIF-8 layer through ligand vapour deposition in an autoclave. This transformation can be taken as the coordination reaction between the metal ions in the gel and the organic linkers. The thickness of the ZIF-8 layer can be manipulated by controlling the coating time and the sol concentration. A ZIF-8 layer of 87 - 757 nm coated on the substrate was fabricated in the reported work. Xia and co-workers have later synthesised a ZIF-8 on anodic aluminium oxide (AAO) composites by spin coating the ZIF seeds containing gel on the substrate, followed by an in situ crystallisation step, revealing the versatility of this gel assisted coating method [322]. Asynchronous

crystallisation between the top and bottom of the gel layer results in larger crystals formed at the top and smaller at the bottom, which is critical to the formation of defect-free ZIF coating. Moreover, the thickness of the coating can be reduced by decreasing the ZIF precursors' concentration in the solution. Therefore, sol-gel coating method holds great potential for the produce of ZIF-based composites and derivatives, due to its excellent controllability over the thickness of ZIF coating, the facile and scalable synthesis process as well as the broad applicability over diverse substrates.

It is worth mentioning that polymers could act as glues to stick ZIF powder on the substrate physically. As reported by Falcaro and co-workers, ZIF-9 could be coated on Si wafer with the help of heat softened phenyltriethoxysilane (PhTES) which could provide a viscous surface for the adhesion of ZIF particles. The deposition and heating steps were repeated to form layers of ZIF-9 crystals until a dense coating was obtained. Polyethyleneimine (PEI) has also been reported as the binder between ZIF and porous alumina support [323].

In conclusion, the incompatible substrates can be modified by acid treatment, linker grafting, surfactant coating, interlayer coating, gel-assisted in situ formation and polymer glue adhesion for the surface coating of ZIFs with controllable thickness and morphology. These composites could open up a new avenue towards complex ZIF-derivatives for various applications.

2.3 Synthesis of ZIF-derivatives

Using different as-synthesized ZIF-based composites as precursors, various kinds of ZIF-derivatives with different compositions, morphologies and structures can be generated via heat treatment. Factors such as heat treatment atmospheres, temperatures, heating process programme and the extra reactive agents used can affect the composition and morphology of the derivatives. Both metals and heteroatoms could be incorporated into the resulting composites through the thermal treatment processes. In general, the synthesis of ZIF-derivatives can be realised via heat treatments in different gas atmosphere, including under protective atmosphere, in reactive atmosphere and in volatile reactant containing atmosphere, which were summarised in **Fig. 2.19** and comprehensively discussed below.

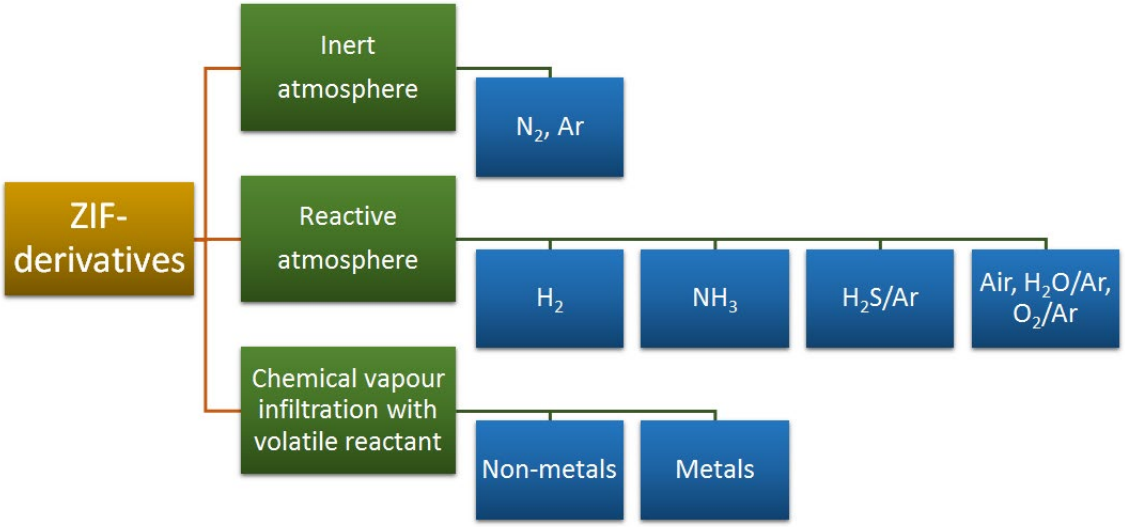

Fig. 2.19 Methods for the preparation of ZIF-derivatives in different gas atmospheres.

2.3.1 Inert Atmosphere

Heat treatment of ZIFs-based composites in inert atmospheres such as argon or nitrogen is one of the most basic operations to obtain carbon-based ZIF-derivatives. Based on TGA study under inert gas, ZIFs would decompose at around 450-600˚C [324, 325]. Therefore, by fine control over the pyrolysis temperature, the composition of the derivatives can be precisely controlled.

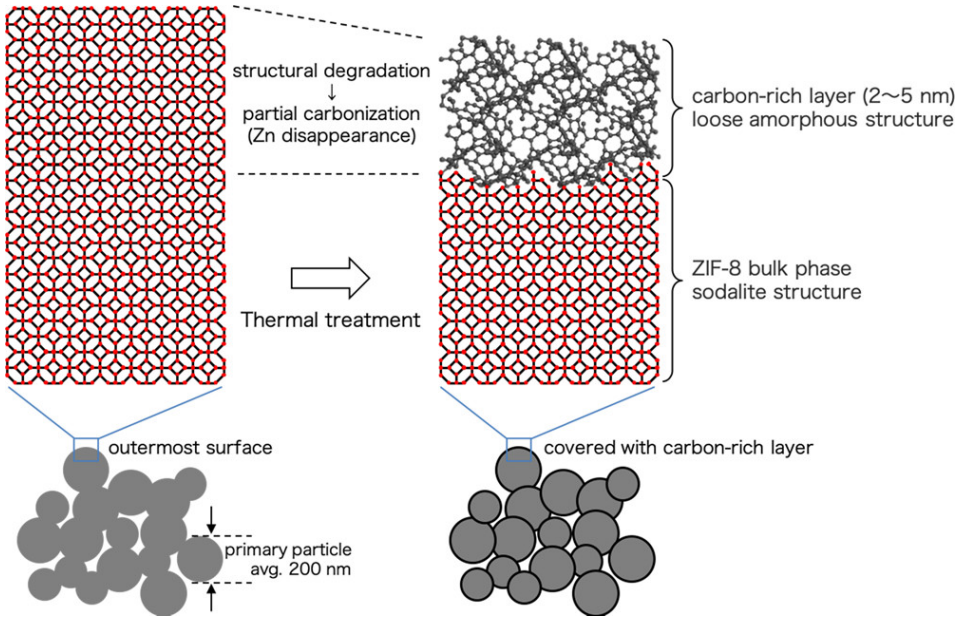

Fig. 2.20 Schematic diagram of the partial carbonisation and formation of the carbon-rich layer on the outermost surface of ZIF-8. [326]

For instance, the organic part of the framework can be partially or fully carbonised depending on the heat treatment temperature used. Tanaka et al. has demonstrated that

ZIF-8 can be partially carbonised at 550˚C [326] (see **Fig. 2.20**). The outmost carbonised layer could prevent the ZIF-8 from hydrolysis in water and improve the hydrothermal stability of the crystals, whereas the sample heat treated at 450˚C in Ar showed no significant change compared with pristine ZIF-8, even if the colour of the sample changed from white to brown. When the heat treatment temperature reaches 650˚C, the structure of ZIF collapses and the organic linker in ZIF is fully carbonised, as shown by the PXRD result. However, research has also shown that ZIF could undergo fractional decomposition at 200, 250 and 300˚C with long heat-treatment time under the inert atmosphere [325]. For the fully carbonised framework, the degree of graphitisation could be controlled by the kind of metal centre and the pyrolysis temperature. Report shows that organic linkers around zinc ions tend to form amorphous carbon, whereas those around cobalt ions tend to form graphitic carbon due to the catalytic graphitisation effect of cobalt nanoparticles [24, 327]. Therefore, with the pyrolysis temperature unchanged, the degree of graphitisation could be adjusted by changing the Co/Zn ratio in the bimetallic ZIF. In addition, the level of graphitisation for carbon is also closely correlated to the pyrolysis temperature [328, 329].

Furthermore, the N-containing organic linkers can result in N-doped carbon matrices with abundant catalytic active sites under inert atmosphere. The amount of N element and N species could be controlled by the pyrolysis temperature. Chao et al. have pyrolysed ZIF-8 under N_2 flow at four different temperatures (range from 600 to 1100 ˚C).[330] According to the XPS results, the total amount of N decreased from 20.47% to 2.78% as temperature increased. Meanwhile, the amount of pyridinic N and pyrrolic N decreased, leading to an increase in the relative percentage of quaternary N at high temperatures. Research also suggested that the increased carbonisation temperature results in the transition of pyridinic N to pyrrolic N and quaternary/oxidised N.[331]

Moreover, the metal ions in the framework can be turned into metal[332, 333], metal oxide[334-336], metal carbide[56, 337] or metal nitride[27], depending on the nature of metal species and the processing temperature. Generally, metal or metal oxide can be obtained at relative low pyrolysis temperatures, whereas metal nitride and carbide can only be obtained at higher temperatures. For instance, Chen et al. have calcined the pristine ZIF-67 at various temperatures (600-2000 ˚C)[332], in which cobalt was formed at temperatures below 1200 ˚C, while cobalt carbide was formed at temperatures above 1600 ˚C. Interestingly, Lou's group has also reported the synthesis of M_xC (M=Mo, W) confined in nitrogen-doped porous carbon by heat-treating the MO_4^{2-} substituted ZIF-8 at relatively

low temperature (800 ˚C) in N_2 atmosphere.[56] Different phases of molybdenum or tungsten carbide could be obtained by adjusting the amount of precursor used during the substitution reaction.

In the case of Zn-based ZIFs, zinc carbides cannot be obtained at high pyrolysis temperatures. The reason is that the Zn ions will first be converted into ZnO at low temperature [334-336], which will be further reduced to Zn metal by the carbon generated from the organic ligand at higher temperature. The Zn metal will start to evaporate when the temperature reaches its boiling point of 907 ˚C, leaving a porous carbon behind [331, 338]. This is also true for the ZIF-derived metal nitride-carbon composites. Lai et al. found that CoN_3 species derived from bimetallic CoZn-ZIF could be formed only when the appropriate amount of Co element was in the parental ZIFs, and the calcination temperature should be above 1000 ˚C [27]. In addition, Co NPs were formed with Co/Zn ratio above 9/91, and only well-dispersed Co single atoms (SAs) were formed with Co/Zn ratio less than 5/95. The bimetallic ZIF was first converted into N-doped carbon accompanied by the release of NH_3 from the decomposition of ZIF. The macropores resulting from the evaporation of Zn at high temperatures enable the contact between the exhaust NH_3 and the derived Co NPs, which promote the generation of CoN_3 species.

It is worth noting that when guest species are present inside the ZIF, the structure of ZIF can be preserved at low heat-treatment temperature while the guest species can undergo some desired change. For example, furfuryl alcohol (FA) that has been introduced into the cages of ZIFs via impregnation could be in situ polymerised within the pores by heating the FA@ZIFs composites at 80 ˚C under inert gas flow. The polymerised furfuryl alcohol (PFA) is immobilised in the framework without changing the crystallinity of ZIFs [131, 132]. Wang et al. have reported the synthesis of carbon nanodots (CNDs) containing ZIF-8 by simply calcining the as-obtained undried ZIF-8 at 200 ˚C [339]. Free organic ligand was carbonized into CNDs while ZIF-8 structure remained untouched, resulting in a tuneable luminescence of the hybrid.

2.3.2 Reactive atmosphere

By heat treatment of ZIFs and ZIF-based composites in a reactive atmosphere, desired elements and compositions can be introduced to or removed from the ZIFs or ZIF-based composites, offering an alternative avenue towards rich and diverse ZIFs-derivatives. Reductive atmosphere such as H_2, NH_3, H_2S and oxidative atmosphere including O_2 and H_2O are typical reactive atmospheres and will be discussed in this section.

2.3.2.1 Hydrogen atmosphere

Hydrogen is a type of reductive atmosphere that could remove oxygen from the carbon matrix and reduce metal oxide to pure metal during the heat treatment of ZIFs [121, 340]. It is usually used in a mixed gas system with inert gas flow, which results in carbon-based composites. Therefore, the process is sometimes referred as reductive carbonisation. Wang et al. heat-treated ZIF-8 under H_2/Ar atmosphere at different temperatures (700-1000 ˚C) and compared the resulting composites with those obtained under Ar and N_2 atmosphere (see **Fig. 2.21**) [341]. The results show that Zn species were reduced to Zn metal by H_2, which evaporated at high temperatures; meanwhile, the carbothermal reduction reaction between zinc and carbon matrix were inhibited, consequently, the composites reduced by H_2 show better-preserved carbon skeleton without shrinkage or structure collapse, resulting in higher surface area, larger pore volume and lower oxygen content than its counterpart obtained in pure inert atmospheres. Wu et al. reported that heat treatment of ZIFs with hydrogen could be used to reduce the guest species in ZIFs and keep the 3D framework partially intact [342]. In specific, pristine ZIF-67 was first soaked in a $Pd(NO_3)_2$ acetone solution overnight, then the composite was subject to heat-treatment in H_2 atmosphere for 2 h at low temperature (150-350 ˚C). The obtained product was a partially decomposed ZIF-67 with Pd nanoparticles on it.

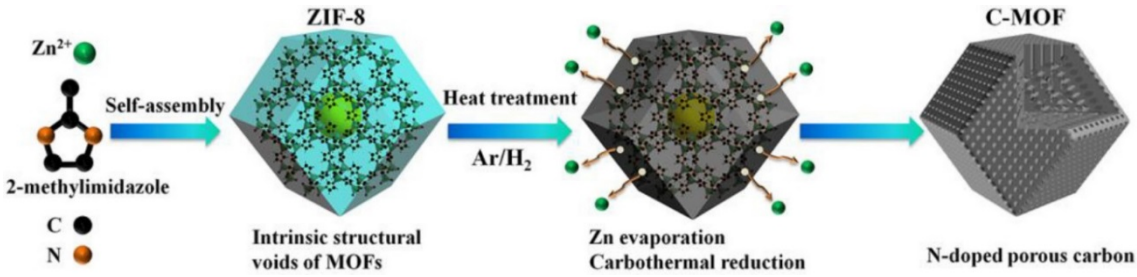

Fig. 2.21 Illustration of the processes and mechanism for the preparation of three-dimensional nitrogen-doped porous carbon from ZIF-8 under H_2/Ar atmosphere [341].

On the other hand, H_2 plays a vital role in the chemical vapour deposition synthesis of carbon nanotubes (CNTs). Research shows that the fraction of H_2 could affect the length, diameter, crystallinity and morphology of CNTs [343-346]. Therefore, with the catalytic effect from the transition metal nanoparticles [347, 348] and the carbon source provided by the organic linkers of ZIFs, composites contain CNTs could be easily produced from ZIFs and ZIF-based composites in the presence of H_2. Yin et al. synthesised porous carbon nanotube/cobalt nanoparticle composites by in situ pyrolysis of ZIF-67 in 5% H_2/Ar [349]. Due to the incomplete pyrolysis of ZIF at 500 ˚C, only small

CNT clusters were formed on the surface of the particles. Higher pyrolysis temperature at 700˚C led to the aggregation of Co NPs and the formation of denser CNTs with larger diameters and longer lengths. SEM and TEM images showed that both products obtained at 500 and 700 ˚C had a hollow structure, whereas the one fabricated at 900 ˚C showed a solid structure with large aggregated Co NPs. These large Co NPs result in fewer CNTs with larger diameters up to 40 nm. The observation suggested that the void was originated from the catalysed growth of CNTs. Xia et al. demonstrated that with increased fraction of H_2 (10%), small Co NPs were formed, which immediately catalysed the growths of CNTs, resulting in the hollow structure at 900 ˚C [350].

2.3.2.2 Ammonia atmosphere

It was reported that treating activated carbon with NH_3 at high temperature will partially gasify carbon through reaction with free radicals created from the decomposition of ammonia, leading to the increase in specific surface area and pore volume in the micropore range [351, 352]. Moreover, ammonia treatment can increase the surface nitrogen content of carbon by reacting with surface oxide to form nitrogen-containing functional group [353-355], and improve the proportion of pyridine N in carbon [356]. Both phenomena have also been observed in ZIFs derived carbon that obtained by heat treatment in NH_3. For instance, Ge et al. synthesised a ZIF-8/CNT composite and treated it in Ar at 1000 ˚C, followed by cooled down to 800˚C and treated it at this temperature in 10 vol% NH_3 atmosphere [357]. The as-obtained composite, N-ZCNT, showed no difference in morphology from the sample treated in pure Ar. However, the total nitrogen content increased with more graphitic N and pyridinic N compared with the sample without ammonia treatment. Tran et al. found that NH_3 heat treatment at 900 ˚C could enhance the specific surface area and pore volume of the $Fe(acac)_3$ decorated ZIF-8 derived carbon composites [358]. The amount of nitrogen content and the degree of graphitisation increased as well. The synergetic contribution of Fe-N_x-C species and pyridinic N have led to a superb ORR activity.

On the other hand, thermal treatment in NH_3 could lead to the formation of metal nitride. Strickland et al. reported the observation of iron nitrides by heat-treating FePhen modified ZIF-8 under NH_3 at 1050 ˚C. Lai et al. reported the control synthesis of CoN_3 embedded in graphitic carbon via in situ pyrolysis of Co/Zn-ZIF-67 (discussed in section 2.3.1 [27]), which also suggested the formation of cobalt nitride via proper NH_3 treatment.

Recently, progress in single-atom catalyst has been reported by Li's group through an NH_3-assisted gas-transport strategy (see **Fig. 2.22**) [359]. At high temperature, the flow

of strongly coordinating NH_3 would react with the superficial atoms from the Cu foam, dragging out volatile $Cu(NH_3)_x$ species. The volatile species were then trapped by the defects in the ZIF-8 derived defects-rich nitrogen-doped carbon support, resulting in the isolated Cu-SAs/N-C catalysts. In a typical synthesis, copper foam and ZIF-8 were placed in a porcelain boat separately; and the furnace was heated to high temperature (such as 900 ˚C) first under Ar atmosphere followed by in ammonia atmosphere. A series of M-SAs/N-C (M=Co or Ni) have been successfully synthesised, marking the generalisation of this gas-migration strategy.

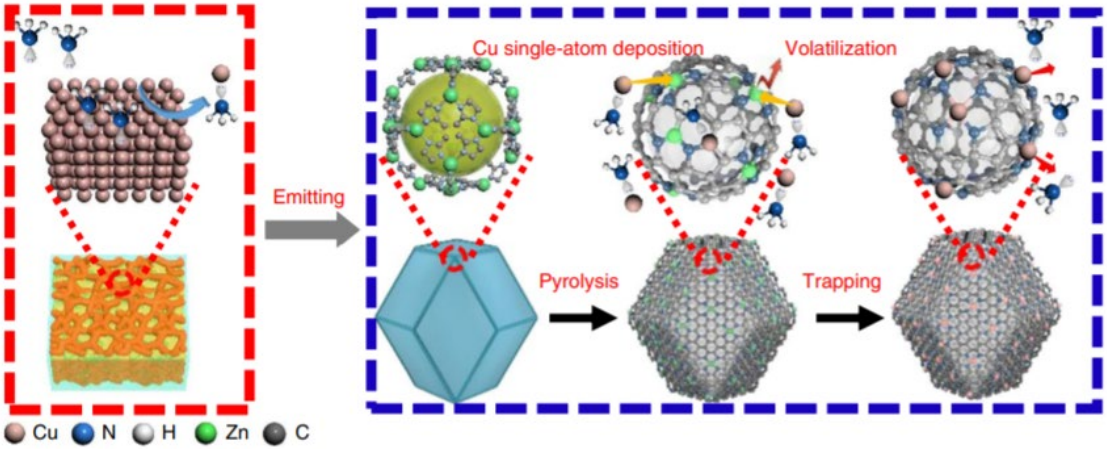

Fig. 2.22 Schematic diagram of the reaction mechanism of Cu-SAs/N-C [359].

2.3.2.3 Hydrogen sulfide atmosphere

H_2S gas is commonly used in the chemical vapour deposition (CVD) process as a reactive gas that not only introduce S element into the materials, but also provide reductive reactive atmosphere. It is also used in the chemical vapour infiltration (CVI) process of porous materials such as ZIFs and their composites, to produce transition metal sulphides (TMSs)/S-doped porous carbon heterostructure nanocomposites. Compared with conventional dry mixing, solution impregnation or in situ encapsulation with sulphur containing chemicals (such as pure sulphur [155], thioacetamide (TAA) [218, 360] and thiourea [98]) before carbonization, CVI method has simplified the process into one step. The controlled sulfurization could be realized by simply adjusting the flow rate, H_2S/inert gas ratio, reaction time and heating temperature.

Park et al. reported a comparison synthesis of MoS_2 nanosheets using H_2S gas or S powder as sulfurization agent [361]. It was found that the number of defects and vacancies on the nanosheet of MoS_2 was closely related to the sulfurization agent used. This might be because sulphur powder only vaporised at temperatures above 200 ˚C, and the S_8 crown ring structure of the vaporised S would lead to inhomogeneous sulfurization. In

contrast, H_2S gas has a low decomposition energy and simple molecular structure which is easy to diffuse and more feasible for the homogeneous reaction.

Chen et al. have synthesised Ni-ZIF-67 derived Ni-Co based sulphide embedded N, S co-doped porous carbon [362] and Huang et al. have synthesised phosphotungstic acid (PTA)@ZIF-67 derived $WS_2/Co_{1-x}S$ embedded N, S co-doped porous carbon [363] by one-step sulfurization and carbonization. It was found that sulphur would be deposited on the composite surface when excess amount of H_2S was introduced or the total gas flow rate was too slow. Therefore, H_2S flow was only introduced into the tube furnace at the target temperature and was stopped while the samples were cooling down naturally under Ar flow. Elemental mapping indicated that the S element distributed evenly throughout the porous carbon matrix, which is beneficial for catalytic applications. It was also found that with a short sulfurization duration (20 min), amorphous metal sulphide NPs that were not completely crystallised were formed. In contrast, with long sulfurization duration (> 1 h), no visible difference in the composition of the nanoparticles was observed [364].

2.3.2.4 Oxidative atmosphere

Treating ZIFs and ZIF-based composites in the air is the most commonly used method to eliminate volatile elements such as C, N and H, whereby porous metal oxide nanostructures with wide applications can be formed. Generally, the calcination temperature needs to be less than 500 ˚C in order to prevent severe sintering of the metal oxide particles and ensure interconnected porosity, which is favourable for target applications. Composites such as $Co_3O_4/ZnCo_2O_4$ [235], ZnO/CuO [121], $NiCo_2O_4$@NiO nanocage [234], $Co_3O_4/CoMoO_4$ [365] and Co_3O_4/SiO_2 [241] was obtained by calcination of ZIF and ZIF-based composites in air atmosphere. Generally speaking, elevated pyrolysis temperature will increase the diameter of metal oxide particles and decrease the BET surface area and pore volume. Using appropriate ZIF-based composites, derivatives with desired compositions and structures could be obtained. For example, Lan et al. oxidised polyoxometalate (POM)@ZIF-67 at 350 ˚C under air flow [91], in which the ZIF was oxidised to Co_3O_4 but the POM molecules were preserved and contributed to the photocatalytic activity of the final composite.

Carbon will burn off at high temperatures in ambient atmosphere. However, carbon matrix can be partially preserved under mild oxidisation conditions, resulting in porous metal oxide/carbon composite. Yi et al. demonstrated the synthesis of NC (nitrogen-doped porous carbon)@Co_3O_4/NC by carbonising ZIF-8@ZIF-67 composite under Argon flow at 700 ˚C for 3 h, followed by gentle oxidisation in air at 350 ˚C for 1 h.

However, directly exposing ZIFs to air is not promising to synthesise metal oxide/carbon composite with controlled oxidation level. The way the sample is packed and the set-up of the furnace can both affect the composition of the final product. In some researches, heating ZIF in air at 350 ˚C would lead to deplete of all carbon species [121, 366].

In order to gain more control over the oxidisation level of carbon, a mixed (or controlled) gas approach was applied. Typically, small amount of oxidative gas was mixed with an inert gas to provide a weak oxidation environment. Oxygen-containing functional groups could be introduced on the carbons at high temperature. Both heating time and the amount of reactive gas would affect the amount of final volatile species and the form of metal in the product, resulting in evenly dispersed functional metal oxide/porous carbon composites. Chen et al. have demonstrated one-step synthesis of atomically homogeneous dispersed ZnO/N-doped porous carbon composites via pyrolysis under water-steam [367]. Specifically, pristine ZIF-8 was heated in a flow-through quartz tube under Ar flow which was replaced by Ar/water vapour (Ar/H_2O) flow when the temperature reached target temperature. Unlike the control sample that was obtained via annealing in air under the same conditions, samples with ZnO paritcles homogeneous embedded in N-doped nanoporous carbon was obtained in Ar/H_2O atmosphere. The resulting composite showed higher surface area and pore volume than the sample pyrolysised under the same conditions in Ar. The surface area and pore volume can be further increased by using the Ar/H_2O atmosphere from the beginning of the heating-up stage. Moreover, abundant oxygen-containing hydrophilic functional groups have been introduced into the carbon matrix via the water-steam treatment, facilitating the photodegradation performance and CO_2 adsorption of the composites. The same research group has recently further investigated the visible light photocatalytic hydrogen evolution reaction of the ZIF-8 derived ZnO/C nanocomposites obtained under water-steam atmosphere and the nanocomposites derived from other MOFs [368]. The results suggested that the nano-sized ZnO particles (sizes less than 10 nm) derived from ZIF-8 were doped by C and N atoms and therefore showed larger lattice spacings and narrower energy band gaps compared with bulk ZnO. Moreover, the porous carbon matrix was crucial to facilitate the charge transfer and prevent the charge recombination; therefore, samples without carbon matrix exhibited a much deteriorated photocatalytic performance towards hydrogen evolution reaction. Besides Ar/H_2O, mild oxidisation could also be realised by mixing a small amount of oxygen with inert gas [369,370,371].

2.3.3 Chemical vapour infiltration with volatile reactant

Different from the aforementioned gas-assisted heat treatment, the gas-phase infiltration, which involves extra volatile reactants, can introduce guest molecules to boost the number of elements introduced to the ZIF and ZIF-derivatives during heat treatment. chemical vapour infiltration (CVI), also named vaporisation and infiltration or sublimation and infiltration depending on the context, is a subclass of chemical vapour deposition (CVD), specifically referring to the modification of porous materials.

In a typical operation, a chemical that contains the desired elements can be physically mixed with ZIFs [372], or placed separately with ZIFs inside the tube furnace [373]. The chemical can be liquid or solid [373, 374], which will vaporise or sublime during the heat treatment process. Usually, an inert carrier gas is continuously fed into the tube, which will protect the ZIFs from unwanted reaction and bring the volatile species in contact with ZIFs for the intended reaction. Treating both ZIFs and the precursors in vacuum to encourage gas-phase infiltration at relatively low temperatures is also very common [155, 375]. Depending on the temperature used, the hosting ZIFs can retain their structure intact or can be carbonised and functionalised simultaneously. Both metal and non-metal elements can be introduced by this method.

2.3.3.1 Non-metal volatile reactant

Instead of using H_2S gas, ZIFs can also be sulphurized by CVI method. For example, Razzaq et al. demonstrated the sublime-infiltrate synthesis of CoS_2-SPAN-CNT by placing sulphur at upstream during the pyrolysis of ZIF-67@PAN-CNT under N_2 flow [373]. Sulphur with 10 times weight than the ZIF-67@PAN-CNT was used to ensure the complete sulphurization. The temperature was first set to 155 ˚C for sulphur encapsulation, then was increased to 400 ˚C to realise the carbonisation and sulphurization of the composite. Feng et al. synthesised CoS_2 nanosheets via mechanically pre-mixing sulphur with ZIF-67 nanosheets before calcination [376]. It is worth mentioning that compared with in situ inclusion of S NPs, mechanically mixing sulphur with ZIF would lead to the presence of large sulphur particles outside the host after sublime-infiltration at 300 ˚C for 7 h under vacuum (see **Fig. 2.23**) [155], which suggests that it is vital to control the amount of volatile sulphur introduced into the system. Moreover, a carrier gas would be necessary for the introduction of the volatile species and the removal of excess unreacted S. Besides mixing ZIFs with sulphur or placing sulphur upstream during the pyrolysis, Zeng et al. has also reported a vapour

infiltration sulphurization of ZIF-67 by flowing N_2 gas through an upstream wash bottle which contains ethanethiol/ethanol solution. The ethanethiol will decompose to H_2S gas at temperature above 325˚C [374]. Moreover, thiourea, ammonium thiocyanate, thiophene and thioacetamide have also been reported as S sources to synthesise composites such as CoN_x/CoS_x containing Co NPs encapsulated N/S-doped conductive carbon matrix from ZIFs [377]. Similarly, phosphorisation, selenisation and tellurisation of ZIFs and ZIF-based composites have also been realised by CVI using NaH_2PO_2 [50, 360, 378], Se powder [379,380,183], and Te powder [381] as volatile reactant respectively.

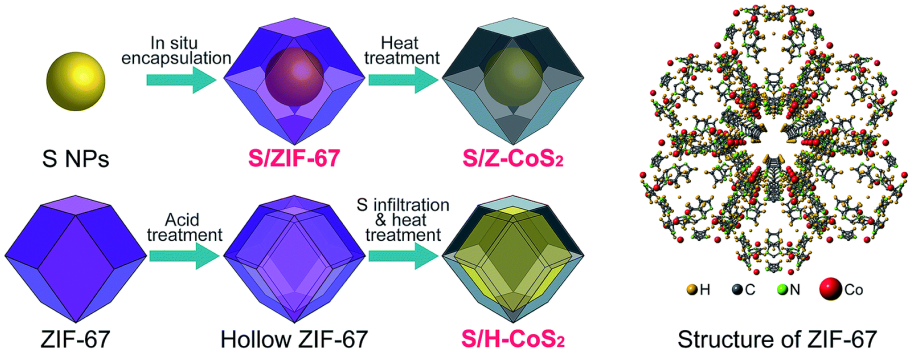

Fig. 2.23 Schematic illustration of the synthesis procedures of S/ZIF-67, S/Z-CoS_2 and S/H-CoS_2 [155].

2.3.3.2 Metal volatile reactant

This approach is applicable for both non-metal and metal elements. In the ammonia-assisted gas-transport strategy mentioned in section 2.3.2.2, Cu single atoms from a separate Cu foam were infiltrated into the downstream ZIF-derivatives [359]. Other transitional metal elements have also been introduced by CVI method. Usually, the metal precursor is a volatile organometallic compound. Depending on the boiling point, handling certain organometallic compounds could be messy, and controlling experimental temperature and atmosphere is required. Due to this peculiarity, high-temperature heat treatment is not always necessary for the gas phase infiltration of the precursor molecules, and those as-obtained unstable composites frequently need to be stored under inert gas at low temperature, or immediately subject to further heat treatment to obtain stable ZIF-derivatives [371, 382]. Volatile metal compound such as nickelocene ($Ni(cp)_2$) [375], ferrocene ($Fe(C_5H_5)_2$) [383] and diethylzinc ($Zn(C_2H_5)_2$) [371] have been reported for the preparation of ZIF-derivatives by CVI method.

Besides transitional metal, post-transitional metal such as gallium has also been introduced via the vaporisation and infiltration method. Instead of elemental gallium, the infiltration of organometallic gallium compound into cavities of ZIF-8 was reported by

Fischer's group [382], which was realised by placing activated ZF-8 and trimethylamine gallane ($(CH_3)_3NGaH_3$) in a glass vial under vacuum at 0 ˚C for 7 days until saturated loading level was achieved. Intermediate $(H_2GaNH_2)_3$@ZIF-8 was obtained by heating the as-made [$(CH_3)_3NGaH_3$)]@ZIF-8 in ammonia gas at 50 ˚C, while GaN@ZIF-8 with GaN quantum dots of 1-3 nm was formed by annealing the intermediate composite under 3 bar ammonia at 150˚C, followed by further heating treatment in dynamic vacuum at 200 ˚C

Similarly, precious metals can be infiltrated into ZIF via the same method. Zahmakiran et al. synthesised IrNPs@ZIF-8 with Ir(COD)(MeCp) and activated ZIF-8 as precursors [384]. The infiltration took place at 40 ˚C under static vacuum for 18 h, resulting in 1.5 wt% loading of Ir in the as-made Ir(COD)(MeCp)@ZIF-8 composite. Then IrNPs@ZIF-8 was obtained via hydrogenolysis in 10% H_2/N_2 at 300 ˚C with Ir NPs of 3.3 ± 1.7 nm in size. The Ir NPs were found to be anchored close to the surface of ZIF crystals. In addition, Zhang et al. reported the CVI synthesis of Pd@ZIF-8 with volatile cyclopentadienyl allyl palladium ($Pd(C_3H_5)(C_5H_5)$) as Pd precursor [385]. The obtained Pd NPs of 1.5-3.5 nm in size are found to be homogeneously distributed on the ZIF-8 support. Some particles with size larger than 10 nm were also observed. Both reports reveal that even with the linker rotation induced gate expansion effect [386, 387], it is still impossible to infiltrate precursors that are larger than the aperture size of the ZIF cages.

In conclusion, CVI is a versatile method to introduce different elements into ZIF and its composites. Deficiencies of solution impregnation could be avoided by carefully tuning experiment conditions and proper selection of volatile precursors. The introduction of non-metallic elements has been widely reported, whereas the introduction of metallic species has been relatively rare due to the technical difficulties in handling and storage of the special organometallic compounds and the use of special apparatus. Nevertheless, this method holds great potential toward delicate ZIF-derived composites for highly active catalytic applications.

2.4 Application of the ZIF-derivatives in water splitting

The fast-growing world energy consumption has pushed the development of alternative sustainable energy sources. Due to the high-energy density and zero-pollution, hydrogen is one of the most promising sustainable energy alternatives. On account of the carbon neutrality target by 2050, green hydrogen produced from water splitting via electrolyser driven by renewable electricity is of great interest [388-391]. However, the efficiency of the

electrolyser is one of the bottlenecks toward mature commercial application. Moreover, the current benchmark electrocatalysts for the cathodic hydrogen evolution reaction (HER) and anodic oxygen evolution reaction (OER) are Pt and IrO_2/RuO_2 respectively [392], but both involve noble metals, which is also undesirable for commercial applications. Therefore, developing cost-effective transition-metal-based electrocatalysts is highly desirable, among which ZIF-based composite derived catalysts have attracted great interest.

2.4.1 Fundamental and mechanism of HER and OER

2.4.1.1 HER

HER is the cathodic half-reaction of electrochemical water splitting, which is a two-electron transfer process consisting of three reaction steps (i.e. adsorption Volmer step, reduction Heyrovsky step and desorption Tafel step) and with two possible reaction pathways (i.e. Volmer-Heyrovsky process and Volmer-Tafel mechanism) for the generation of H_2 that happened on the surface of an electrode [393]. The overall reaction and elementary steps of HER in acidic electrolyte and alkaline electrolyte are shown in **Table 2.1**.

Table 2.1 The overall reaction and elementary steps of HER in acidic electrolyte and alkaline electrolyte [393].

For HER	In Acidic electrolyte	In Alkaline electrolyte
Overall reaction	$* + 2H^+ + 2e^- \rightarrow H_2$	$* + 2H_2O + 2e^- \rightarrow H_2 + 2OH^-$
Elementary steps	Volmer step: $* + H^+ + e^- \rightarrow *H$ Heyrovsky step: $*H + H^+ + e^- \rightarrow * + H_2$ Tafel step: $2*H \rightarrow 2* + H_2$	Volmer step: $* + H_2O + e^- \rightarrow *H + OH^-$ Heyrovsky step: $*H + H_2O + e^- \rightarrow * + H_2 + OH^-$ Tafel step: $2*H \rightarrow 2* + H_2$

Where * denotes active site on the surface of an electrocatalyst.

HER is highly depending on the pH of the reaction environment. Volmer step in alkaline media requires the breaking of water molecules before adsorbing hydrogen atoms, which is more difficult than reducing the hydronium cation in acidic media [394]. Therefore, HER in alkaline electrolyte is usually worse than in acidic electrolyte. After the Volmer reaction, adsorbed hydrogen is then combined to form H_2 via Heyrovsky or Tafel step. The pathways strongly depend on the inherent electronic and chemical properties of the electrode surface.

The ability of the catalyst to absorb and desorb the hydrogen intermediate (H^*) is vital to the rate-determining of the reaction. Theoretical calculated Gibbs free energy for

hydrogen adsorption (ΔG_{H^*}) on a catalyst surface is a great activity descriptor for the HER reaction in acidic media. Usually, $\Delta G_{H^*} < 0$ indicates a strong hydrogen adsorption, which may lead to blockage of the active site and fail to evolve hydrogen; As a result, the desorption step will be the rate-determining step (*rds*); whereas $\Delta G_{H^*} > 0$ indicates a weak hydrogen adsorption, which may lead to difficulty in capturing the intermediate and hence unable to start the reaction, so the Volmer step is the *rds* of HER. By plotting the exchange current densities vs ΔG_{H^*}, a volcano-shaped plot was obtained (see **Fig. 2.24**) [395]. Metals situated at the peak of the volcano will have close to zero ΔG_{H^*} and the highest activity possible. However, for HER in alkaline media, the validity of ΔG_{H^*} as activity descriptor remains debatable as the reaction involves dissociation of water molecule and with OH^- as intermediate [396].

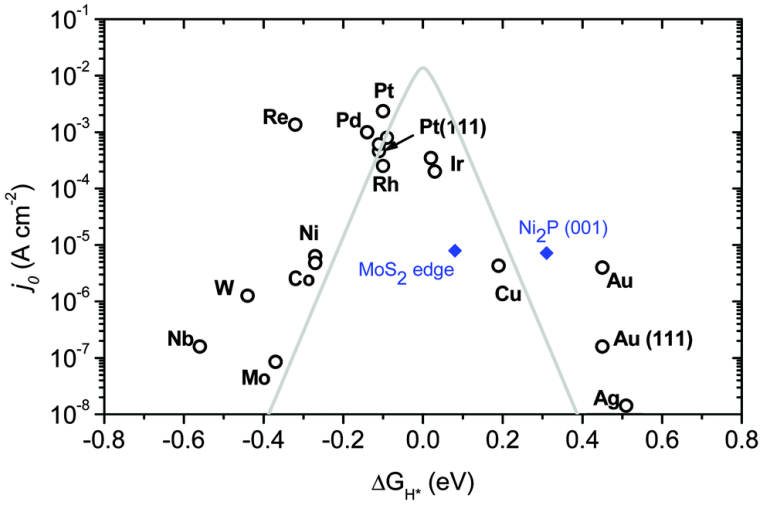

Fig. 2.24 A volcano plot of the experimentally measured exchange current density as a function of the DFT-calculated Gibbs free energy of adsorbed atomic hydrogen. The simple kinetic model to explain the origin of the volcano plot is shown by the solid line [395].

The equilibrium potential of HER is 0 V vs standard hydrogen electrode (SHE). Parameters such as onset potential, potential to achieve current density of 10 mA cm^{-2} (η_{10}) and Tafel slope are usually used to determine the activity of HER electrocatalysts, and are acquired from the polarisation curve of the catalyst.

2.4.1.2 OER

OER is the anodic half-reaction of electrochemical water splitting. It is a four-electrode transfer process with more complicated multistep reactions. The reaction can take place in both acidic and alkaline conditions, and the reaction mechanisms are shown in **Table 2.2** [397].

Table 2.2 The overall reaction and elementary steps of OER in acidic electrolyte and alkaline electrolyte [397].

	In Acidic electrolyte	In Alkaline electrolyte
Overall reaction	$2H_2O \rightarrow O_2 + 4H^+ + 4e^-$	$4OH^- \rightarrow O_2 + 2H_2O + 4e^-$
Elementary steps	$* + H_2O \rightarrow *OH + H^+ + e^-$	$* + OH^- \rightarrow *OH + e^-$
	$*OH \rightarrow *O + H^+ + e^-$	$*OH + OH^- \rightarrow *O + H_2O + e^-$
	$H_2O + *O \rightarrow *OOH + H^+ + e^-$	$*O + OH^- \rightarrow *OOH + e^-$
	$*OOH \rightarrow * + O_2 + H^+ + e^-$	$*OOH + OH^- \rightarrow * + O_2 + H_2O + e^-$

Where * denotes active site on the surface of an electrocatalyst.

Unlike HER, OER is more favourable in alkaline media due to the abundant hydroxyl groups in the electrolyte. However, because proton exchange membrane (PEM) water electrolysers based on acidic media show more advantages than alkaline water electrolysers, OER in acidic media has become more attractive than in alkaline media and is desirable for industrial application [398]. For acidic OER, the break of O-H bond in H_2O molecules requires higher energy, therefore leading to less favourable reaction kinetics.

The equilibrium potential of OER is 1.23 V vs. SHE, which is also the theoretical thermodynamic voltage for the overall water splitting to proceed. The sluggish kinetics of the OER leads to the bottleneck of the overall water splitting, and commercial water splitting usually has a working voltage of 1.8-2.0 V [399]. Similar to HER, parameters like onset potential, η_{10}, and Tafel slope are frequently used to evaluate the activities of the OER electrocatalyst.

2.4.2 ZIF-derivatives for HER and OER

2.4.2.1 HER

Good HER electrocatalysts can readily reduce the applied voltage for the H_2 molecular evolution and increase the amount of hydrogen generated per unit time. Both heteroatom and metal doped ZIF derivatives have been reported to improve the HER activity [400, 401]. For example, Zhou et al. reported ZIF-derived HER electrocatalysts via W, Cr, Mo or Ce-doping [21]. Both experimental and theoretical results show that metal-doping can tune the electron distribution between metallic Co and N-doped carbon of the Co@N-C systems, reducing the adsorption free energies of H_2O and H on the Co-N_x active sites and consequently improving the charge transfer and enhancing the intrinsic HER activity of the ZIF-derived catalysts. Moreover, nitrogen in the organic linkers of ZIFs can result in

N-doped carbon after pyrolysis, which offers abundant non-metallic active sites and further improves the electrochemistry activity [400].

With a great variety of elements that ZIF-based composites can offer, HER favourable heterostructures can be obtained. The complex interface is the key to enhance HER performance. For example, Wu et al. synthesised ZIF-derivatives with Co@CoO Mott–Schottky heterojunctions anchored on graphene. DFT calculations elucidate that the contact of Co and CoO can induce a band bending between the conduction and the valence bands in CoO, leading to electrons being transferred to CoO at the heterointerface [402]. This electron redistribution constructs a built-in electric field for a continuous electron transfer path, making it close to the reduction potential of H intermediate. Moreover, the heterointerfaces enable the O-enriched sites on the surface of CoO to be the trapping sites for water dissociation, therefore boosting HER performance. ZIF-derived heterojunctions such as Co_3O_4/RuO_2 [403], $Co(PO_3)_2/MoS_2$ [404], Co/CoP [405], $WC/Co_3W_3N/Co$ [406], and Co_2P/CoP [407] with improved HER performance have been reported.

ZIF-based composites are very efficient precursors for the preparation of nanostructured derivatives with highly accessible active site density due to their interconnected pores and homogeneous metal-containing ordered frameworks. In detail, the organic linkers could be readily transformed into porous carbon matrix, which could improve the electron conductivity of the ZIF-derived hybrids [408], effectively prevent the aggregation of metal species during pyrolysis [409], and allow easy mass transports during the electrochemical process [410], which are all favourable for the HER application. Heterogeneous catalysts containing single atomic sites [409], quantum dots [411], nanoparticles, or nanosheets [412] obtained from ZIF-based composite precursors have been reported, which show outstanding improvement in HER.

The morphology of the ZIF-derivatives plays a vital role in achieving high electrocatalytic activity. By incorporating ZIFs with high dimension structures such as 2D nanofibers [413] and 3D foams [414]; or by forming architectures such as hollow nanocages [415], nano arrays [416], and ordered macroporous superstructure [417], hierarchical nanostructured composites could be obtained. By doing so, surface area of such hierarchical nanostructured composites can be increased, and the accessibility of active sites can be optimised. Due to the shortened mass-transportation pathways, the fast charge transferability, and the resulting intended HER active compositions can synergistically contribute to the enhanced HER performance.

2.4.2.2 OER

Similar to ZIF-derivatives for HER applications, N-doped carbon derived from ZIFs can facilitate the OER performance by modulating the electronic structure of the carbon matrix [418, 419]. For example, Wang et al. reported a controllable N-doping strategy to synthesise N-doped Co_3O_4 NPs/N-doped carbon framework strongly coupled porous nanocubes (N-Co_3O_4@NC) from ZIF-67 [420]. Synchrotron X-ray absorption fine structure (XAFS), XPS and electron spin resonance (ESR) analyses indicate that oxygen vacancies were formed in the Co_3O_4 by N-doping, which is believed to optimise the electronic configuration and contribute to the excellent electrocatalysts for water oxidation. DFT calculation reveals that N-doping in N-Co_3O_4 could improve the catalytic activity by optimising the intermediate adsorption energy, improving electronic conductivity and accelerating reaction kinetics. Reports also show that the OER activities can be improved by introducing other heteroatoms e.g. O, S, P, N [421-423].

Furthermore, the composition engineering via metal-doping could also improve the OER performance of the ZIF-derivatives. For example, Gu et al. have lately reported a ZIF-FeCo MOFs derived FeCo fluoride N-doped carbon nanocomposite with surface oxidation (ZIF-FeCo-F) as efficient OER catalyst [419]. By comparing it with the single metal containing catalysts ZIF-Fe-F and ZIF-Co-F, the authors conclude that the enhanced OER performance is ascribed to the synergistic effect of Fe and Co. In specific, the strong electronegativity of F leads to the formation of highly polarised Metal-F bonds, modulating the neighbouring electron environment and generating unsaturated sites as the active sites for the OER reaction. In addition, fluorination results in the etching of the material, inducing a high electrochemical surface area with more exposed active sites. Other ZIF-derived metal-doped composites such as carbon decorated Mn-doped cobaltites [424], Mo anchored N-doped carbon [425], Fe-doped nickel-cobalt sulfide composites [22], Ce-doped spinel-type cobalt oxide [426], trimetallic (W/Co/Fe) carbon nanoflakes [427], N-doped carbon-coated cobalt-cobalt molybdenum carbide [428], and iron-cobalt bimetallic phosphide carbon composites [429] have also been reported and shown excellent OER performance.

It is worth noting that many transition metal oxide catalysts undergo near-surface self-reconstruction during the OER process, and the resulting new phase is the true active sites for OER [423, 430]. This surface transformation is limited by the penetration of electrolytes and the exposure of reactive sites, therefore largely depends on the surface area of the catalysts. In this respect, nanostructuring is a great way to improve the

proportion of the surface transformation layer and hence the OER activity. Naveen et al. have recently synthesised nanostructured porous $ZnCo_2O_4$ (P-$ZnCo_2O_4$) from a bimetallic ZIF and investigated the effect of nanostructuring [431]. Compared with bulk $ZnCo_2O_4$ (B-$ZnCo_2O_4$) and single metal oxide P-Co_3O_4, P-$ZnCo_2O_4$ shows dramatic improvement in OER activity. Raman spectrum reveals that the OER active CoOOH phase was formed after electrolysis of the P-$ZnCo_2O_4$, and the extent of the surface reconstruction process was much higher in P-$ZnCo_2O_4$.

Besides tuning the chemical composition, another key to improve the intrinsic OER activity is by sculpting the ZIF derivatives with 3D architectures, such as nanoflower [423, 432], nanocapsules [433] and hierarchical porous structure [434], which can facilitate the exposure of more accessible active sites and improve the mass transport ability of the catalyst. The synergistic effect of the composition and morphology of the hybrid can also boosts OER performance. For example, Huang et al. have designed a yolk-shell structure of Fe_2O_3 nanotube@hollow Co_9S_8 nanocage@Carbon shell using Fe_2O_3 nanotube@ZIF-67 core-shell structure as the precursor [435]. The outstanding OER performance is the synergistic coordination of different merits. First, the yolk-shell structure enables easy access to active sites and the Fe_2O_3 nanotube increases channels for gas spillage during the OER, which are conducive to good reaction stability. Second, the well-dispersed Co_9S_8 also improves the electrical conductivity of the composite and provides active sites for OER. Third, the porous carbon enhances the electrical conductivity of the material and allows the electrolyte to penetrate, thereby shortening the diffusion path of the intermediate and accelerating the reaction kinetics.

Chapter 3 Experimental methodology

3.1 Introduction

All synthesis and characterisation methodology for this research work is presented in this chapter. Three sets of samples were synthesised, corresponding to the samples in Chapter 4-6.

3.2 Synthesis of PTA@ZIF-67 and carbon-based derivatives

3.2.1 Chemicals

2-Methylimidazole (99%, abbreviated as MeIM), Cobalt nitrate hexahydrate ($Co(NO_3)_2 \cdot 6H_2O$) and Phosphotungstic acid hydrate ($H_3PW_{12}O_{40} \cdot xH_2O$, abbreviated as PTA) were bought from Sigma-Aldrich and used without further purification.

3.2.2 Sample preparation

3.2.2.1 Preparation of ZIF-67

ZIF-67 was synthesised by the hydrothermal method in an aqueous solution. 1.125 g $Co(NO_3)_2 \cdot 6H_2O$ and 13.75 g MeIM were dissolved separately in distilled water (with a total amount of 57.5 ml) before mixing together under magnetic stirring at room temperature for 24 h. The resulting mixture was centrifuged to separate the purple ZIF-67 and the solution. ZIF-67 was then washed with water and methanol each for three times to remove the excess MeIM. Finally, the purple powder was separated from the solution by centrifuge (7000 rpm, 10 min) and dried in a fuming cupboard for several days before being subject to further heat treatment.

3.2.2.2 Preparation of PTA@ZIF-67

Synthesis of PTA@ZIF-67 is similar to the synthesis procedure of ZIF-67, except PTA was dissolved in water together with $Co(NO_3)_2 \cdot 6H_2O$ before mixing with MeIM solution. Three composites with different amounts of PTA (1.113 g, 0.557 g and 0.371 g) were synthesised. The resulting samples were denoted as W30@Z67, W20@Z67 and W10@Z67, respectively.

3.2.2.3 Preparation of bimetallic $WS_2/Co_{1-x}S/N$, S co-doped porous carbon nanocomposites

To obtain porous carbon composite, 0.2 g dried sample powder in a ceramic boat was placed in a horizontal flow-through quartz tube in a tube furnace. Samples were heated to different temperatures (600, 800 and 1000 °C) at a heating rate of 10 °C min^{-1} under Argon atmosphere. After reaching the target temperature, hydrogen sulphide gas at a flow rate of 50 mL min^{-1} was introduced to sulfurise the sample, and this process was maintained for 1 h. After 1 h, H_2S was switched off, and the furnace was allowed to cool down naturally to room temperature under Ar flow. The final product was labelled as xWZ-y, where x is the ratio of Cobalt nitrate hexahydrate to PTA and y is the heat treatment temperature. For example, 20WZ-800 stands for the sample obtained by heat treatment of the precursor sample W20@Z67 at 800 °C. For comparison, PTA-800 was also produced by heat treatment of net PTA at 800 °C for 1 h in the H_2S atmosphere.

Table 3.1 Summery of the name and compositions of the samples in this section 3.2 and Chapter 4.

Composition	Sample name	Amount of PTA (g)		Heat treatment under Ar/H_2S gas for 1h			
				Composition	600°C	800°C	1000°C
PTA@ZIF-67	W10@Z67	0.371	→	$WS_2/Co_{1-x}S/N$, S co-doped porous carbon	-	10WZ-800	10WZ-1000
	W20@Z67	0.557			20WZ-600	20WZ-800	20WZ-1000
	W30@Z67	1.113			-	30WZ-800	30WZ-1000
ZIF-67	ZIF-67	0		$Co_{1-x}S/N$, S co-doped porous carbon	Z67-600	Z67-800	Z67-1000
PTA	PTA	-		WS_2	PTA-800	-	-

3.3 Synthesis of PMA@ZIF-67@PDA, PTA@ZIF-67@PDA and carbon-based derivatives

3.3.1 Chemicals

All reagents, including Cobalt (II) nitrate hexahydrate ($Co(NO_3)_2 \cdot 6H_2O$, 99%,), 2-Methylimidazole ($C_4H_6N_2$, 99%, abbreviated as MeIM), Phosphomolybdic acid hydrate

($H_3PMo_{12}O_{40}\cdot xH_2O$, abbreviated as PMA), Phosphotungstic acid hydrate ($H_3PW_{12}O_{40}\cdot xH_2O$, abbreviated as PTA), Cetyltrimethylammonium bromide ($C_{19}H_{42}BrN$, 99+%, abbreviated as CTAB), TRIS-buffer solution (0.5M, pH=8.5) and Dopamine hydrochloride ($C_8H_{11}NO_2\cdot HCl$, 99%), were purchased from Fisher Scientific and used without further purification.

3.3.2 Sample preparation

3.3.2.1 Preparation of ZIF-67 nanocubes

ZIF-67 nanocubes (Z67) were synthesized based on the previous report with slight modification to scale up the production.[436] In a typical synthesis, 1.16 g of $Co(NO_3)_2\cdot 6H_2O$ and 0.02 g of CTAB were dissolved in 40 ml of distilled water while 18.16 g of MeIM was dissolved in 280 ml of distilled water separately. The mixture of $Co(NO_3)_2\cdot 6H_2O$ and CTAB was then rapidly poured into the MeIM solution under vigorous stirring at 500 rpm, followed by continuously stirring for 20 min at room temperature. The purple powder was collected by centrifugation at 7000 rpm for 5 min and washed twice by water and once by ethanol. The obtained sample was dried in a fume hood for 2 days and stored in a glass vial for further treatment.

3.3.2.2 Preparation of PMA@ZIF-67@PDA nanocubes

To obtain PMA@ZIF-67@PDA nanocubes (Mo-Z67-D), three solutions were prepared in advance: solution A, 34 ml of 0.01 M Tris-buffer solution was prepared by adding 2 ml 0.5 M Tris-buffer solution (pH=8.5) into 32 ml of distilled water; solution B, 0.05 g of dopamine hydrochloride was dissolved in 17 mL of distilled water; solution C, 0.2 g PMA was dissolved in 50 ml distilled water. Then 0.15 g of dried ZIF-67 powder was dispersed in 51 mL of distilled water under sonication for 5 min. An extra 1 mL of ethanol was added before the water to achieve better dispersion of the hydrophobic ZIF nanocubes. The ZIF-67 dispersion solution was stirred at 500 RPM, followed by the addition of solutions A and B. The polydopamine started to decorate and coat on the surface of the ZIF-67 nanocubes, changing the colour of the mixture from purple to dark purple. Then solution C was introduced, and the mixture was kept stirring for another 20 min. Finally, the resultant composite was collected via centrifugation at 7000 RPM and washed with ethanol three times. The obtained sample was dried in a fume hood for 2 days.

3.3.2.3 Preparation of PTA@ZIF-67@PDA nanocubes

PTA@ZIF-67@PDA nanocubes (W-Z67-D) were synthesized via a similar procedure for the synthesis of Mo-Z67-D, except the replacement of PMA solution by the same amount of PTA solution. In addition, ZIF-67@PDA nanocubes (Z67-D) were also prepared for comparison, following the same procedure for the synthesis of Mo/W-Z67-D, only replacing the PMA/PTA solution with the same amount of distilled water.

3.3.2.4 Preparation of bimetallic Co-Mo and Co-W Sulphide/ N, S-doped porous carbon nanocomposite

The as-synthesised Z67 as well as the Mo-Z67-D and W-Z67-D were then subjected to pyrolysis at three different temperatures (600, 800 and 1000 °C) to obtain a series of carbon-based nanocomposites. In a typical synthesis, 0.05 g of dry sample powder was loaded into a ceramic boat and pyrolysed in a flow-through tube furnace in Ar with a flow rate of 50 mL min^{-1} and heating ramp rate of 10 °C min^{-1} or 2 °C min^{-1}. After reaching the target pyrolysis temperature, H_2S gas was introduced into the tube for 1 hour. Followed by the sulfurisation/carbonisation process, the sample was naturally cooled down to room temperature under Ar flow. The obtained samples were named CoMoS-X or CoWS-X, where X stands for the pyrolysis temperature of the samples. For samples obtained under a heating rate of 10 °C min^{-1} an extra "-10" was added in the sample names. For example, CoMoS-600 refers to sample derived from Mo-Z67-D at pyrolysis temperature of 600 °C and heating ramp rate of 2 °C min^{-1}, whereas CoWS-800-10 refers to sample derived from W-Z67-D at pyrolysis temperature of 800 °C and heating ramp rate of 10 °C min^{-1}. PMA and PTA were also heated at 800 °C under the same H_2S/Ar atmosphere for comparison, and the obtained samples were designated as PMA-C and PTA-C respectively.

Table 3.2 Summery of the name and compositions of the samples in this section 3.3 and Chapter 5.

Composition	Sample name		Heat treatment under Ar/H_2S gas for 1h				
			Composition	Heating rate (°C/min)	600°C	800°C	1000°C
ZIF-67@PDA	Z67-D		-	-	-	-	-
PMA@ZIF-67@PDA	Mo-Z67-D	→	Co-Mo-S@N, S-doped porous carbon	2	CoMoS-600	CoMoS-800	CoMoS-1000
				10	CoMoS-600-10	CoMoS-800-10	CoMoS-1000-10
PTA@ZIF-67@PDA	W-Z67-D		Co-W-S/C	2	CoWS-600	CoWS-800	CoWS-1000
				10	CoWS-600-10	CoWS-800-10	CoWS-1000-10
ZIF-67	Z67		CoS/C	2	CoS-600	CoS-800	CoS-1000
PMA	-		MoS_2	2	-	PMA-C	-
PTA	-		WS_2	2	-	PTA-C	-

3.4 Synthesis of PMA@MIL-100 and carbon-based derivatives

3.4.1 Chemicals

All reagents were purchased from Fisher Scientific and used without further purification: Iron (III) chloride anhydrous ($FeCl_3$, 98 %), Trimethyl-1, 3, 5-benzenetricarboxylate ($C_6H_3(CO_2CH_3)_3$, 99 %, abbreviated as Me3btc), Phosphomolybdic acid hydrate ($H_3PMo_{12}O_{40}\cdot xH_2O$, abbreviated as PMA).

3.4.2 Sample preparation

3.4.2.1 Preparation of MIL-100

MIL-100(Fe) was synthesised according to the previous report [32]. 0.694 g (2.75 mmol) of Trimethyl-1, 3, 5-benzenetricarboxylate was first dissolved in 25 mL of H_2O, then 0.811 g of $FeCl_3$ was added and dissolved in the same solution. This mixture solution was then transferred to a Teflon-lined stainless steel autoclave and placed in an oven at 130 °C for 72 h, followed by cooling the autoclave naturally down to room temperature. The orange powder was then collected via centrifugation at 5500 rpm for 5 min, washed once with water, then twice with hot acetone. This collected sample was denoted as MIL-100.

3.4.2.3 Preparation of PMA@MIL-100

Similar to the synthesis of pure MIL-100(Fe), 0.694 g of Trimethyl-1, 3, 5-benzenetricarboxylate (Me3btc), and 0.811 g $FeCl_3$ were added into 20 mL of water to form a solution. Then the calculated amount of phosphomolybdic acid hydrate (PMA) was first dissolved in 5 mL of water to form another solution, which was then added to the mixture solution containing Me3btc and $FeCl_3$. The resulting mixture was transferred to a Teflon-lined stainless steel autoclave and placed in an oven at 130 °C for 72 h. The remaining steps are identical to that of pure MIL-100. The as-made PMA@MIL-100 samples were denoted as 1-PMA@MIL, 2-PMA@MIL, and 3-PMA@MIL with 150, 250, and 350 mg of PMA used during the synthesis, respectively.

3.4.2.3 Preparation of bimetallic Fe-Mo sulphide/S-doped carbon nanocomposite

To obtain the metal sulphide/carbon composites, typically 0.05 g dried 1-PMA@MIL powder was loaded in a ceramic boat and subjected to pyrolysis under an H_2S atmosphere in a horizontal flow-through tube furnace. First, the tube in the furnace was flushed with Ar to remove the remaining air inside, followed by heating the furnace at a ramp rate of 10 °C min^{-1} in continuous Ar flow of 50 mL min^{-1}. After the furnace temperature arrived at the target temperature (600, 800, and 1000 °C, respectively), H_2S gas flow of 50 mL min^{-1} was introduced together with the Ar flow at the target temperature for 1 h. Afterwards, H_2S was switched off, and the furnace was left to cool down naturally with Ar flow remaining. The obtained samples were labelled as xMo@MIL-y, where x represents which parental PMA@MIL was used (for example, x = 1 when the sample was derived from 1-PMA@MIL) and y represents the pyrolysis temperature of the PMA@MIL. For example, a sample derived from 1-PMA@MIL pyrolysed at 800 °C is denoted as 1Mo@MIL-800. For comparison, MIL-100 was also pyrolysed in H_2S at 600, 800, and 1000 °C for 1 h, and the resulting samples were labelled as MIL-600, MIL-800, and MIL-1000, respectively.

Table 3.3 Summery of the name and compositions of the samples in this section 3.4 and Chapter 6.

Composition	Sample name	Amount of PTA (mg)		Heat treatment under Ar/H_2S gas for 1h					
				Composition	Heating time (h)	600°C	800°C	800°C	1000°C
						Heating rate (°C/min)			
						10°C/min	10°C/min	2°C/min	10°C/min
PMA@ MIL-100	1-PMA@MIL	150	→	Fe-Mo sulphide/S-doped porous carbon	1/3 (20min)	-	1Mo@MIL-800-2min	-	-
					1	1Mo@MIL-600	1Mo@MIL-800	1Mo@MIL-800-2C/min	1Mo@MIL-1000
					2	-	1Mo@MIL-800-2h	-	-
					1h in Ar + 1h in Ar/H_2S	-	1Mo@MIL-800-1hAr-1hH2S	-	-
	2-PMA@MIL	250			1	-	2Mo@MIL-800	-	-
	3-PMA@MIL	350			1	-	3Mo@MIL-800	-	-
MIL-100(Fe)	MIL-100	0		Fe sulphide/S-doped porous carbon	1	MIL-600	MIL-800	MIL-800-2C/min	MIL-1000

3.5 Characterisation techniques

3.5.1 XRD

X-ray diffraction (XRD) is a robust non-destructive technique for the study of crystalline materials. It can provide information including but not limited to structures, phases, crystallinity, average grain size, and crystal defects. XRD peaks are produced by collecting the intensity information of the scattered X-ray from a sample that is irradiated by a monochromatic beam of X-ray at different angles. The relationship between the incident and reflected X-ray can be described by Bragg's law [437]:

$$n\lambda = 2d \sin\theta \qquad (3.1)$$

Where n is an integer, λ is the wavelength of the X-rays, d is the inter-planar spacing that generates the diffraction, and θ is the incident angle. XRD spectrum can be obtained by plotting the angular position versus the intensity of the reflected X-ray. Peak position can be converted to correspond lattice-spacing by Bragg's equation (3.1).

In this thesis, XRD spectra were obtained with *Bruker D8 advanced X-ray diffractometer* with Cu-Kα radiation at 40 mA and 40 kV, step time of 1 s, and step size

of 0.02~0.05 °. The crystalline phases were identified with the software Bruker Advanced X-ray Solutions and JADE.

3.5.2 SEM

Scanning electron microscopy (SEM) is used to collect the surface morphology of the sample under high magnification. For the standard SEM instrument (see **Fig 3.1a**), a stable electron beam is generated by an electron gun located on the top of the SEM column. This electron beam will go through electromagnetic lenses and apertures in order to form a small, focused electron spot on the specimen. Different signals (such as backscattered electrons (BSE) which are generated through elastic interactions, and secondary electrons (SE), which are generated through inelastic interactions) excited by the electron beam, are then collected by different detectors for SEM observation. A high-vacuum environment is needed to avoid electrons scattered by air.[438]

In this work, SEM images were taken with a *Helios Nanolab 600i scanning electron microscope/Focused ion beam DualBeam workstation* at an acceleration voltage of 10 kV. Samples were fixed on a conductive carbon double-sided sticky tape and coated with gold (ca.10 nm) by a sputter coater to reduce charging effects.

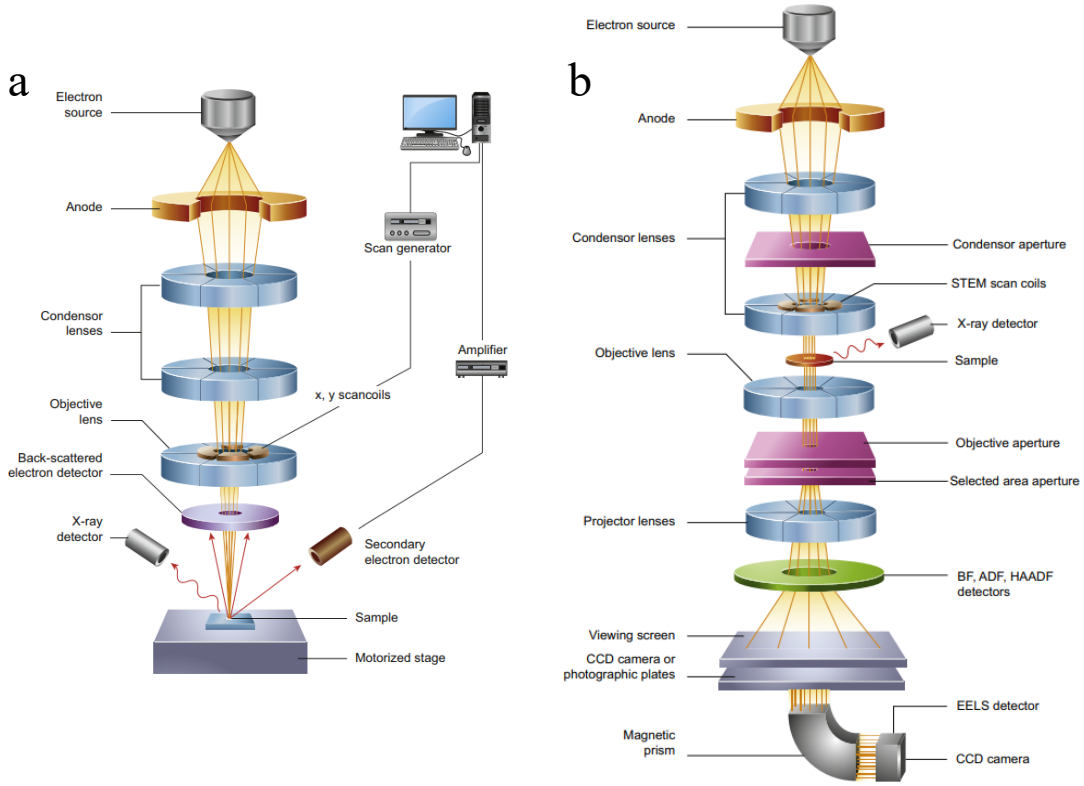

Fig. 3.1 Schematic diagram of the core components of a) SEM and b) TEM [439].

3.5.3 TEM

Transmission electron microscopy (TEM) is a powerful tool capable of attaining very fine nano-structural information. Compared with SEM, TEM can provide information about the internal structures of an ultra-thin sample as the electron beam is transmitted through the sample, and the information is acquired from the transmitted electrons. In a typical TEM (see **Fig. 3.1b**), the electron source is located on the top of the instrument. Electrons generated by the source will be accelerated and focused by a series of condenser lenses and apertures. The parallel beam with controlled diameter and convergence will then pass through the sample, generate elastically and inelastically scattered electrons. The transmitted electrons are then refocused and magnified by lenses and apertures and projected to a camera or a fluorescent screen for TEM imaging.[440] A high-resolution TEM (HRTEM) image can reveal the crystallographic structure, showing lattices with atomic-level resolution. Except for images, selected area electron diffraction (SAED) pattern can be obtained by TEM, which could be used to identify the crystal structure, crystallinity, and lattice spacing based on diffraction contrast.

TEM images were obtained by a *JOEL-2100 LaB6 transmission electron microscope* in this work. Samples were dispersed by sonication in absolute ethanol for 10 min and were deposited on a holey carbon copper grid and dried before TEM analysis.

3.5.4 EDX

Energy-dispersive X-ray spectroscopy (EDX) is used to determine the elemental composition and can be performed in point scan, line scan, or mapping mode. It collects the x-rays emitted from the sample after striking by an electron beam. Therefore, EDX is typically performed in conjunction with SEM and TEM. In short, EDX generated by the primary electron beam will eject from the electron shell of the atoms, leaving holes behind. To compensate for the energy change, electrons at higher-energy states will then fill the holes, shedding their excess energy in the form of X-rays. The energy of these characteristic X-rays is specifically related to the atomic structure of the emitting element, as such different elements can be identified.[441, 442]

EDX line scans and mapping are carried out on the previously mentioned SEM and TEM instrument using an *Oxford Instrument X-MAXN EDS detector* in this thesis.

3.5.5 FT-IR

Fourier-transform infrared (FT-IR) spectroscopy is a versatile tool used to obtain infrared spectrum which absorbed or transmitted by a solid, liquid, or gas. When exposed to IR,

sample molecules will selectively absorb radiation of a specific wavelength, resulting in the vibration of molecular bonds. Each sample will have a distinctive 'fingerprint' depending on the number of vibration freedom and the vibrational energy gap of the molecule. Therefore, by analysing the IR spectrum, abundant structure information of a molecule can be obtained.[443]

In this work, FT-IR spectra were recorded in the wavelength range of 500-1300 cm^{-1} on a *Shimadzu IRTracer-100 spectrometer*, and samples were prepared by the KBr pellet method.

3.5.6 Raman spectroscopy

Raman spectroscopy is a spectroscopic technique that can determine molecular vibrations information of molecules. Similar to FT-IR, Raman spectroscopy can provide 'fingerprint' spectrum of a sample, by which the molecular structure can be revealed. Raman spectroscopy relies on inelastic scattering of photons, in which both exchanges of energy and change in photons direction occur. This inelastic scattering is so-called Raman scattering and only occupied a fraction of total scattering. Raman spectrum was obtained by irradiating the sample with monochromatic laser light and recording the intensity of the scattered radiation of different frequencies.[444] It is a powerful technique to investigate carbonaceous materials.[445-447]

Raman spectra were acquired with *Renishaw inVia Raman microscope* using a 20× objective lens and an excitation laser beam of 532 nm in wavelength in this work. Powder samples were pressed flatly onto a silicon wafer before being placed under the microscope.

3.5.7 TGA

Thermogravimetric analysis (TGA) is a thermal analysis that investigates changes in the weight of a sample when the temperature changes. It is a destructive characterisation tool often used to determine the thermal stability and the thermal degradation pathways of a known test sample.

In this thesis, some samples were subject to TGA using a *TA SDT Q600 instrument*, with a target temperature of 800 °C, heating ramp of 10 °C min^{-1} and air flow rate of 100 mL min^{-1}.

3.5.8 N_2 sorption analysis

N_2 sorption analysis is used to determine the physical adsorption of N_2 molecules in solid materials, hence determining the texture properties of the sample. In particular, the

adsorption and desorption isotherms are calculated by Brunauer-Emmett-Teller (BET) method to estimate the number of physically adsorbed gas molecules in porous materials and hence the surface area of the samples. BET theory applies to systems with multilayer adsorbate with main assumptions include: i) adsorption take place on a homogeneous surface and all surface sites have identical adsorption energy for adsorbate, ii) no steric limitation to the number of layers of the adsorbate, iii) there are not lateral interactions between adsorbate molecules, and iv) the successive layers start to build up only before the first one has been completed.[448]

In this work, N_2 sorption analysis was carried out on a Quantachrome Autosorb-iQ gas sorptometer by using the conventional volumetric technique. Before the actual gas analysis, samples were outgassed under vacuum at 150 °C for 3 h. Adsorption data in the partial pressure (P/P_0) range of 0.05-0.2 was used for the BET calculation. Total pore volume was determined from the amount of adsorbed N_2 at P/P_0 ca. 0.99. Furthermore, the pore size distribution of the sample was analysed using the Non-Local Density Functional Theory (NLDFT) model.

3.5.9 XPS

X-ray photoelectron spectroscopy (XPS) is a surface-sensitive spectroscopic analytic technique based on the photoelectric effect. It can identify the elements and provide chemical states information from the surface of the samples. In the XPS system, the sample is irradiated with monochromatic X-rays, and the ejected photoelectrons are analysed by an electrostatic or electromagnetic analyser for their kinetic energy. The kinetic energy can determine the corresponding binding energy of those escaped electrons. Note that the specific binding energy is tightly related to the electron configuration of the elements and compounds. The elements and chemical states of the elements can therefore be determined.[449]

XPS was performed on a *Kratos Axis Ultra system* with a monochromated Al Kr X-ray source operated at 10 mA emission current and 15 kV anode potential in this thesis.

3.5.10 Electrocatalysts measurements

Electrochemistry measurements were carried out on a CHI660E electrochemical workstation at room temperature. A classic three-electrode cell set up was used where a glassy carbon (GC) electrode (with a working area of 3 mm in diameter) was used as the working electrode, a Pt wire (or carbon rod) was used as the counter electrode, and an Ag/AgCl electrode was used as the reference electrodes. Moreover, 1 M KOH solution

and 0.5 M H_2SO_4 solution were used as the electrolyte for OER and HER analysis, respectively. The experiment set-up is shown in **Fig. 3.2** Note that the rotating disk electrode (RDE) measurements were performed with the help of CHI 760D potentiostat.

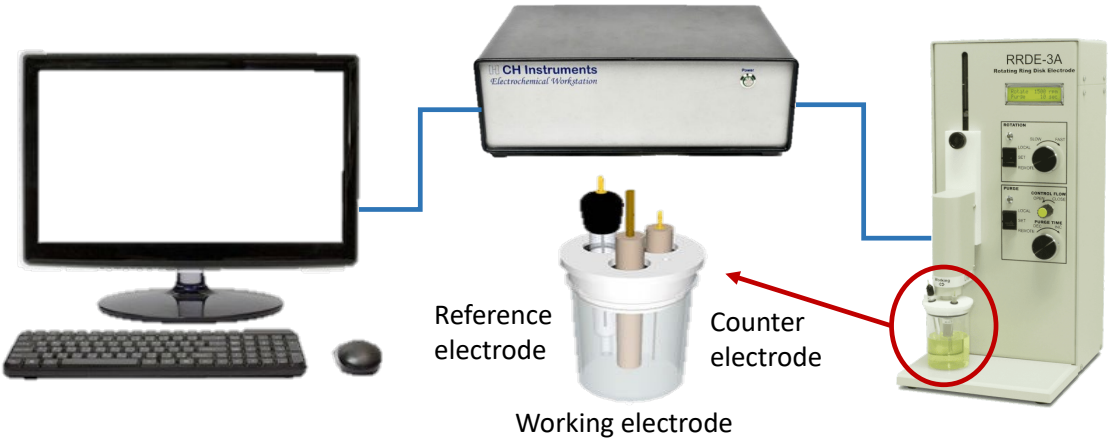

Fig. 3.2 Schematic diagram of the electrochemical set up.

In order to prepare the working electrode, the bare GC electrode was first polished with 0.05 µm alumina slurries on the BAS Diamond polishing pad then on the BAS Alumina polishing pad to obtain a mirror-like finish. After polishing, the electrodes were cleaned with an excess amount of distilled water and dried with an RS PRO butane duster. Then, 5 µL of freshly prepared sample ink, which was obtained by ultrasonically dispersing 3 mg of the sample into 1 mL of water-ethanol (4:1 v/v) solution with an additional 5 µL of 5 wt% Nafion solution for 30 min, was drop cast onto the working surface of the GC electrode with the aid of Eppendorf micropipette and dried naturally to form a uniform thin film. The calculated loading of each catalyst is approximately 21 mg cm^{-2} based on the above ink preparation recipe. For the OER test, the working electrode was spun at 1600 rpm during the measurement, and the electrolyte was purged with high purity oxygen with a flow rate of 20 ml min^{-1} prior to the exact measurement to achieve an O_2-saturated condition. Although there is debate on saturating the solution with O_2 for OER testing, it seems to have become an often-employed practice. Amada et al. suggested that the precent of O_2 in the electrolyte has no effect (or a negative) on the activity of the OER, and saturating the electrolyte with oxygen may closely resemble the situation in a real electrolyser [612]. Therefore to keep the consistency of the testing, O_2-saturated condition was applied to all OER testing in this thesis.

In order to prevent bubbles on the electrode-electrolyte interface, a small amount of distilled water was used to wet the electrode before immersing it into the electrolyte. All potentials were measured vs the Ag/AgCl reference electrode and reported vs the

reversible hydrogen electrode (RHE). The conversion of $E_{Ag/AgCl}$ to E_{RHE} was calculated with Nernst equation[450]:

$$E_{RHE} = E_{Ag/AgCl} + 0.059 \times (\text{pH}) + 0.197 \quad (3.2)$$

Where pH is the pH value of the electrolyte solution.

Due to the effect of ohmic resistance on intrinsic catalytic activity, all the polarization curves are presented with iR compensation for further analysis. The uncompensated resistance was obtained using the software built-in function, with test potential at the open circuit potential and a compensation level of 95%. The iR correction was manually apply to the measured LSV curve potential data (using equation 3.3, E_{iR} is the iR corrected potential, i is the measured current and R_u is the measured uncompensated resistance) and compared with the auto-compensated LSV curves obtained by the software in order to prevent overcompensation.

$$E_{iR} = E_{RHE} - \text{i} * R_u \quad (3.3)$$

To better interpret the polarization curve (i.e. the linear sweep voltammograms (LSV) curve), the reaction mechanism indicator, Tafel slope, was calculated from the Tafel equation to evaluate the Electrocatalytic activity of the sample:

$$\eta = a + blog(j) \quad (3.4)$$

Where η is the overpotential, j is the exchange current density, a is the interception (i.e. $\log(j_0)$) and b is the Tafel slope. By plotting the potential versus the current density in logarithm (i.e. the Tafel plot) and fitting the linear portion of the plot, b can be easily obtained.[451] The Tafel plots of different samples are constructed based on the corresponding LSV curves.

Chapter 4 POM@ZIF derived bimetallic W-Co sulphide/porous carbon nanocomposites

4.1 Introduction

Due to the advantages of high energy density, zero-emission of pollutants, non-toxicity and renewability, hydrogen (H_2) has emerged as a promising alternative energy carrier to conventional hydrocarbon-based petrochemicals. In the past decades, massive efforts have been dedicated to substituting precious metal catalysts with cheaper transition metal-based materials.

The group six transition metal chalcogenides (MX_2 where M = Mo, W and X = S, Se) are one of the most exciting catalyst families [452], and show promising electrochemical applications in recent publications [453]. Among these transition metal dichalcogenides, MoS_2 is one of the most widely studied metal chalcogenides as an electrochemical water-splitting catalyst. In bulk, it is a semiconductor with poor performance in HER, whereas in nanostructured form, MoS_2 frequently exhibits much enhanced HER performance [454, 455]. Its analogue WS_2 also has a similar prospective [456] and experiences the same issues as that of MoS_2 has, such as low active site density and poor electronic conductivity, which inevitably inhibit their electrocatalytic performance in HER. The active site density of the catalyst can usually be increased by the formation of nanoscale structures or dispersion of the active components in highly porous supports [457, 458]. In contrast, the electronic conductivity of the catalyst can normally be enhanced via the combination of the catalytic active components with electronic conductive substrates such as carbon nanotubes, graphene, and so on [459, 460]. On the other hand, cobalt sulphide is a typical kind of transition metal chalcogenide, which is earth-abundant and frequently exhibits good OER activities [461]. It is, therefore, anticipated that a composite containing cobalt sulphide and tungsten sulphide, as well as conducting carbon substrate, is potential bifunctional electrocatalysts towards both HER and OER. However, such a complex composite is difficult to generate via conventional material process methods, not to mention the desire for homogeneous nanostructures that could expose more catalytic active sites and enable better mass transport for the reactions of interest. However, components in these complicated composites are generally less homogeneous presented in the samples, and only the HER performances of these composites were evaluated [462-464].

In recent decades, Zeolitic imidazolate frameworks (ZIFs) have been ardently investigated as sacrificial templates for various complex composites due to their natural compositions, porous structures and easy tailorability. Given that ZIF-67 possesses a sodalite zeolite-type structure with a cavity size of 1.14 nm and aperture size of 0.33 nm [465], it is potentially an excellent porous host to confine specific molecular structures with sizes larger than its aperture size. This feature has been actually demonstrated that ZIF-67 could perfectly encapsulate Keggin-type polyoxometalate (POM) clusters, such as phosphotungstic acid (PTA), which can readily hydrolyse into Keggin type α-$PW_{12}O_{40}^{3-}$ with a size of 1 nm [466], and remain stable in the cages of MOFs without leaching during the hydrothermal synthesis of POM@MOF composite. The produced POM@MOF composites, which are characterized with the combination advantages of both MOFs and POMs, together with homogeneous distribution of the POM clusters within the 3D MOF matrix, have attracted increased interest in the past several years [467, 468], due to their great capability to provide not only the regular arranged organic linkers but also W, Mo, etc. sources that can result in the generation of W or Mo-based electrochemical active catalysts on porous carbons with high specific surface areas via carbonization process [469, 470]. The generated composites are mainly transition metal carbides or oxides particles homogeneously distributed on porous carbon materials and showed much improved electrocatalytic performance in HER [469-473], due to the fact that the in situ formed porous carbon substrates can not only remarkably increase the electronic conductivity of the composites, but also efficiently prevent the agglomeration of the electrocatatlytic active metal carbide or oxide particles [472, 473].

In this Chapter, for the first time, we presented a facile one-step sulfurization/ carbonization approach to produce bimetallic tungsten-cobalt sulphide-based heteroatom doped porous carbon (WS_2/ $Co_{1-x}S$@N, S co-doped porous carbon) nanocomposites utilizing the in situ synthesized PTA@ZIF-67 as precursors, where the PTA can provide abundant tungsten source, the metal ion in ZIF-67 acts as cobalt source. At the same time, the organic linker in ZIF-67 is the source of the carbon substrate. The homogeneous confinement of PTA molecular clusters in ZIF-67 can eventually lead to the formation of a homogenous dispersion of tungsten sulphide and cobalt sulphide particles within the ZIF-derived 3D porous carbon matrix after heat treatment in the H_2S atmosphere. The resulting bimetallic Co-W sulphides/porous carbon composites not only exhibit the prominent improvement in electrocatalytic activities towards both HER and OER, but also show increased stability in electrocatalytic performance due to the effective

prevention of the agglomeration of metal sulphide particles via the in situ formed porous carbon matrix.

4.2 Results and discussion

4.2.1 Characterizations of as-made PTA@ZIF67

PTA@ZIF-67 hybrids were first synthesized through in situ self-assembly of 2-methylimidazole (MeIM), cobalt nitrate hexahydrate and phosphotungstic acid hydrate (PTA) in one pot, followed by heat treatment of the in situ formed PTA@ZIF67 in H_2S atmosphere at higher temperature to generate the bimetallic tungsten-cobalt sulphide on heteroatom doped porous carbon nanocomposite, as schematically demonstrated in **Fig. 4.1**. Due to the acidic sensitivity of ZIF-67, an excess amount of MeIM was necessary to buffer the acidity of PTA [474]. Therefore, a green aqueous synthesis method that required a large amount of MeIM [475] to in situ synthesize PTA@ZIF-67 was adopted in this study. This simple, facile, and environmentally friendly synthesis method enables to prepare gram-scale precursor products efficiently.

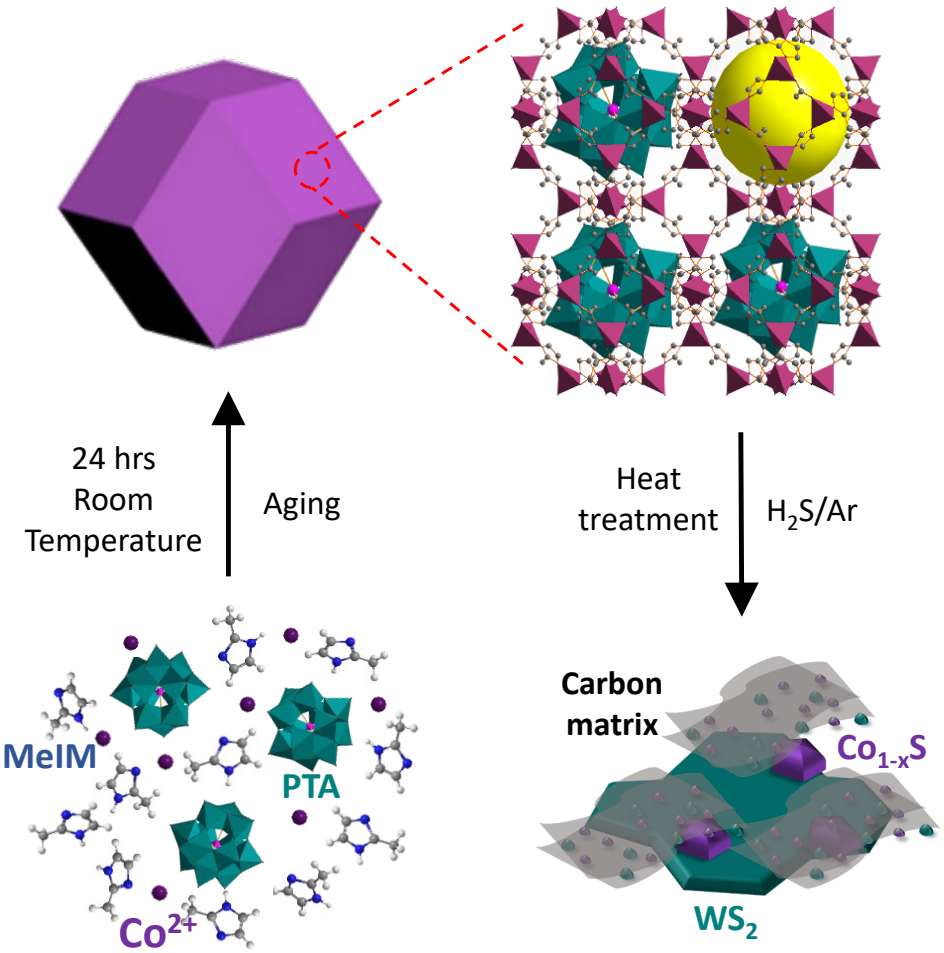

Fig. 4.1 Schematic diagram of the preparation of WS_2/ $Co_{1-x}S$@N, S co-doped carbon nanocomposite.

The structures of the as-made PTA@ZIF-67 were characterized by FT-IR, XRD and TGA and presented in **Fig. 4.2**. Note that there are four characteristic IR bands associate with Keggin-type PTA: 1080, 981,889 and 801 cm^{-1}, which are assigned to P-O_a stretching vibration (O_a corresponds to the oxygen atom in tetrahedral phosphate group), W=O_t stretching vibration (O_t corresponds to the terminal oxygen atoms in the exterior WO_6 octahedron), W-O_b-W stretching vibration (O_b corresponds to the bridging oxygen atom connect with two tungsten atoms) and W-O_c-W stretching vibration (O_c corresponds to oxygen atom at the corners of the keggin structure) respectively [476-478]. As demonstrate by the FT-IR spectra (**Fig. 4.2A**), all PTA@ZIF-67 hybrids show the νas (P-Oa) at 1104 cm^{-1}, υ_{as} (W-Ot) at 1053 cm^{-1}, υ_{as} (W-Ob-W) at 950 cm^{-1} and υ_{as} (W-Oc-W) at 815 cm^{-1}, where ZIF-67 has no apparent absorptions in these regions, indicating the presence of PTA. The red-shift and split of the peaks compare with the pure PTA spectrum could possibly due to the change in chemical environment after encapsulation as well as the partly dissociation of PTA. The deteriorated powder XRD diffraction peaks

(**Fig. 4.2B**) associate with the increasing amount of PTA introduced into the composites indicate that the PTA can affect the formation of ZIF structures. Moreover, incorporating a controlled amount of PTA is vital for maintaining the well-defined ZIF-67 structures indicate by the flat XRD pattern of W30@Z67. Furthermore, the PTA may be well confined in the cages of ZIF-67 as no characteristic diffraction peaks of PTA can be identified in the XRD measurement results. TGA curves (**Fig. 4.2C**) clearly show that PTA has been successfully introduced in the resulting as-synthesized precursors, evidenced by the elevated remaining weight for the increased PTA amount used during the synthesis.

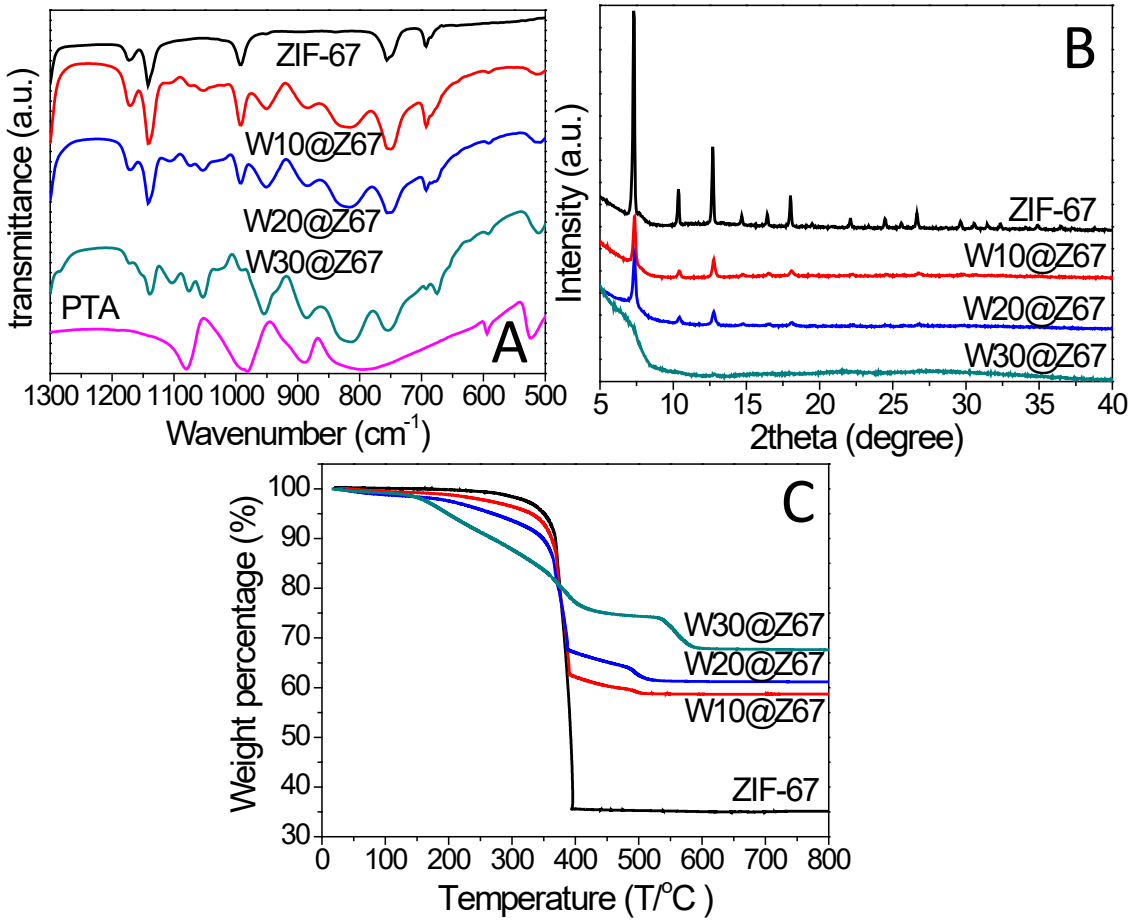

Fig. 4.2 A) FT-IR spectra of ZIF-67, W10@Z67, W20@Z67, W30@Z67 and PTA; B) powder XRD, and C) TGA curves obtained under Air atmosphere for as synthesis ZIF-67, W30@Z67, W20@Z67 and W10@Z67.

In addition, the textural properties of pure ZIF-67 and the representative PTA modified sample W20@Z67 were determined by N_2 sorption. Specific surface area, and the total pore volume were summarized in **Table 4.1**. ZIF-67 got a specific surface area 1.3 times of W20@Z67, and the total pore volume decreased 23% after modification. These observations further confirm that the PTA molecules are encapsulated in the pore

channels and/or some cages of ZIF-67, which results in the decrease in surface area and pore volume of the precursors.

Table 4.1 Specific surface area and total pore volume of as-made ZIF-67 and W20@Z67.

Sample	BET surface area ($m^2 g^{-1}$)	Total pore volume ($cm^3 g^{-1}$)
ZIF-67	1436	1.3
W20@Z67	1097	1.0

In conclusion, all the analysis results suggested that PTA molecules have been successfully encapsulated within the sodalite (SOD) cages of ZIF-67 without dramatically altering its 3D structures. The obtained PTA@ZIF-67 were then subject to heat-treatment in Ar/H_2S mixed gas atmosphere at 600, 800 and 1000 °C respectively for 1 h to generate W, Co sulphide/N, S co-doped carbon nanocomposites.

4.2.2 Characterizations of PTA@ZIF-67 derived nanocomposites

The XRD patterns of the composites obtained by heat treatment of W20@Z67 under different heat process temperatures of 600, 800 and 1000 °C, respectively, are shown in **Fig. 4.3A**. For comparison, the XRD patterns of samples Z67-800 and PTA-800 prepared by heat treatment of pristine ZIF-67 and pure PTA under the same atmosphere at 800 °C are also included. While sample PTA-800 exhibited diffraction peaks similar to the patterns of IF-WS_2 (JCPDS No. 08-0237) [479], the XRD patterns of the PTA modified composites mainly show diffraction peaks indexed to $Co_{1-x}S$ (JCPDS No. 42-0826) [480] and WS_2. Moreover, the sharpness and the intensity of the cobalt sulfide and tungsten sulfide peaks increase with the increase of heat process temperature, suggesting that higher heat process temperature results in higher crystallinity of metal sulfides. There is no observable diffraction peak at 2θ of 26 °, maybe due to the amorphous nature of the carbon with lower diffraction intensity compared with crystalline sulfides.

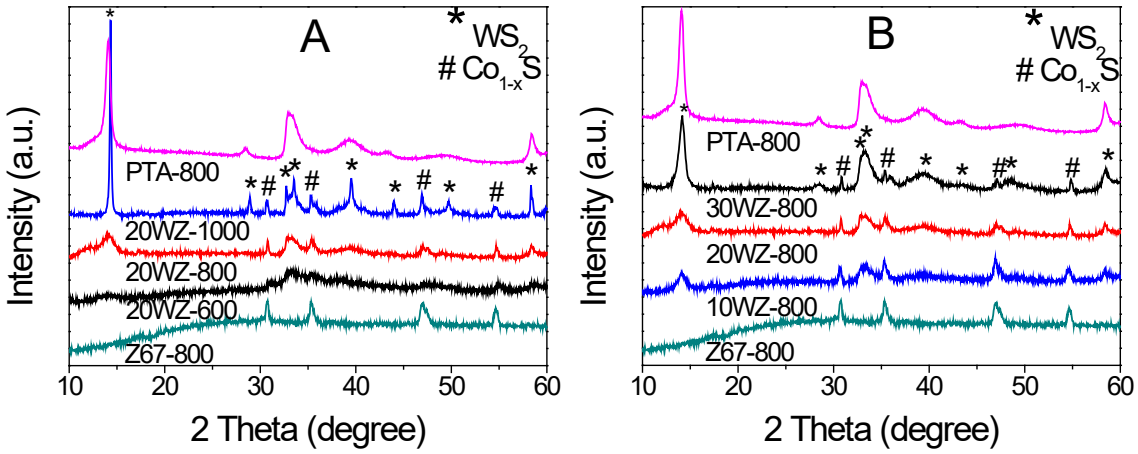

Fig. 4.3 XRD patterns of different nanocomposites. A). PTA-800, 20WZ-1000, 20WZ-800, 20WZ-600 and Z67-800. B). PTA-800, 10WZ-800, 20WZ-800, 30WZ-800 and Z67-800.

The representative SEM images of Z67-800 and the heat-treated W20@Z67 in the H_2S atmosphere at various temperatures are shown in **Fig. 4.4**. Comparing with the pristine ZIF-67 (see **Fig. 4.5A**), the composite derived from ZIF-67 (sample Z67-800 in **Fig. 4.4A**) largely retains the shape and size of its precursor but shows a lumpy surface. As heat treatment temperature increased, the particles have gradually shrunk and collapsed to smaller particles with rough surfaces (**Fig. 4.5C and D**). In contrast, PTA modified composite obtained at 600 °C (sample 20WZ-600) displays a larger particle shape and size but a downy surface (**Fig. 4.4B**). At 800 °C, the particles in sample 20WZ-800 were collapsed, and a large amount of small flakes with the size of around 100 nm has appeared between smaller downy particles (**Fig. 4.4C**). As the temperature increased to 1000 °C, the size of thin flakes in 20WZ-1000 grows up to 1 μm (**Fig. 4.4D**). These observations clearly imply that the morphologies of the W20@Z67 derived composites can be remarkably affected by the heat process temperature of the samples.

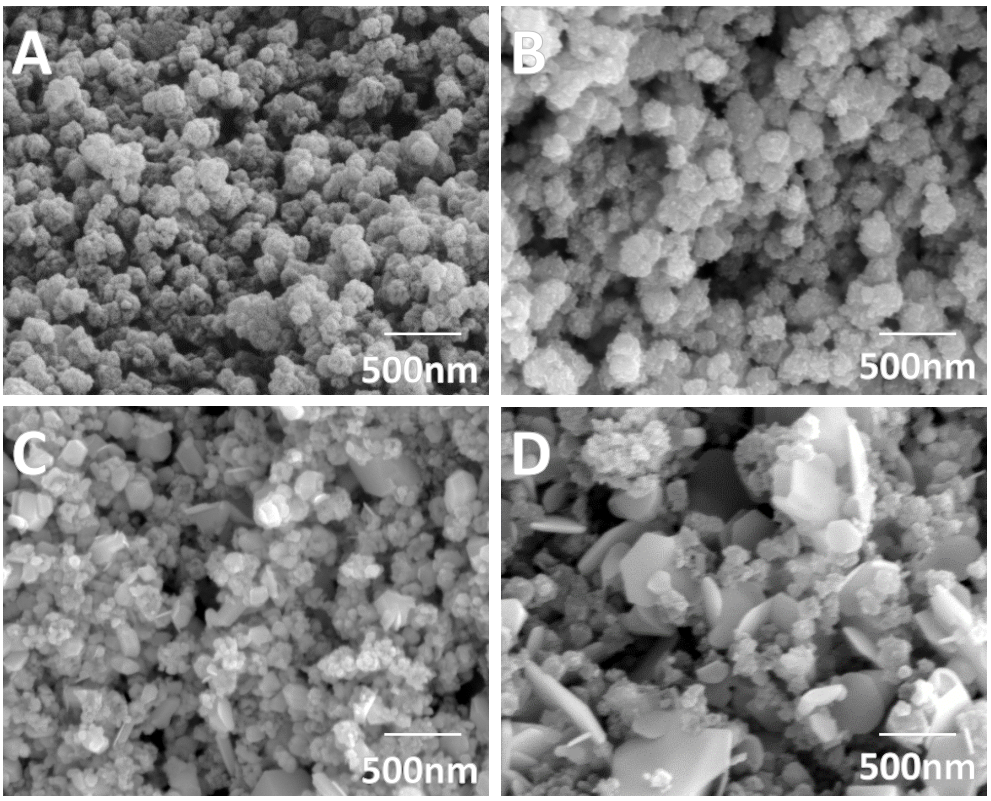

Fig. 4.4 Representative SEM images of different nanocomposites. (A) Z67-800, (B) 20WZ-600, (C) 20WZ-800 and (D) 20WZ-1000.

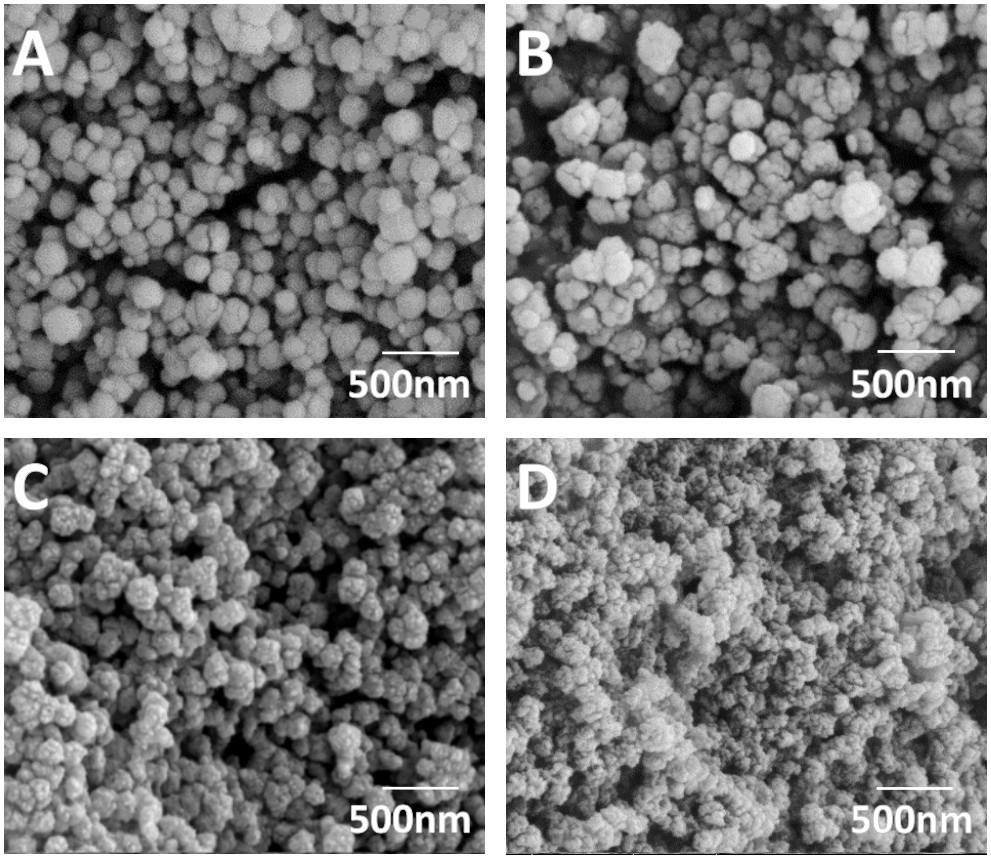

Fig. 4.5 SEM images of A) as-made ZIF-67, B) W20@Z67, C) Z67-600 and D) Z67-1000.

Fig. 4.6 presents the typical TEM images of Z67-800, 20WZ-600, 20WZ-800 and 20WZ-1000. As shown in **Fig. 4.6A1**, only a small amount of black cobalt sulfide particles are clearly observed in Z67-800. The d-spacing between the lattice fringes of (101) for cobalt sulphide in the composite Z67-800 is calculated to be 0.25 nm (**Fig. 4.6A2**), which interactively agreed with the value obtained from the XRD results in Fig. 2A. However, in the 20WZ series composites derived from the heat process of 20W@Z67 in the H_2S atmosphere at high temperatures (**Fig. 4.6B1-D1**), there are obviously more metal sulfide black particles. In addition, both the amount and the size of the black particles increase with the heat process temperature. High magnification TEM images (**Fig. 4.6B2-D2**) clearly exhibit the lattice fringes of 6.3 Å and 3.1 Å, which corresponds to the (002) and (00) planes of 2H-WS_2 respectively for all three 20WZ samples obtained under different heat treatment temperatures, confirming the existence of WS_2 flakes. Moreover, apart from WS_2 particles, composites 20WZ-800 and 20WZ-1000 were obtained by heat treatment of 20W@Z67 at 800, and 1000 °C (**Fig. 4.6C2 and D2**) also confirm the presence of $Co_{1-x}S$ particles with d-spacing of 0.25 nm for the (101) crystalline planes. These TEM images are in excellent agreement with the aforementioned XRD and SEM results. In particular, the general shape of the ZIF-67 crystal is more or less still observable in the 600 °C heat processed sample (**Fig. 4.6B1**) as the formation of tiny flaky WS_2 brings a downy appearance to the surface of the particles. With the increase of the pyrolysis temperature, both Co and W bimetallic sulphides with improved crystallinity are formed, evidenced by both the increased XRD peak intensities in **Fig. 4.3** and the observed fringes for both cobalt sulphide and tungsten sulphide in **Fig. 4.6C2 and D2**, leading to significant changes in morphologies of these samples.

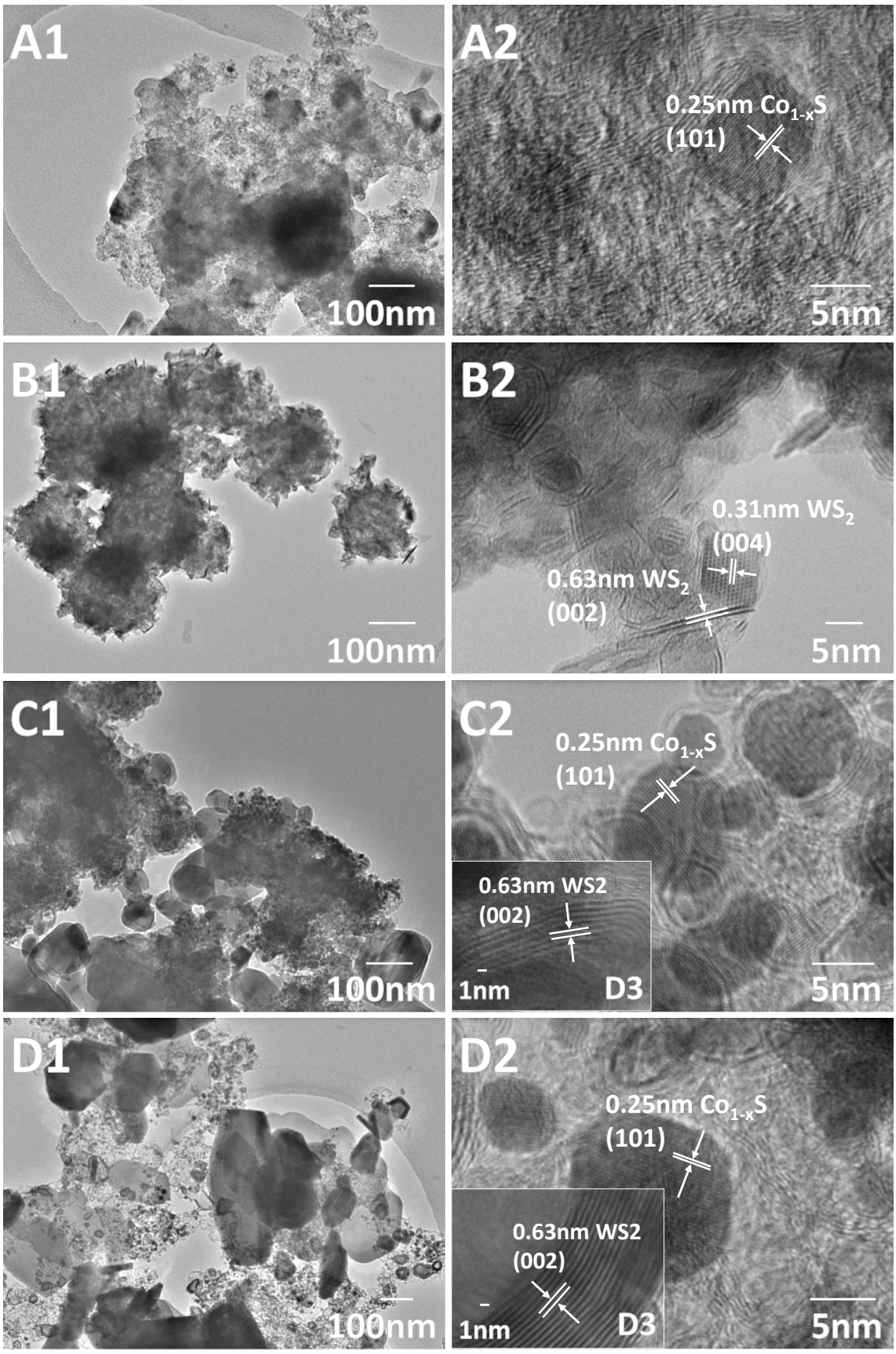

Fig. 4.6 Representative TEM images of different nanocomposites. A) Z67-800, B) 20WZ-600, C) 20WZ-800 and D) 20WZ-1000.

Moreover, sample 20WZ-800 (**Fig. 4.6C1**) shows large particles outside the carbon matrix with sizes approximately in the range of 50-100 nm, which possibly originates from the migration and agglomeration of small metal sulfide particles within the carbon matrix driven by thermal gradient during the heat process. HRTEM image of this sample in **Fig. 4.6C2** and **Fig. 4.7B** indicates that there are small $Co_{1-x}S$ spheres and onion-like inorganic fullerene (IF-WS_2) particles with a size of around 5-10 nm embedded in an in situ formed carbon matrix derived from the carbonization of the organic linkers in W20@Z67. As the heat treatment temperature increases to 1000 °C, the resulting sample 20WZ-1000 (as shown in **Fig. 4.6D2** and **Fig. 4.7C**) displays larger $Co_{1-x}S$ particles in the carbon matrix with a size up to 15 nm in diameter. Meanwhile, the number of onion layers of the carbon wrapped IF-WS_2 particles have increased as well. It is believed that the confined molecular PTA clusters within the ZIF-67 cages could first decompose to tungsten oxide species at high heat process temperatures, the formed tungsten species then react with H_2S gas to form layer WS_2 particles. The formation of this layer WS_2 structure may be based on the outside-in growth mechanism proposed by Feldman et al. that the S atom and H atom decomposed from H_2S will diffuse into and react with the as-formed nanoparticle WO_x to further produce layers of WS_2 [481, 482]. The O atoms in the tungsten oxide nanoparticles will be gradually replaced by S atoms, and eventually, a WS_2 onion ball (IF-WS_2) is formed. At higher heat process temperatures, large WS_2 flakes with a size up to 1 μm are formed (see both **Fig. 4.6C, D** and **Fig. 4.7C**). Additionally, large $Co_{1-x}S$ crystals size up to 200 nm also grow along the outside of the carbon matrix, which results from the migration and agglomeration of $Co_{1-x}S$ nanocrystals under the heat treatment process (as shown in both **Fig. 4.6** and **Fig. 4.7B and C**).

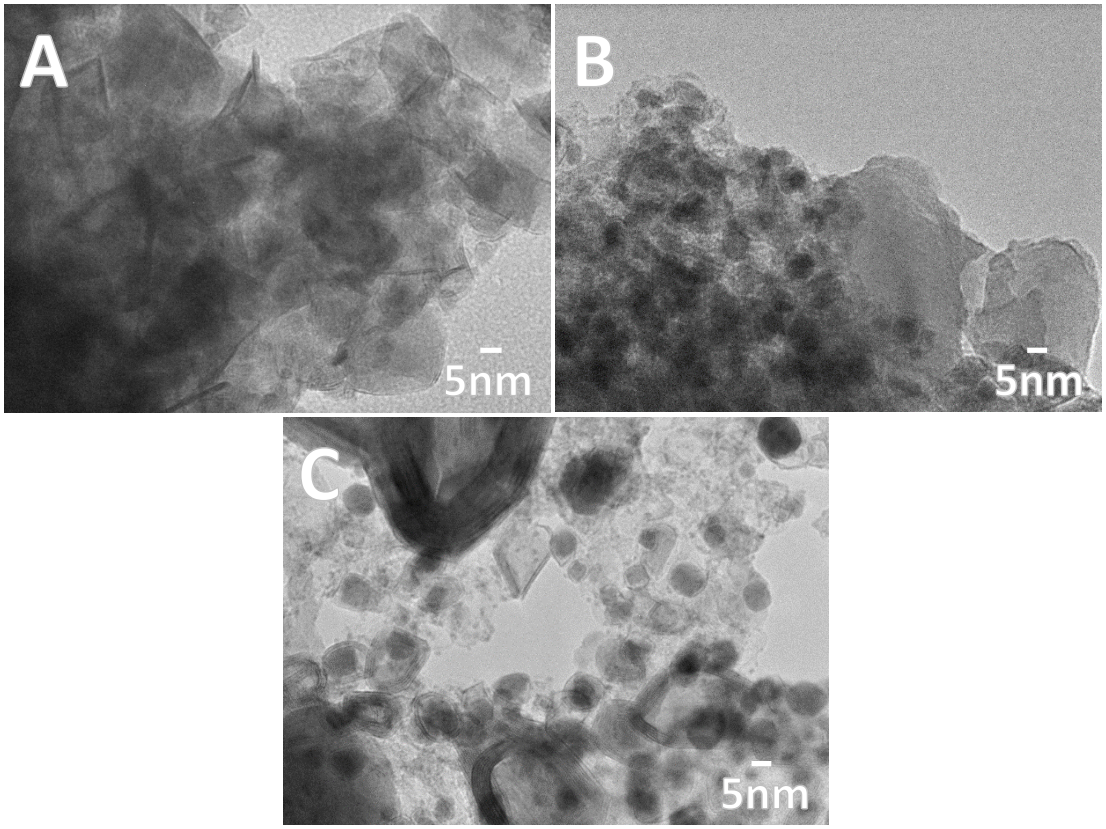

Fig. 4.7 High resolution TEM images of A) 20WZ-600 B) 20WZ-800 and C) 20WZ-1000.

To gain more information on the surface composition and chemical state of the as-synthesized nanocomposites, TEM-EDX and XPS analysis was performed, and the results are shown in **Fig. 4.8 and 4.10**, respectively. The elemental mappings and EDX spectrum in **Fig. 4.8** and **Fig. 4.9** clearly confirm the presence of C, S, Co and W in the composite, which is consistent with the XRD. In addition, the element distribution mappings together with the corresponding TEM image have suggest the homogeneous distribution of all the elements in the samples.

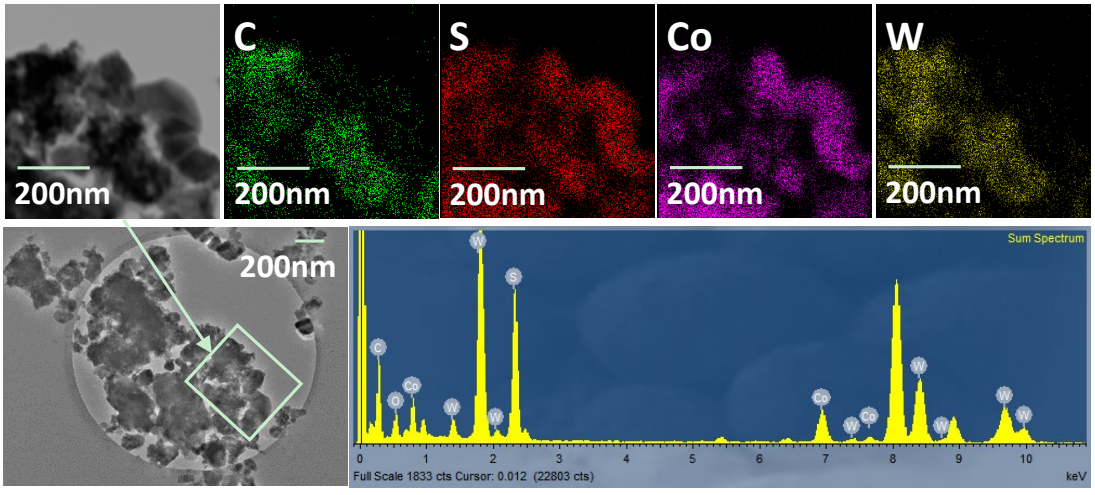

Fig. 4.8 TEM images, elemental mappings and element spectrum of 20WZ-800.

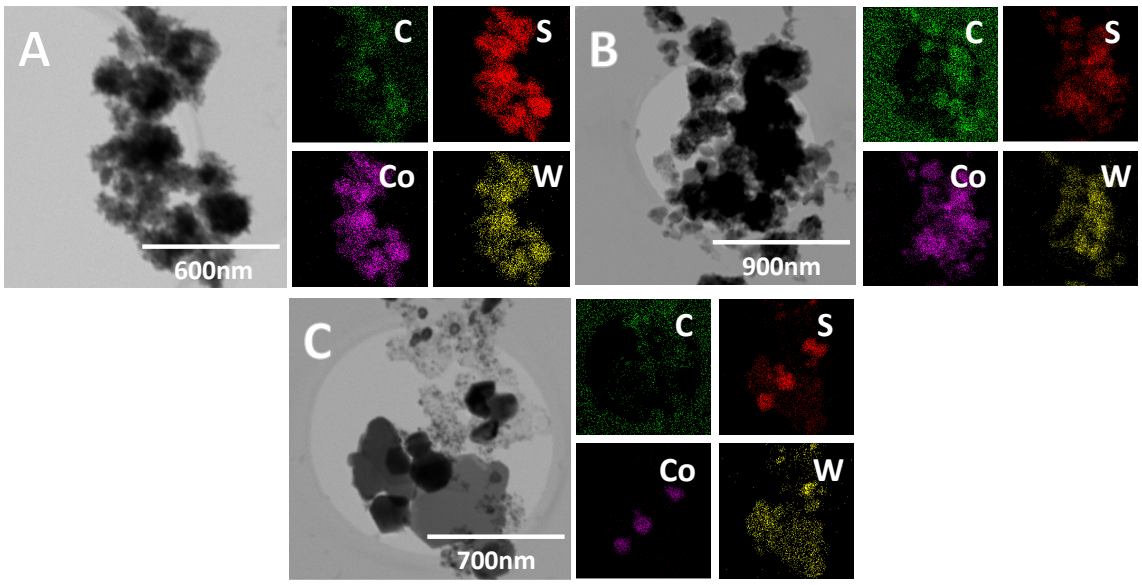

Fig. 4.9 TEM images and elemental mappings of A) 20WZ-600, B) 20WZ-800 and C) 20WZ-1000.

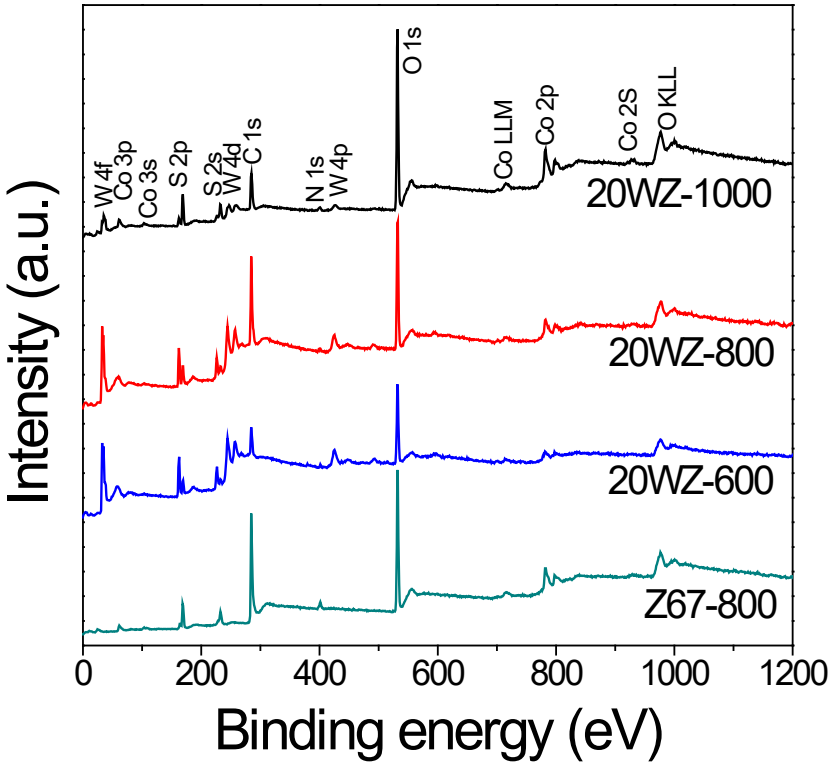

Fig. 4.10 Elemental survey of XPS for sample 20WZ-1000, 20WZ-800, 20WZ-600 and Z67-800.

Element survey carried out on XPS and presented in **Fig. 4.10** further confirms the presence of W, Co, S, C, N and O in all the PTA@ZIF-67 derived composites. High-resolution XPS spectra of N 1s and C 1s (**Fig. 4.12D and E**) have suggested that the carbon matrix was co-doped with N and S.

Fig. 4.12A presents the high-resolution XPS spectra of Co 2p for 20WZ obtained at 600, 800 and 1000 °C, respectively. The two spin-orbit doublets peaks at approximately 781.8 (2p 1/2) and 798.1 eV (2p 3/2) are the characteristics of Co^{2+} oxidation state in the surface species, belonging to the Co-S bond due to the formation of $Co_{1-x}S$ [483]. While the peaks at around 785 and 802 eV are the corresponding shake-up satellite peaks [484], the two spin-orbit doublet peaks at around 793.7 (2p 1/2) and 778.7 eV (2p 3/2) only observable for sample 20WZ-800 and 20WZ-1000 can be ascribed to Co^{3+} oxidation state. Therefore, it is suggested that mixed oxidation states (both Co^{2+} and Co^{3+}) existed in high temperature derived samples, which is consistent with the previous report [480]. Moreover, comparing the XPS spectra of Z67-800 with that of 20WZ samples, the 2p 3/2 peak for Co^{3+} and Co^{2+} has shifted from 778.4/781.9 eV (Z67-800) through 778.5/781.7 eV (20WZ-800) to 778.7/ 781.8 eV (20WZ-1000) respectively (**Fig. 4.11**), which is very close to the Co 2p spectra of Co-W-S phases at 778.6~778.8 eV [485, 486], indicating an increasing strong interaction between $Co_{1-x}S$ and WS_2 as temperature increases.

Moreover, in the W 4f spectrum shown in **Fig. 4.12B**, all the 20WZ samples can be deconvoluted into four peaks. Peaks at around 38.0 (4f 5/2) and 35.8 eV (4f 7/2) indicate the presence of W^{6+} species [487], which could be due to the thermal decomposition intermediates of PTA. At high temperatures in the H_2S atmosphere, the W^{6+} species will gradually react with H_2S gas to form WS_2; hence the relative intensity of W^{6+} peaks decreases with increasing temperature. The other two peaks at around 34.7 (4f 5/2) and 32.6 eV (4f 7/2) indicate the presence of W^{4+} species, which could be assigned to the formed WS_2 [486]. This result is also in line with the above XRD results. The relative area of the W^{4+} species are much bigger for the 800 and 1000 °C samples than 600 °C one, which clearly suggests that under relatively high pyrolysis temperature in the H_2S atmosphere, more WS_2 formed from W^{6+} species. It is worth mentioning that 20WZ-600 exhibits an extra pair of weak peaks at 36.50 and 34.73 eV, which can be assigned to W^{5+}, indicating the presence of oxygen vacancies in the WO_x precursor [488], possibly from the decomposition intermediate of PTA.

In addition, high-resolution XPS spectra for S 2p are shown in **Fig. 4.12C**. The peaks observed at around 162.2 and 163.39 eV correspond to the S 2p5/2 and S 2p3/2 doublets with a binding energy separation of 1.19 eV, corresponding to the S^{2-} species of WS_2 [489, 490]. The second pair peaks located at around 168.8 and 169.9 eV are assigned to the S 2p3/2 and S 2p1/2 peaks of oxidized S species, such as sulphate groups [491], which could be due to the oxidation of sulphur in the air [492], or intermediate products formed

during the transformation of WS_2 from PTA and H_2S. At lower pyrolysis temperature in H_2S, the oxidized S species are dominant in sample 20WZ-600. However, with the increase of the pyrolysis temperature, WS_2 gradually becomes the dominant component in the sample 20WZ-800 and 20WZ-1000, consequently the peak areas for S^{2-} species are much larger in the 800 and 1000 °C samples than that in the 600 °C sample.

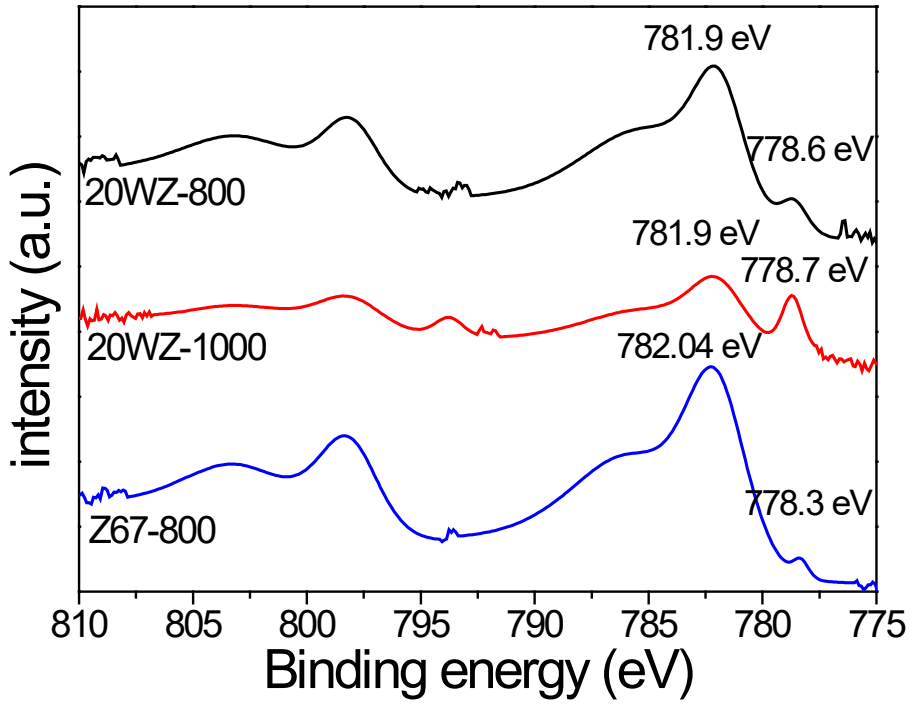

Fig. 4.11 XPS of Co 2p 3/2 for sample Z67-800, 20WZ-800 and 20WZ-1000.

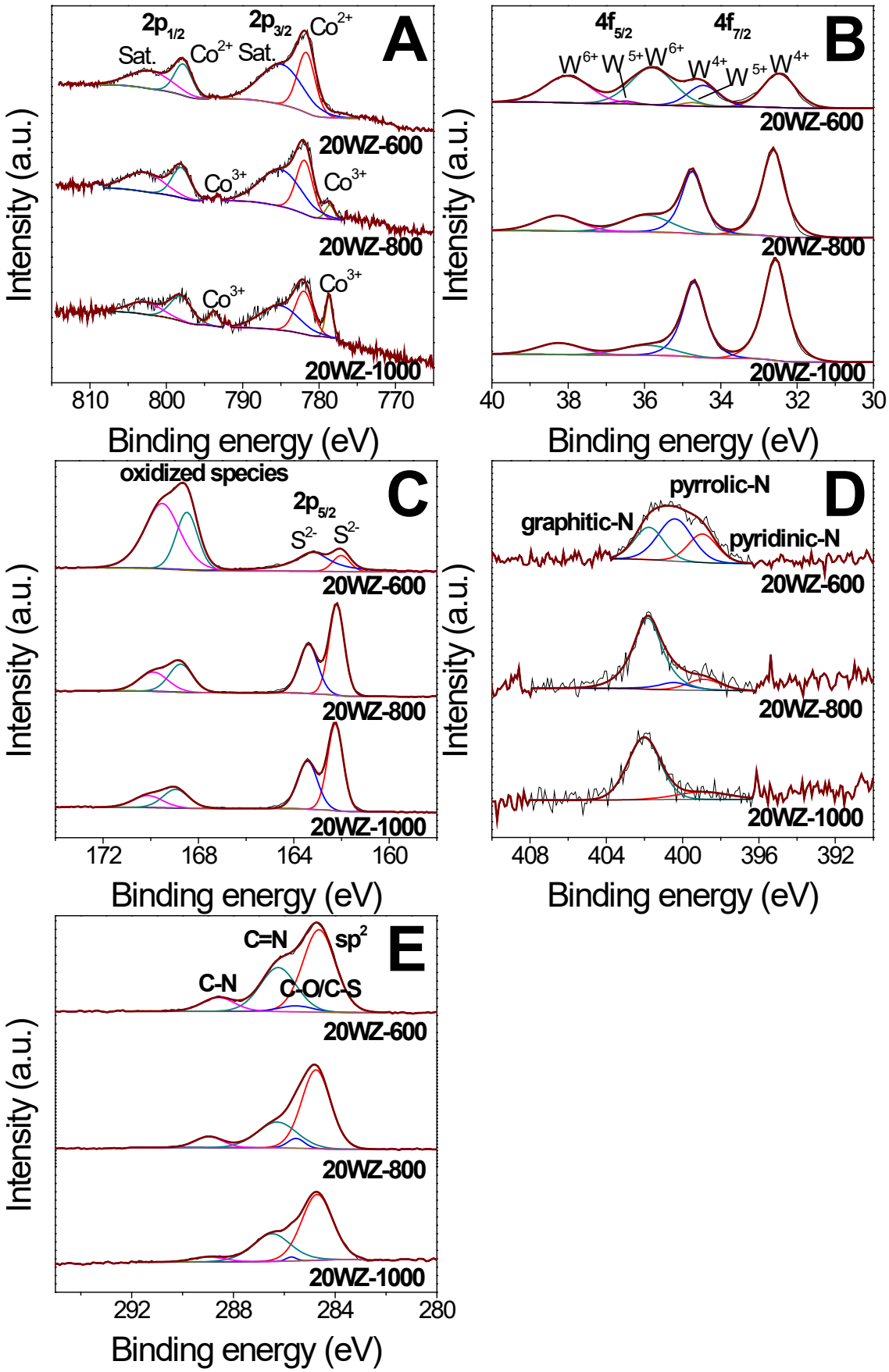

Fig. 4.12 High-resolution XPS spectra of A) Co 2p, B) W 4f, C) S 2p, D) N 1s and E) C 1s for 20WZ-600, 20WZ-800 and 20WZ-1000.

The Raman spectra in **Fig. 4.13** show that all three bi-metallic composites clearly present G band and D band at 1590 and 1340 cm^{-1}, respectively. The G band suggested the existence of non-crystalline carbons and sp^2-hybridized carbon atoms resulted from the carbonization of the samples, while the D band indicated the presence of a more ordered carbon [493]. The relative intensity of two peaks, i.e. I_D/I_G, has increased with increased temperature, indicating the increased amount of edge and topological defects with higher carbonization/sulfurization temperatures [494].

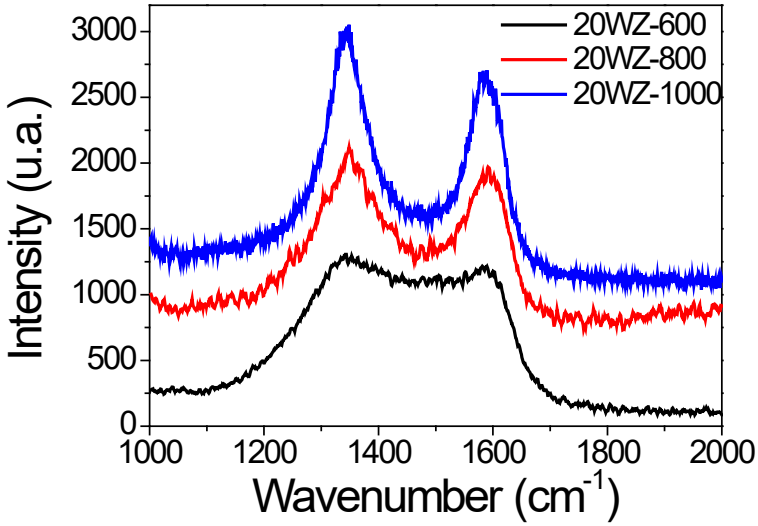

Fig. 4.13 Raman spectra of 20WZ-600, 20WZ-800 and 20WZ-1000.

Moreover, gas sorption analysis of the sulphurized tungsten modified samples shows that an increase in specific surface area and total pore volume (as shown in **Table 4.2**), which may be due to the migration and agglutination of nano-size metal sulphide from the carbon matrix to the surrounding leaving pores behind in the carbon matrix.

Table 4.2 BET specific surface area and total pore volume of 20WZ-600, 20WZ-800, 20WZ-1000 and Z67-800.

Sample	Specific surface area (m^2 g^{-1})	Total pore volume (mL g^{-1})
20WZ-600	15	0.10
20WZ-800	24	0.12
20WZ-1000	42	0.28
Z67-800	78	1.37

4.2.3 Electrocatalytic performance of generated materials

The electrochemical performance of the produced WS_2/Co_xS_y@N, S-codoped carbon nanocomposites are evaluated as electrocatalysts at room temperature in a three-electrode setup. 0.5 M H_2SO_4 electrolyte was used for the HER test. To be more prudent, in this study the commonly reported potential at a current density of 10 mA cm^{-2} is adopted for comparison[495], and the relevant HER measurement results are presented in **Fig. 4.14** and **Table 4.3**. It is clear that sample 20WZ-600 shows the lowest potential of 0.221 V (vs RHE) to achieve a current density of -10 mA cm^{-2} amongst all the W-modified samples (as shown in **Fig. 4.14A** and **Table 4.3**); however, it does not show a higher current density as voltage increases. The early start of the HER may be ascribed to the oxygen vacancies that existed in the intermediate non-stoichiometric tungsten oxide [496, 497], which was proofed by the XPS result earlier. As the reaction continues, the non-stoichiometric compound is gradually oxidised to form stoichiometric tungsten oxide, WO_3. The increased ΔG_H and inferior electrical conductivity of WO_3 results in degrading electrocatalytic activities, as evidenced by the gradual gradient of the polarization curve [497]. The HER activities at higher voltage could be due to the activate site provided by the WS_2 particles embedded in the carbon matrix, as shown in the previous TEM results. The poor crystallinity of carbon could also be one of the reasons for the inferior HER performance. In contrast, 20WZ-800 shows the best overall HER performance with the highest current density at higher potential, and it only requires a relatively low potential of 0.250 V (vs RHE) to reach a current density of -10 mA cm^{-2}. By comparing the LSV curves of the modified ZIF-67 derived catalysts and the pristine ZIF-67 derived ones, it is clear that the bimetallic sulphide carbon composite exhibits an overall better HER catalytic activities than the pristine cobalt sulphide carbon composite. In addition, the HER performances of these composites are, in general, still inferior to the benchmark 20% Pt/C sample.

To better interpret the polarization curve, the reaction mechanism indicator, Tafel slope, was calculated from the Tafel equation to evaluate the electrocatalytic activity:

$$\eta = a + b\log(j)$$

Where η is the overpotential, j is the exchange current density, a is the interception (i.e. $\log(j_0)$), and b is the Tafel slope. By plotting the potential versus the current density in logarithm (the so-called Tafel plot) and fitting the linear portion of the plot, b can be easily obtained [498]. The Tafel plots for HER of different samples are constructed based on the corresponding LSV curves in **Fig. 4.14A** and are presented in **Fig. 4.14B**.

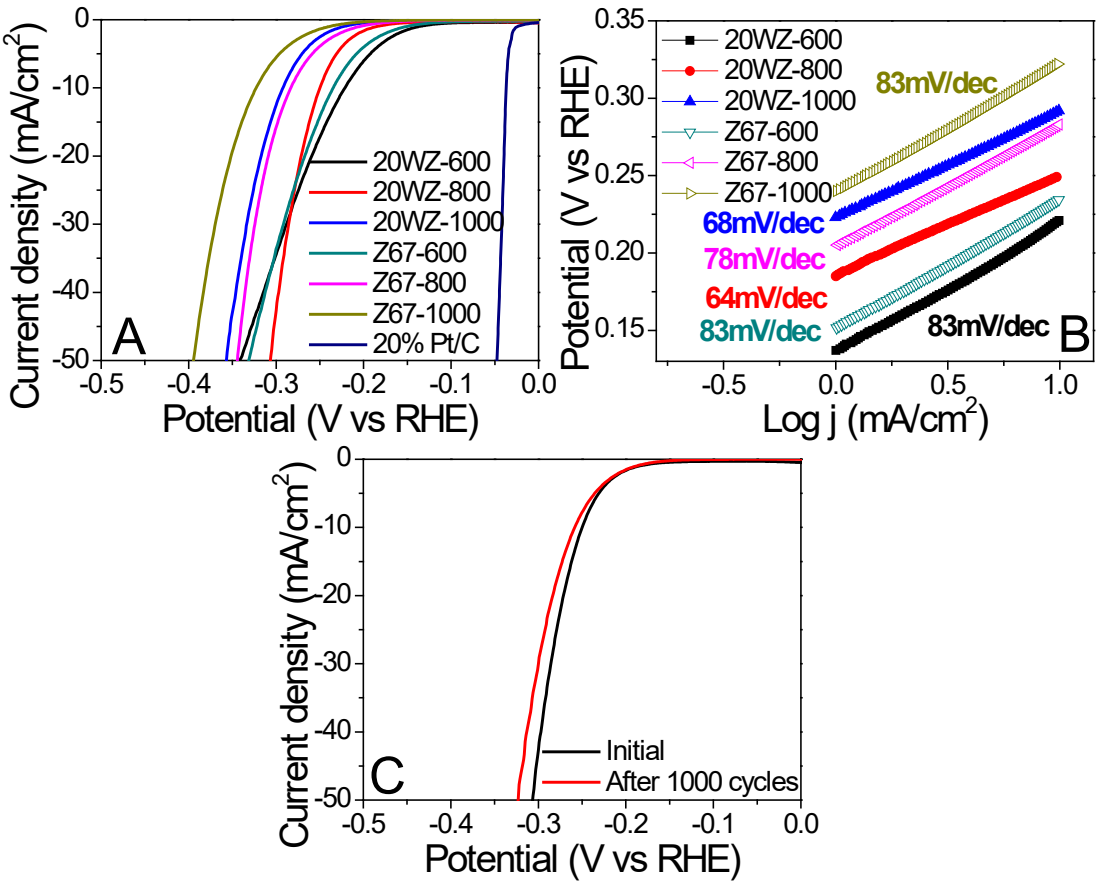

Fig. 4.14 A) HER polarization curves of benchmark catalyst 20% Pt/C, carbonised/sulfurised W20@Z67 and ZIF-67 at 600, 800 and 1000 °C; B) The corresponding Tafel plots and C) HER polarization curves of 20WZ-800 recorded before and after 1000 CV cycles. All the polarization curves were iR corrected at a scan rate of 5 mV s^{-1} in 0.5 M H_2SO_4 electrolyte solution.

In 0.5M H_2SO_4 electrolyte, samples Z67-600, Z67-1000 and 20WZ-600 exhibit a relative high Tafel slope of 83 mV dec^{-1}, while Z67-800 shows a Tafel slope of 78 mV dec^{-1}. However, the corresponding $WS_2/Co_{1-x}S$@N, S-codoped carbon nanocomposites including both 20WZ-1000 and 20WZ-800 present much lower Tafel slopes. In particular, sample 20WZ-800 exhibits the lowest Tafel slope of 64 mV dec^{-1} among all the studied composites and the lowest potential required to achieve a current density of 10 mA cm^{-2} (see **Table 4.3**), implying a good HER reaction kinetics of the sample. Actually, the Tafel slope for sample 20WZ-800 surpasses most of the reported Co-W-S/C series electrocatalysts in HER (**Table 4.4**).

The good HER activity is attributed to the novel structure of the composites. The pristine metal sulphides have low conductivity, which largely limits their electrochemical performances in HER. However, in the case of 20WZ-800, both $Co_{1-x}S$ and WS_2 nanoparticles are uniformly dispersed in the heteroatom-doped carbon matrix, with WS_2 being a typical HER electrocatalytic component, leading to more active sites in the

composites. Moreover, the carbon matrix allows better charge and mass transport between the adsorbed H^+ and the electrode. In addition, the existence of N species that can result in changes in the electronic structure of neighbouring carbon atoms, together with the asymmetrical spin and change in charge density originated from the co-doping of N and S, can lead to the increase in the number of active sites [499] and hence enhancement in the HER activity.

Table 4.3 Overpotential at 10 mA cm^{-2} and Tafel slope for samples in this work.

Sample	HER		OER	
	|Overpotential @-10 mA cm^{-2}| (V vs RHE)	**Tafel slope (mV dec^{-1})**	**Overpotential @10 mA cm^{-2} (V vs RHE)**	**Tafel slope (mV dec^{-1})**
20% Pt/C	0.035	30	-	-
IrO_2	-	-	0.417	54
Z67-600	0.235	83	0.505	93
Z67-800	0.283	78	0.440	74
Z67-1000	0.323	83	0.396	70
20WZ-600	0.221	83	0.410	72
20WZ -800	0.250	64	0.398	64
20WZ -1000	0.292	68	0.365	53

Table 4.4 Comparison of the HER performances for CoS_2/WS_2-based electrocatalytical materials in recently published results.

Catalysts	Electrolyte concentration (mol L^{-1})	Catalyst loading (mg cm^{-2})	|Potential at -10 mA cm^{-2}| (V vs. RHE)	Tafel slope (mV dec^{-1})	Ref.
20WZ-800	0. 5 M H_2SO_4	0.21	0.250	64	This work
CoS_2/CC	0.5 M H_2SO_4	18.6	0.288	210.7	[500]
rGO/WS_2	0.5 M H_2SO_4	-	0.229	73	[501]
CoS_2@WS_2 /CC	0.5 M H_2SO_4	2.9	0.097	66	[462]
CoS_2@WS_2 nanosheets	0.5 M H_2SO_4	0.91	0.119	68	[502]
Co_xS_y/WS_2 nanosheet @CC	0.5 M H_2SO_4	-	0.120	89	[503]
CoWS	0.5 M H_2SO_4	-	0.330	74	[504]

Besides the improved HER performance, W20@Z67 derived composites also show promising OER activities. The test was carried out in an oxygen-saturated 1 M KOH aqueous solution at room temperature with an electrode spinning rate at 1600 rpm. **Fig. 4.15A** presents the linear sweep voltammograms (LSVs) polarization curves of the OER benchmark catalyst IrO_2, W20@Z67, and ZIF-67 derived catalysts at different calcination temperatures. To achieve a current density of 10 mA cm^{-2}, W20@Z67 derived sample at 600, 800, and 1000 °C requires an overpotential of 0.410, 0.398 and 0.365 V (vs RHE) respectively, while ZIF-67 derived sample at 600, 800, and 1000 °C needs a higher overpotential of 0.505, 0.440 and 0.396 V (vs RHE) respectively to achieve the same current density. Obviously, the incorporation of WS_2 species in the 20WZ series samples

dramatically improves the OER performance of the composites. Particularly, the OER activities of all the 20WZ series samples over-perform that of the benchmark IrO_2 catalyst, and 20WZ-1000 exhibits the highest OER performance among all the studied samples and this sample only need the lowest overpotential of 0.365 V (vs RHE) to achieve the current density of 10 mA cm^{-2} (as shown in **Table 4.3**).

The high OER activities of 20WZ-1000 could be due to several reasons. Firstly, the presence of defect-rich carbon sites (see Raman spectra in **Fig. 4.13**) can modulate the electronic and surface properties of the composites, thus changing the adsorption energies of electrochemical reaction steps [505]. This is supported by a recent report that suggested defect-rich carbon shows better electrocatalytic activities than the N doped carbon [499], which could result in the 1000 °C composite with fewer N species in the carbon matrix still shows better catalytic activities than the 800 °C sample. Secondly, the generated strong electron transfer between Co and W via the intermediate sulphur atoms, i.e. the formation of Co-W-S phases between the $Co_{1-x}S$-WS_2 interface, as suggested by Zhang's work [462]. Similar result has been demonstrated by Du et al. in the Co_9S_8@MoS_2 system [506]. Finally, the relative high BET surface area of the 1000 °C sample (see **Table 4.2**) could also contribute to the high activity by providing loose textures and open space for the easy transportation of evolved gas bubbles and the instant diffusion of the electrolytes, which can help to take the full advantage of active sites in metal sulphides. As the catalyst is a complicated multiphase system, it is difficult to evaluate the individual composition contribution to the synergistic effect of the catalyst system without disturbing the overall structures.

The corresponding OER Tafel slopes in O_2-saturated 1M KOH electrolyte (**Fig. 4.15B**) show a similar trend to that for HER where the W, Co sulphide-based carbon nanocomposites in general exhibit lower Tafel slopes than their counterparts of ZIF-67 derived samples under the same sulphurization temperatures; this clearly indicates that the introduction of WS_2 results in the remarkable enhancement of the reaction kinetics over their pristine counterparts. Among the W, Co sulphide-based carbon nanocomposites, 20WZ-600 shows the highest Tafel slope of 72 mV dec^{-1} and 20WZ-1000 gives the lowest Tafel slope of 53 mV dec^{-1}, which is even lower than the value for benchmark IrO_2 catalyst (54 mV dec^{-1}, see Table S3 in SI), indicating that 20WZ-1000 is the best OER electrocatalyst among all the studied samples, outperforming the benchmark IrO_2 catalyst. The overpotential at 10 mA cm^{-2} and Tafel slope data for both HER and OER were summarised and presented in Table 4.5. As a matter of fact, the Tafel slope for

sample 20WZ-1000 surpasses many of the reported CoS/C based electrocatalysts in OER (see **Table 4.5**).

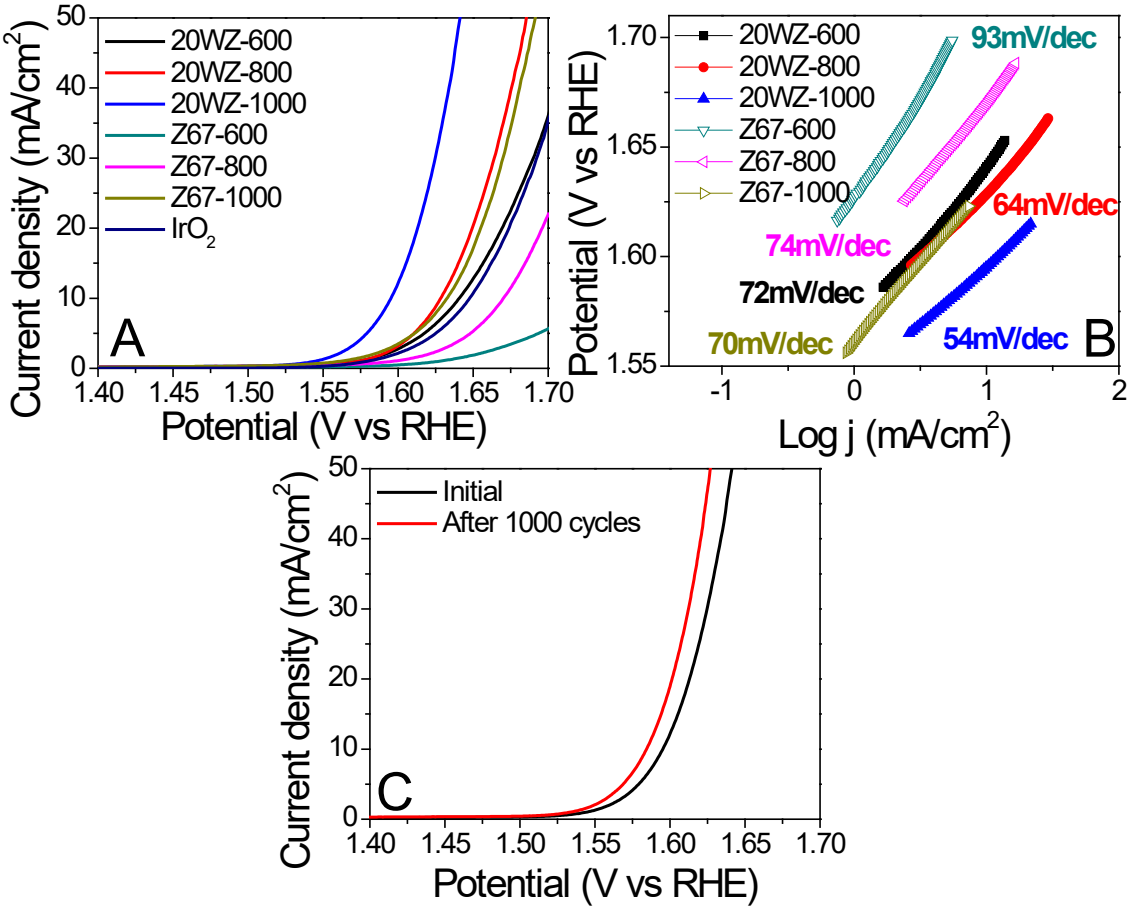

Fig. 4.15 The LSV polarization curves of benchmark catalysts IrO_2, carbonised/sulfurised W20@Z67 and ZIF-67 under 600°C, 800°C and 1000°C, B) Tafel plots and C) OER Polarization curves of 20WZ-1000 recorded before and after 1000 CV cycles. All the polarization curves were iR corrected with a scan rate of 5 mV s^{-1} in O_2-saturated 1 M KOH electrolyte solution.

Table 4.5 Comparison of OER performances for CoS_2/WS_2-based electrocatalysts.

Catalysts	Electrolyte concentration (mol L^{-1})	Catalyst loading (mg cm^{-2})	Overpotential@10 mA cm^{-2} (V vs RHE)	Tafel slope (mV dec^{-1})	Ref.
20WZ-1000	1 M KOH	0.21	0.365	53	This work
Co-N_x/C nanorod array	0.1 M KOH	0.51	≈300	62.3	[507]
Co_9S_8@CoS@CoO@C NPs	1 M KOH	0.2	150	96	[508]
Co/Co_9S_8@S, N-doped graphene	0.1 M KOH	1	290	-	[509]
CoS/carbon tubes/carbon paper	1 M KOH	0.32	190	72	[510]
CoS@Nickle Foam	1 M KOH	0.5	297	106	[511]
Mo-N/C@MoS_2	0.1 M KOH	-	390	72	[512]
Co_9S_8/WS_2/Ti	1 M KOH	2.2	420	-	[456]

To examine the HER/OER bifunctional behaviour for the composites, the combined HER and OER LSV curves were presented in **Fig. 4.16**, where both HER and OER of the representative samples were evaluated in 1 M KOH media. The W-modified sample 20WZ-800 again shows remarkably improved electrochemistry performances in both

HER and OER compared with the W-free sample Z67-800. Moreover, sample 20WZ-800 requires a potential of 0.337 V (vs RHE) to realise a current density of 10 mA cm^{-2} in 1 M KOH media for HER, which is merely around 0.087 V reduction for the same composite to achieve the same current density of 10 mA cm^{-2} in 0.5 M H_2SO_4 solution, much smaller than the reduction of potential for benchmark Pt/C catalyst to realise 10 mA cm^{-2} in 1 M KOH solution. Obviously, the representative 20WZ-800 sample exhibits good bifunctional electrocatalytic performance towards both OER and HER in an alkaline environment.

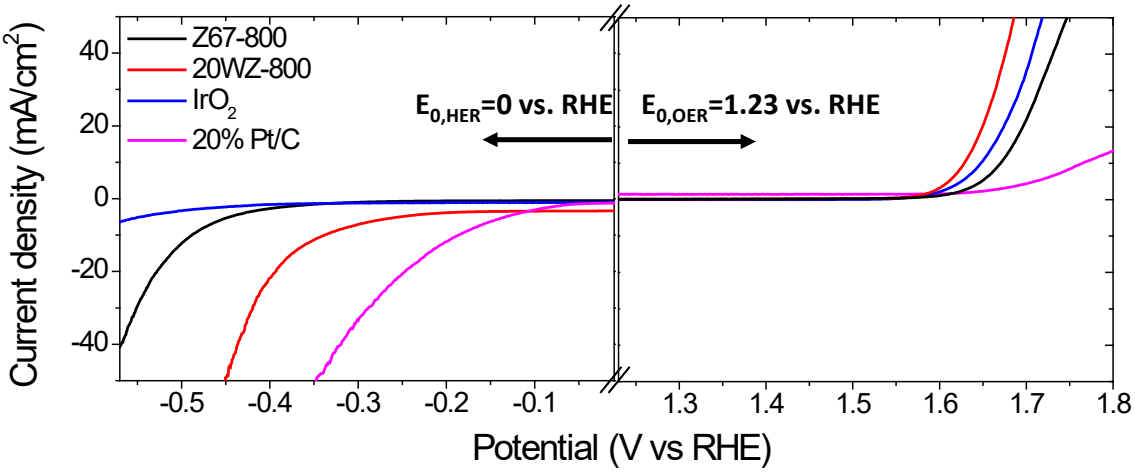

Fig. 4.16 Combined HER and OER LSV polarization curves for Z67-800, 20WZ-800, IrO_2 and 20% Pt/C in 1 M KOH. All the curves were iR corrected.

The kinetics performance of the representative electrode materials was also evaluated by electrochemical impedance spectroscopy (EIS), as presented in **Fig. 4.17**. The charge transfer resistance (R_{ct}) of material can be derived from the diameter of the semi-circle. It is worth noting that the fast interfacial kinetic is indicated by the small value of the obtained charge transfer resistance. Obviously, 20WZ-800 shows a much smaller R_{ct} than the Z67-800 sample, which indicated that the introduction of WS_2 into the sample Z67-800 plays a significant role in altering the electronic properties of the composite 20WZ-800. Moreover, benchmark IrO_2 catalyst shows a larger R_{ct} than 20WZ-800, which is in agreement with the results in LSV curves and Tafel plots.

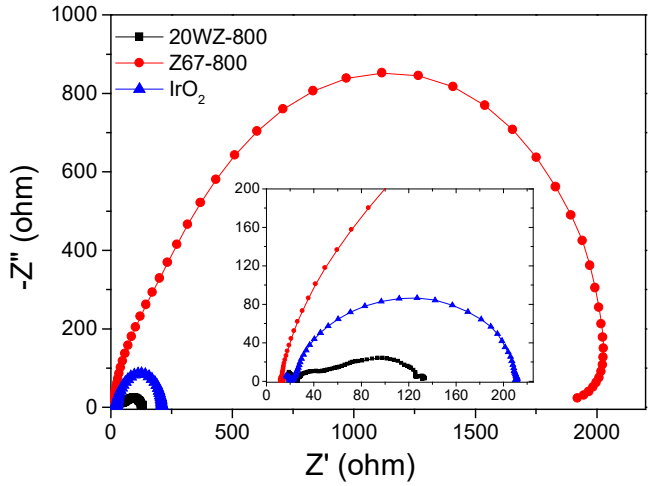

Fig. 4.17 EIS spectra (Nyquist plots) of 20WZ-800, Z67-800 and benchmark IrO_2 electrocatalyst recorded at 0.6V (vs. Ag/AgCl), measured in the frequency range of 10^{-1}-10^5 Hz in 1 M KOH solution.

The stability of the best-performed samples, i.e. 20WZ-800 for HER and 20WZ-1000 for OER, were evaluated by the LSV curves, and the results were presented in **Fig. 4.14C** and **Fig. 4.15C**. The polarization curve after 1000 cycles is similar to the initial cycle. In particular, the overpotential of 20WZ-800 has dropped only 0.008 V at 10 mA cm^{-2}, while the overpotential of 20WZ-1000 has slightly increased 0.011 V at 10 mA cm^{-2}. The stabilities of both samples were further confirmed by the chronoamperometric curves, which were tested at -0.3 V in 0.5 M H_2SO_4 and 0.57 V in 1 M KOH, respectively over 8000 s. As shown in **Fig. 4.18A and B**, sample 20WZ-800 retains 88% of its relative current density after 8000 s, implying excellent stability of this sample in HER. Meanwhile, sample 20WZ-1000 shows good durability in OER and can retain 84% of its relative current density after 8000 s, which is higher than our previous reported core-shell based Co_xS_y/C sample produced under the same carbonisation temperature that retains 80% of current density [480], further underlining the important role of the introduce of WS_2 species in the composites. These observed good durability for the studied electrocatalysts are largely due to the stabilising effect of porous carbon matrix on the metal sulphide catalysts, which can also provide a conducting network and electrochemical coupling between the metal sulphide active sites and the reacting species.

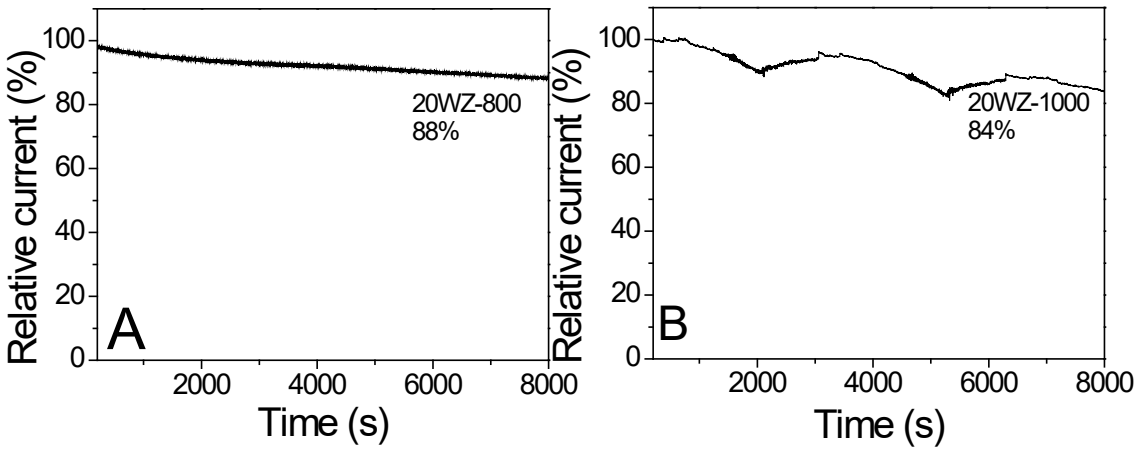

Fig. 4.18 Current-time chronoamperometric response of A) 20WZ-800 at -0.3 V in 0.5 M H_2SO_4 solution and B) 20WZ-800 at 0.57 V in O_2-saturated 1 M KOH solution (1600 rpm).

Since 20WZ-800 gives the best HER performance and 20WZ-1000 shows the highest OER performances among studied composites, it is interesting to find out the influence of W content on the electrocatalytic activities. In this regard, two other samples with different amounts of PTA were synthesised and denoted as W10@Z67 and W30@Z67, respectively, which were used as precursors to carbonise and sulphurized at high temperatures to obtain the electrochemical evaluation samples derived at 800 °C for HER and 1000 °C for OER. **Fig. 4.3B** presents the XRD patterns of these samples obtained at 800 °C. All three samples show diffraction peaks corresponding to metal sulphides. 30WZ-800 reveals sharper WS_2 peaks due to its much higher W content, vice versa for 10WZ-800.

The HER and OER polarization curves of the WZ-67 and ZIF-67 derived composites, curves for benchmark Pt/C and IrO_2 catalysts were also plotted for comparison. In **Fig. 4.19A**, although all the composites are inferior to the benchmark Pt/C in HER, 20WZ-800 shows the best performance among them. On the other hand, in **Fig. 4.19B**, all the composites except 30WZ-1000 outperform the benchmark IrO_2 in OER, and the 20WZ-1000 shows the best performance towards OER among the studied samples. Therefore, in both cases of HER and OER, the samples derived from W20@Z67 exhibits the best electrochemical performance. As has been discussed above, the generated strong electron transfer between Co and W via the intermediate sulphur atoms, i.e. the formation of Co-W-S phase between $Co_{1-x}S$-WS_2 interfaces, could play a role in the electrochemical performance; therefore, the contents of Co and W will affect the electron transfer between Co and W. While W10@Z67 (0.371g of PTA) may provide too little W and 30W@Z67 (1.113g of PTA) contains too much W, but the W20@Z67

(0.557g of PTA) leads to the appropriate amount of W required for the formation of $Co_{1-x}S$-WS_2 phase, to give the best electrochemical performances in both HER and OER.

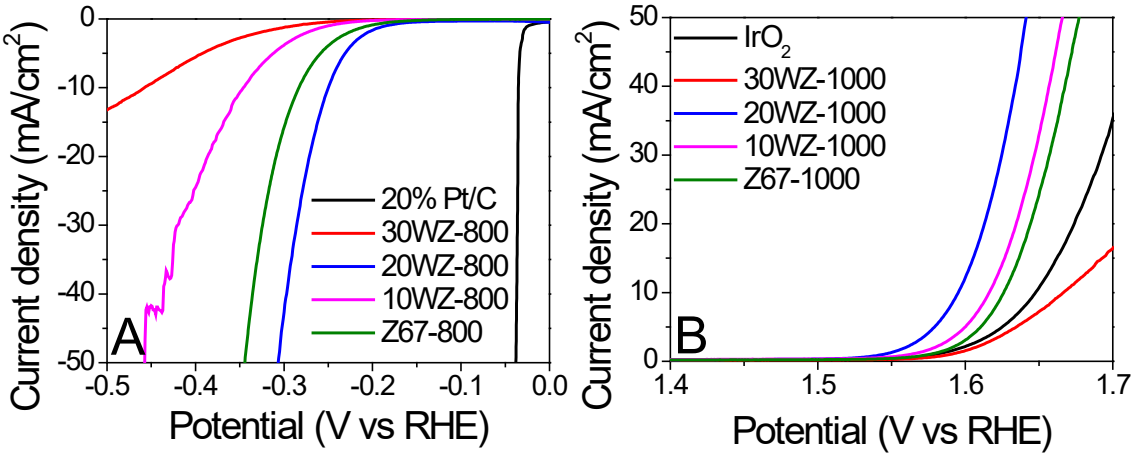

Fig. 4.19 HER polarization curves for 10WZ-800, 20WZ-800, 30WZ-800 and 20% Pt/C and B) OER polarization curve for 10WZ-1000, 20WZ-1000, 30WZ-1000 and IrO2. All polarization curves were iR corrected.

4.3 Summary

In summary, using the in situ synthesised PTA@ZIF-67 as the precursor, facile one-step carbonisation and sulphurization route has been successfully developed to generate tungsten/cobalt sulphide-based carbon nanocomposite as efficient bifunctional electrocatalysts. Through the immobilisation of POM molecular clusters within the confined space of ZIF-67 cages followed by heat treatment at high temperatures under the H_2S atmosphere, a homogeneous dispersion of tungsten sulphide and cobalt sulphide particles within a carbon matrix can be achieved. The resulting bimetallic Co-W sulphide/heteroatom doped porous carbon composites exhibit a prominent improvement in HER with a Tafel slope of 64 mV/dec and an overpotential of -0.250 V (vs RHE) at the current density of 10 mA cm^{-2}. Moreover, the bimetallic Co-W sulphide/porous carbon composites also demonstrated excellent OER activities with Tafel slope of 53 mV/dec and an overpotential of 0.365 V (vs RHE) at the current density of 10 mA cm^{-2}, out-performing the benchmark IrO_2 catalyst. This work offers a new strategy to prepare homogeneous transition metal sulphide decorated porous carbon nanostructures and open up a new way to obtain low-cost bifunctional electrocatalysts towards both OER and HER.

Chapter 5: Bimetallic Co-Mo sulphide/carbon nanocomposites derived from POM@ZIF@PDA nanocubes

5.1 Introduction

Two-dimensional layered transition metal dichalcogenides (2D TMDs) have been one of the most popular material families for electrochemical energy-related applications due to their unique structures and intrinsic properties [513, 514]. MoS_2 is one of the well-studied materials in the 2D TMDs family. Both theoretical simulations and experimental works confirm that the unsaturated chalcogens and metals on the exposed edges are the active sites for the HER reactions [515, 516]. However it is well known that MoS_2 possesses poor OER activities [517]. To develop bifunctional catalysts that are active towards both HER and OER, hybridising MoS_2 with 3d transition metal (i.e. Co, Fe or Ni) sulphides have been extensively adopted [518]. This multi-interface engineering strategy can also improve the conductivity and adsorption of electrochemical intermediates of the electrocatalysts [519]. In particular, cobalt sulphides incorporated MoS_2 have been widely explored. For example, recently Huang et al. have synthesised a mesoporous CoS/MoS_2 for water splitting application [520], Ganesan et al. have created a multi-shelled CoS_2-MoS_2 hollow sphere for efficient water splitting [521], and Gao et al. have assembled a core-shell Co_3S_4@MoS_2 for both HER and OER [522].

Besides introducing cobalt into MoS_2, the electrochemical efficiency of the electrocatalysts can be strategically promoted by active site engineering strategies, including edge-site formation, nano-sized TMD and highly curved structures formed on the MoS_2 crystals [523]. Those ultra-fine open-ended nanostructures and rich defects enable the catalysts to expose a higher density of active sites for the key reactions, consequently leads to improved electrocatalytic activity [524, 525]. In order to maintain the fine nanostructure of electrocatalysts, to prevent heat-induced sintering [526] and high surface energy induced agglomeration of the active components [527], graphitic carbon matrix can be introduced to isolate the electrocatalytic active MoS_2 nanoparticles [528, 529]. Meanwhile, the excellent electronic conductivity of graphitic carbon benefits fast charge transfer in the composites, resulting in enhanced activities [529, 530]. More interestingly, porosity can be introduced into the graphitic carbon matrix. As a result, the porous graphitic carbon

matrix can not only isolate the electrocatalytic active sites to avoid agglomeration, but also promote the mass transports during the electrocatalytic reactions, thereby enabling the active sites to be readily accessible by reactants [410]. Moreover, the porous carbon matrix can be doped with heteroatoms such as N and/or S, which can modulate the electronic structure of the composites and create more catalytic active sites, therefore further improving the electrocatalytic activities of the heterostructured composites [531]. Built on the above considerations, the porous zeolitic imidazolate framework (i.e. ZIF-67) is an ideal precursor to develop heteroatom functionalised carbon-rich and transition metal Co-based composites.

Previously, we reported HER and OER active $WS_2/Co_{1-x}S$/porous carbon nanocomposites derived from in situ synthesised polyoxometalates (POM)@ZIF-67 [532]. However, since ZIF-67 is unstable in acidic environment [533], attempts to in situ synthesise Mo-containing counterpart via a similar method were unsuccessful due to the strong acidity and the uncertainty of molecular weight of phosphomolybdic acid hydrate (PMA, a Mo-containing POM) [534]. In this chapter, we developed an acid-resistance polydopamine (PDA) coating [535] on the pre-synthesised ZIF-67 as a buffer layer to protect ZIF-67 from PMA etching, and to synthesise PMA modified ZIF-67 composite PMA@ZIF-67@PDA. Moreover, Tris-buffer solution for dopamine polymerisation is further used to avoid drastic dissociation of the ZIF when the strong acidic PMA is introduced. In this synthesis strategy, N-containing PDA can also act as another N source for N-doping besides the organic linker 2-Methylimidazole (MeIM) in ZIF-67. Since the PDA decorated on hydrophobic surfaces is less stable to acid medium than on hydrophilic surfaces [535], cetyltrimethylammonium bromide (CTAB) was added during the synthesis of ZIF-67 in order to tune the hydrophobic surface of ZIF [536] into a hydrophilic surface. Meanwhile, the addition of CTAB has led to the cubical morphology of ZIF-67 crystals. In addition, PDA not only protects ZIF-67 from the strong acidity of PMA, but also provides rich functional groups that have strong chelating capability with metal ions. Therefore PDA can chelate with free PMA molecules as well as Co^{2+} dissociated from the ZIF, which results in an increased amount of active sites in the final derivatives. One-step carbonisation and sulphurization of the as-synthesised PMA@ZIF-67@PDA at high temperature in hydrogen sulphide atmosphere can generate bimetallic Co-Mo sulphide supported on carbon nanocomposites. The optimised Co-Mo-S@N, S-doped porous carbon composites exhibit significantly enhanced HER and OER performance compared with the counterparts derived from ZIF-67 nanocubes. This synthesis approach can be

further expanded to synthesise phosphotungstic acid (PTA)@ZIF-67@PDA, and the corresponding derivatives are also good electrocatalysts with enhanced performance in HER and OER.

5.2 Results and discussion

5.2.1 Characterization of the as-synthesized PMA@ZIF-67@PDA nanocubes

As shown in **Fig. 5.1**, to obtain the precursor POM@ZIF-67@PDA nanocubes, cubical ZIF-67 was first synthesised at room temperature via the hydrothermal method in the presence of surfactant CTAB. ZIF-67@PDA nanocubes were then synthesised by depositing a thin layer of PDA on the surface of the ZIF-67 nanocubes via in situ polymerisation. Finally, POM (i.e. PMA or PTA) was introduced into the ZIF-67@PDA solution. The acidic POM molecules can penetrate through the PDA coating layer outside the ZIF-67 cubes and reach the ZIF-67 cubes, resulting in partly dissociation of the ZIF-67 core. Meanwhile, the Co^{2+} dissociated from the ZIF-67 by acid etching, as well as some of the POM molecules were stuck in the PDA layer via functional group chelation. The obtained POM@ZIF-67@PDA nanocubes were then subjected to one-step carbonisation/sulphurization at high temperatures in H_2S/Ar atmosphere to derive bimetallic Co-Mo-S/N, S-doped porous carbon composites as HER and OER catalysts.

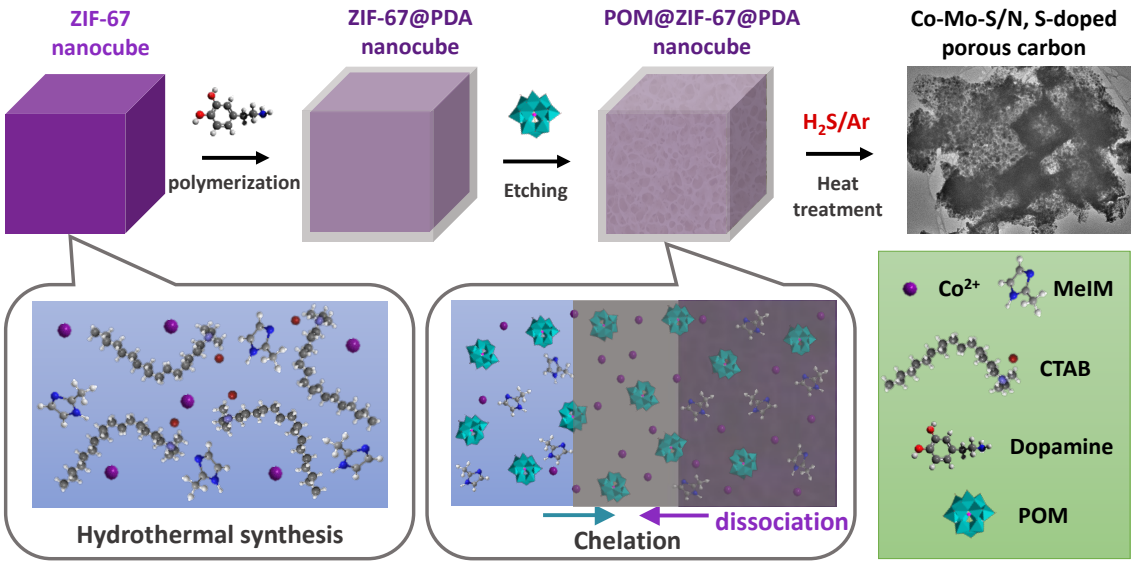

Fig. 5.1 Diagram of the synthesis of POM@ZIF-67@PDA precursor and bimetallic N, S-doped porous carbon composites.

The SEM images (**Fig. 5.2**) of all the as-synthesised precursors present highly uniform cubic nanoparticles with diameters of around 600 nm. The pristine ZIF-67 nanocubes (Z67) have a smooth surface compared to the other three PDA decorated samples. With the PDA coating and the POM (i.e. PMA or PTA) modification, the surfaces of the cubes have become rough and lumpy. TEM image (**insert in Fig. 5.2A**) and elemental mapping (**Fig. 5.3A**) show that homogeneous ZIF-67 cubes are formed with the help of surfactant CTAB. After the deposition of PDA, Z67-D is obtained with a thin layer of PDA coated on the surface of the cubes (**insert in Fig. 5.2B**). An oxygen-rich outer layer is found in the corresponding elemental mapping (**Fig. 5.3B**), which also confirms the formation of PDA coating. With the incorporation of PMA, Mo-Z67-D shows a well-defined cubical shape with a porous interior (**insert in Fig. 5.2C**). It is believed that the acidic PMA molecules can penetrate through the acid-resistant PDA coating [535] and react with the acid intolerance ZIF core, leading to partial dissociation of the ZIF-67 structure, which is consistent with the previous report [436]. Accumulation of Mo, O and P elements are observed on the nanocube surface from the elemental mapping in **Fig. 5.3C**, revealing that some PMA molecules have stuck in the coating layer via chelation with PDA functional groups. It is likely that the chelation mechanism of the PMA is as follows: At high pH (resulted from the tris-buff solution, pH=8.5), PMA may undergo a series of hydrolysis reactions, leading to the formation of lacunary phosphomolybdates [537,538]. Some of the negatively charged lacunary phosphomolybdates and the sheded charged Mo species such as MoO_4^{2-} and MoO_2^{2+} can then chelate with the functional groups of PDA [539, 540]. Moreover, a small amount of C and Co is found in the outer layer of cubes as well, indicating that trace amounts of free Co^{2+} from the dissociation of ZIF-67 has chelated with coated PDA.

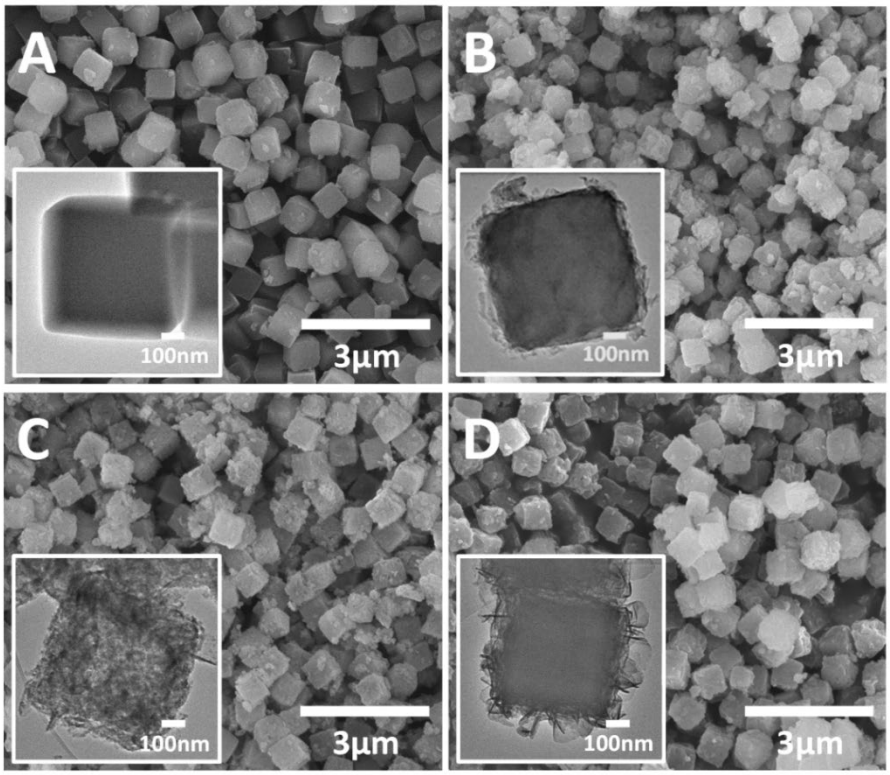

Fig. 5.2 SEM and TEM images (inserts) of A) Z67, B) Z67-D, C) Mo-Z67-D and D) W-Z67-D.

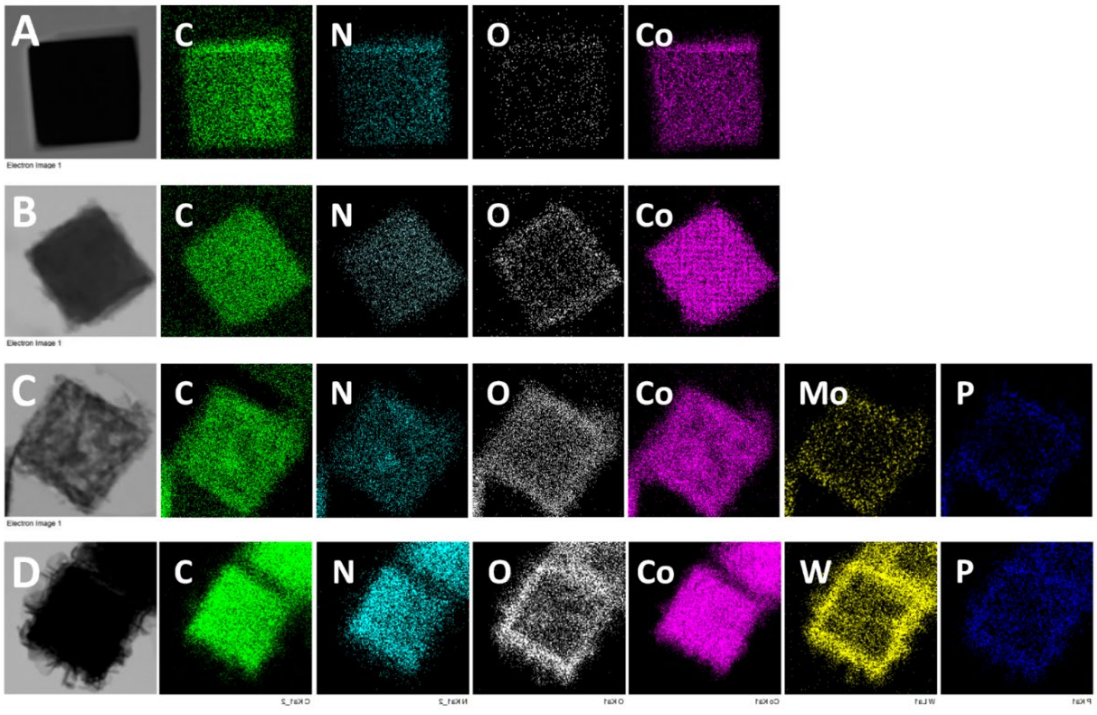

Fig. 5.3 Elemental mappings of A) Z67, B) Z67-D, C) Mo-Z67-D and D) W-Z67-D.

Elemental line scanning for individual cubic particles was conducted during TEM-EDX analysis, re-affirm the effect of PMA on the morphology of the composite and the chelation of PMA with the coated PDA. For Z67 (**Fig. 5.4A**), all the elements distribute

evenly across the cubes. With PDA coating, small amounts of O and C is found at the edge of the Z67-D cubes (**Fig. 5.4B**). The slightly uneven distribution of Co and C reveals that PDA coating could lead to mild dissociation of ZIF-67, which has been reported previously [191, 541]. The overlapped edge region of the Co and O spectrum indicates the chelation of Co on coated PDA. On the other hand, the uneven distribution of Co, C, N across the Mo-Z67-D in the line spectra (**Fig. 5.4C**) suggests that the PMA penetrates through the PDA coating and generates cavities in the core by acid etching. Weak peaks of O, P and Mo on the edge of cubes imply that some PMA molecules have chelated with coated PDA. Whereas for W-Z67-D (**Fig. 5.4D**), elements O, P, W are mainly distributed at the edge of the cubes and Co, C, N are mainly distributed in the middle of the cubes with mild variation, which suggests that the majority of PTA molecules are chelated with the coated PDA.

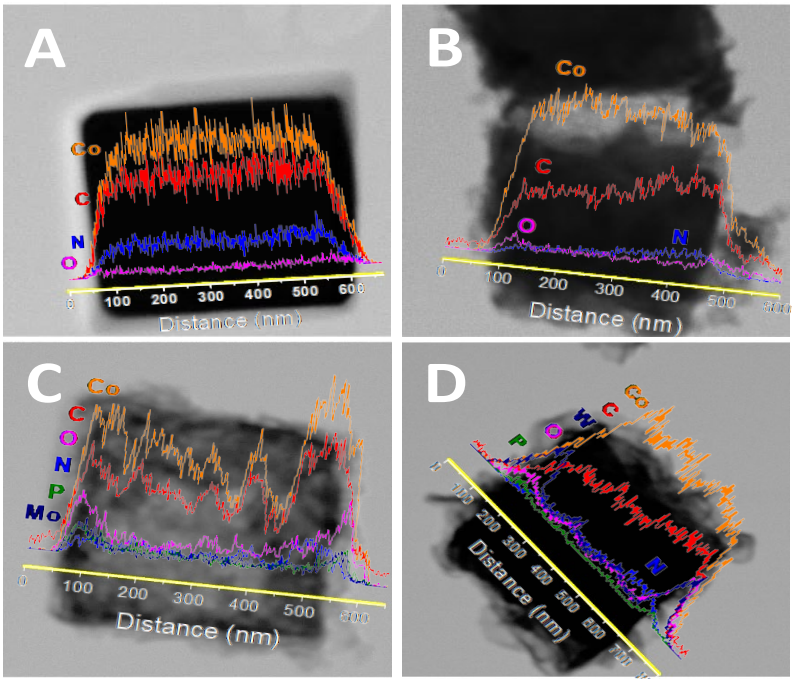

Fig. 5.4 TEM images and elemental line profiles of A) Z67, B) Z67-D, C) Mo-Z67-D and D) W- Z67-D.

All the modified samples show characteristic XRD peaks of ZIF-67 (**Fig. 5.5A**), indicating the basic ZIF-67 structure is retained in these modified samples irrespective of the PDA coating or the introduction of PMA. Both Z67-D and Mo-Z67-D show a slight decrease in the intensity of the characteristic diffraction peaks, possibly due to the partial dissociation of ZIF core caused by PDA coating and PMA etching. The FT-IR spectra (**Fig. 5.5B**) are in good agreement with the XRD results, revealing that the ZIF-67 structure is not significantly affected by the presence of CTAB, PDA coating and the

PMA etching. Mo-Z67-D shows the characteristic peaks of both ZIF-67 and PMA, confirming the successful introduction of PMA. The slight peak shift and splitting of the PMA peaks of the modified structure are attributed to the change of chemical environment [528, 532] and the dissociation of PMA itself due to the high pH value (pH=8.5) during the synthesis process [537].

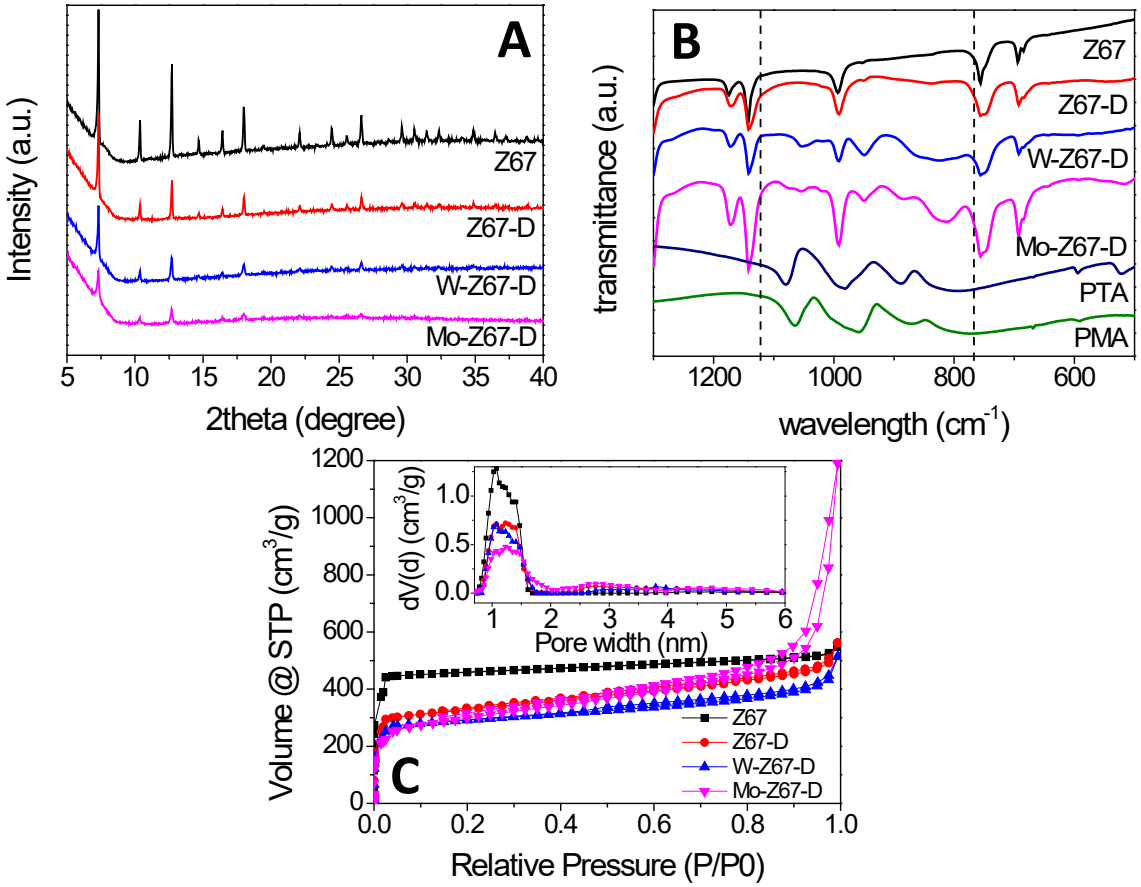

Fig. 5.5 A) XRD patterns of the as-made Z67, Z67-D, W-Z67-D and Mo-Z67-D; B) FT-IR spectra of PTA, PMA and four as-made samples; C) Nitrogen sorption isotherms and the DFT pore size distribution (insert) of the as-synthesized Z67, W-Z67-D and Mo-Z67-D.

Textural properties of the as-synthesised samples were analysed by nitrogen gas sorption, and the obtained isotherms and pore size distributions are shown in **Fig. 5.5C**. All samples exhibit typical type I isotherm based on the IUPAC classification, which is associated with the microporous structure of ZIF-67 [542]. Small hysteresis loops are observed for Z67-D and Mo-Z67-D, possibly due to small amounts of micropores being destroyed by the etching and hydrolysis of ZIF-67, which results in pores larger than 2 nm [543]. The same conclusion can also be drawn from the pore size distributions of the modified samples (insert in **Fig. 5.5C**), in which larger pores with a diameter of 2-8 nm are observed. Moreover, macropores are found for the Mo-Z67-D sample at $P/P_0 \geqslant 0.8$

[544], suggesting the formation of hierarchical pores in this sample, which is in good agreement with TEM results. The BET surface area (S_{BET}) and total pore volume (V_{total}) of the as-synthesised samples are summarised in **Table 5.1**. The surface area drops from 1549 m^2 g^{-1} for Z67 to 1123 and 1037 m^{-2} g^{-1} for Z67-D and Mo-Z67-D respectively. While Z67-D shows no significant change in V_{total}, Mo-Z67-D exhibits a prominent increase in V_{total} which further confirms that large amounts of pores are generated due to PMA etching. This observation is in good agreement with the above TEM results.

Table 5.1 BET surface area and total pore volume of the four as-made samples.

Sample	Z67	Z67-D	W-Z67-D	Mo-Z67-D
BET Surface Area, S_{BET} (m^2 g^{-1})	1549	1123	993	1037
Total pore volume, V_{total} (cm^3 g^{-1})	0.85	0.87	0.80	1.84

5.2.2 Characterization of PMA@ZIF-67 derived nanocomposites

Bimetallic Co-Mo-S/C nanocomposites can be readily produced via one-step sulphurization/carbonisation of the as-synthesised Mo-Z67-D in H_2S/Ar atmosphere at three different temperatures with variable ramp rates. XRD patterns in **Fig. 5.6A** show that these Mo-containing composites mainly present characteristic diffraction peaks attributed to $CoMoS_{3.13}$ (JCPDS #16-0439), accompanied by a trace amount of Mo_4O_{11} (JCPDS #13-0142) and Mo_2S_3 (JCPDS #40-0972). In contrast, Z67 derived sample CoS-1000 only shows the characteristic peaks of $Co_{1-x}S$ (JCPDS #42-0826), which is in good agreement with our previous works [480, 532]. This confirms that CTAB surfactant, PDA coating and the shape of the ZIF-67 crystal do not affect the composition of the pyrolysed samples. The XRD patterns of Mo-Z67-D derived samples at various temperatures, and heating rates are presented in **Fig. 5.6B**. It is found that the crystallinity of the metal sulphides in the composites improved with elevated pyrolysis temperature and a slower ramp rate. Moreover, there are more oxidised species in sample that is pyrolysed at 600 °C than those that is pyrolysed at 1000 °C. The shift of peak position and the broadening of the asymmetrical peak (see **Fig. 5.7A**) of samples obtained at lower pyrolysis temperature indicate that the metal sulphide in CoMoS-600 and CoMoS-600-10 possess smaller crystal sizes, possibly due to the non-uniform lattice distortions and

crystallographic defects [545]. Obviously, the introduction of PMA prominently changes the composition of the composites. It is worth mentioning that no diffraction peaks from oxides are observable in the Z67 nanocube derived samples, but diffraction peaks for both MoO_2 (JCPDS #32-0671) and MoS_2 (JCPDS #37-1492) appear in sample PMA-C (**Fig. 5.7B**), implying that the oxygen element is likely originated from the coated PDA and PMA molecules.

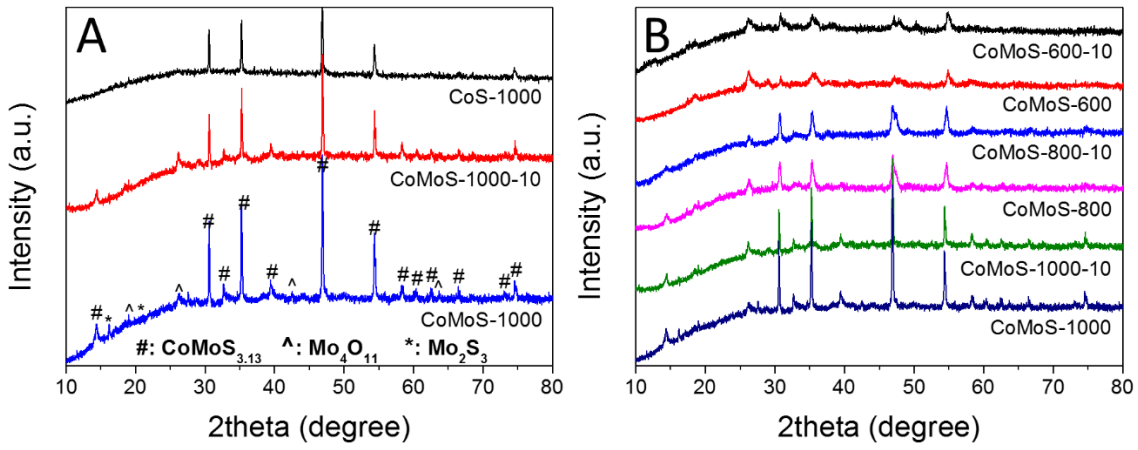

Fig. 5.6 XRD patterns of A) CoS-1000, CoMoS-1000-10 and CoMoS-1000 and B) samples derived from Mo-Z67-D at 600, 800, 1000 °C with heating ramp rate of 10 and 2 °C min-1 respectively.

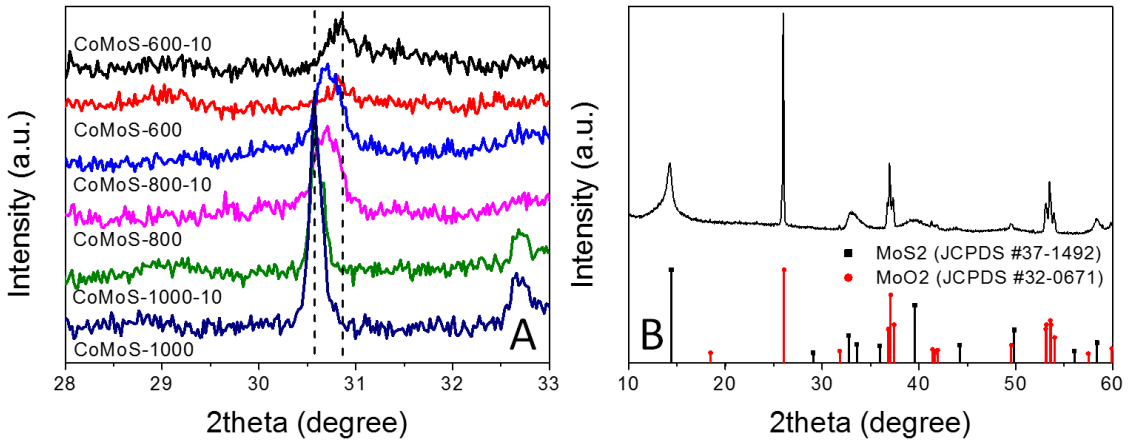

Fig. 5.7 A) XRD peak shifts and asymmetrical peak broadening observed in Mo-Z67-D derived samples as the heat treatment temperature and heating ramp rate changed; B) XRD pattern of PMA-C (PMA calcined at 800 °C in H2S/Ar atmosphere).

The Raman spectra of all the bimetallic Co-Mo-S/C samples (**Fig. 5.8A and B**) exhibit broad peaks with pronounced G band and D band. The G band at around 1593 cm^{-1} is associated with the in-plane stretching of the graphite lattice, whereas the D band at

around 1342 cm^{-1} indicates the presence of a disordered band caused by the breathing mode of the graphite edges [447, 546, 547]. These results indicate that the amorphous sp^2-hybridized carbon with a high density of defects dominates the carbon matrix originated from the carbonisation of ZIF-67. Moreover, the degree of the graphitisation of carbon in the composites can be estimated by the relative intensity between the two bands (i.e. I_D/I_G). As shown in **Table 5.2**, the I_D/I_G ratio decreases with the increase of pyrolysis temperature and slower heating ramp rate due to the formation of more graphitic carbon. It is well recognised that the degree of graphitisation of carbon can affect the conductivity of the carbon matrix [548] and hence alter the charge transfer kinetics of the composites, which may contribute to the better electrocatalytic performance of the carbon-based catalysts [549-551].

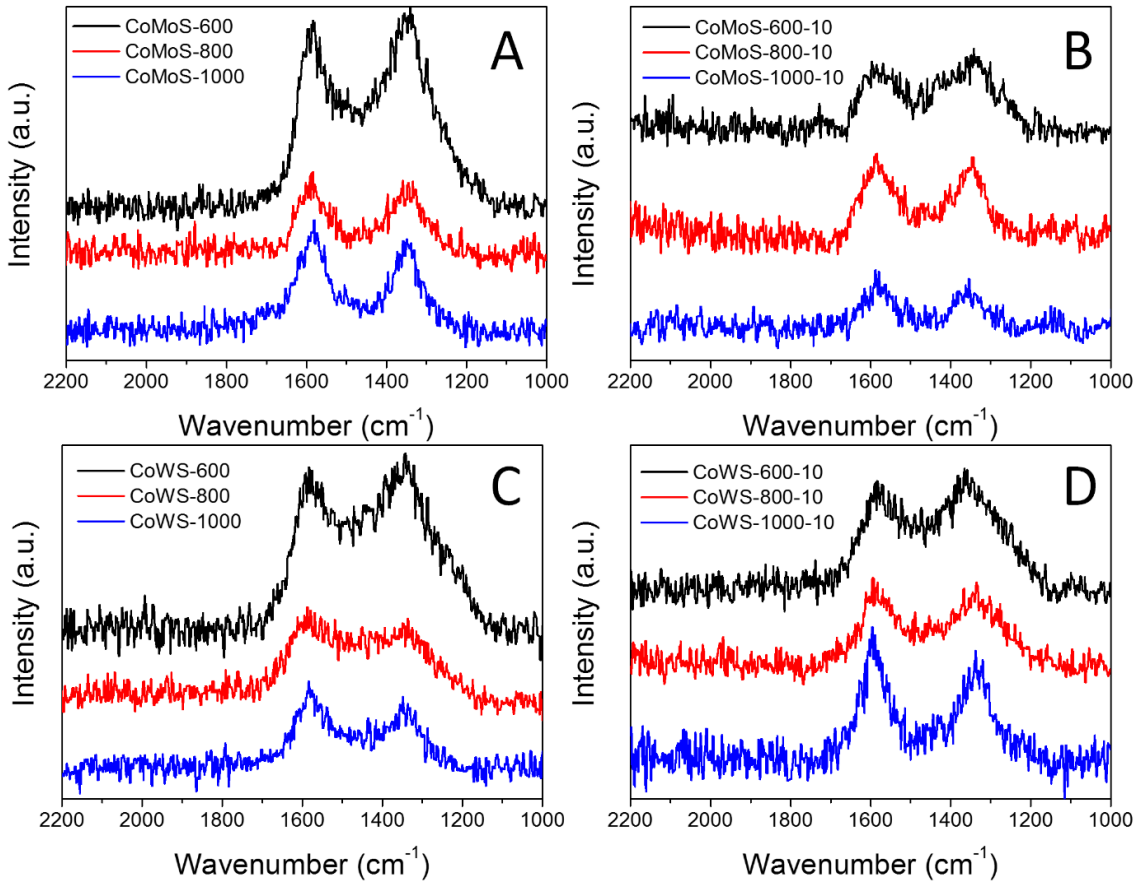

Fig. 5.8 Raman spectra of A) CoMoS-600, CoMoS-800, CoMoS-1000; B) CoMoS-600-10, CoMoS-800-10, CoMoS-1000-10; C) CoWS-600, CoWS-800, CoWS-1000 and D) CoWS-600-10, CoWS-800-10, CoWS-1000-10.

Table 5.2 I_D/I_G ratio of Mo-Z67-D and W-Z67-D nanocubes derived samples.

Precursor	**Mo-Z67-D**		**W-Z67-D**	
Heat ramp rate / **Pyrolysis temperature**	**10 °C/min**	**2 °C/min**	**10 °C/min**	**2 °C/min**
600 °C	1.17	1.06	1.11	1.08
800 °C	0.96	0.91	0.95	0.87
1000 °C	0.86	0.84	0.84	0.83

The morphology of the composites was first investigated by SEM. As shown in **Fig. 5.9A**, CoS-600 shows a nanocube morphology similar to the parental Z67. By increasing the pyrolysis temperature to 800 °C, nanocubes with the concave surface are observed for sample CoS-800 (**Fig. 5.9B**). Further increasing the pyrolysis temperature to 1000 °C, sample CoS-1000 shows distorted concave nanocube morphology decorated with small particles on the surface (**Fig. 5.9C**). In contrast, Mo-Z67-D derived CoMoS-600 shows mixed morphologies (**Fig. 5.9D**) of nanocubes, nanocube fragments with cracks and squared flakes. This observation further confirms that the PMA molecules not only chelate with the coated PDA, but also penetrate through the PDA coating to the inner core of the Mo-Z67-D leading to the etching of the inner core. The etching induced porous core is prone to collapse even at low pyrolysis temperature. More nanocube fragments decorated with small particles on the surface can be observed in sample CoMoS-800 (**Fig. 5.9E**). As pyrolysis temperature increased to 1000 °C, all nanocubes collapsed, and larger irregular particles appeared in sample CoMoS-1000 (**Fig. 5.9F**).

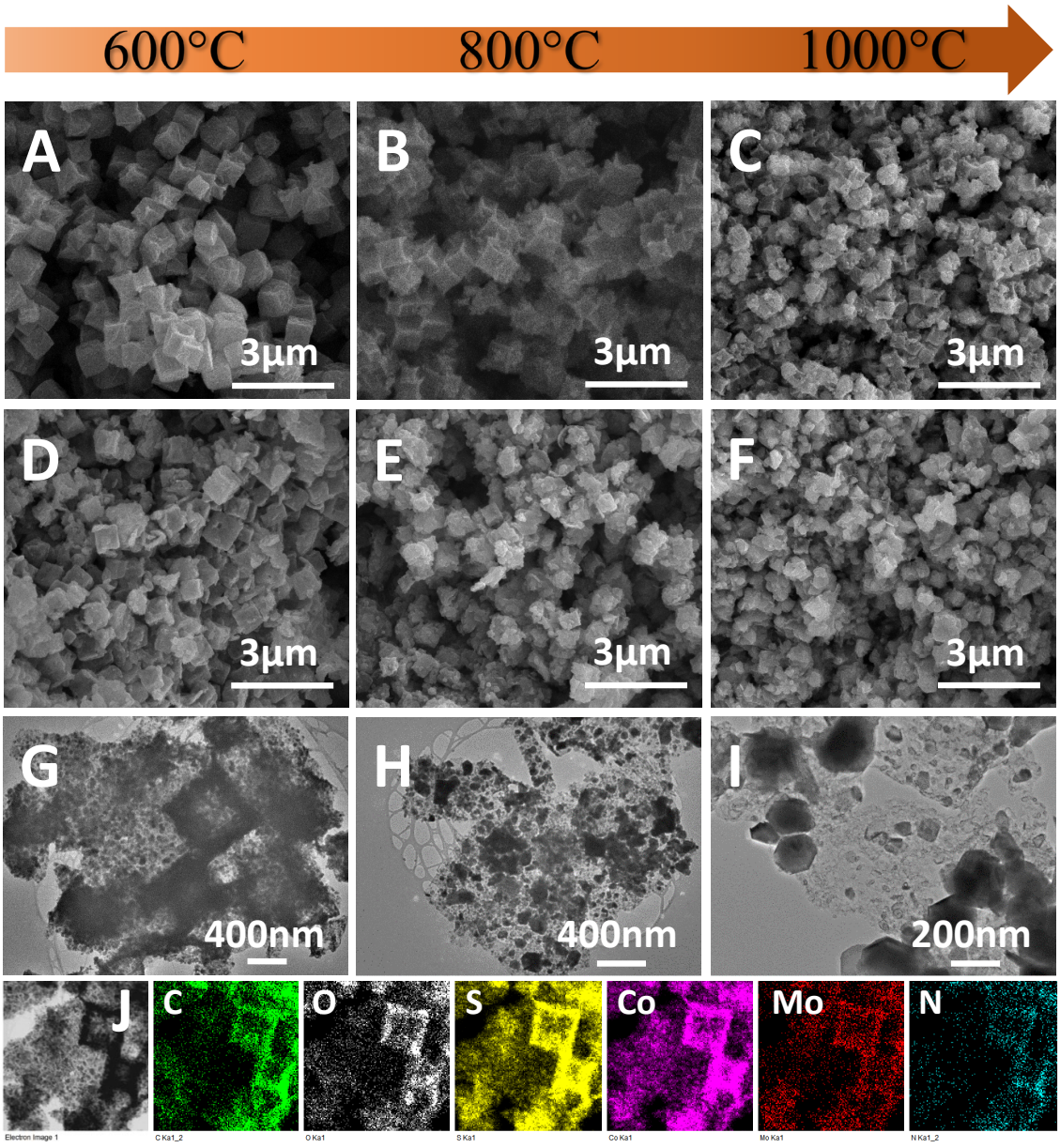

Fig. 5.9 SEM images of A) CoS-600, B) CoS-800, C) CoS-1000, D) CoMoS-600, E) CoMoS-800, F) CoMoS-1000; TEM images of G) CoMoS-600, H) CoMoS-800, I) CoMoS-1000 and J) Elemental mappings of CoMoS-600 obtained from TEM.

The morphologies of Mo-Z67-D derived composites were further investigated by TEM. As shown in **Fig. 5.9G**, large numbers of fine nanoparticles are formed at 600 °C, which are evenly distributed in the carbon matrix. The elemental mappings of sample CoMoS-600 in **Fig. 5.9J** show that all elements including C, O, S, Co, Mo and N are evenly distributed throughout the carbon matrix, but no P element is detected in the sample, possibly due to the high volatility of elemental phosphorus at high temperature. When the pyrolysis temperature increases to 800 °C (**Fig. 5.9H**), the small particles agglomerate to form larger particles with sizes up to 200 nm. Smaller particles are still

embedded in the carbon matrix, while larger ones accumulate at the edge of the matrix. For the sample obtained at 1000 °C (**Fig. 5.9I**), severe agglomeration is observed, and most of the metal sulphide particles migrate away from the carbon matrix to form aggregated large particles with sizes up to 500 nm. The elemental mappings of both CoMoS-800 and CoMoS-1000 are shown in **Fig. 5.10**. Similar to the sample obtained at 600 °C, elements C, O, S, Co, Mo and N are detected for both CoMoS-800 and CoMoS-1000 composites. The agglomerated metal sulphide particles are dominated by Co, Mo and S elements, which is in good agreement with the aforementioned XRD results. Small amount of thin flakes that mainly contain Mo and S are observed for the sample CoMoS-1000, which may be the formed Mo_2S_3 particles [552]. Based on the TEM-EDX results (see **Table 5.3**), Co/Mo ratio for CoMoS-600 is approximately 4.6:1, very close to 4.5:1 for the parental Mo-Z67-D.

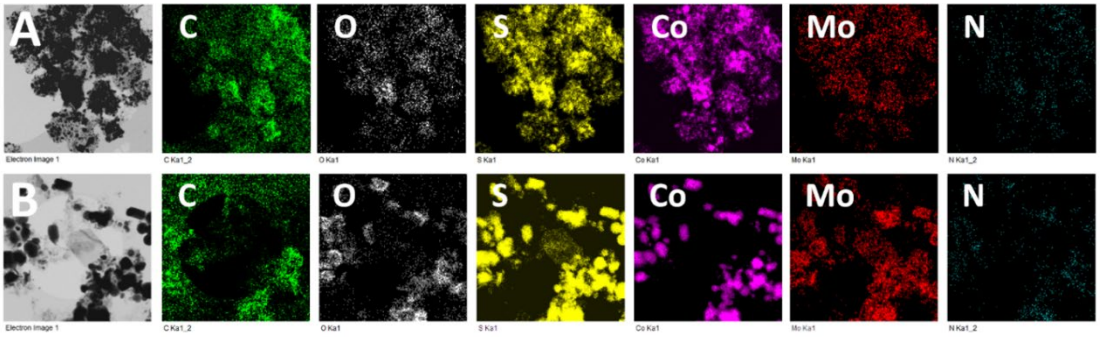

Fig. 5.10 TEM elemental mappings of A) CoMoS-800 and B) CoMoS-1000.

Table 5.3 TEM-EDX results and Co/Mo ratio of Mo-Z67-D and CoMoS-600.

Mo-Z67-D		**CoMoS-600**	
Element	**Atomic%**	**Element**	**Atomic%**
C	50.35	C	45.21
Co	11.54	Co	14.62
Mo	2.51	Mo	3.28
Co/Mo	4.60	**Co/Mo**	4.46

The fine microstructures of the Mo-Z67-D derived bimetallic Co-Mo-S/C composites were studied via TEM and presented in **Fig. 5.11**. Comparing the samples obtained at different temperatures (**Fig. 5.11A, B and C**), it is obvious that large numbers of nanoparticles with maximum diameters of 20 nm are embedded in or supported on the amorphous carbon matrix for sample CoMoS-600. Higher pyrolysis temperature results in remarkably increased particle sizes. As shown in **Fig. 5.11A, A1, A2 and A3**, sample CoMoS-600 contains large amounts curved lattices and grain boundaries. The lattice spacings of three kinds of nanoparticles are found as labelled in the images, where the d-spacing of 0.56 nm corresponds to Mo_4O_{11} [553]; 0.54 nm belongs to Mo_2S_3 [554], while 0.62 and 0.29 nm are related to $CoMoS_{3.13}$ [555]. The interlayer distances of $CoMoS_{3.13}$ vary in the range of 0.62 ―0.75 nm, which could be due to the formation of large amounts of lattice distortion and defects in the 1-3 layers of $CoMoS_{3.13}$ crystals, which may benefit the electrochemical performance [556, 557]. SAED pattern in the **insert of Fig. 5.11A** indicates the polycrystalline nature of sample CoMoS-600 and that the $CoMoS_{3.13}$ is the dominant crystalline phase of the composite. In samples CoMoS-800 and CoMoS-1000 (**Fig. 5.11B and C**), larger and thicker metal sulphide particles are clearly observed. The high-resolution TEM image in **Fig. 5.12A** for sample CoMoS-800 shows that a more intact $CoMoS_{3.13}$ crystal structure is formed with an increased number of layers and reduced interlayer distances (ranging from 0.62-0.66 nm). Compared to the composite obtained at 600°C, sample CoMoS-800 exhibits fewer defects in the crystals. For sample CoMoS-1000, most metal sulphides agglomerate to form large particles (**Fig. 5.12B and C**). Moreover, compared with samples CoMoS-600/800, sample CoMoS-1000 exhibits $CoMoS_{3.13}$ crystals with further increased thickness inside the carbon matrix (**Fig. 5.12D**). In addition, the interlayer distance of $CoMoS_{3.13}$ in sample CoMoS-1000 is exactly 0.62 nm, indicating the reduction of defects at high pyrolysis temperature. Graphitic carbon is observable in CoMoS-1000, as shown in **Fig. 5.12E**. These TEM observations are well in line with the above XRD results.

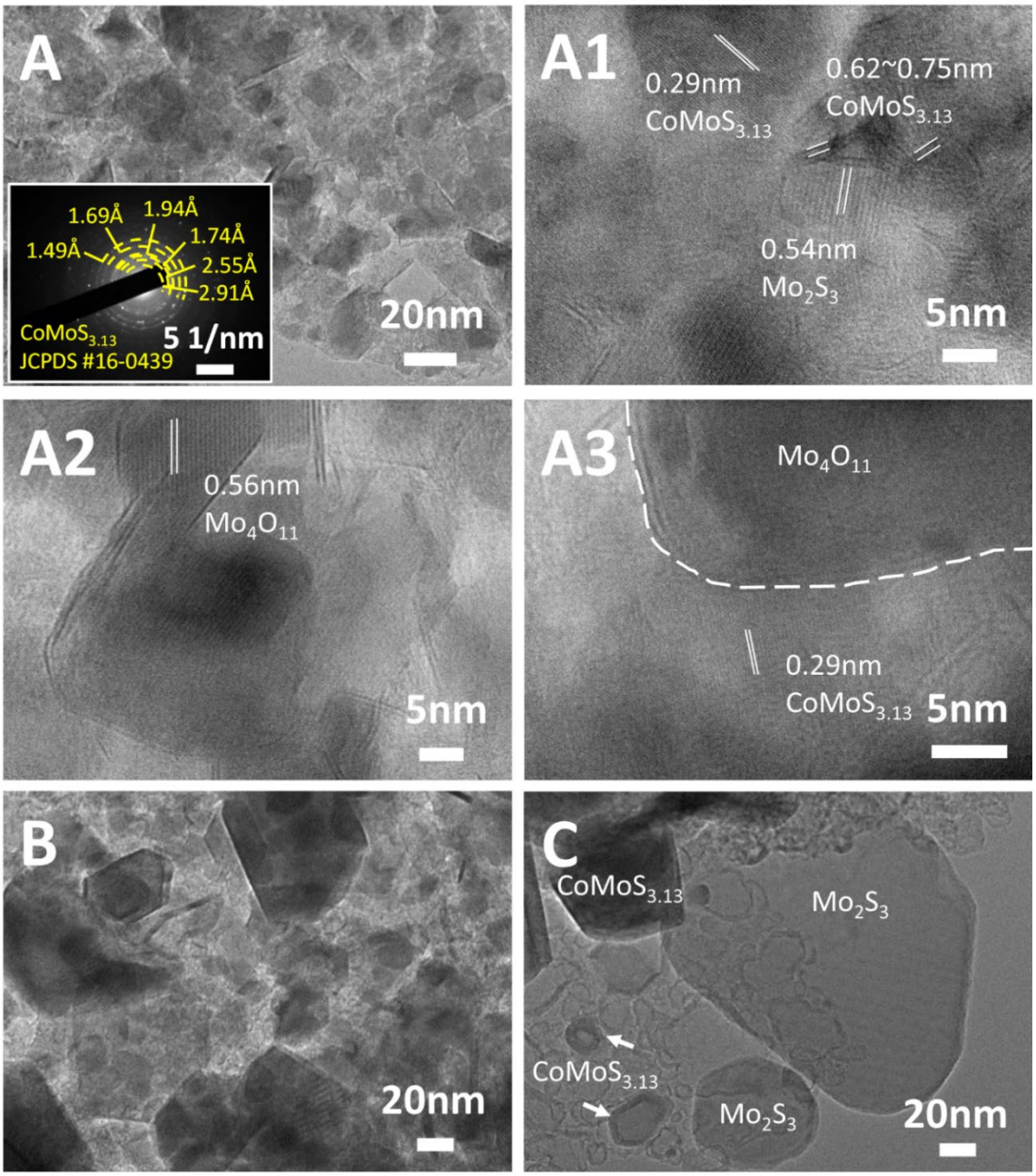

Fig. 5.11 TEM images of A) CoMoS-600, B) CoMoS-800 and C) CoMoS-1000. The insert in A) is the SAED pattern of CoMoS-600. A1), A2) and A3) are high resolution TEM images of CoMoS-600.

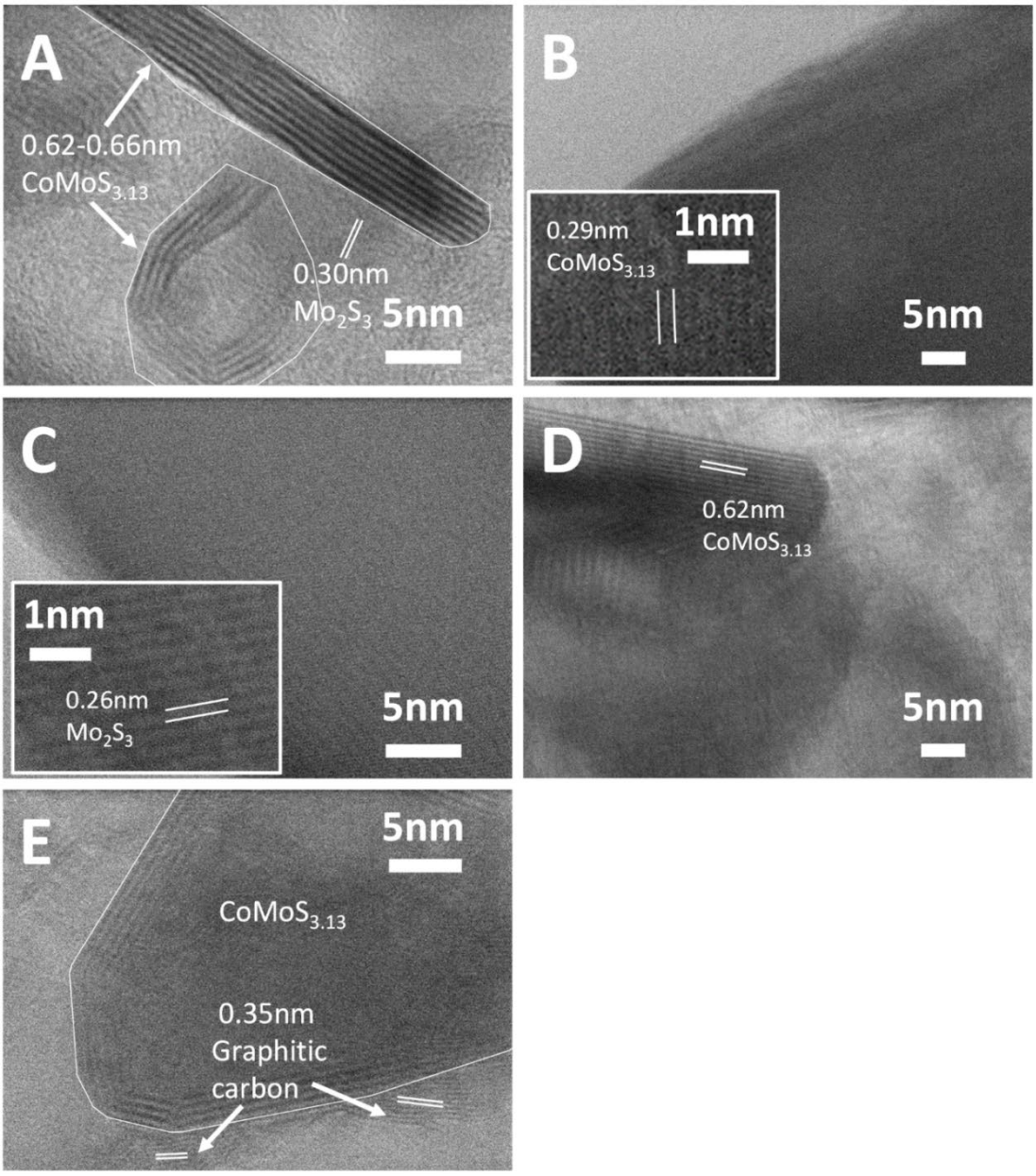

Fig. 5.12 High resolution TEM images of A) $CoMoS_{3.13}$ and Mo_2S_3 crystals in CoMoS-800; agglomerated B) $CoMoS_{3.13}$ crystal and C) Mo_2S_3 crystals in CoMoS-1000; D) fine $CoMoS_{3.13}$ crystal on the carbon matrix of CoMoS-1000 and E) graphitic carbon in CoMoS-1000.

Texture properties of the three Co-Mo-S/C composites obtained at different pyrolysis temperatures are summarised in **Table 5.4**. Both BET surface area and total pore volume are in the order of CoMoS-800 > CoMoS-1000 > CoMoS-600, with CoMoS-800 possessing the highest surface area and pore volume, which can benefit mass and ion transportation during the electrochemical reactions.

Table 5.4 Textural properties of Co-Mo-S/C samples obtained from N_2 sorption analysis.

Sample	CoMoS-600	CoMoS-800	CoMoS-1000
BET surface area ($m^2\ g^{-1}$)	76	147	128
Total pore volume ($cm^3\ g^{-1}$)	0.21	0.48	0.26

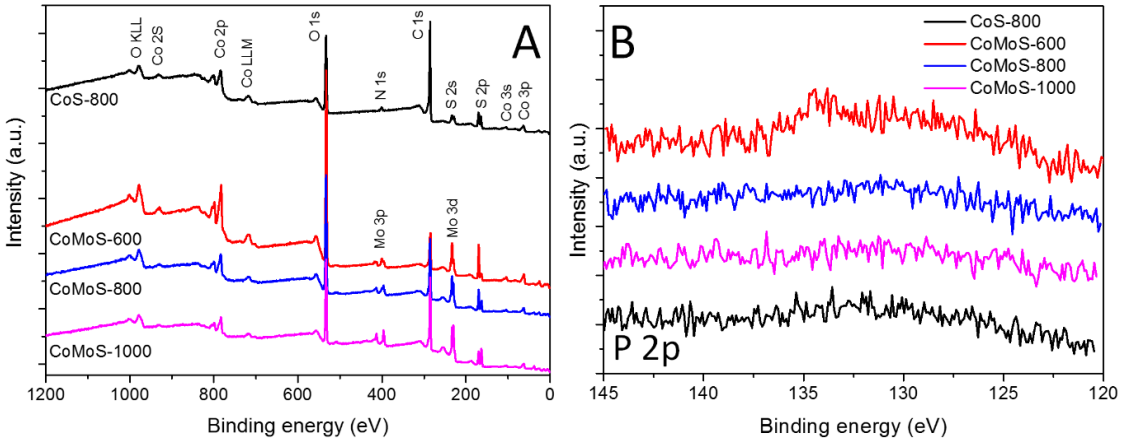

Fig. 5.13 A) XPS element survey and B) high-resolution P 2p spectra of samples CoS-800, CoMoS-600, CoMoS-800 and CoMoS-1000.

The surface chemistry of the samples was analysed by XPS. The XPS element survey is presented in **Fig. 5.13A**, which confirms the presence of O, C, N, S and Co in the samples derived from both the Mo-modified and PDA decorated ZIF67 and the pristine Z67, whereas the Mo element only appears in the Mo-modified samples. This is consistent with the XRD and elemental mapping results. In addition, only a trace amount of P is detected in sample CoMoS-600, which is negligible in composites CoMoS-800 and CoMoS-1000 (**Fig. 5.13B**) due to the high volatility of the elemental P during the pyrolysis. This small amount of P may lead to extra active sites in the Co-Mo-S/C composites, which contributes to the extraordinary electrochemistry performance of the composites [558, 559].

High-resolution XPS spectra of Mo 3d for samples CoMoS-600, CoMoS-800 and CoMoS-1000 are presented in **Fig. 5.14A**. The peak at ca. 227 eV is assigned to the S 2s peak due to the overlapping of Mo 3d and S 2s. Three doublets at around 229.4/232.5 eV, 231.8/234.9 eV and 233.4/236.5 eV are assigned to Mo $3d_{5/2}$ and $3d_{3/2}$ peaks of Mo^{4+}, Mo^{5+} and Mo^{6+} respectively, which are close to those previously reported binding

energies [560] with the spin-orbital splitting of 3.1 eV [561]. As the pyrolysis temperature increases, the amount of Mo^{6+} and Mo^{5+} decreases while that of Mo^{4+} increases. The high intensity of Mo^{4+} peaks in all samples evidences the presence of $CoMoS_{3.13}$ [555, 562]. Interestingly, the binding energy of the Mo^{4+} $3d_{5/2}$ peak for sample CoMoS-600 redshifts 0.3 eV compared to that of samples CoMoS-800 and CoMoS-1000, revealing the increase in electron density around Mo due to the electrons transferred from the less electronegative Co to Mo [562], resulting in a stronger interaction between Co and Mo in CoMoS-600, which is beneficial to its electrochemistry performance [563].

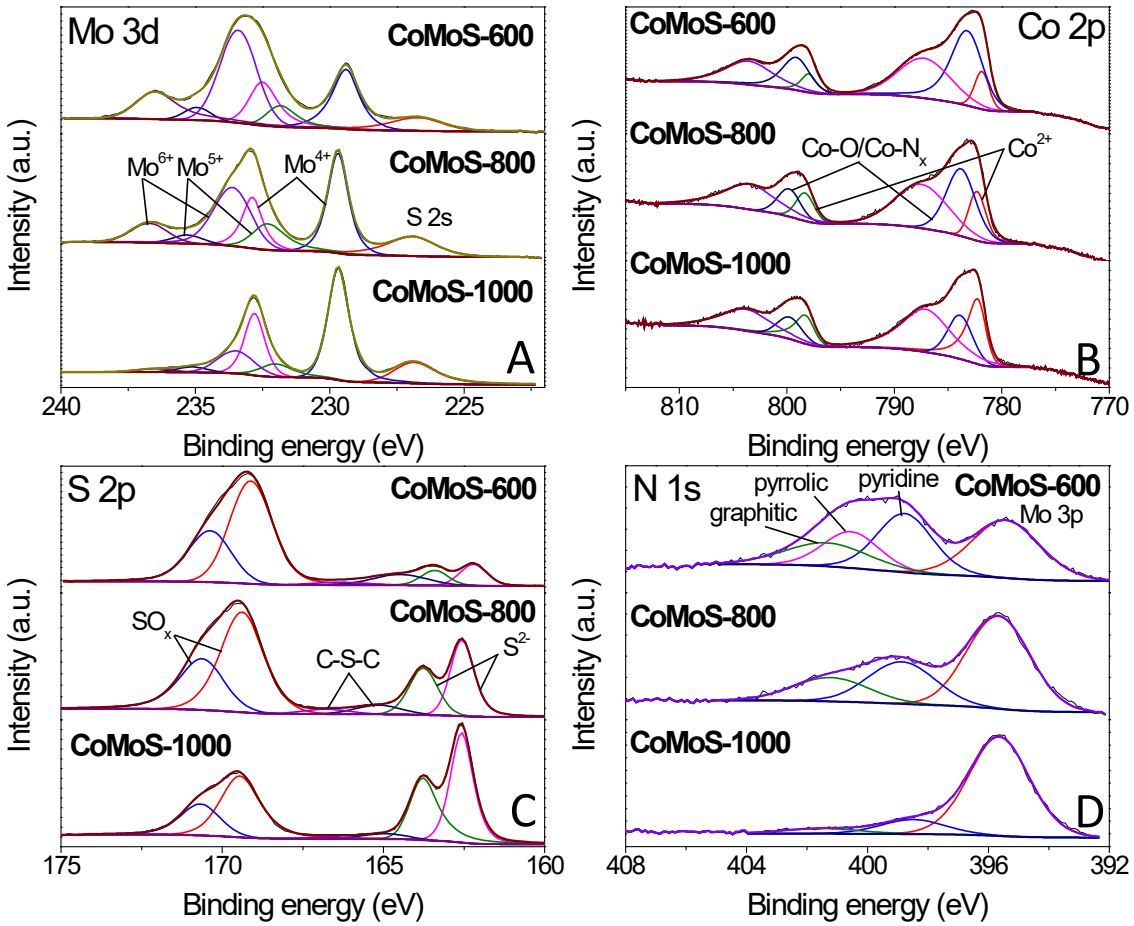

Fig. 5.14 High-resolution XPS spectra of A) Mo 3d, B) Co 2p, C) S 2p and D) N 1s for CoMoS-600, CoMoS-800 and CoMoS-1000.

Moreover, the XPS spectra of Co 2p for all the CoMoS samples are presented in **Fig. 5.14B**. The Co 2p peaks can be deconvoluted into three Co $2p_{3/2}$ and $2p_{1/2}$ doublets with the spin-orbit splitting of 16 eV. The peaks that appeared at around 781.9/798.0 eV ascribed to $2p_{3/2}$ and $2p_{1/2}$ of Co^{2+} respectively [532], whereas the doublets at around 783.2/799.1 eV represent Co with a higher oxidation state, which is reduced as pyrolysis temperature increases. The latter can be ascribed to the formed intermediate cobalt oxide species [564] at low pyrolysis temperature, and Co-N_x species [565] that originate from the

combination of Co ions with N element from PDA and MeIM. It is believed that OER performance can be enhanced by the presence of Co-N_x [550, 566, 567]. The last pair of doublets at around 787.2/803.5 eV are the shake-up satellite peaks of Co 2p.

Furthermore, high-resolution XPS spectra of S 2p are presented in **Fig. 5.14C**. Peaks at around 162.2/163.4 eV correspond to the $2p_{3/2}$ and $2p_{1/2}$ of S^{2-} [532], confirming the formation of Co-Mo-S phase. The other set of doublets at 163.4/164.5 eV is attributed to the C-S-C bond [568, 569], indicating the doping of the S element in the carbon matrix. It is obvious that an increased amount of S doped in the carbon matrix at low pyrolysis temperature results in enhanced modification of electronic structure and improved catalytic active sites, which are expected to improve the HER and OER performance. The doublets at 169.1/170.4eV are attributed to oxidised S species, which is partly due to the intermediate oxide formed during the pyrolysis and partly due to the surface oxidation of the samples during the XPS inspection [528, 532, 570].

Lastly, the N 1s spectra of the composites are shown in **Fig. 5.14D**. Except for the Mo 3p peak at around 395.4 eV, the N 1s spectra can be deconvoluted into three peaks at around 398.8, 400.5 and 401.3 eV, which can be assigned to pyridine N, pyrrolic N and graphitic N, respectively [555]. These N species indicate that the carbon matrix in the Co-Mo-S/C composites has been doped by N element, which can change the electronic structure of neighbouring carbon atoms, promoting the formation of increased catalytic active sites that can improve the HER and OER activities [531, 532]. Similar to S-doping, the level of N-doping in the composites decreases with increasing pyrolysis temperature.

5.2.3 Electrochemistry performance of Co-Mo-S/C composites

The hydrogen evolution reaction (HER) performance of all the Mo-Z67-D derived samples were evaluated in 0.5 M H_2SO_4 electrolyte with a three-electrode setup. The benchmark HER catalyst 20% Pt/C as well as Z67 derived CoS-600 are also assessed for comparison. As shown by the linear sweep voltammograms (LSV) curves in **Fig. 5.15A**, the onset potential (η_{onset}) and overpotential to achieve current density of 10 mA cm^{-2} (η_{10}) for sample CoMoS-600 is -0.167 and -0.235 V respectively, apparently lower than that of samples CoMoS-800 (η_{onset} = -0.206 V, η_{10} = -0.274 V) and CoMoS-1000 (η_{onset} = -0.251 V, η_{10} = -0.327 V). Compared with CoS-600 (η_{onset} = -0.205 V, η_{10} = -0.359 V), CoMoS-600 shows a 38 mV and 124 mV more positive in onset potential and η_{10} respectively, which indicates that the introduction of PDA coating and PMA molecules have introduced a large number of active sites into the derived composites.

Moreover, the reaction kinetics of the catalysts are estimated by linear fitting of Tafel plots (**Fig. 5.15B**) derived from the polarization curves. Generally, the smaller the Tafel slope, the faster the reaction kinetics. A dramatic improvement in Tafel slope is observed for CoMoS-600 (65.50 mV dec^{-1}) compared to its Mo-free counterpart (153.24 mV dec^{-1}). Interestingly, sample CoMoS-800 shows a slightly smaller Tafel slope (61.47 mV dec^{-1}) than sample CoMoS-600, possibly due to the much higher surface area and the better conductivity of the graphitised carbon matrix of CoMoS-800. However, overall CoMoS-600 still shows the best performance among all Mo-containing composites since the electrocatalytic activities of the bimetallic Co-Mo-S/C composites are the synergistic coordination effect of the graphitisation degree of the carbon matrix, the exposed active sites originated from the ultra-small nanoparticles and the amount of heteroatoms N, S and even P doping in the carbon matrix.

The electrochemical impedance spectroscopy (EIS) of the Co-Mo-S/C composites were examined to evaluate the kinetic difference of the catalysts. As shown in the Nyquist plot (**Fig. 5.15C**), all samples show depressed semi-circles, which can be modelled by an equivalent circuit consisting of series resistance (R_S), a constant phase element (CPE) and a charge-transfer resistance (R_{ct}). Sample CoMoS-600 exhibits the smallest R_{ct} of 54.75 Ω than that of CoMoS-800 (62.96 Ω) and CoMoS-1000 (86.92 Ω), which possesses a higher degree of graphitisation and a better conductive substrate. This indicates that, firstly, sample CoMoS-600 possesses a better electron transferability at the interface between the electrocatalyst and the electrolyte; secondly, the number of exposed active sites from the ultra-small defect-rich nanoparticles are the dominant factor towards faster HER process for sample CoMoS-600.

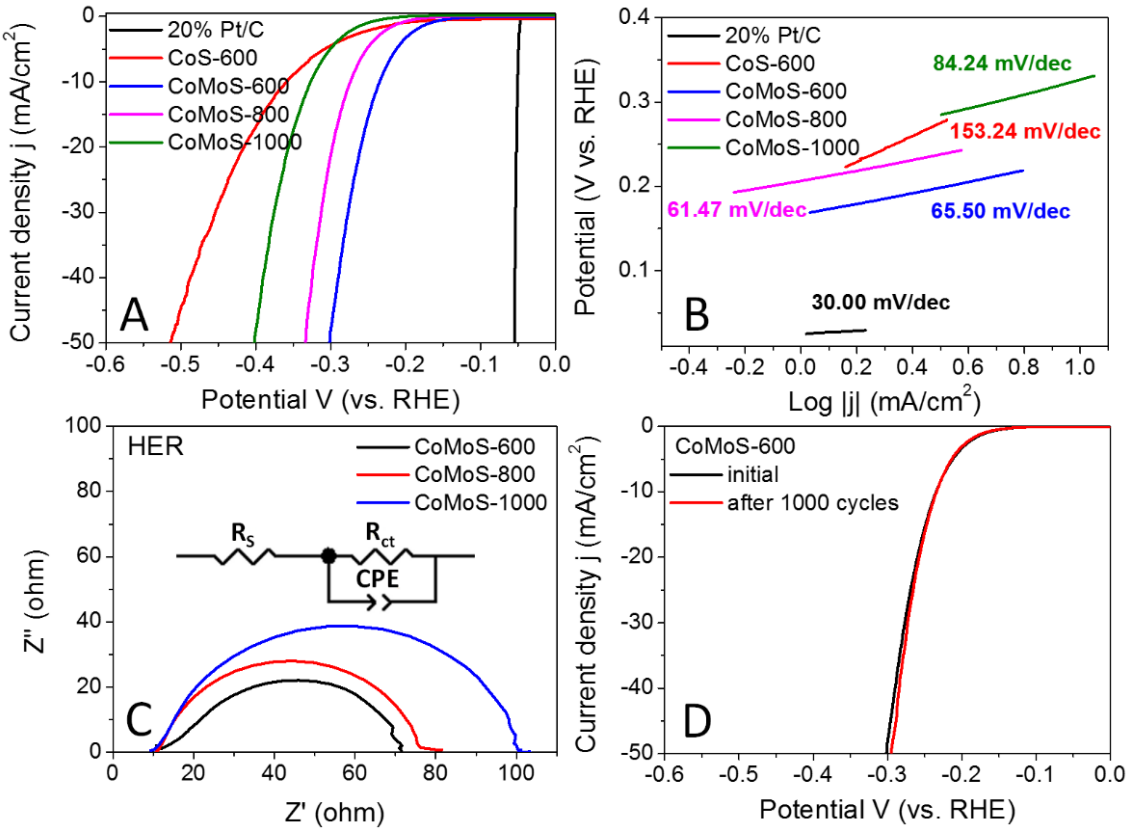

Fig. 5.15 A) HER polarization curves and B) corresponding Tafel plots of benchmark 20% Pt/C, CoS-600, CoMoS-600, CoMoS-800 and CoMoS-1000; C) EIS of CoMoS-600, CoMoS-800 and CoMoS-1000 and D) Polarization curves of CoMoS-600 before and after 1000 CV cycles in 0.5 M H_2SO_4. All polarization curves are iR corrected. EIS spectra recorded at η_{10}, measured in the frequency range of 10^{-1}-10^4 Hz.

In addition, the long-term stability of sample CoMoS-600 was also evaluated by the polarization curves before and after 1000 cyclic voltammetry (CV) cycles. **Fig. 5.15D** shows that the difference between the two polarization curves is negligible, which suggests good stability for sample CoMoS-600.

The oxygen evolution reaction (OER) catalytic activities of these bimetallic Co-Mo-S/C composites were examined in O_2 saturated 1 M KOH electrolyte at 1600 RPM, and the results are presented in **Fig. 5.16A**. All the Co-Mo-S/C composites exclusively exhibit dramatically improved OER performance compared to that of CoS-600 and the benchmark IrO_2 catalysts. Sample CoMoS-600 displays OER performance of η_{onset}=0.248 V and η_{10}=0.350 V, while sample CoMoS-800 exhibits OER performance of η_{onset}=0.293 V and η_{10}=0.359V, which are significantly lower than that of sample CoMoS-1000 (η_{onset}=0.340 V, η_{10}=0.396 V). Compared with Mo-free sample CoS-600 (η_{onset}=0.409 V, η_{10}=0.481 V), sample CoMoS-600 shows a prominent improvement of 161 mV downshift

in onset potential and 131 mV decrease in η_{10}, which indicates that the introduced Mo-containing active sites are favourable for OER performance.

Moreover, the reaction kinetics of the catalysts towards OER are demonstrated in **Fig. 5.16B**. Sample CoMoS-800 exhibits a slightly faster reaction kinetics than sample CoMoS-600, as indicated by the smaller Tafel slope. However, overall sample CoMoS-600 is the best performed OER catalyst among the three Mo-containing composites. EIS of these Co-Mo-S/C composites were examined and fitted with a similar equivalent circuit used for the above HER (**Fig. 5.16C**). Sample CoMoS-600 exhibits the smallest R_{ct} of 45.1 Ω amongst the three Co-Mo-S/C samples, indicating that CoMoS-600 possesses the highest electron transferability in the OER process.

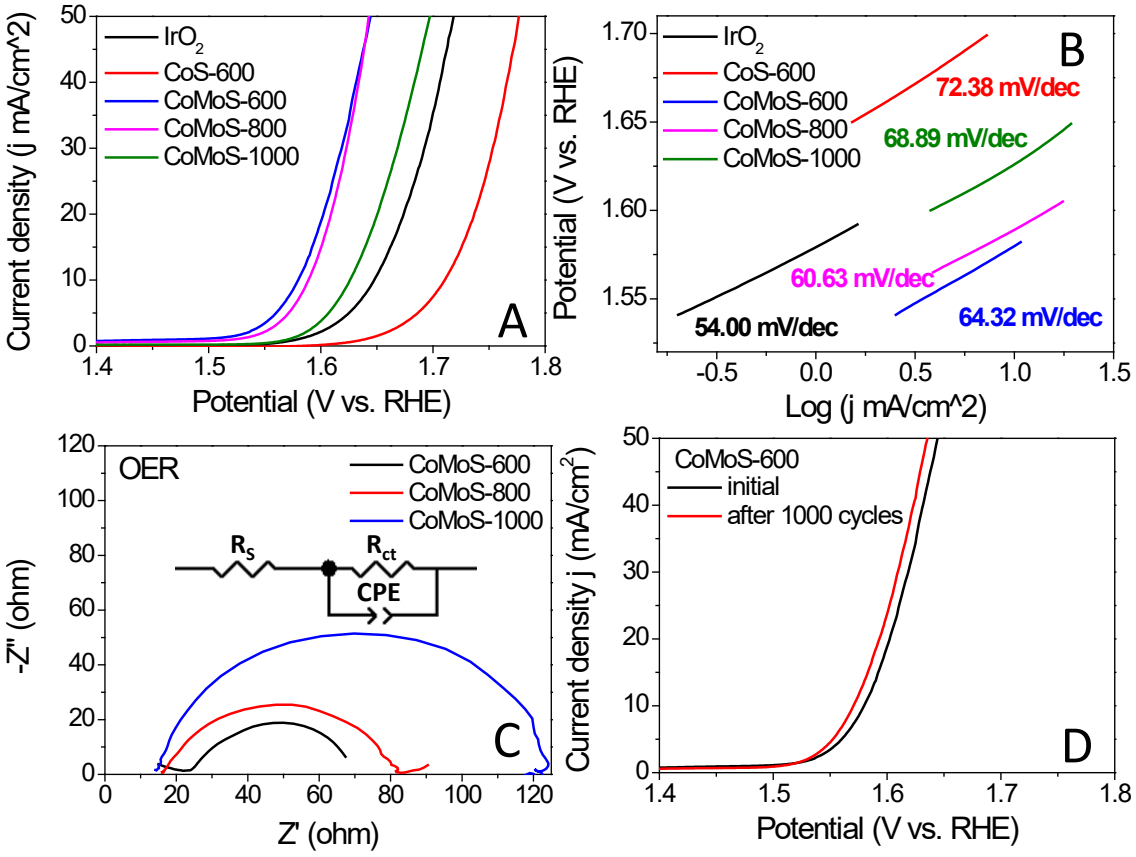

Fig. 5.16 A) OER polarization curves and B) corresponding Tafel plots of the benchmark IrO_2, CoS-600, CoMoS-600, CoMoS-800 and CoMoS-1000. C) EIS of CoMoS-600, CoMoS-800 and CoMoS-1000. D) Polarization curves of CoMoS-600 before and after 1000 CV cycles in 1 M KOH. All polarization curves are iR corrected. EIS spectra recorded at η_{10}, measured in the frequency range of 10^{-1}-10^{4} Hz.

Furthermore, the stability of the best-performed sample, CoMoS-600, was also evaluated, and the polarization curves before and after 1000 CV cycles results are presented in **Fig. 5.16D**. A 0.01V decrease in η_{10} is observed, implying a mild

improvement in OER activities after 1000 CV cycles. Moreover, XRD and SEM of the sample CoMoS-600 after 1000 CV cycles of OER measurements (see **Fig. 5.17A and B**) still show the same characteristic peaks and morphologies without obvious difference compared with the original sample, which further confirms the stability of the catalyst.

It is worth noting that the Co-Mo-S/C composites derived from Mo-Z67-D at a heating ramp rate of 2 °C min^{-1} generally exhibit slight better electrocatalytic HER and OER performance than those obtained at a heating ramp rate of 10 °C min^{-1} (**Fig. 5.18A and B**). This may be due to the relatively higher level of graphitisation of the carbon matrix obtained at a slower heating ramp rate (**Table 5.2**), which provides a relatively better charge transferability during the electrocatalytic process compared to the sample obtained at a fast heating ramp rate.

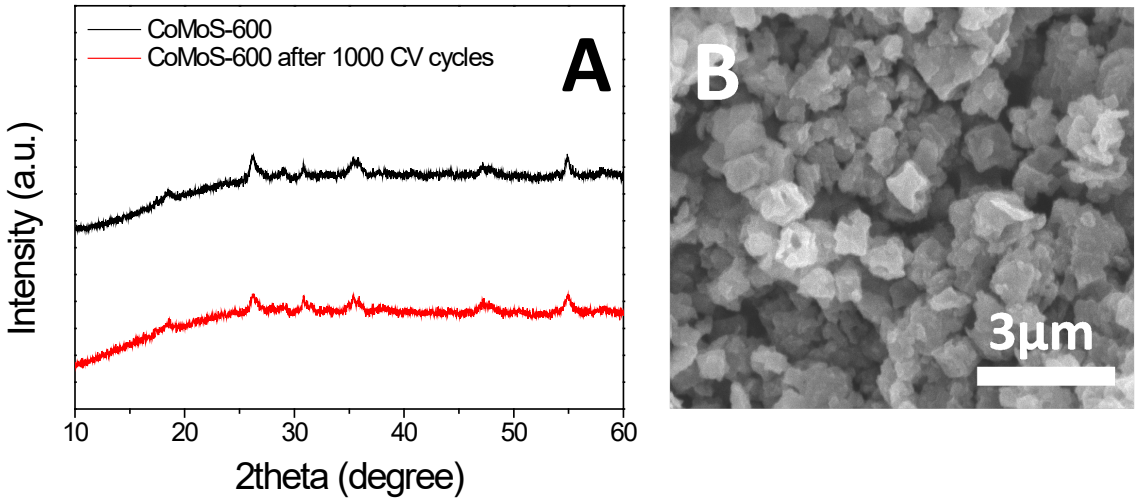

Fig. 5.17 A) XRD pattern of MoCoS-600 before and after 1000 CV cycles, B) SEM image of MoCoS-600 after 1000 CV cycles.

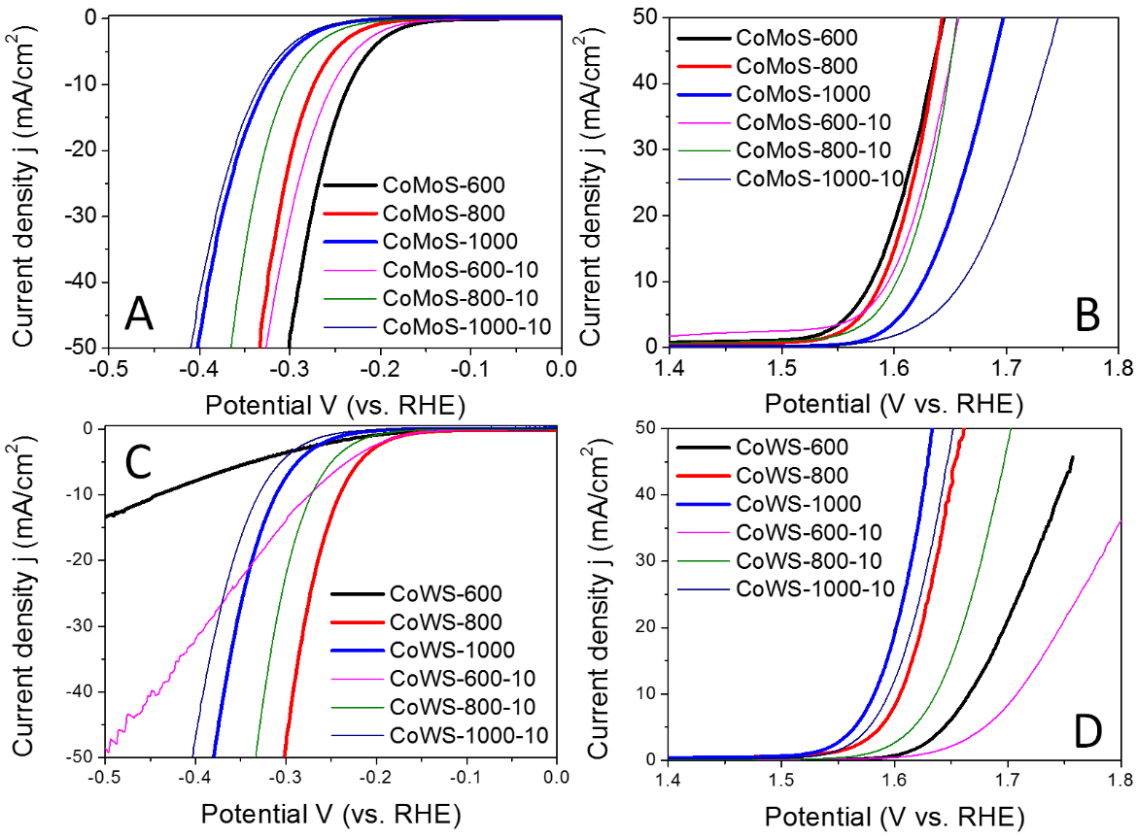

Fig. 5.18 A) HER and B) OER polarization curves of Mo-Z67-D derived Co-Mo-S/C composites obtained at different pyrolysis temperatures and two different heating ramp rates; C) HER and D) OER polarization curves of W-Z67-D derived Co-W-S/C composites obtained at different pyrolysis temperatures and two different heating ramp rates.

Based on the electrocatalytic performance and the material characterisation results, the remarkable improvement in electrocatalytic performance of the bimetallic Co-Mo-S/C composite obtained at 600°C can be ascribed to the synergistic effect of following factors: 1) the evenly distributed ultra-small defect-rich Co-Mo-S phase nanoparticles that maximise the active-surface-area-to-volume-ratio and increase the number of exposed active sites; the abundant lattice distortions, defects in the ultra-small nanoparticles are active sites for HER and OER [523, 524]; 2) heteroatoms including S element from H_2S gas, as well as N element from PDA coating and organic linker in ZIF-67, even trace amount of P derived from PMA, lead to heteroatom N and S-doped composites, which modulates the electronic structure of neighbouring C atoms and provides enhanced active sites for HER and OER [531, 532]; 3) the strong interaction between Co and Mo in the Co-Mo-S phase improve the electron conductivity o the composites and is favourable for the charge transfer during the electrocatalytic reaction [562, 563]; and 4) the porous carbon support offers

high surface area and provides access routes to the reaction active sites, facilitate the easy mass transportation during the electrocatalytic reaction [529, 530].

5.2.4 Characterization and electrocatalytic performance of bimetallic Co-W-S/C composites derived from PTA@ZIF-67@PDA nanocubes

The same synthesis approach is further expanded to synthesise phosphotungstic acid (PTA)@ZIF-67@PDA to demonstrate the generalisation of this material synthesis method. As shown in **Fig. 5.2D**, the TEM image of the as-obtained PTA@ZIF-67@PDA, i.e. W-Z67-D, shows a slightly different morphology from the parental Z67-D sample that lamellar petal-like W-PDA complex with greater thickness is coated on the cubes with random free-end protruding, no hollow cavity is observed in the core. Obviously, no observable dissociation of ZIF-67 occurred. The presence of homogeneous and intact core in W-Z67-D indicates that the addition of the same weight amount of PTA does not etch the core of the composite nor alter the structure and morphology of ZIF-67. The elemental mappings of W-Z67-D (**Fig 5.3D**) show that O, P and W elements mostly accumulate on the surface of the nanocubes, whereas N and Co elements distribute evenly across the cubes, indicating that majority of PTA molecules are chelated with the coated PDA. The corresponding elemental line scanning (**Fig. 5.4D**) also supports this conclusion. Both XRD patterns (**Fig. 5.5A**) and FT-IR spectra (**Fig. 5.5B**) support that the PTA has been successfully introduced into the PDA decorated ZIF-67 composites without changing the structure of ZIF-67. W-Z67-D possesses a S_{BET} close to that of Z67-D, suggesting that PTA etching does not occur and extra hierarchical pores are not generated by the introduction of PTA.

The as-synthesised W-Z67-D was also subjected to similar heat treatments applied to Mo-Z67-D. XRD patterns in **Fig. 5.19A** show that the derived samples are mainly composed of $Co_{1-x}S$ (JCPDS #42-0826) and WS_2 (JCPDS #08-0237), whereas only $Co_{1-x}S$ (JCPDS #42-0826) is observed in the Z67-D derived composite. Similar to Mo-Z67-D derived composites, high heat treatment temperatures and slow heating ramp rates result in metal sulphides with better crystallinity and larger grain size, which is supported by the narrower and sharper characteristic diffraction peaks of the obtained composites (**Fig. 5.19B**). The detailed XRD patterns (**Fig. 5.19C**) suggest that the change of the asymmetrical main peaks and the shift in peak position are clearly observed, which may be due to the lattice distortions and crystallographic defects of the crystalline components.

It is worth noting that the direct heat process of pure PMA and PTA powder in H_2S/Ar leads to distinct different samples: PMA-C (**Fig. 5.7B**) exhibits mixed composition phases including metal dichalcogenides and metal oxide, whereas PTA-C (**Fig. 5.19D**) only consists of pure metal dichalcogenides phase. This difference is also reflected in the compositions of the PMA/PTA modified Z67-D derivatives.

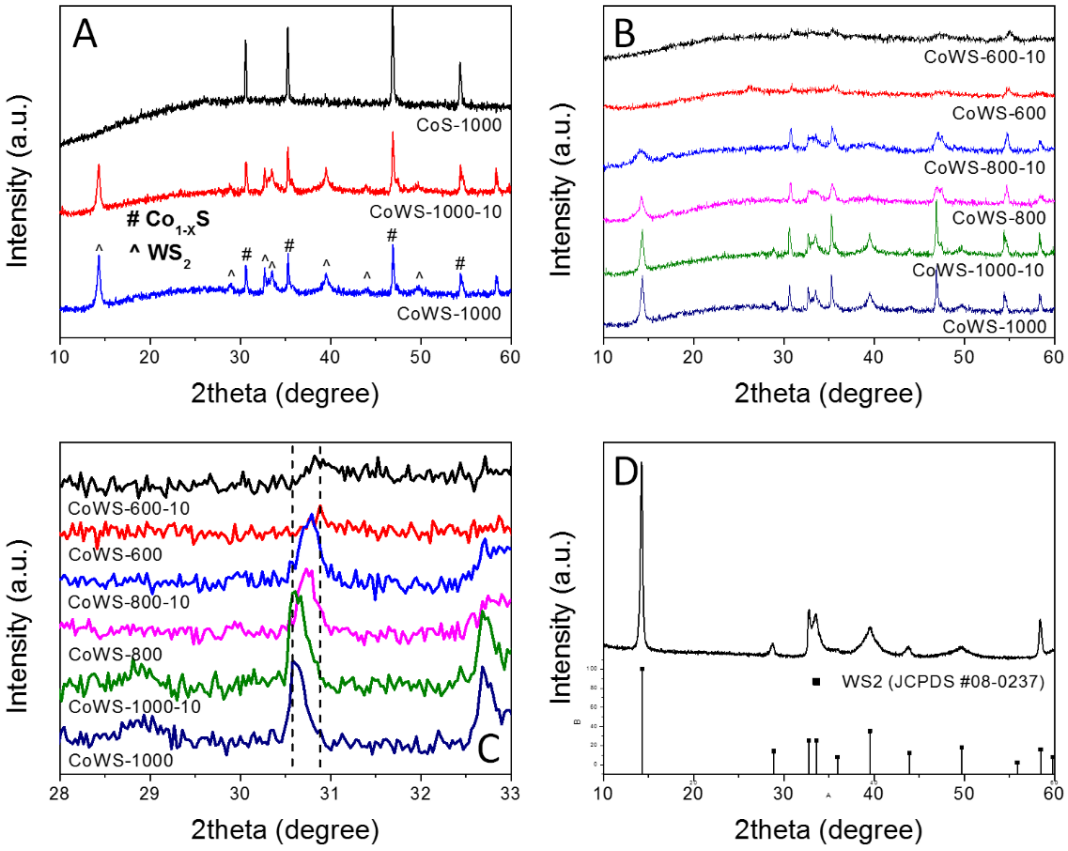

Fig. 5.19 XRD patterns of A) CoS-1000, CoWS-1000-10 and CoWS-1000, B) W-Z67-D derived Co-W-S/C samples obtained at different pyrolysis temperatures and ramp rates, C) enlarged XRD peak shifts of W-Z67-D derived Co-W-S/C samples at different heat treatment temperatures and ramp rate and D) PTA-C.

The Raman spectra (**Fig. 5.8C and D**) of the W-Z67-D derivatives and their I_D/I_G ratios (**Table 5.2**) are similar to the Mo-Z67-D derivatives, and slower heating ramp rate results in a higher degree of graphitisation of the carbon matrix. Compared with Mo-Z67-D derived composites, W-Z67-D derived Co-W-S/C composites show a similar agglomeration and crystallisation trend as the pyrolysis temperature increases.

TEM images of Co-W-S/C composites are presented in **Fig. 5.20**. At 600 °C (**Fig. 5.20A and A1**), small nanocrystals of size around 20 nm are formed on the carbon matrix, without observable agglomerated large crystals at the edge of the carbon support. At 800

°C (**Fig. 5.20B**), agglomeration of $Co_{1-x}S$ crystals and WS_2 flakes are observed. The size of the small nanocrystals in the carbon matrix turns larger and thicker, with maximum diameters around 50 nm (**Fig. 5.20B1**). When the pyrolysis temperature increases to 1000 °C (**Fig. 5.20C**), most metal compounds are separated from the carbon matrix and agglomerated into large $Co_{1-x}S$ spheres with average diameters of 200 nm, accompanied with WS_2 flakes with diameter up to 400 nm and thickness up to 40 nm. Moreover, large amounts of ultra-small crystals with sizes under 5 nm remain in the carbon matrix (**Fig. 5.20C1**), which allow more exposed active sites during the electrochemical process, contributing to the enhanced OER performance of the CoWS-1000.

The crystallinity of the WS_2 improves at elevated pyrolysis temperature, leading to the transformation of the lattice spacing as shown in **Fig. 5.20A2, B2 and C2**. Obviously, fewer defects exist in the crystal of the composites obtained at higher pyrolysis temperature, which can cause deterioration in electrochemistry performance, as suggested by Ling et al. [571]. However, unlike the defect-rich sample CoMoS-600, which outperforms the CoMoS-800 in HER performance, sample CoWS-800 displays better HER activity than the defect-rich CoWS-600. It may be due to the fact that graphitic carbon was formed in CoWS-800 (**Fig. 5.20B2 insert**), whereas no graphitic carbon was observed in CoMoS-800 (**Fig. 5.12A**). This difference in the degree of graphitisation is also verified by the corresponding I_D/I_G value, as shown in **Table 5.2**. TEM elemental mappings of Co-W-S/C samples are shown in **Fig. 5.21.** Elements C, O, S, Co, W and N are found in all three composites, and all elements distribute evenly throughout the composites.

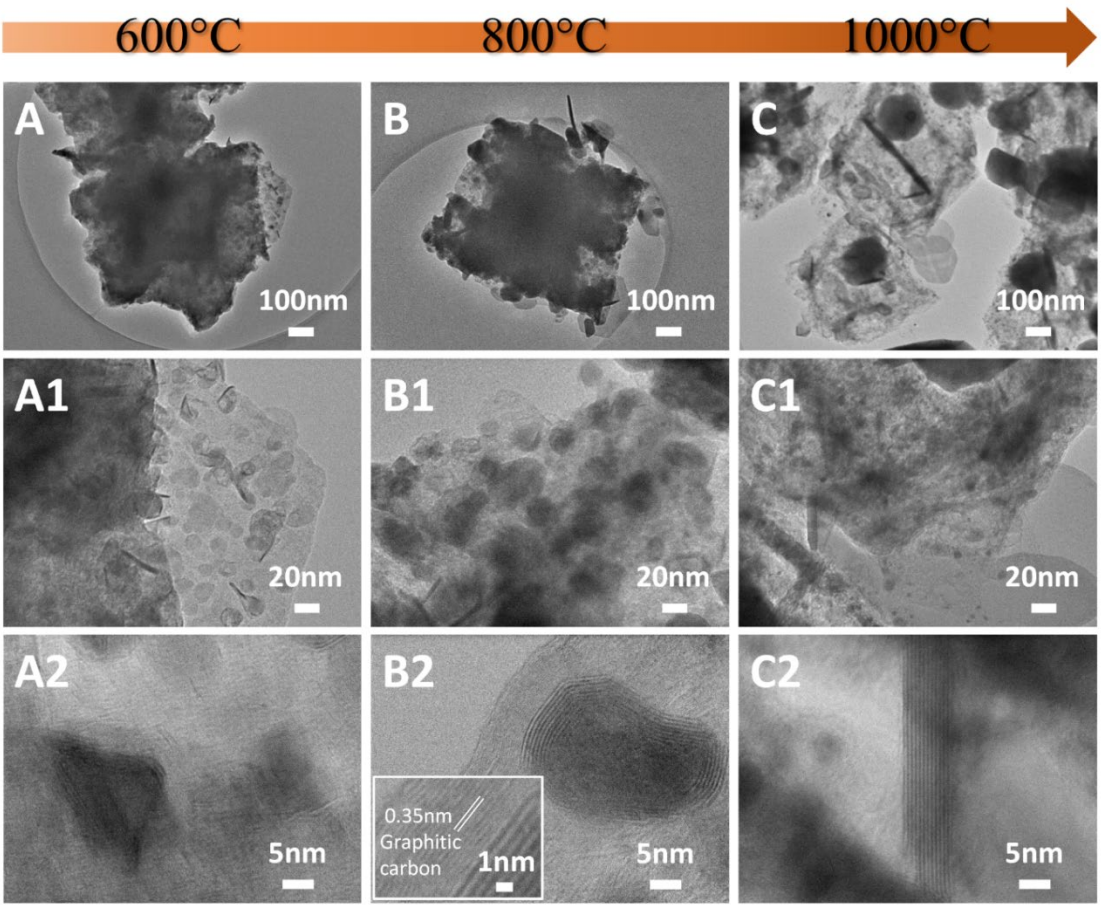

Fig. 5.20 TEM images of A) & A1): CoWS-600, B) & B1): CoWS-800 and C) & C2): CoWS-1000; high resolution TEM image of A2): CoWS-600, B2): CoWS-800 and C2): CoWS-1000.

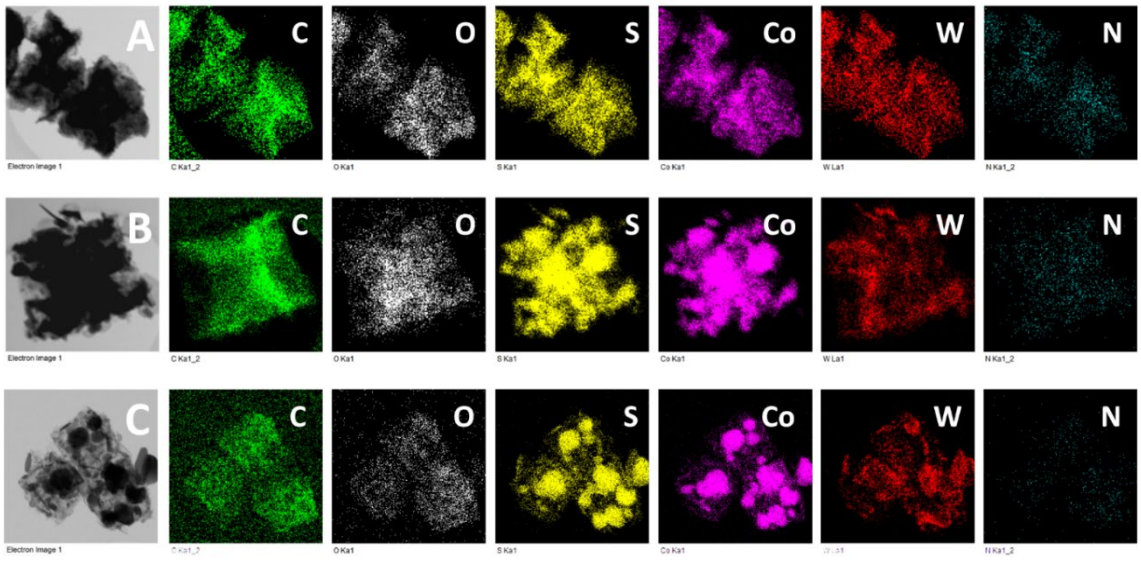

Fig. 5.21 TEM elemental mappings of A) CoWS-600, B) CoWS-800 and C) CoWS-1000.

Unsurprisingly, Co-W-S/C composites also show enhanced electrocatalytic activities towards HER and OER but with completely different performance orders for the samples (**Fig. 5.22 and Table 5.5**). The HER LSV curves and Tafel slopes are present in **Fig. 5.22A** and **Fig. 5.22B**. Composite CoWS-800 shows the smallest onset potential of -0.171 V, an overpotential of -0.240 V to achieve the current density of 10 mA cm^{-2} and Tafel slope of 71.13 mV dec^{-1}, which is much smaller than those of W-free CoS composites obtained under the same heat treatment conditions. EIS of three Co-W-S/C samples shows R_{ct} of 171.5 Ω, 54.89 Ω and 72.35 Ω, respectively for samples CoWS-600, CoWS-800 and CoWS-1000 (**Fig5.22 C**), revealing that sample CoWS-800 possesses the fastest electron transfer rate at the electrode material and electrolyte interface. It is believed that the improved HER performance of CoWS-800 is due to the synergistic effect of highly graphitised carbon matrix (see Raman spectra in **Fig. 5.8** and I_D/I_G ratio in **Table 5.2**) and large numbers of small WS_2 and $Co_{1-x}S$ nanoparticles that are encapsulated in or supported on the conductive carbon matrix (see TEM images in **Fig. 5.20B**).

On the other hand, composite CoWS-1000 shows the best OER activity amongst the Co-W-S/C composites, as indicated by the smallest onset potential of 0.293 V, an overpotential of 0.352 V to realise a current density of 10 mA cm^{-2} and Tafel slope of 55.85 mV dec^{-1}, as shown in **Fig. 5.22E and F**. Moreover, sample CoWS-1000 exhibits the smallest semi-circle in the Nyquist plot (**Fig. 5.22G**), indicating the fastest electron transferability of this sample. It is likely that the ultra-small nanoparticles (< 5 nm, as shown in **Fig. 5.20C1 and C2**) embedded in the carbon matrix after 1000 °C heat treatment is the key toward the excellent OER performance of this composite. In contrast, no such kind of ultra-fine nanoparticles is observed in sample CoMoS-1000. Both HER and OER results are consistent with the performance of one-pot synthesised POM@ZIF-67 derived $WS_2/Co_{1-x}S$/N, S co-doped porous carbon reported in Chapter 4.

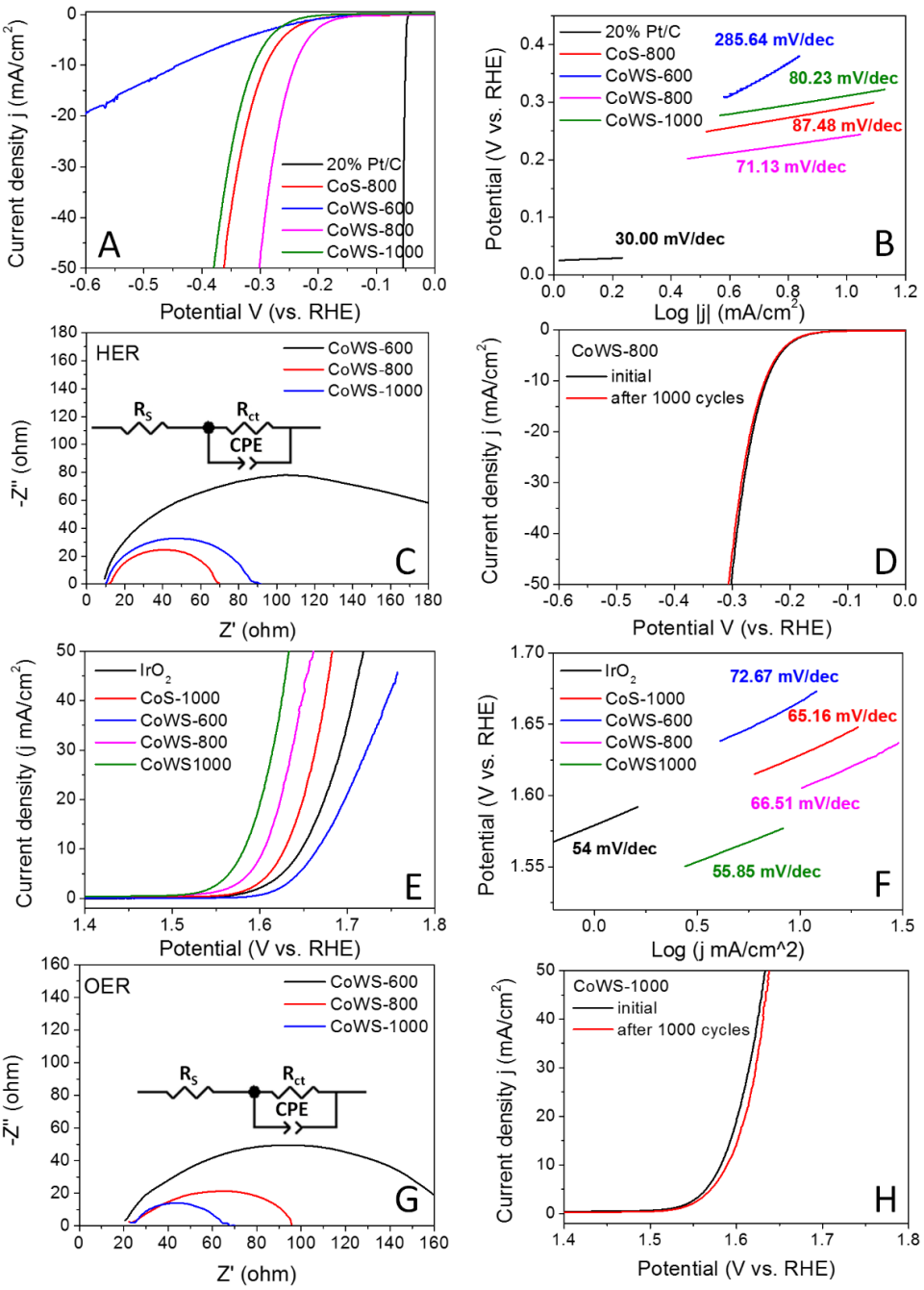

Fig. 5.22 A) HER polarization curves and B) corresponding Tafel plots of the benchmark 20% Pt/C, CoS-800, CoWS-600, CoWS-800 and CoWS-1000; C) EIS of CoWS-600, CoWS-800 and CoWS-1000; D) Polarization curves of CoWS-800 before and after 1000 CV cycles. All polarization curves are iR corrected and obtained in 0.5 M H_2SO_4 electrolyte; E) OER polarization curves and F) corresponding Tafel plots of the benchmark IrO_2, CoS-600, CoWS-600, CoWS-800 and CoWS-1000; G) EIS of CoWS-600, CoWS-800 and CoWS-1000; H) Polarization curves of CoWS-600 before and after 1000 CV cycles. All polarization curves are iR corrected and obtained in O_2-saturated 1 M KOH electrolyte. EIS spectra recorded at η_{10}, measured in the frequency range of 10^{-1}-10^4 Hz.

Table 5.5 HER and OER electrochemical performance of Co-W-S/C composites.

HER	Onset potential @1 mA cm^{-2} (η_{onset}, V vs. RHE)	Overpotential @ 10 mA cm^{-2} (η_{10}, V vs. RHE)	Tafel slope (mV dec^{-1})	Charge transfer resistance (R_{ct}, Ω)
20% Pt/C	-0.047	-0.050	30.00	-
CoS-800	-0.021	-0.291	87.48	-
CoWS-600	-0.021	-0.442	285.64	171.50
CoWS-800	-0.171	-0.240	71.13	55.85
CoWS-1000	-0.237	-0.311	80.23	72.35
OER	**Onset potential @1 mA cm^{-2} (η_{onset}, V vs. RHE)**	**Overpotential @ 10 mA cm^{-2} (η_{10}, V vs. RHE)**	**Tafel slope (mV dec^{-1})**	**Charge transfer resistance (R_{ct}, Ω)**
IrO_2	0.349	0.418	54.00	-
CoS-1000	0.340	0.398	65.16	-
CoWS-600	0.377	0.436	72.67	140.40
CoWS-800	0.307	0.375	66.51	71.48
CoWS-1000	0.293	0.352	55.85	37.40

It is believed that the different order of performance between PMA and PTA@ZIF-67@PDA derivatives is due to i) the different types of active sites in the composites and ii) the different morphologies of the composites derived under the same temperature. However, the effect of the heating ramp rate on the electrocatalytic performance of the Mo-Z67-D derived samples and W-Z67-D derivatives are the same. That sample obtained at a slow heating ramp rate shows a slightly better electrocatalytic performance (**Fig. 5.18 C and D**). It is again likely due to the relatively higher degree of graphitisation of the carbon matrix obtained at a slower heating ramp rate (**Table 5.2**) that provides a relative better charge transferability during the electrochemical reaction process.

5.3 Summary

In summary, we have successfully developed a generalised approach to synthesise both HER and OER active, defect-rich ultra-fine bimetallic Co-Mo sulphide nanoparticles supported on N, S-doped porous carbon composites from PMA@ZIF-67@PDA nanocubes via carbonisation/sulphurization. PDA decorating on ZIF-67 cubes can prevent the over-dissociation of ZIF-67 from PMA etching by chelating with the PMA molecules, and acts as an additional N source for N-doping. Moreover, the partially dissociated Co^{2+} from ZIF-67 can be captured by the coated PDA via chelation, resulting in more evenly dispersed active sites throughout the heterogeneous composite after pyrolysis. The resulting bimetallic CoMoS-600 composite exhibits remarkable improvement in HER (with overpotential of -0.235 V vs. RHE at current density of 10 mA cm^{-2} and Tafel slope of 65.50 mV dec^{-1}) and OER performance (with overpotential of 0.350 V vs. RHE at current density of 10 mA cm^{-2} and Tafel slope of 64.32 mV dec^{-1}). The outstanding performance can be attributed to the synergistic effect of ultra-fine and defect-rich Co-Mo-S nanoparticle exposed active sites and N, S-doped porous carbons in the composites. Moreover, HER and OER active W-containing bimetallic Co-W-S/C composites can be readily obtained by replacing PMA with PTA, proving the universality of this synthesis approach. Compared with the Mo-containing nanocomposites, the W-containing nanocomposites did not show analogical compositions, despite similar elemental properties W and Mo shared, analogue precursors used in synthesis, and the same heat treatment conditions employed. Different types of compounds and compositions clearly lead to different active sites and reaction mechanisms, as revealed by the optimised catalysts obtained under different heat treatment temperatures. Nevertheless, this work offers a new synthesis strategy to modify acid-sensitive ZIFs with acidic compounds, providing an alternative approach to develop other advanced metal sulphides/porous carbon functional materials for energy and environmental applications.

Chapter 6 Bimetallic Fe-Mo sulphide/carbon nanocomposites derived from POM@MIL-100

6.1 Introduction

The fast-growing global energy consumption has urged the development of novel and sustainable alternative energy solutions. Hydrogen (H_2) is the most promising, zero-emission clean energy due to its vast and easily accessible reserves. To bring the produced clean H_2 energy into large-scale practical utilisation, it is pivotal to develop cost-effective and stable electrocatalysts. A growing amount of heterogeneous, non-precious metal-based HER catalysts have emerged in the past years [572].

In particular, MoS_2 has shown great potential as a promising electrocatalyst for HER [495]. Initially, bulk MoS_2 was considered inactive catalysts due to the extremely high hydrogen adsorption free energy ((ΔG_H) of 1.92 eV at its basal plane [573]. It was later proved by both theoretical simulations and experimental discoveries that the metallic edge sites of the MoS_2 (i.e. Mo-edge) are active in HER for water splitting [574, 575]. With the ΔG_H close to zero [576], the number of edge sites exposed in MoS_2 significantly increased, which results in enhanced electrocatalytic HER activity of the material. Indeed, significant progress has been made in this exciting field that abundant edge-exposed nanostructured MoS_2 has been developed to achieve better electrocatalytic HER performance [572].

Moreover, the catalytic activity of MoS_2 can be further improved via activation of the theoretically inactive basal plane and its S-edge [577]. The report has suggested that incorporating transition metal ions such as Co, Ni and Fe into the edge sites can reduce the ΔG_H of the S-edge, therefore improving its electrocatalytic HER activity. Meanwhile, doping metal ions such as Co^{2+} or Zn^{2+} into MoS_2 in-plane can decrease the electron number of the S atom to compensate for the mismatching of the energy levels, thus enhancing the adsorption of H and increasing the HER activity [578, 579]. Hakala et al. carried out DFT calculations and found that in-plane doping of MoS_2 with Fe, Co, Ni, Cu, Pd and Pt could bring the ΔG_H of the MoS_2 at S sites towards the optimal adsorption condition, which could be beneficial to electrochemistry applications [580]. On the other hand, iron sulphide-based materials including FeS [581], FeS_2, Fe_3S_4, Fe_9S_{10} [582] and Fe_7S_8 [583] have shown electrocatalytic activity for HER in water splitting. Therefore some composites such as FeS_2@MoS_2/rGO [584], Fe-MoS_2 [585], Fe-MoS_2 nanoflower [586], $Fe_{1-x}S$/MoS_2 [587] and

FeS@MoS_2/CFC [588] have been further developed and shown great potential in electrochemical energy applications.

In this chapter, the in situ encapsulation strategy demonstrated on the ZIF-based composite in Chapter 4 was applied to an iron-containing metal-organic frameworks (MOFs), MIL-100, which contains two types of confined pores with diameters of 25 and 29 Å and corresponding pore apertures of 5.5 and 8.6 Å, respectively [589], to synthesis phosphomolybdic acid (PMA)@MOF guest/host composites. These PMA@MIL-100 composites are an excellent precursor to provide sources of molybdenum, iron and carbon simultaneously. Bimetallic Fe-Mo sulphide/S-doped carbon nanocomposites were successfully fabricated by treating the composites in the H_2S atmosphere, and exhibit good electrocatalytic activity for hydrogen generation from water splitting.

6.2 Results and discussion

6.2.1 Characterization of the as-made PMA@MIL-100

The parental PMA@MIL precursor was first synthesised via a simple one-pot hydrothermal method by ageing a mixture solution of Trimethyl-1, 3, 5-benzenetricarboxylate (Me3btc), $FeCl_3$ and calculated amount of phosphomolybdic acid hydrate (PMA) in H_2O at 130 ^oC for 72 hours. The as-synthesised PMA@MIL was then subjected to high-temperature pyrolysis in H_2S/Ar atmosphere to generate the target Fe-Mo bimetallic sulphide/carbon nanocomposites. The whole process is shown in the schematic diagram in **Fig. 6.1**.

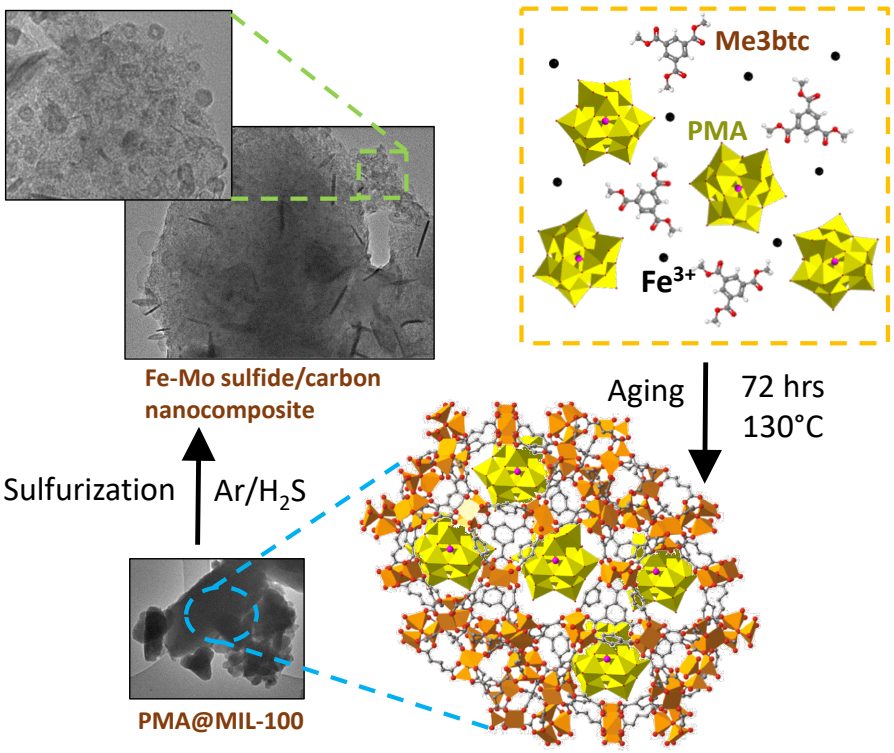

Fig. 6.1 Schematic diagram of the synthesis of Fe-Mo bimetallic sulphide/carbon composites.

Powder X-ray diffraction (XRD) of all the PMA-containing samples (**Fig. 6.2A**) show pronounced MIL-100 characteristic peaks, but the intensity of the characteristic peaks at 3° to 8° decreases or eventually disappears with the increasing amount of PMA. Obviously, introducing a high amount of PMA into MIL-100 is detrimental to the structures of PMA@MIL composite, which is consistent with the previous report [590]. Moreover, no XRD peaks from PMA were observed regardless of the amount of PMA in PMA@MIL composite, suggesting that amount of PMA is too small to be detected by XRD, or PMA are fully confined in the pores of MIL-100 and completely shielded from the X-ray. FT-IR spectra (**Fig. 6.2B**) of all the PMA@MIL samples show the characteristic bands of MIL-100 and four notable characteristic bands of PMA located at 1060, 959, 878, 813 cm^{-1} respectively [591], revealing the successful introduction of PMA. It is worth noting that with the increasing amount of PMA in the PMA@MIL composite, the relative intensity of the characteristic peaks of PMA increases, though those characteristic peaks shift slightly due to the effect of the complex chemical environment of the MIL-100. Thermogravimetric analysis (TGA) curves of MIL-100 and PMo@MIL-100 samples carried out in air are presented in **Fig. 6.2C**. The residual weight of the samples increased with the amount of PMA introduced during the synthesis, indicating more PMA molecules, and therefore more Mo species were introduced into the PMA@MIL composites.

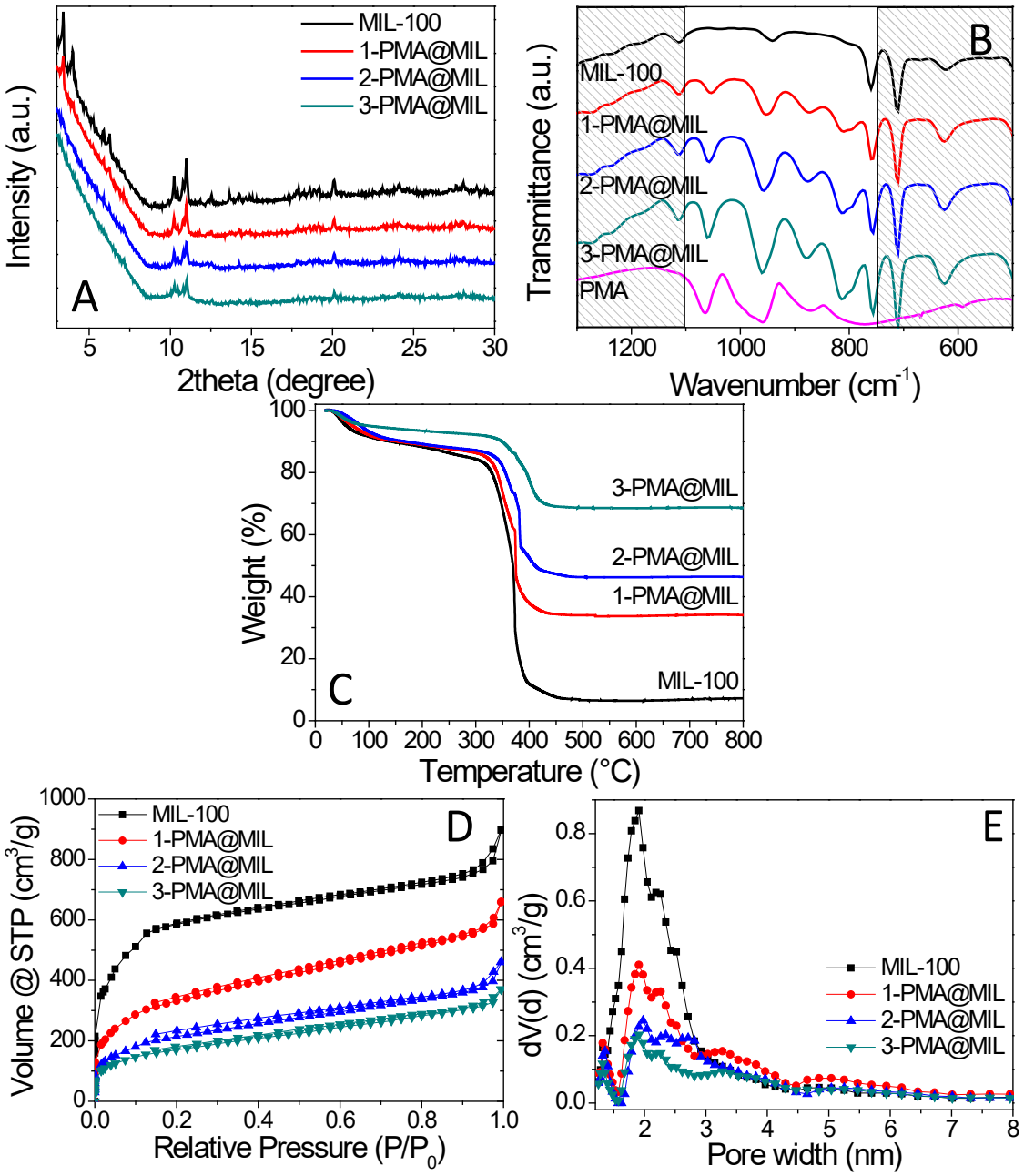

Fig. 6.2 A) XRD patterns, B) FT-IR spectra, C) TGA curves, D) Nitrogen sorption isotherms and E) pore size distribution of pristine MIL-100 and as-made PMA@MIL with different PMA contents. For comparison, the FTIR of pure PMA is also included in B).

Nitrogen sorption isotherm curves of the samples measured at 77 K are shown in **Fig. 6.2D**, and their textural properties are summarised in **Table 6.1**. The pristine MIL-100 sample shows the highest BET surface area of 1941 m^2 g^{-1}, while the PMA@MIL composites exhibit dramatically decreased surface area with the increased amount of PMA introduced. The composite 3-PMA@MIL with the highest PMA content display the lowest specific surface area of 619 m^2 g^{-1}. Pore size distribution (**Fig. 6.2E**) of the pristine MIL-100 displays a dominated peak at around 2-3 nm, while the PMA@MIL

composites exhibit fewer pores at around 2-3 nm due to the encapsulation of PMA in the pores of MIL-100. The total pore volumes of PMA@MIL also decrease remarkably compared to that of MIL-100 due to the blockage of pore channels by the encapsulated PMA as well as the added weight from the heavy PMA molecules. Both SEM images and TEM images (see **Fig. 6.3**) of pristine MIL-100 and 1-PMA@MIL do not show any significant difference in morphology and local structure. Moreover, the TEM elemental mappings for pristine MIL-100 and 1-PMA@MIL (**Fig. 6.4**) indicate the homogeneous distribution of all the elements in both samples.

Table 6.1 Textural properties of MIL-100 and PMA@MIL-100 samples.

Sample	MIL-100	1-PMA@MIL	2-PMA@MIL	3-PMA@MIL
Surface area ($m^2\ g^{-1}$)	1941	1213	795	619
Pore volume ($cm^3\ g^{-1}$)	1.39	1.02	0.71	0.57

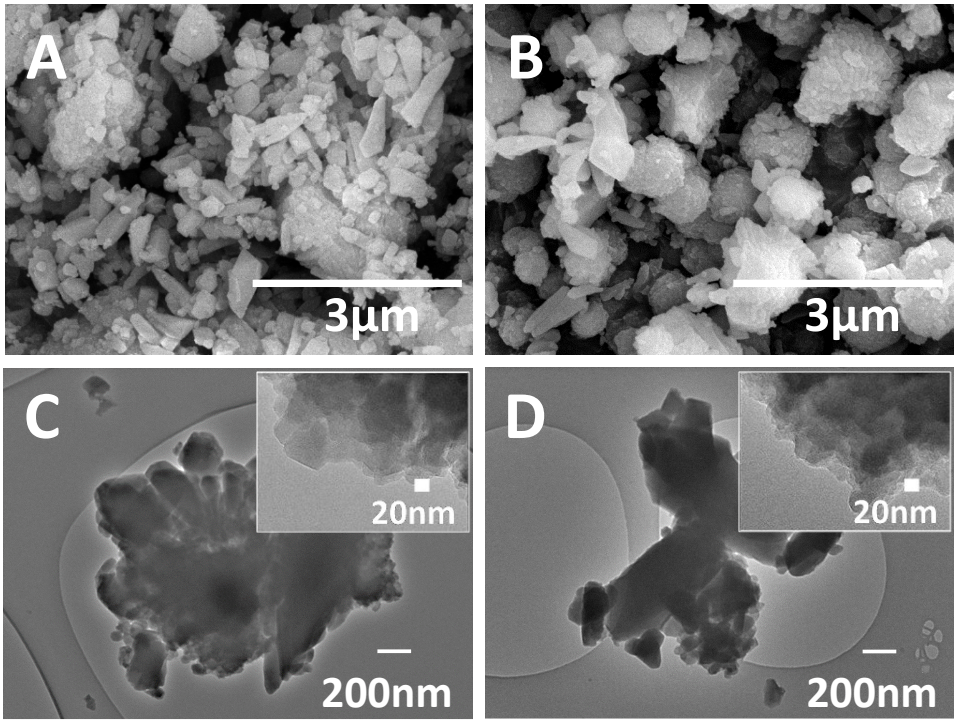

Fig. 6.3 Representative SEM images of as-made A) MIL-100 and B) 1-PMA@MIL, representative TEM images of as-made C) MIL-100 and D) 1-PMA@MIL.

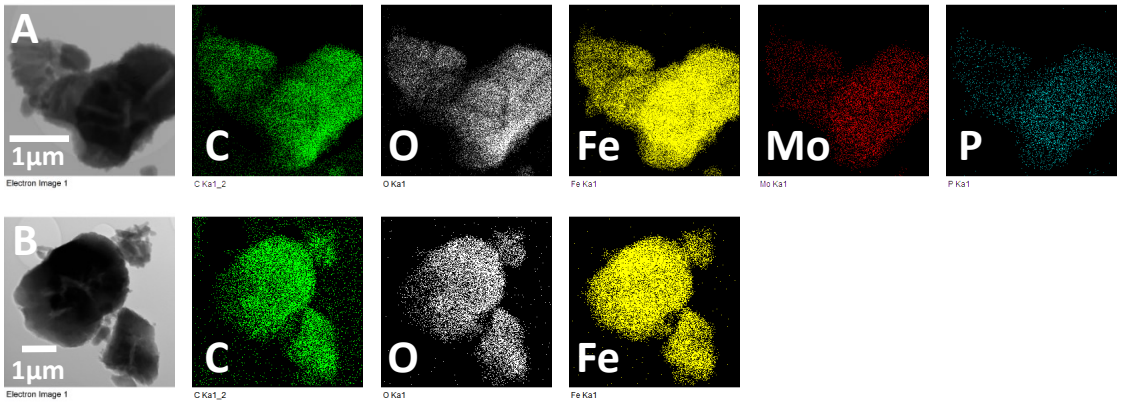

Fig. 6.4 TEM elemental mappings of A)1-PMA@MIL and B) MIL-100.

6.2.2 Characterization of the carbon-based composites derived from PMA@MIL-100

Fig. 6.5A shows the XRD patterns of the composites obtained via the pyrolysis of pristine MIL-100 and 1-PMA@MIL in H_2S atmosphere under three different temperatures: 600, 800 and 1000 °C. While the XRD for MIL-100 derived composites exclusively show characteristic diffraction peaks attributed to the Fe_7S_8 phase (PDF#71-0647), the XRD patterns for PMA@MIL derived composites are dominated by the Fe_7S_8 phase accompanied with diffraction peaks indexed to the MoS_2 phase (PDF#73-1508). Moreover, the XRD patterns of these composites exhibit sharper diffraction peaks at higher sulphurization temperatures, indicating that higher sulphurization temperature results in increased crystallinity. It is worth noting that the characteristic (002) peak of MoS_2 in composite 1Mo@MIL-1000 appears at 2θ of 14°, however this characteristic peak in composites 1Mo@MIL-600 and 1Mo@MIL-800 shift to around 11° with broad peak width; This may be due to the incomplete sulphurization of Mo species and the formation of amorphous MoS_2 nanoparticles under lower sulphurization temperatures.

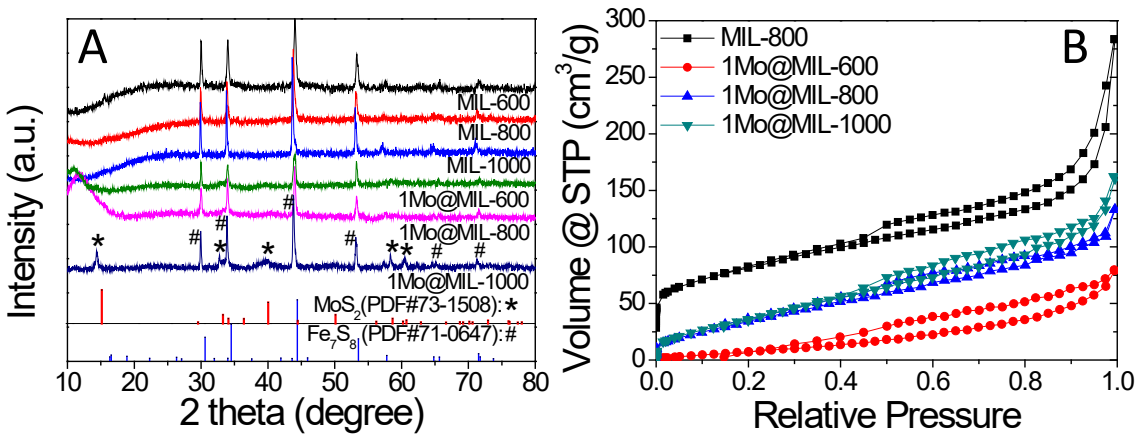

Fig. 6.5 XRD patterns of A) MIL-600, MIL-800, MIL-1000, 1Mo@MIL-600, 1Mo@MIL-800 and 1Mo@MIL-1000; B) N2 sorption isotherms of MIL-800, 1Mo@MIL-600, 1Mo@MIL-800 and 1Mo@MIL-1000.

Table 6.2 Textural properties of samples MIL-800, 1Mo@MIL-600, 1Mo@MIL-800 and 1Mo@MIL-1000.

Sample	MIL-800	1Mo@MIL-600	1Mo@MIL-800	1Mo@MIL-1000
Surface area ($m^2\ g^{-1}$)	289	39	141	143
Pore volume ($cm^3 g^{-1}$)	0.32	0.12	0.21	0.25

Fig. 6.5B presents the N_2 sorption isotherms of the PMA modified composites sulphurized at 600, 800 and 1000 °C, and also the sample MIL-100 sulphurized at 800 °C for comparison. All four samples show type IV isotherms, indicating the formation of a mesoporous structure after the sulphurization. 1Mo@MIL-800 possesses a surface area of 141 $m^2\ g^{-1}$, only half of that of MIL-800, which is likely due to the increased mass of the introduced Mo species. Among the 1-PMA@MIL derived composites, sample 1Mo@MIL-600 sulphurized under 600 °C shows the lowest BET surface area of 39 $m^2\ g^{-1}$ and lowest total pore volume of 0.12 $cm^3\ g^{-1}$, possibly owing to the incomplete carbonisation of the precursor. However, with the increase of sulphurization temperatures, the resulting composites exhibited enhanced BET surface area and total pore volume (see **Table 6.2**). Representative pore size distribution of 1Mo@MIL-800 (**Fig. 6.6**) shows that this material displays a wider size distribution that shifts toward a larger pore size compared with the parental 1-PMA@MIL, which may be due to the removal of oxygen and hydrogen from the MOF ligand resulting in the partial collapse of the smaller pores during the sulphurization and carbonisation of the MIL-100 framework.

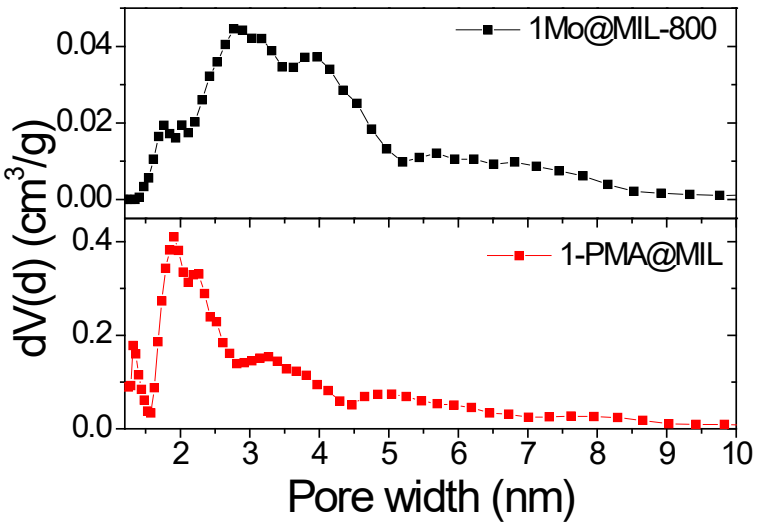

Fig. 6.6 Pore size distribution of 1Mo@MIL-800 and 1-PMA@MIL obtained using NLDFT model.

The TEM images of sample 1Mo@MIL-600, which derived from 1-PMA@MIL sulphurized at 600 °C, exhibit 2 to 4 atomic layers of MoS_2 crumbs evenly distributed throughout the amorphous carbon matrix (**Fig. 6.7A**). Meanwhile, it is challenging to identify iron sulphide within the matrix, possibly due to its small sizes and homogeneous distribution in the formed carbons. Black particles observed on the carbon matrix (see **Fig. 6.7A1 inset**) may be the free-standing iron species and elemental mapping in **Fig. 6.8A** indicates that these particles may be large iron sulphide particles. On the other hand, sample 1Mo@MIL-800 obtained at sulphurization of 800 °C displays thin flakes of 50 nm in diameter and 5-10 layers in thickness (**Fig. 6.7B1**) and small onion-like spheres with a size around 10 nm (**Fig. 6.7B2**) appear, which are evenly embedded in the carbon matrix. At 1000 °C, the flakes become larger in diameter and thickness (**Fig. 6.7C1**). The onion-like spheres also grow larger to size up to 50 nm (**Fig. 6.7C2**). By measuring the lattice spacing, it is found that with the increase of the sulphurization temperature, the d values change from 0.80 to 0.62 nm, which is in line with the wide XRD peak at around 11° of 1Mo@MIL-600/800 (**Fig. 6.5A**). Consistent with the pronounced sharp peak at 14° in 1Mo@MIL-1000, a lattice spacing of 0.62 nm is observed in the TEM image (**Fig. 6.7C2**), which belongs to the (002) plane of MoS_2. In addition, thin flakes of lighter colour are also observed in both 1Mo@MIL-800/1000 (see **Fig. 6.7B1 and C1**). The lattice spacing is shown in the inserts of **Fig. 3B2 and C2,** and a measured lattice spacing is 0.26 nm, which belongs to the (203) plane of Fe_7S_8, indicating the presence of the Fe_7S_8 nanocrystals within the carbon matrix. The TEM elemental mapping of the three samples

(**Fig. 6.8**) shows that all the elements (Fe, Mo, S, C and O) are homogeneously distributed throughout the samples.

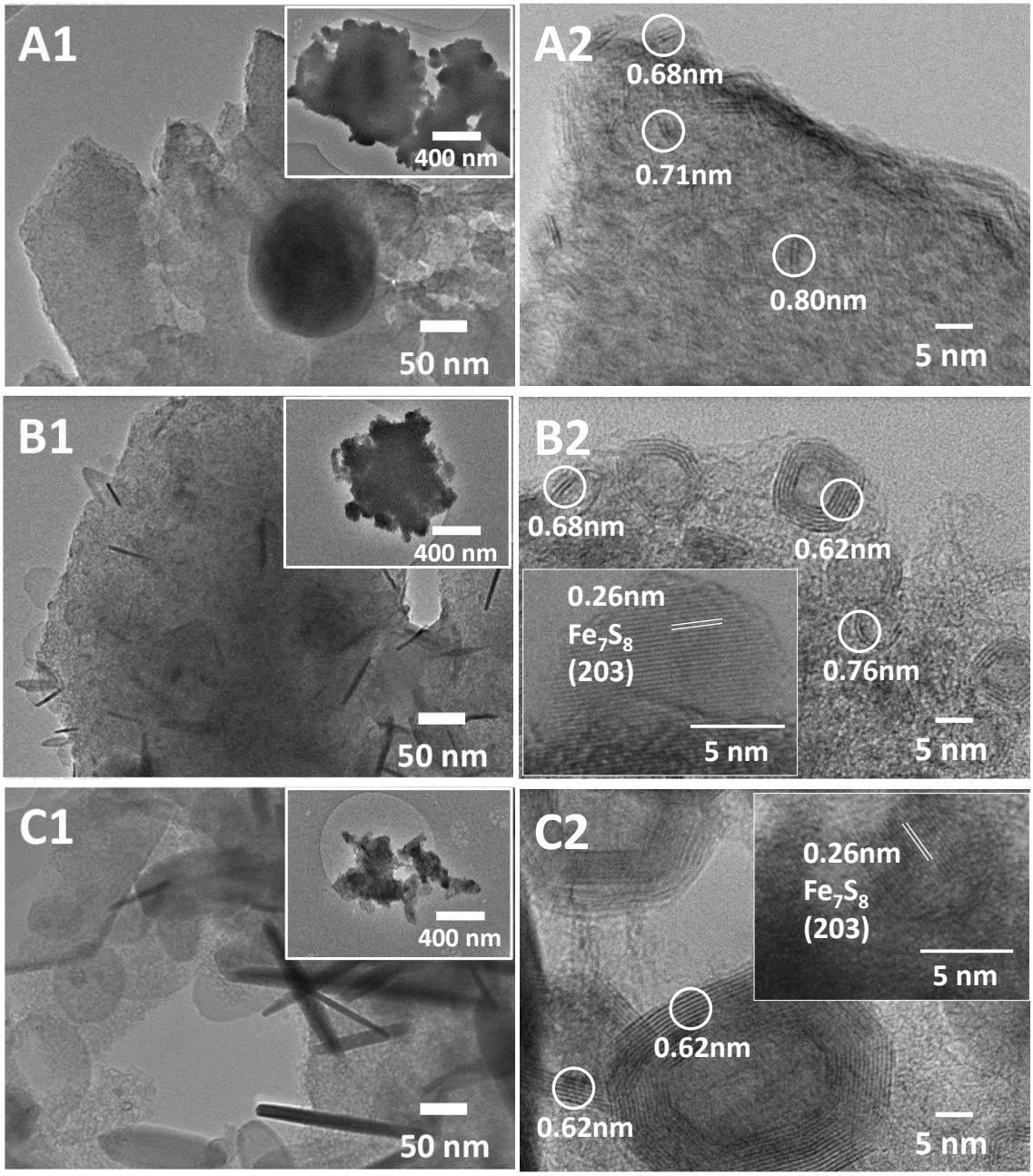

Fig. 6.7 TEM images of 1-PMA@MIL sulphurized at A) 600°C, B) 800°C and C) 1000°C.

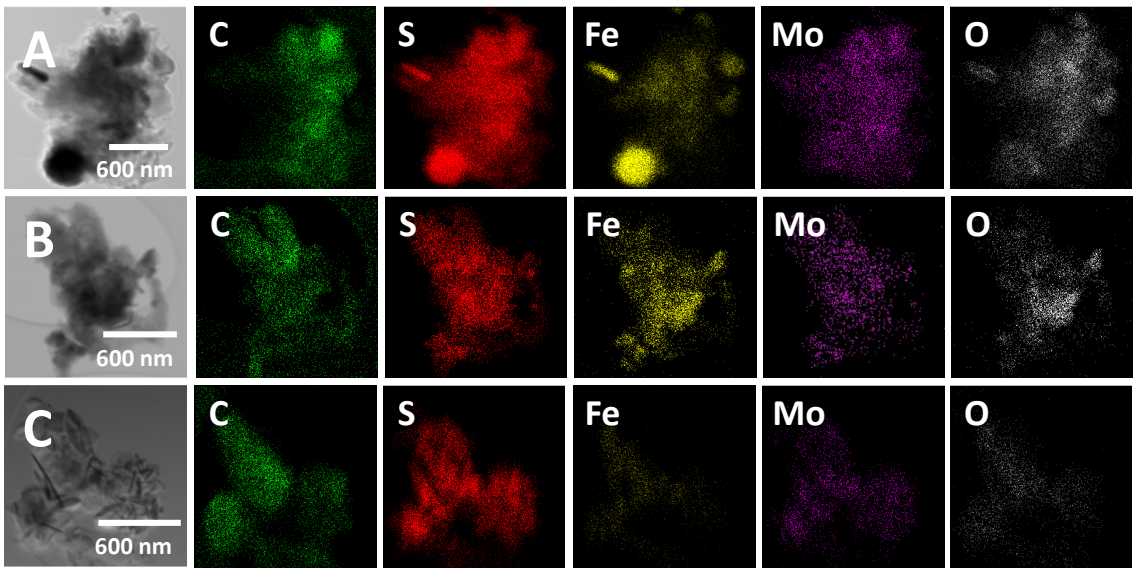

Fig. 6.8 Elemental mappings of A) 1Mo@MIL-600, B) 1Mo@MIL-800 and C) 1Mo@MIL-1000.

SEM images of the sulphurized MIL-100 and 1-PMA@MIL at 600, 800 and 1000 °C are presented in **Fig. 6.9**. In general, all the samples exhibit irregularly shaped particle morphologies. The composites derived from both the pristine and the PMA encapsulated precursors at low sulphurization temperature show no observable difference in morphology (**Fig. 6.9A and D**). However, the SEM image for 1Mo@MIL-800, which was obtained at sulphurization temperature of 800 °C, exhibits tiny flakes covered on the surface of the particles resulting in a rough surface (**Fig. 6.9B**), while the flakes tended to grow to larger sizes up to 500 nm when the sulphurization temperature increases to 1000 °C (**Fig. 6.9C**). In contrast, the samples derived from pristine MIL-100 sulphurized at 800 and 1000 °C did not show any visible flakes on the particle surfaces (**Fig. 6.9E and F**). This observation indicates that the thin flakes are likely to be the MoS_2 particles from the sulphurization of PMA under high temperatures, which is consistent with XRD results in **Fig. 6.5A**.

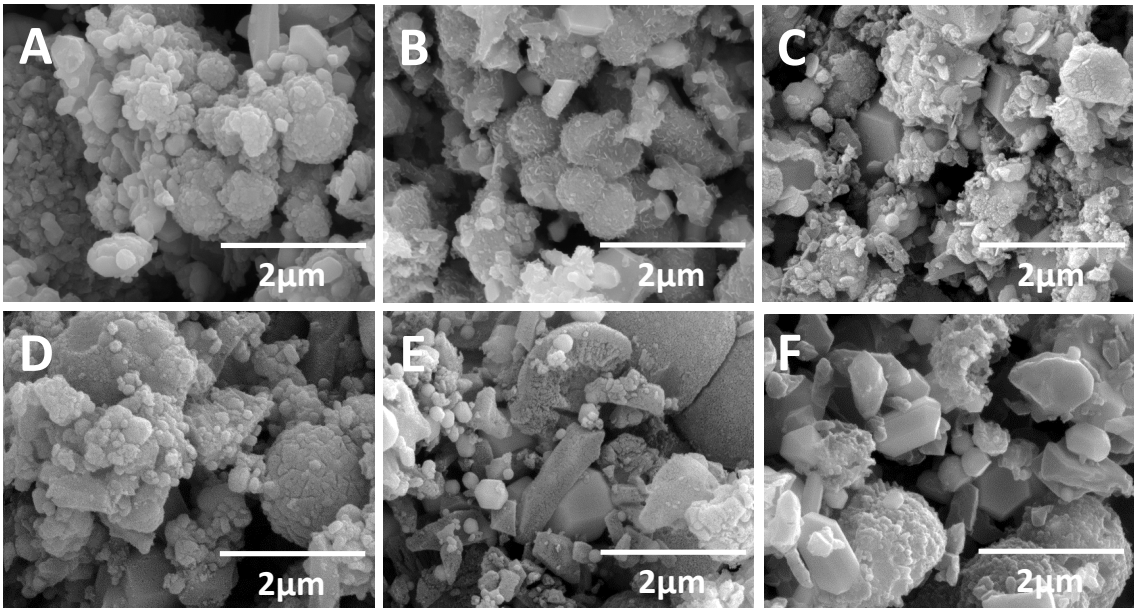

Fig. 6.9 SEM images of 1-PMA@MIL sulphurized at different temperatures: A) 600 °C, B) 800 °C and C) 1000 °C; and pristine MIL-100 sulphurized at different temperatures D) 600 °C, E) 800 °C and F) 1000 °C.

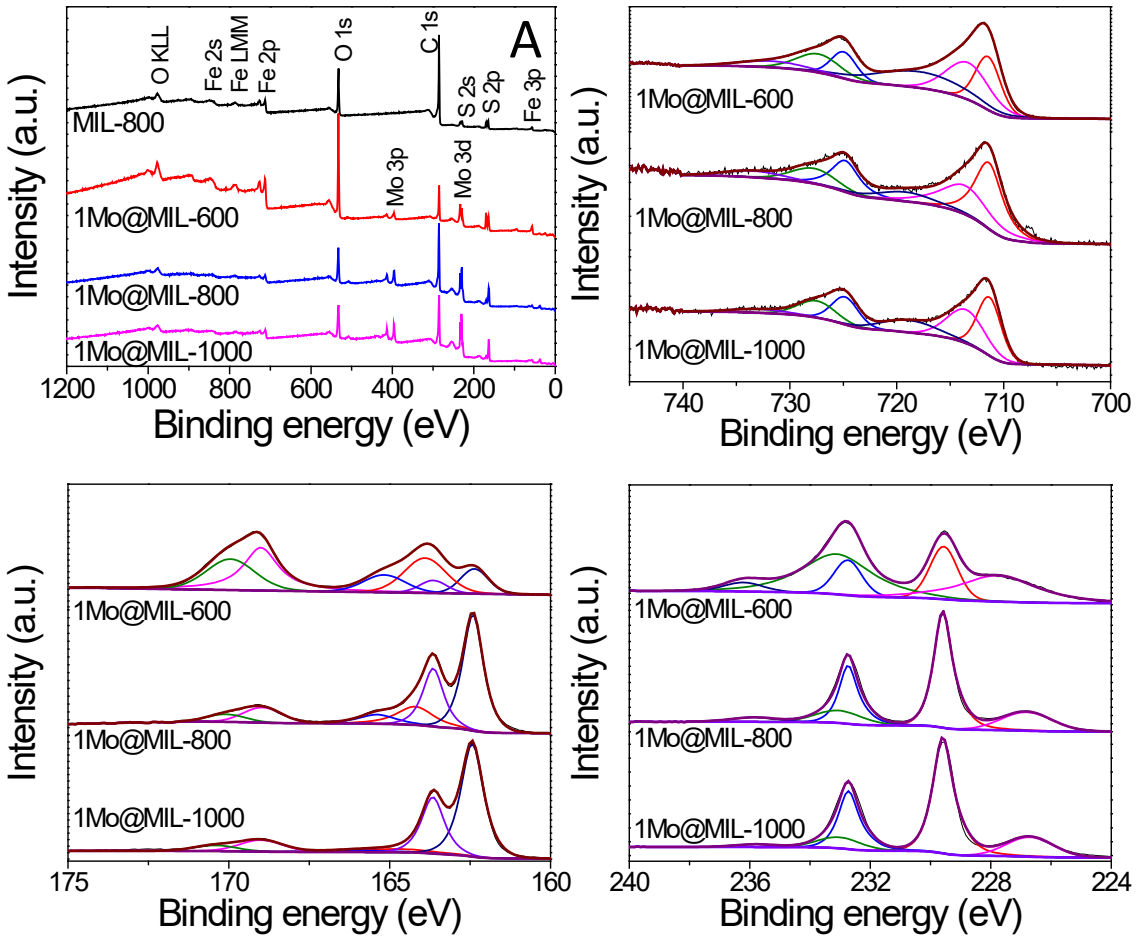

Fig. 6.10 A) XPS element survey and high-resolution XPS spectra of B) Fe 2p, C) S 2p and D) Mo 3d.

The elements and their chemical status of samples MIL-800 and 1-PMA@MIL that are sulphurized at different temperatures are studied by XPS. The element survey spectra inclusively confirm the existence of Fe, O, S and C in all four samples (**Fig. 6.10A**), but the 1-PMA@MIL derived samples show the presence of Mo, which is as expected and in good agreement with the above XRD and TEM results.

The high-resolution XPS spectra of Fe 2p for the three samples derived from the sulphurization of 1-PMA@MIL at different temperatures show two main peaks, with each one deconvoluted into three peaks (**Fig. 6.10B**). Peaks around 711.4/724.8 eV are attributed to the Fe $2p_{3/2}$ and Fe $2p_{1/2}$ of Fe^{2+} species with 13.4 eV of peak separation [592, 593], while the other pair of peaks located at 713.6/727.7 eV are ascribed to the Fe $2p_{3/2}$ and Fe $2p_{1/2}$ for Fe^{3+} species [594-596]. The last pair of peaks at around 719.1/733.5 eV are the shakeup satellite peaks of Fe $2p_{3/2}$ and Fe $2p_{1/2}$ [595, 596]. These results are consistent with the previous report [592]. Compared with sample MIL-800, sample 1Mo@MIL-800 exhibit a slight increase in binding energy of the Fe $2p_{3/2}$ and Fe $2p_{1/2}$ peaks (**Fig. 6.11**), suggesting a strong interaction between Fe_7S_8 and MoS_2 particles and the possible formation of Fe-Mo-S species; This will benefit their catalytic applications since previous reports found that the formation of M-Mo-S phase (M stand for metal such as Co, Ni and Fe) can reduce the energy barriers for the catalytic reaction and enhance the activity toward HER [577, 597, 598].

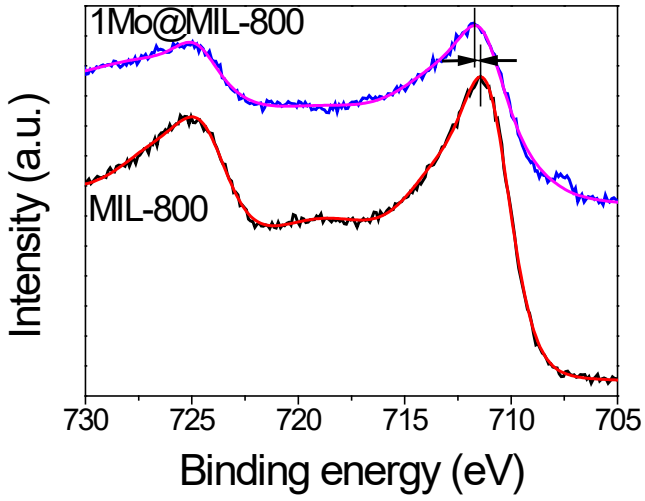

Fig. 6.11 High-resolution XPS spectra of Fe 2p for sample 1Mo@MIL-800 and MIL-800.

The high-resolution S 2p XPS spectra of the three samples derived from 1-PMA@MIL sulphurized at different temperatures is presented in **Fig. 6.10C**. The peaks at around 162.4/163.6 eV correspond to S $2p_{3/2}$ and S $2p_{1/2}$ of the S^{2-} species, which are originated from the Fe_7S_8 [599] and MoS_2 [600] composition in the composites. In addition, the

peaks at around 168.9/170.0 eV are the pair signals of the S $2p_{3/2}$ and S $2p_{1/2}$ for SO_x species [601]. It is believed that this is due to the surface oxidation of the samples as well as the possible intermediate product (see previous XRD and TEM analysis) in the sample obtained at lower sulphurization temperature, i.e. 1Mo@MIL-600. Increasing the sulphurization temperatures, the amount of oxidised species in the resulting samples decrease dramatically. The paired S 2p peaks at around 164.2/165.3 eV are due to the doping of S species into the carbon matrix in the form of C-S-C and/or C=S, respectively [602]. The doping of S in the carbon matrix may introduce active sites favourable for HER [603]. However, this doped S species in the composite decrease with the increase of the sulphurization temperature. Actually, no doped S species can be identified in sample 1Mo@MIL-1000.

The high-resolution XPS spectra of Mo 3d are shown in **Fig. 6.10D**. The first peak at the lower energy end of the spectra is assigned to the S 2s peak due to the overlap region of Mo 3d and S 2s spectra. The intense pair of peaks at around 229.6/232.7 eV for all the three samples are originated from Mo $3d_{5/2}$ and Mo $3d_{3/2}$ of Mo^{4+} state in MoS_2 [604]. Moreover, two doublets at around 233.0/235.8eV in sample 1Mo@MIL-600 are attributed to Mo $3d_{5/2}$ and Mo $3d_{3/2}$ of Mo^{6+} state of the molybdenum species, but those peaks are negligible or virtually disappeared in sample 1Mo@MIL-800 and 1Mo@MIL-1000. Obviously, the intensity of binding energy of those Mo^{6+} species decreases with increased sulphurization temperature [605], which is, as discussed earlier, possibly due to the surface oxidation of the molybdenum to form intermediate product during the process of MoS_2 generation.

6.2.3 Electrochemistry performance evaluation

The electrochemical hydrogen evolution reaction (HER) performance of all the samples derived from sulphurized MIL-100 and 1-PMA@MIL under different temperatures are presented in Fig. 6, and relevant HER data are summarised in **Table 6.3**. The composite derived from sulphurization of pristine MIL-100 at higher temperatures exhibits improved HER activities in acidic media (**Fig. 6.12A**). With the introduction of Mo species, all three composites derived from the sulphurization of 1-PTA@MIL under different temperatures exclusively show a dramatic increase of the onset potential in HER compared to those samples derived from the sulphurized MIL-100 under the same conditions. Moreover, the HER activity of sample 1Mo@MIL-800 is much higher than that of samples 1Mo@MIL-1000 and 1Mo@MIL-600. Actually, sample 1Mo@MIL-800 exhibits the lowest onset potential of -0.241 V (vs. RHE at current density of -1 mA cm^{-}

^{2}) and requires the lowest overpotential of -0.321 V (vs. RHE) to achieve the current density of -10 mA cm^{-2}, indicating that 1Mo@MIL-800 composite is the highest HER active sample amongst all the studied composites. It is worth noting that, as shown in **Table 6.3**, the Mo-containing samples 1Mo@MIL-800 and 1Mo@MIL-1000 exhibit a remarkable decrease in the onset potential for HER of 0.251 and 0.348 V compared with their Mo-free counterpart MIL-800 and MIL-100, respectively. These results indicate that new catalytic active sites may originate from the introduced MoS_2, the dual metallic Fe-Mo-S phase, as well as S-doped carbon (as confirmed in XPS analysis) in the composites, which result in the significant improvement in electrocatalytic HER activities of the bimetallic Fe-Mo sulphide/carbon systems. Nevertheless, the HER performances of these composites are generally still inferior to the benchmark 20% Pt/C sample.

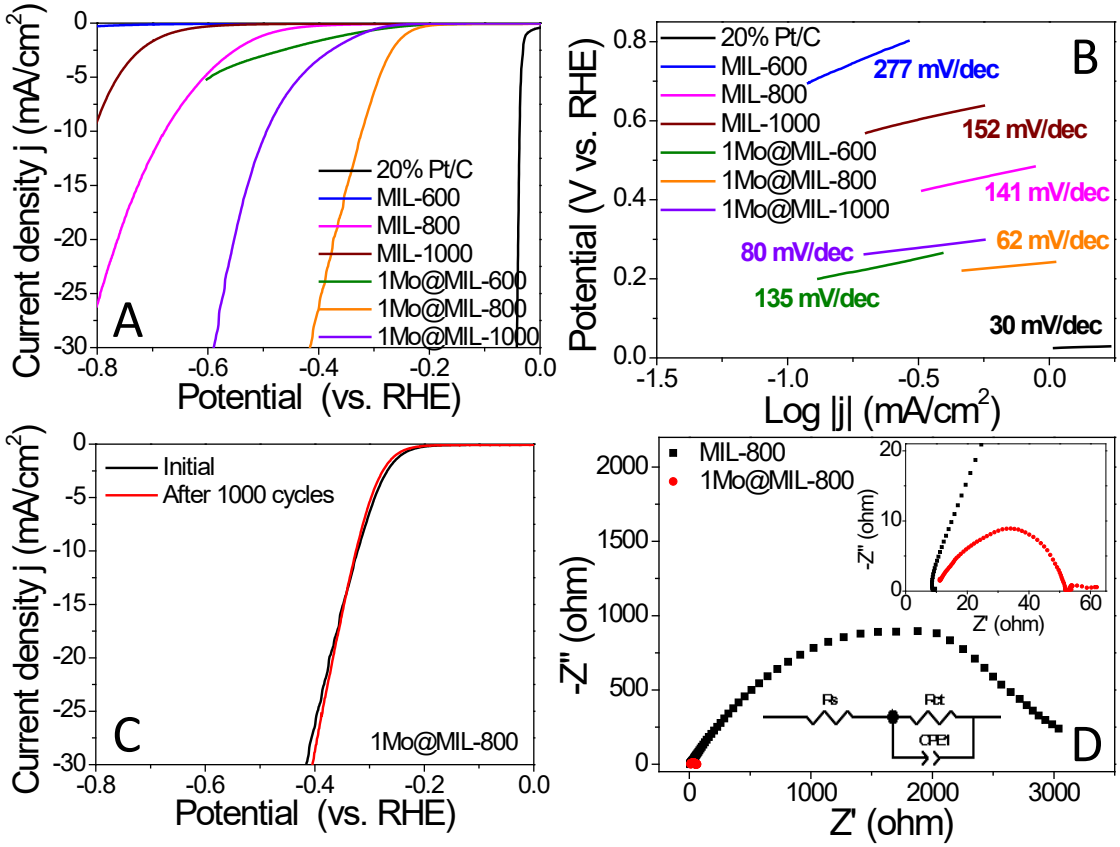

Fig. 6.12 A) HER polarization curves of MIL-600, MIL-800, MIL-1000 and 1Mo@MIL-600, 1Mo@MIL-800, 1Mo@MIL-1000 and B) The corresponding Tafel plots of the samples presented in A). C) Polarization curves of 1Mo@MIL100-800 before and after 1000 cycles and D) EIS of MIL-800 and 1Mo@MIL-800. 0.5 M H_2SO_4 was used as electrolyte, all polarization curves are iR corrected. EIS spectra recorded at -0.6 V (vs. Ag/AgCl), measured in the frequency range of 10^{-1}-10^{5} Hz.

Table 0.3 Summary of the electrochemical HER performance data of different samples.

Sample	Onset potential @-1 mA cm^{-2} (V vs. RHE)	Overpotential @-10 mA cm^{-2} (V vs. RHE)	Tafel slope (mV dec^{-1})
MIL-600	-[1]	-[1]	277
MIL-800	-0.492	-0.678	141
MIL-1000	-0.670	-0.807[2]	152
1Mo@MIL-600	-0.342	-[1]	135
1Mo@MIL-800	-0.241	-0.321	62
1Mo@MIL-1000	-0.322	-0.493	80
20% Pt/C	-0.024	-0.037	30

[1] The current density could not reach -10 mA cm^{-2} within the potential window.

[2] Value obtained by extrapolation of the curve.

Tafel plots derived from the HER polarization curves of the samples are presented in **Fig. 6.12B**, and the corresponding values of Tafel slope are labelled in the plots. The three Mo-free samples, MIL-600, MIL-800 and MIL-1000, show Tafel slope of 277, 141 and 152 mV dec^{-1}, respectively, indicating poor reaction kinetics of these samples. In contrast, all the Mo-containing samples exclusively exhibit much reduced Tafel slope values, suggesting faster reaction kinetics of these bimetallic Fe-Mo sulfide/carbon composites in electrocatalytic HER performance in acidic media. It is noteworthy that among all the studied composites, sample 1Mo@MIL-800 exhibit the smallest Tafel slope value of 60 mV dec^{-1}, implying the best HER performance amongst all the studied samples. It is widely accepted that an HER process includes Volmer step, Heyrovsky step or Tafel step, and both the Volmer-Heyrovsky and the Volmer-Tafel mechanisms lead to the formation of H_2 [606]. It is believed that as a rate-determine step, Tafel slope value of ca. 30, 40 and 120 mV dec^{-1} is required for the Tafel step, Heyrovsky step and Volmer step, respectively [495]. Therefore, the HER process of sample 1Mo@MIL-800 possess a Volmer-Heyrovsky mechanism, and the electrochemical recombination is the rate-determination step during the HER process [607, 608].

For overall water splitting, the performance of the catalyst in different pH media is essential. Therefore, the sample1Mo@MIL-800 with the highest HER activity in acidic media was further evaluated in alkaline and neutral media, respectively (**Fig. 6.13**). This

catalyst needs an overpotential of -0.452 V in 1 M KOH and -0.772 V in 0.5 M Na_2SO_4 to achieve a current density of -10 mA cm^{-2}, which is 0.130 V and 0.451 V higher than that in acidic solution. Clearly, the HER performance of the composite in acidic solution is better than that of in alkaline or neutral solution. It is also clear that the HER performance of 1Mo@MIL-800 in both alkaline and acid solutions shows a remarkable improvement compared with the Mo-free composite MIL-800 under the same conditions.

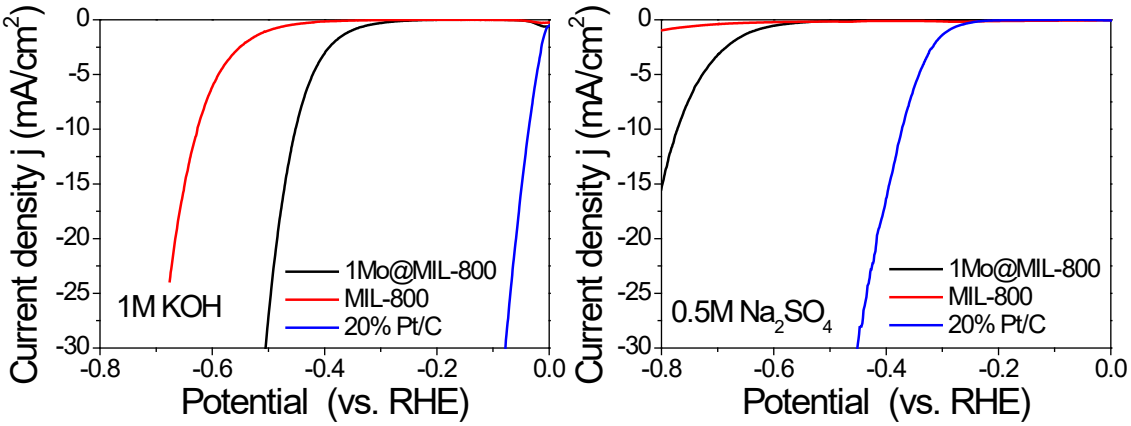

Fig. 6.13 HER polarization curves of MIL-800, 1Mo@MIL-800 and 20% Pt/C in A) 1 M KOH electrolyte and B) 0.5 M Na_2SO_4 electrolyte.

It was reported that when Pt is used as the counter electrode during the HER test, it could transfer to the working electrode and affects the catalytic performance of the measured sample [609], we therefore validated the HER test of the best-performed sample, 1Mo@MIL-800 using graphite rod instead of Pt wire as the counter electrode. As shown in **Fig. 6.14A**, there is no obvious difference in the HER performance when using graphite rod as the counter electrode, compared with Pt wire electrode. Even after 1000 cycles test using the graphite rod as the counter electrode, the HER performance of the composite largely remains unchanged, indicating the use of different counter electrodes has a negligible effect on the electrocatalytic performance of the composite.

The stability of the best performed composite 1Mo@MIL-800 was evaluated by comparing the LSV curves before and after 1000 cycles of measurements. The result in **Fig. 6.12C** shows a negligible decay of current density after 1000 cycles of HER tests, indicating excellent stability of this composite. Moreover, the time dependence on the current curve of this sample (**Fig. 6.14B**) displays that the current density only decreased slightly after 8000 s of testing in HER, suggesting good stability of the catalyst under the studied constant voltage.

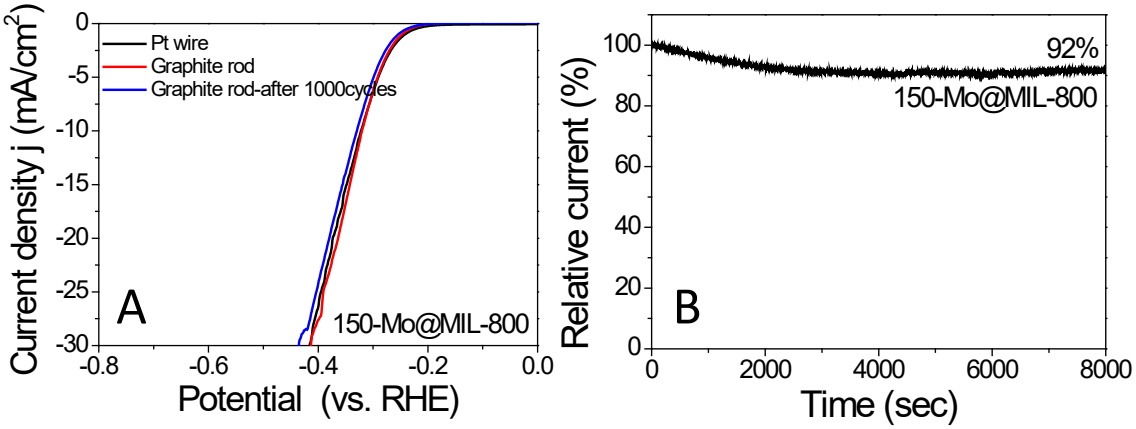

Fig. 6.14 A) HER polarization curves of 1Mo@MIL-800 using Pt wire and graphite rod as counter electrode and LSV before and after 1000 cycles using graphite electrode. B) Current-time chronoamperometric response of 1Mo@MIL-800 at -0.5 V in 0.5 M H_2SO_4 solution.

The electrochemical impedance spectroscopy (EIS) of 1Mo@MIL-800 was further analysed in the frequency range of 10^5 to 0.1 Hz at -0.6 V (vs. RHE), and the EIS of MIL-800 was also included for comparison. The Nyquist plots in **Fig. 6.12D** exhibit semi-circle shapes. Both samples can be modelled by an electric circuit consist of a series resistance (R_s), a constant phase element (CPE), and a charge-transfer resistance (R_{ct}), as shown in the insert of **Fig. 6.12D**. The value of R_{ct} can be calculated from the diameter of the semi-circle at high frequency in the Nyquist plot, and the smaller the value of R_{ct}, the higher the charge transfer rate, therefore the faster the interfacial kinetics and the better performance of the composite. Based on the curve fitting, the value of R_{ct} for sample 1Mo@MIL-800 is 48 Ω which is much smaller than that of sample MIL-800 (3491 Ω), indicating that the presence of MoS_2 generates catalytically active sites and the formation of Fe-Mo-S species in the composite dramatically promote faster interfacial kinetics [610].

As discussed above, the pyrolysis temperatures of the precursor remarkably affect the HER performance of the resulting materials. Other parameters such as the amount of PMA in the precursor, the heating ramp rate to the target sulphurization temperature, and the sulphurization duration that can potentially influence the electrocatalytic HER activities of the resulting materials were also explored.

The effect of the amount of PMA in the precursor on the XRD patterns of the composites obtained via pyrolysis of pristine MIL-100 and PMA@MIL at 800 °C in H_2S atmosphere was presented in **Fig. 6.15A**. While MIL-800 only exhibits the diffraction peaks that can be indexed to iron sulphide phase like Fe_7S_8 (PDF#71-0647), all the three composites derived from PMA@MIL with different PMA content show characteristic

peaks that are indexed to Fe_7S_8 and MoS_2 (PDF#73-1508), suggesting the formation of Fe-Mo bimetallic sulphides in the composites. Moreover, the relative intensity of the peaks indexed to the MoS_2 phase in the composites increases with the amount of introduced PMA in the precursor. While the characteristic (002) peak of MoS_2 phase in composite 3Mo@MIL-800 and 2Mo@MIL-800 that derived from higher PMA content precursor appears at 2θ of 14°, but the characteristic peaks in composite 1Mo@MIL-800, which is derived from lower PMA content precursor, shifts to lower 2θ range of 11° with broader peak. In addition, element content obtained from SEM-EDX also confirmed that with the increased amount of PMA introduced into the precursor, the resulting sample Mo@MIL-800 exhibited increased Mo content in the composites (**Table 6.4**).

Table 6.4 Element content of sample Mo@MIL-800 obtained from SEM-EDX analysis.

Sample	Element content (wt %)				
	C	**O**	**S**	**Fe**	**Mo**
1Mo@MIL-800	38.1	23.6	16.2	14.6	7.4
2Mo@MIL-800	35.3	8.8	22.8	16.4	16.7
3Mo@MIL-800	25.2	7.1	25.3	17.4	22.2

The HER performance of the composites with variable molybdenum content in the Mo@MIL-800 samples is also evaluated and presented in **Fig. 6.15B** and **C**. Obviously, with the increase of the Mo content in Mo@MIL-800 composites, their catalytic activities actually decrease. The overpotential to achieve a current density of -10 mA cm^{-2} decreases from -0.321 V for sample 1Mo@MIL-800, to –0.482 V for sample 3Mo@MIL-800, and the Tafel slope value increases from 60 mV dec^{-1} for sample 1Mo@MIL-800 to 127 mV dec^{-1} for sample 3Mo@MIL-800, which almost doubles the value of 1Mo@MIL-800 composite. These results imply that the increased amount of Mo content in the Mo@MIL-800 composites deteriorates their HER performance, which may be due to the agglomeration of MoS_2 at higher amount, leading to the hindering of the access to the catalytic active sites in the composite.

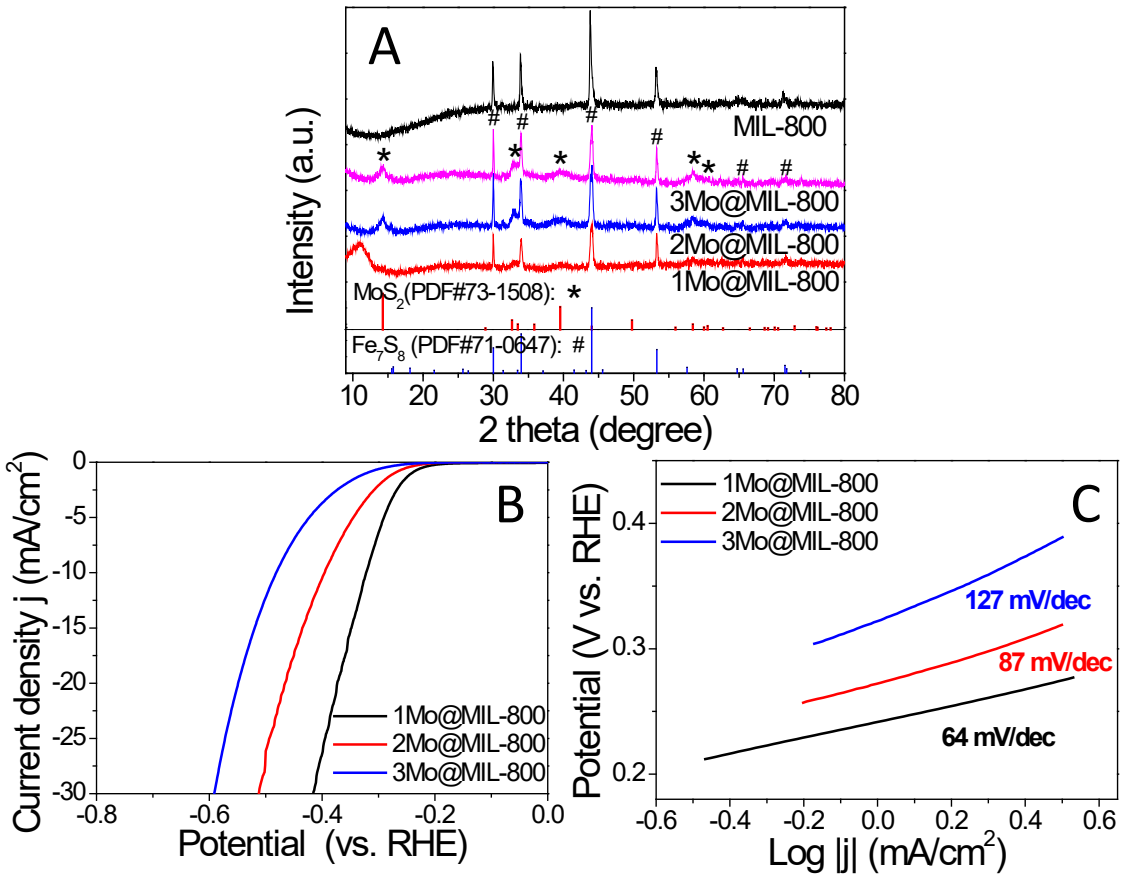

Fig. 6.15 A) Power XRD patterns, B) HER performance and C) the corresponding Tafel plots of Mo@MIL-800 with variable Mo content. In the HER measurement in B), 0.5 M H_2SO_4 was used as electrolyte, and all polarization curves are iR corrected.

The effect of heat ramp rate on the sulphurization temperature, and the sulphurization duration on the electrocatalytic performances of the samples, have also been studied. **Fig. 6.16A** and **B** show the XRD patterns of samples obtained at different heating ramp rates (10 or 2 °C min^{-1}) and sulphurization time (20 min or 2 h in H_2S gas, or 1 h in Ar followed by 1 h in H_2S). All samples exclusively exhibit XRD diffraction peaks indexed to both Fe_7S_8 and MoS_2 phases. With a slower heating ramp rate, the diffraction peaks for MoS_2 become more pronounced, and the broader peak at lower 2θ angle disappears, indicating a better crystallinity and well established MoS_2 lattice structure under a slow heating ramp rate. As for the effect of sulphurization time on the XRD patterns of resulting samples, there is no visible difference between the sample obtained in H_2S for 2 h and the one in Ar for 1 h followed by in H_2S for 1 h. However, the sample sulphurized for only 20 min in H_2S shows a broad peak at lower 2θ angle, suggesting the incomplete sulphurization of Mo species and the formation of amorphous MoS_2 nanoparticles.

The HER polarization curves (**Fig. 6.16C**) indicate that the sample obtained via a slower heating rate exhibits slightly inferior HER performance than the sample prepared from a faster heating ramp rate. This is possible due to the fact that electrocatalytic HER active sites are located on the defects and exposed edges of metal sulphides [495], and a slower heating rate provide higher opportunities for the metal sulphide to establish its crystallinity [611], which result in less exposed active sites and consequently unsatisfactory HER performance. On the other hand, the change of sulphurization time does not cause a significant difference in the HER performance (**Fig. 6.16D**), indicating that the sulphurization time is not a major factor that affects the electrocatalytic HER activity of the composites.

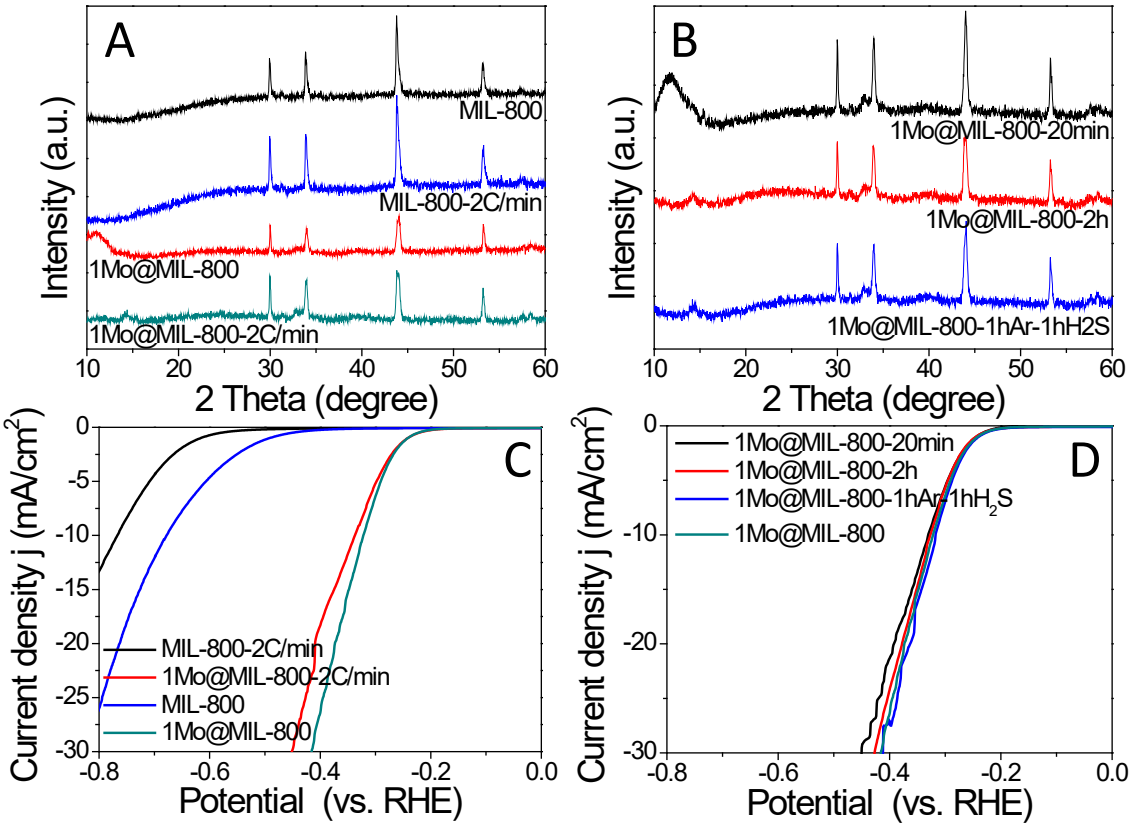

Fig. 6.16 Effect of pyrolysis ramp rate and durations on the structures and HER performance. A) XRD and C) HER polarization curves of MIL-800 and 1Mo@MIL-800 obtained via pyrolysis at 800 °C for 1 hour with ramp rate 10°C/min and 2 °C/min respectively; B) XRD and D) HER polarization curves of 1Mo@MIL-800 obtained via pyrolysis at 800 °C in H_2S atmosphere for 20 min, 1 hour, 2 hours and 1 hour in Ar plus 1 hour in H_2S. All polarization curves are iR corrected.

6.3 Summary

In summary, we have successfully fabricated bimetallic Fe-Mo sulphide/S-doped carbon nanocomposites from PMA@MIL precursors. Nanosized metal sulphide crystals are homogeneously embedded in the porous carbon matrix, leading to significant improvement in HER activities under acidic condition. In particular, composite 1Mo@MIL-800 exhibits an overpotential of -0.321V to realise a current density of -10 mA cm^{-2} and a Tafel slope of 62 mV dec^{-1}, which shows a 53% reduction in overpotential to achieve the same current density compared with Mo-free composite MIL-800. This dramatic improvement in HER performance of the PMA@MIL derived nanocomposites can be attributed to (1) large amount of active sites are introduced by the evenly distributed nanosized MoS_2 throughout the carbon matrix; (2) strong interactions are formed between the two metallic sulphides, forming Fe-Mo-S phases that are favourable for HER and (3) more HER active sites have been created by S-doping in the carbon matrix. Moreover, the Fe-Mo sulphide/carbon composites are electrocatalytic active for HER not only in acidic media but also in alkaline and neutral media. In addition, It was also found that although the sulphurization time of the composites does not affect the HER performance, both higher Mo amount and higher heating ramp rate for the composites lead to deteriorated HER performance. This work offers a feasible way to generate complex heterogeneous electrocatalytic composites with great potential for diverse applications.

Chapter 7 Conclusions and future work

7.1 Conclusions

In this thesis, novel ZIF-based composites and their nanostructured derivatives have been designed and synthesised; electrochemical performance of the produced materials has also been evaluated. The crystal structures, textural properties and morphologies of the as-synthesised ZIFs-based/MOFs-based composites and their derivatives were characterised using combined techniques. In addition, the significantly improved performance of the as-derived carbon-based nanocomposites in energy applications such as HER and OER was thoroughly discussed and compared with relevant reference samples. Furthermore, the correlation between the properties and structures of materials are linked.

The proposed objectives have been achieved: tungsten and molybdenum, the convention backbone modification unachievable metal species, have been successfully introduced into the cages of ZIFs through two novel approaches: one-pot in situ hydrothermal synthesis and post-synthetic modification. The difficulty of adapting acidic guest species into the acid vulnerable ZIFs has been addressed by carefully balancing the amount of POMs used during the synthesis or introducing a layer of PDA as the protective coating. Followed by heat treatment of the composites under H_2S/Ar atmosphere at certain temperatures, a series of bimetallic transition metal sulphides /heteroatoms-doped porous carbon nanocomposites, with evenly dispersed metal component particles and a large number of exposed active sites, were obtained. Moreover, the encapsulation strategy and chemical vapour sulphurization has been extended to a cage-type MOF, MIL-100. The PMA@MIL-100 composites have led to dual metallic Fe-Mo sulphide@carbon nanocomposites, which proves the universality of the developed synthesis approach. In details:

In Chapter 4, a facile one-pot in situ synthesis of PTA@ZIF-67 followed by one-step carbonisation and sulphurization was presented. By immobilising PTA molecular clusters within the confined space of ZIF-67 cages and the successive heat treatment at high temperatures under the H_2S atmosphere, a homogeneous dispersion of tungsten sulphide and cobalt sulphide particles within a carbon matrix can be achieved. The resulting bimetallic Co-W sulphide/heteroatom doped porous carbon composites exhibit a prominent improvement in HER with a Tafel slope of 64 mV dec^{-1} and an overpotential of -0.250 V (vs RHE) at the current density of 10 mA cm^{-2}. Moreover, the bimetallic Co-

W sulphide/porous carbon composites also demonstrated excellent OER activities with Tafel slope of 53 mV dec^{-1} and an overpotential of 0.365 V (vs RHE) at the current density of 10 mA cm^{-2}, out-performing the benchmark IrO_2 catalyst. This work offers a new strategy to prepare homogeneous transition metal sulphide decorated porous carbon nanostructures and open up a new way to obtain low-cost bifunctional electrocatalysts towards both OER and HER.

In Chapter 5, PTA was introduced into ZIF-67 with a different approach. Moreover, PMA, a molybdenum-containing POM that is unable to be introduced into ZIF-67 with the method mentioned in Chapter 4, has been successfully encapsulated into modified ZIF-67 in this chapter. HER and OER active, defect-rich ultra-fine bimetallic Co-Mo sulphide nanoparticles supported on N, S-doped porous carbon composites were derived from PMA@ZIF-67@PDA nanocube precursors via carbonisation/sulphurization. PDA decorating on ZIF-67 cubes can prevent the over-dissociation of ZIF-67 from PMA etching by chelating with the PMA molecules and acts as an additional N source for N-doping. Moreover, the partially dissociated Co^{2+} from ZIF-67 can be captured by the coated PDA via chelation, resulting in more evenly dispersed active sites throughout the heterogeneous composite after pyrolysis. The resulting bimetallic CoMoS-600 composite exhibits remarkable improvement in HER (with overpotential of -0.235 V vs. RHE at current density of 10 mA cm^{-2} and Tafel slope of 65.50 mV dec^{-1}) and OER performance (with overpotential of 0.350 V vs. RHE at current density of 10 mA cm^{-2} and Tafel slope of 64.32 mV dec^{-1}). The outstanding performance can be attributed to the synergistic effect of ultra-fine and defect-rich Co-Mo-S nanoparticle exposed active sites and N, S-doped porous carbons in the composites. Moreover, HER and OER active W-containing bimetallic Co-W-S/C composites can be readily obtained by replacing PMA with PTA, proving the universality of this synthesis approach. This work offers a new synthesis strategy to modify acid-sensitive ZIFs with acidic compounds, providing an alternative approach to develop other advanced metal sulphides/porous carbon functional materials for energy and environmental applications.

In Chapter 6, the synthesis strategy demonstrated in Chapter 4 was applied to molecular cages containing MOF, MIL-100. A bimetallic Fe-Mo sulphide/S-doped carbon nanocomposite was successfully fabricated from PMA@MIL-100 precursors. Nanosized metal sulphide crystals are homogeneously embedded in the porous carbon matrix, leading to significant improvement in HER activities under acidic conditions. In particular, composite 1Mo@MIL-800 exhibits an overpotential of -0.321 V to realise a

current density of -10 mA cm^{-2} and a Tafel slope of 62 mV dec^{-1}, which shows a 53% reduction in overpotential to achieve the same current density compared with Mo-free composite MIL-800. This dramatic improvement in HER performance of the PMA@MIL derived nanocomposites can be attributed to (1) the large amount of active sites introduced by the evenly distributed nanosized MoS_2 throughout the carbon matrix; (2) the strong interactions formed between the two metallic sulphides, in which Fe-Mo-S phases are favourable for HER and (3) the increased HER active sites created by S-doping in the carbon matrix. Moreover, the Fe-Mo sulphide/carbon composites are electrocatalytic active for HER not only in acidic media but also in alkaline and neutral media. In addition, it was also found that although the sulphurization time of the composites does not affect the HER performance, both higher Mo amount and higher heating ramp rate for the composites lead to deteriorated HER performance. This work offers a feasible way to generate complex heterogeneous electrocatalytic composites with great potential for diverse applications.

Comparing the findings in Chapter 4, 5 and 6, it is clear that using ZIFs and MOFs as the precursor is the key to the formation of porous morphology and nanostructure of the derivatives. The W-based nanocomposites in Chapter 4 and 5 demonstrated that although two different synthesis approaches were used, they can both lead to similar multiphase composite systems. The similar compositions and nanostructure can therefore result in similar electrochemical performance. However, different synthesis methods can be beneficial for the introduction of certain previously incompatible species, as demonstrated by the PMA incorporated ZIF-67 in Chapter 5. Comparing Chapter 4 and 5 with Chapter 6, it is clear that cobalt sulphide plays a vital role in the OER activity of the composites. Moreover, bifunctional electrocatalysts that combine the HER active specie with the OER active species in one composite can be readily produced.

Overall, this thesis develops rational and effective design and synthesis approaches towards efficient electrocatalytic composite materials with desired active species and morphologies which could be beneficial for future research.

7.2 Suggestions for future work

Based on the findings in this thesis, suggestions for the future work relevant to this project are proposed as follows:

- The effect of heating rate, heating temperature and sulphurization duration on the morphology and composition of the ZIFs derived nanocomposites have been briefly explored. However, a more detailed and systematic investigation would be useful for finer control on the morphology and porosity of the ZIF-derivatives, and the size, dispersion and composition of the carbon matrix wrapped metal nanoparticles.
- Metal sulphides/carbon nanocomposites with fine nanoparticles trapped in the carbon matrix have been successfully prepared, which lead to excellent HER and OER properties. However, some metal sulphides agglomerate at the outside of the carbon matrices after high-temperatures treatment. These large metal sulphide crystals are lack of electrochemical active sites, which lead to unserviceable parts of the composites. Reducing and removing the unserviceable parts or turning them into electrochemical active species will be an interesting subject.
- Conduct the ICP-OES test to investigate the amount of Mo/W/S elements that has been actually introduced into the nanocomposites, and the ratio between them and the Co element in order to gain further understanding of how the content and their formed structures affect the electrocatalytic performance.
- Further optimization of the electrocatalysts is needed to improve the HER and OER activities to a more competitive level before subject to full device operation test.
- Materials with atomic dispersed metal active sites on carbon matrix have attracted great interest, it would be interesting to design and synthesise such kind of catalyst from ZIFs-based composites with similar composition and compare their electrocatalytic performance with catalysts mentioned in this thesis.
- Investigation on the local active sites and the underlying reaction kinetic of this kind of multiphase complex system remain challenge, therefore development and application of effective advanced in-situ characterization and analysis technologies to tackle this challenge is highly desired.

References

1. J. Zhu, L. Hu, P. Zhao, L. Y. S. Lee and K.-Y. Wong, *Chem. Rev.*, 2020, **120**, 851-918.
2. D. G. M. Vladimir A. Blagojević, Jasmina Grbović Novaković and Dragica M. Minic, in *Hydrogen Energy-Challenges and Perspectives*, ed. D. Minic, IntechOpen, 1 edn., 2012, ch. 1, p. online.
3. S. Zhang, X. Zhang, Y. Rui, R. Wang and X. Li, *Green Energy Environ.*, 2021, **6**, 458-478.
4. J. Gao, H. Tao and B. Liu, *Adv. Mater.*, 2021, **33**, 2003786.
5. R. Ahmad, U. A. Khan, N. Iqbal and T. Noor, *RSC Adv.*, 2020, **10**, 43733-43750.
6. B. Ding, J. Wang, Z. Chang, G. Xu, X. Hao, L. Shen, H. Dou and X. Zhang, *ChemElectroChem*, 2016, **3**, 668-674.
7. H. K. Chae, D. Y. Siberio-Pérez, J. Kim, Y. Go, M. Eddaoudi, A. J. Matzger, M. O'Keeffe, O. M. Yaghi, D. Materials and G. Discovery, *Nature*, 2004, **427**, 523-527.
8. M. Eddaoudi, J. Kim, N. Rosi, D. Vodak, J. Wachter, M. O'Keeffe and M. Yaghi Omar, *Science*, 2002, **295**, 469-472.
9. P. Deria, J. E. Mondloch, O. Karagiaridi, W. Bury, J. T. Hupp and O. K. Farha, *Chem. Soc. Rev.*, 2014, **43**, 5896-5912.
10. J. L. C. Rowsell and O. M. Yaghi, *Microporous Mesoporous Mater.*, 2004, **73**, 3-14.
11. R. Lehnert and F. Seel, *Z. Anorg. Allg. Chem.*, 1980, **464**, 187-194.
12. K. S. Park, Z. Ni, A. P. Côté, J. Y. Choi, R. Huang, F. J. Uribe-Romo, H. K. Chae, M. O'Keeffe and O. M. Yaghi, *Proc. Natl. Acad. Sci. USA*, 2006, **103**, 10186.
13. B. Chen, Z. Yang, Y. Zhu and Y. Xia, *J. Mater. Chem. A*, 2014, **2**, 16811-16831.
14. W. W. Clark and J. Rifkin, *Energy Policy*, 2006, **34**, 2630-2639.
15. R. Banerjee, A. Phan, B. Wang, C. Knobler, H. Furukawa, M. O'Keeffe and M. Yaghi Omar, *Science*, 2008, **319**, 939-943.
16. R. Banerjee, H. Furukawa, D. Britt, C. Knobler, M. O'Keeffe and O. M. Yaghi, *J. Am. Chem. Soc*, 2009, **131**, 3875-3877.
17. W. Morris, C. J. Doonan, H. Furukawa, R. Banerjee and O. M. Yaghi, *J. Am. Chem. Soc*, 2008, **130**, 12626-12627.
18. W. Morris, B. Leung, H. Furukawa, O. K. Yaghi, N. He, H. Hayashi, Y. Houndonougbo, M. Asta, B. B. Laird and O. M. Yaghi, *J. Am. Chem. Soc*, 2010, **132**, 11006-11008.
19. W. Morris, N. He, K. G. Ray, P. Klonowski, H. Furukawa, I. N. Daniels, Y. A. Houndonougbo, M. Asta, O. M. Yaghi and B. B. Laird, *J. Phys. Chem. C*, 2012, **116**, 24084-24090.
20. B. Wang, A. P. Côté, H. Furukawa, M. O'Keeffe and O. M. Yaghi, *Nature*, 2008, **453**, 207-211.
21. P. Zhou, L. Wang, J. Lv, R. Li, F. Gao, X. Huang, Y. Lu and G. Wang, *J. Mater. Chem. A*, 2022, **10**, 4981-4991.
22. R. Liu, S. Xu, X. Shao, Y. Wen, X. Shi, L. Huang, M. Hong, J. Hu and Z. Yang, *ACS Appl. Mater. Interfaces*, 2021, **13**, 47717-47727.
23. G. Kaur, R. K. Rai, D. Tyagi, X. Yao, P.-Z. Li, X.-C. Yang, Y. Zhao, Q. Xu and S. K. Singh, *J. Mater. Chem. A*, 2016, **4**, 14932-14938.
24. J. Tang, R. R. Salunkhe, H. Zhang, V. Malgras, T. Ahamad, S. M. Alshehri, N. Kobayashi, S. Tominaka, Y. Ide, J. H. Kim and Y. Yamauchi, *Sci. Rep.*, 2016, **6**, 30295.

25. K. Zhou, B. Mousavi, Z. Luo, S. Phatanasri, S. Chaemchuen and F. Verpoort, *J. Mater. Chem. A*, 2017, **5**, 952-957.
26. J. K. Zaręba, M. Nyk and M. Samoć, *Cryst. Growth Des.*, 2016, **16**, 6419-6425.
27. S. Lai, L. Xu, H. Liu, S. Chen, R. Cai, L. Zhang, W. Theis, J. Sun, D. Yang and X. Zhao, *J. Mater. Chem. A*, 2019, **7**, 21884-21891.
28. H. Yang, X.-W. He, F. Wang, Y. Kang and J. Zhang, *J. Mater. Chem.*, 2012, **22**, 21849-21851.
29. A. Schejn, A. Aboulaich, L. Balan, V. Falk, J. Lalevée, G. Medjahdi, L. Aranda, K. Mozet and R. Schneider, *Catal. Sci. Technol.*, 2015, **5**, 1829-1839.
30. R. Li, X. Ren, H. Ma, X. Feng, Z. Lin, X. Li, C. Hu and B. Wang, *J. Mater. Chem. A*, 2014, **2**, 5724-5729.
31. M. T. Thanh, T. V. Thien, P. D. Du, N. P. Hung and D. Q. Khieu, *J. Porous Mater.*, 2018, **25**, 857-869.
32. X. Wang, H. Zhang, H. Lin, S. Gupta, C. Wang, Z. Tao, H. Fu, T. Wang, J. Zheng, G. Wu and X. Li, *Nano Energy*, 2016, **25**, 110-119.
33. W. Xu, H. Chen, K. Jie, Z. Yang, T. Li and S. Dai, *Angew. Chem. Int. Ed.*, 2019, **58**, 5018-5022.
34. S. Horike, K. Kadota, T. Itakura, M. Inukai and S. Kitagawa, *Dalton Trans.*, 2015, **44**, 15107-15110.
35. K. Kadota, E. Sivaniah, S. Bureekaew, S. Kitagawa and S. Horike, *Inorg. Chem.*, 2017, **56**, 8744-8747.
36. J. López-Cabrelles, J. Romero, G. Abellán, M. Giménez-Marqués, M. Palomino, S. Valencia, F. Rey and G. Mínguez Espallargas, *J. Am. Chem. Soc*, 2019, **141**, 7173-7180.
37. Y. Deng, Y. Dong, G. Wang, K. Sun, X. Shi, L. Zheng, X. Li and S. Liao, *ACS Appl. Mater. Interfaces*, 2017, **9**, 9699-9709.
38. L. Osmieri, *ChemEngineering*, 2019, **3**, 16.
39. S. Ji, Y. Chen, Z. Zhang, W.-C. Cheong, Z. Liu, D. Wang and Y. Li, *Nanoscale Horiz.*, 2019, **4**, 902-906.
40. H. Tian, H. Tian, S. Wang, S. Chen, F. Zhang, L. Song, H. Liu, J. Liu and G. Wang, *Nat. Commun.*, 2020, **11**, 5025.
41. Z.-F. Huang, J. Song, K. Li, M. Tahir, Y.-T. Wang, L. Pan, L. Wang, X. Zhang and J.-J. Zou, *J. Am. Chem. Soc*, 2016, **138**, 1359-1365.
42. J. Yang, Y.-B. Zhang, Q. Liu, C. A. Trickett, E. Gutiérrez-Puebla, M. Á. Monge, H. Cong, A. Aldossary, H. Deng and O. M. Yaghi, *J. Am. Chem. Soc*, 2017, **139**, 6448-6455.
43. E. V. Perez, C. Karunaweera, I. H. Musselman, K. J. Balkus and J. P. Ferraris, *Processes*, 2016, **4**, 32.
44. T. Palaniselvam, B. P. Biswal, R. Banerjee and S. Kurungot, *Chem. Eur. J.*, 2013, **19**, 9335-9342.
45. D. Zhao, J.-L. Shui, L. R. Grabstanowicz, C. Chen, S. M. Commet, T. Xu, J. Lu and D.-J. Liu, *Adv. Mater.*, 2014, **26**, 1093-1097.
46. V. Armel, J. Hannauer and F. Jaouen, *Catalysts*, 2015, **5**, 1333-1351.
47. V. Armel, S. Hindocha, F. Salles, S. Bennett, D. Jones and F. Jaouen, *J. Am. Chem. Soc*, 2017, **139**, 453-464.
48. S. Sun, Z. Yang, J. Cao, Y. Wang and W. Xiong, *J. Solid State Chem.*, 2020, **285**, 121219.
49. H. Zhang, S. Hwang, M. Wang, Z. Feng, S. Karakalos, L. Luo, Z. Qiao, X. Xie, C. Wang, D. Su, Y. Shao and G. Wu, *J. Am. Chem. Soc*, 2017, **139**, 14143-14149.
50. L. Li, W. Xie, J. Chen and J. Yang, *J. Solid State Chem.*, 2018, **264**, 1-5.

51. C. Zhao, X. Dai, T. Yao, W. Chen, X. Wang, J. Wang, J. Yang, S. Wei, Y. Wu and Y. Li, *J. Am. Chem. Soc*, 2017, **139**, 8078-8081.
52. H. Fei, J. F. Cahill, K. A. Prather and S. M. Cohen, *Inorg. Chem.*, 2013, **52**, 4011-4016.
53. Y. Ban , Y. Li, Y. Peng , H. Jin , W. Jiao , X. Liu and W. Yang, *Chem. Eur. J.*, 2014, **20**, 11402-11409.
54. L. Tang, S. Zhang, Q. Wu, X. Wang, H. Wu and Z. Jiang, *J. Mater. Chem. A*, 2018, **6**, 2964-2973.
55. Y.-B. Hao, Z.-S. Shao, C. Cheng, X.-Y. Xie, J. Zhang, W.-J. Song and H.-S. Wang, *ACS Appl. Mater. Interfaces*, 2019, **11**, 31755-31762.
56. X. F. Lu, L. Yu, J. Zhang and X. W. Lou, *Adv. Mater.*, 2019, **31**, 1900699.
57. W. Xu, X. Cui, Z. Xie, G. Dietrich and Y. Wang, *Electrochim. Acta*, 2016, **222**, 1021-1028.
58. L. Zhang and Y. H. Hu, *J. Phys. Chem. C*, 2011, **115**, 7967-7971.
59. O. Karagiaridi, M. B. Lalonde, W. Bury, A. A. Sarjeant, O. K. Farha and J. T. Hupp, *J. Am. Chem. Soc*, 2012, **134**, 18790-18796.
60. J. Sánchez-Laínez, B. Zornoza, A. F. Orsi, M. M. Łozińska, D. M. Dawson, S. E. Ashbrook, S. M. Francis, P. A. Wright, V. Benoit, P. L. Llewellyn, C. Téllez and J. Coronas, *Chem. Eur. J.*, 2018, **24**, 11211-11219.
61. J.-Q. Jiang, C.-X. Yang and X.-P. Yan, *Chem. Commun.*, 2015, **51**, 6540-6543.
62. R. Zhao, W. Xia, C. Lin, J. Sun, A. Mahmood, Q. Wang, B. Qiu, H. Tabassum and R. Zou, *Carbon*, 2017, **114**, 284-290.
63. S. Bhattacharjee, Y.-R. Lee and W.-S. Ahn, *CrystEngComm*, 2015, **17**, 2575-2582.
64. L.-X. You, B.-B. Zhao, S.-X. Yao, G. Xiong, I. Dragutan, V. Dragutan, F. Ding and Y.-G. Sun, *J Catal.*, 2020, **392**, 80-87.
65. V. J. Pastore, T. R. Cook and J. Rzayev, *Chem. Mater.*, 2018, **30**, 8639-8649.
66. J. V. Morabito, L.-Y. Chou, Z. Li, C. M. Manna, C. A. Petroff, R. J. Kyada, J. M. Palomba, J. A. Byers and C.-K. Tsung, *J. Am. Chem. Soc*, 2014, **136**, 12540-12543.
67. J. Marreiros, L. Van Dommelen, G. Fleury, R. de Oliveira-Silva, T. Stassin, P. Iacomi, S. Furukawa, D. Sakellariou, P. L. Llewellyn, M. Roeffaers and R. Ameloot, *Angew. Chem. Int. Ed.*, 2019, **58**, 18471-18475.
68. W. Wu, J. Su, M. Jia, Z. Li, G. Liu and W. Li, *Sci. Adv.*, 2020, **6**, 1-7.
69. J. Wang, Z. Huang, W. Liu, C. Chang, H. Tang, Z. Li, W. Chen, C. Jia, T. Yao, S. Wei, Y. Wu and Y. Li, *J. Am. Chem. Soc*, 2017, **139**, 17281-17284.
70. R. Jin, C. Zeng, M. Zhou and Y. Chen, *Chem. Rev.*, 2016, **116**, 10346-10413.
71. Y. Luo, S. Fan, W. Yu, Z. Wu, D. A. Cullen, C. Liang, J. Shi and C. Su, *Adv. Mater.*, 2018, **30**, 1704576.
72. L. Sun, Y. Yun, H. Sheng, Y. Du, Y. Ding, P. Wu, P. Li and M. Zhu, *J. Mater. Chem. A*, 2018, **6**, 15371-15376.
73. T. G. Schaaff, M. N. Shafigullin, J. T. Khoury, I. Vezmar, R. L. Whetten, W. G. Cullen, P. N. First, C. Gutiérrez-Wing, J. Ascensio and M. J. Jose-Yacamán, *J. Phys. Chem. B*, 1997, **101**, 7885-7891.
74. Y. Chen, S. Ji, Y. Wang, J. Dong, W. Chen, Z. Li, R. Shen, L. Zheng, Z. Zhuang, D. Wang and Y. Li, *Angew. Chem. Int. Ed.*, 2017, **56**, 6937-6941.
75. M. Xiao, J. Zhu, L. Ma, Z. Jin, J. Ge, X. Deng, Y. Hou, Q. He, J. Li, Q. Jia, S. Mukerjee, R. Yang, Z. Jiang, D. Su, C. Liu and W. Xing, *ACS Catal.*, 2018, **8**, 2824-2832.
76. S. Ji, Y. Chen, S. Zhao, W. Chen, L. Shi, Y. Wang, J. Dong, Z. Li, F. Li, C. Chen, Q. Peng, J. Li, D. Wang and Y. Li, *Angew. Chem. Int. Ed.*, 2019, **58**, 4271-4275.

77. Y. Xiong, J. Dong, Z.-Q. Huang, P. Xin, W. Chen, Y. Wang, Z. Li, Z. Jin, W. Xing, Z. Zhuang, J. Ye, X. Wei, R. Cao, L. Gu, S. Sun, L. Zhuang, X. Chen, H. Yang, C. Chen, Q. Peng, C.-R. Chang, D. Wang and Y. Li, *Nat. Nanotechnol.*, 2020, **15**, 390-397.
78. Z. Li, Y. Chen, S. Ji, Y. Tang, W. Chen, A. Li, J. Zhao, Y. Xiong, Y. Wu, Y. Gong, T. Yao, W. Liu, L. Zheng, J. Dong, Y. Wang, Z. Zhuang, W. Xing, C.-T. He, C. Peng, W.-C. Cheong, Q. Li, M. Zhang, Z. Chen, N. Fu, X. Gao, W. Zhu, J. Wan, J. Zhang, L. Gu, S. Wei, P. Hu, J. Luo, J. Li, C. Chen, Q. Peng, X. Duan, Y. Huang, X.-M. Chen, D. Wang and Y. Li, *Nat. Chem.*, 2020, **12**, 764-772.
79. J. Han, X. Meng, L. Lu, J. Bian, Z. Li and C. Sun, *Adv. Funct. Mater.*, 2019, **29**, 1808872.
80. S. Mukhopadhyay, O. Basu, A. Kar and S. K. Das, *Inorg. Chem.*, 2020, **59**, 472-483.
81. Y. Ye, F. Cai, H. Li, H. Wu, G. Wang, Y. Li, S. Miao, S. Xie, R. Si, J. Wang and X. Bao, *Nano Energy*, 2017, **38**, 281-289.
82. R. Jiang, L. Li, T. Sheng, G. Hu, Y. Chen and L. Wang, *J. Am. Chem. Soc*, 2018, **140**, 11594-11598.
83. F. Chen, L. Wang, Y. Xing and J. Zhang, *J. Colloid Interface Sci.*, 2018, **527**, 68-77.
84. A. R. Bagheri, N. Aramesh, J. Chen, W. Liu, W. Shen, S. Tang and H. K. Lee, *Anal. Chim. Acta*, 2022, **1209**, 339509.
85. B. D'Cruz, M. O. Amin and E. Al-Hetlani, *Ind. Eng. Chem. Res.*, 2021, **60**, 10960-10977.
86. M. T. Pope and A. Müller, *Angew. Chem. Int. Ed.*, 1991, **30**, 34-48.
87. R. Canioni, C. Roch-Marchal, M. Haouas, A. Vimont, P. Horcajada, F. Secheresse and C. Serre, *Curr. Inorg. Chem.*, 2017, **7**, 145-156.
88. J. J. Walsh, A. M. Bond, R. J. Forster and T. E. Keyes, *Coord. Chem. Rev.*, 2016, **306**, 217-234.
89. L. Zhang, T. Mi, M. A. Ziaee, L. Liang and R. Wang, *J. Mater. Chem. A*, 2018, **6**, 1639-1647.
90. R. S. Malkar and G. D. Yadav, *Appl. Catal. A: Gen*, 2018, **560**, 54-65.
91. Q. Lan, Z.-M. Zhang, C. Qin, X.-L. Wang, Y.-G. Li, H.-Q. Tan and E.-B. Wang, *Chem. Eur. J.*, 2016, **22**, 15513-15520.
92. Z. Kou, W. Zang, Y. Ma, Z. Pan, S. Mu, X. Gao, B. Tang, M. Xiong, X. Zhao, A. K. Cheetham, L. Zheng and J. Wang, *Nano Energy*, 2020, **67**, 104288.
93. S. Mukhopadhyay, J. Debgupta, C. Singh, A. Kar and S. K. Das, *Angew. Chem. Int. Ed.*, 2018, **57**, 1918-1923.
94. P. Wang, X. Zou, H. Tan, S. Wu, L. Jiang and G. Zhu, *J. Mater. Chem. C*, 2018, **6**, 5412-5419.
95. J. Ran, L. Xiao, W. Wang, S. Jia and J. Zhang, *Chem. Commun.*, 2018, **54**, 13786-13789.
96. V. K. Abdelkader-Fernández, D. M. Fernandes, S. S. Balula, L. Cunha-Silva and C. Freire, *ACS Appl. Energy Mater.*, 2020, **3**, 2925-2934.
97. R. S. Malkar, H. Daly, C. Hardacre and G. D. Yadav, *ACS Sustain. Chem. Eng.*, 2019, **7**, 16215-16224.
98. J. S. Lee, H. Rajan, M. Christy and S. C. Yi, *Int. J. Hydrog. Energy*, 2021, **46**, 10739-10748.
99. D. M. E. Hellner, *Acta Cryst.*, 1978, **B34**, 2789-2794.
100. L. Tang, J. Shi, H. Wu, S. Zhang, H. Liu, H. Zou, Y. Wu, J. Zhao and Z. Jiang, *Nanotechnology*, 2017, **28**, 365604.

101. C. Li, M. Zhang, X. Di, D. Yin, W. Li and C. Liang, *Chinese J. Catal.*, 2016, **37**, 1555-1561.
102. N. Davoodian, A. Nakhaei Pour, M. Izadyar, A. Mohammadi, A. Salimi and S. M. Kamali Shahri, *Appl. Organomet. Chem.*, 2020, **34**, e5747.
103. Z. Dong, J. Zhao, Y. Tian, B. Zhang and Y. Wu, *Catalysts*, 2020, **10**, 455.
104. L. Bai, H. Zheng, J. Ma, J. Wang, Z. Chen and Q. Huang, *Inorg. Chem.*, 2019, **58**, 8884-8889.
105. Y. Zhu and Z. Bai, *Catalysts*, 2020, **10**, 174.
106. S. Mei, B. Yang, X. Wei, H. Dai, Z. Chen, Z. Cui, G. Zhang, F. Xie, W. Zhang and R. Guo, *Nanomaterials (Basel)*, 2019, **9**, 832.
107. J. Liu, J. He, L. Wang, R. Li, P. Chen, X. Rao, L. Deng, L. Rong and J. Lei, *Sci. Rep.*, 2016, **6**, 23667.
108. W. Zhou, B. Zou, W. Zhang, D. Tian, W. Huang and F. Huo, *Nanoscale*, 2015, **7**, 8720-8724.
109. H. Zhou, J. Zhang, J. Zhang, X.-F. Yan, X.-P. Shen and A.-H. Yuan, *Inorg. Chem. Commun.*, 2015, **54**, 54-56.
110. E. Marceau, X. Carrier and M. Che, in *Synthesis of Solid Catalysts*, ed. K. P. de Jong, Wiley, 2009, ch. 4, pp. 59-82.
111. P. Munnik, P. E. de Jongh and K. P. de Jong, *Chem. Rev.*, 2015, **115**, 6687-6718.
112. Q.-L. Zhu, J. Li and Q. Xu, *J. Am. Chem. Soc*, 2013, **135**, 10210-10213.
113. D. B. Christensen, R. L. Mortensen, S. Kramer and S. Kegnæs, *Catal. Lett.*, 2020, **150**, 1537-1545.
114. N. R. Bennedsen, S. Kramer, J. J. Mielby and S. Kegnæs, *Catal. Sci. Technol.*, 2018, **8**, 2434-2440.
115. A. Poungsombate, T. Imyen, P. Dittanet, B. Embley and P. Kongkachuichay, *J. Taiwan Inst. Chem. Eng.*, 2017, **80**, 16-24.
116. W.-T. Koo, S.-J. Choi, J.-S. Jang and I.-D. Kim, *Sci. Rep.*, 2017, **7**, 45074.
117. B. Xia, N. Cao, H. Dai, J. Su, X. Wu, W. Luo and G. Cheng, *ChemCatChem*, 2014, **6**, 2549-2552.
118. L. Liu, Y. Song, H. Chong, S. Yang, J. Xiang, S. Jin, X. Kang, J. Zhang, H. Yu and M. Zhu, *Nanoscale*, 2016, **8**, 1407-1412.
119. M. Yurderi, A. Bulut, M. Zahmakiran, M. Gülcan and S. Özkar, *Appl. Catal. B: Environ.*, 2014, **160-161**, 534-541.
120. L. Shi, X. Zhu, T. Liu, H. Zhao and M. Lan, *Sens. Actuators B: Chem.*, 2016, **227**, 583-590.
121. B. Hu, Y. Yin, Z. Zhong, D. Wu, G. Liu and X. Hong, *Catal. Sci. Technol.*, 2019, **9**, 2673-2681.
122. T. Zhou, Z. Qin, X. Wang, C. Wu, X. Tang, T. Zhang, H. Wang, C. Xie and D. Zeng, *Chem. Commun.*, 2019, **55**, 11045-11048.
123. F. Fu, C. Wang, Q. Wang, A. M. Martinez-Villacorta, A. Escobar, H. Chong, X. Wang, S. Moya, L. Salmon, E. Fouquet, J. Ruiz and D. Astruc, *J. Am. Chem. Soc*, 2018, **140**, 10034-10042.
124. H.-L. Jiang, T. Akita, T. Ishida, M. Haruta and Q. Xu, *J. Am. Chem. Soc*, 2011, **133**, 1304-1306.
125. J.-W. Huang, Q.-Q. Cheng, Y.-C. Huang, H.-C. Yao, H.-B. Zhu and H. Yang, *ACS Appl. Energy Mater.*, 2019, **2**, 3194-3203.
126. C.-W. Chang, Z.-J. Gong, N.-C. Huang, C.-Y. Wang and W.-Y. Yu, *Catal. Today*, 2020, **351**, 21-29.
127. M. N. Shaikh, M. A. Aziz, A. Helal, A. N. Kalanthoden and Z. H. Yamani, *ChemistrySelect*, 2017, **2**, 9052-9057.

128. Y.-H. Zhou, X. Cao, J. Ning, C. Ji, Y. Cheng and J. Gu, *Int. J. Hydrog. Energy*, 2020, **45**, 31440-31451.
129. M. Tao, Z. Xin, X. Meng, Y. Lv and Z. Bian, *RSC Adv.*, 2016, **6**, 35875-35883.
130. Y. Jiao, J. Li, A. Xie, F. Wu, K. Zhang, W. Dong and X. Zhu, *Compos. Sci. Technol.*, 2019, **174**, 232-240.
131. H.-L. Jiang, B. Liu, Y.-Q. Lan, K. Kuratani, T. Akita, H. Shioyama, F. Zong and Q. Xu, *J. Am. Chem. Soc*, 2011, **133**, 11854-11857.
132. P. Pachfule, B. P. Biswal and R. Banerjee, *Chem. Eur. J.*, 2012, **18**, 11399-11408.
133. X. Ma, L. Li, R. Chen, C. Wang, H. Li and H. Li, *Chem.: Asian J.*, 2018, **13**, 2069-2076.
134. P. Zhang, F. Sun, Z. Xiang, Z. Shen, J. Yun and D. Cao, *Energy Environ. Sci.*, 2014, **7**, 442-450.
135. F. Chen, Q. Lu, T. Fan, R. Fang and Y. Li, *Catal. Today*, 2020, **351**, 94-102.
136. H. J. Lee, W. Cho and M. Oh, *Chem. Commun.*, 2012, **48**, 221-223.
137. S. Sorribas, B. Zornoza, C. Téllez and J. Coronas, *Chem. Commun.*, 2012, **48**, 9388-9390.
138. T. Feng and M. Zhang, *Chem. Commun.*, 2018, **54**, 11570-11573.
139. P. Wang, J. Zhao, X. Li, Y. Yang, Q. Yang and C. Li, *Chem. Commun.*, 2013, **49**, 3330-3332.
140. A. Malik, M. Nath, S. Mohiyuddin and G. Packirisamy, *ACS Omega*, 2018, **3**, 8288-8308.
141. W.-T. Koo, J.-S. Jang, S.-J. Choi, H.-J. Cho and I.-D. Kim, *ACS Appl. Mater. Interfaces*, 2017, **9**, 18069-18077.
142. Z. Qi, Y. Pei, T. W. Goh, Z. Wang, X. Li, M. Lowe, R. V. Maligal-Ganesh and W. Huang, *Nano Res.*, 2018, **11**, 3469-3479.
143. K. M. Koczkur, S. Mourdikoudis, L. Polavarapu and S. E. Skrabalak, *Dalton Trans.*, 2015, **44**, 17883-17905.
144. H. Jiang, Q. Yan, R. Chen and W. Xing, *Microporous Mesoporous Mater.*, 2016, **225**, 33-40.
145. L. Chen, Y. Peng, H. Wang, Z. Gu and C. Duan, *Chem. Commun.*, 2014, **50**, 8651-8654.
146. T. Ohhashi, T. Tsuruoka, T. Matsuyama, Y. Takashima, H. Nawafune, H. Minami and K. Akamatsu, *J. Colloid Interface Sci.*, 2015, **451**, 212-215.
147. C. Rösler, D. Esken, C. Wiktor, H. Kobayashi, T. Yamamoto, S. Matsumura, H. Kitagawa and R. A. Fischer, *Eur. J. Inorg. Chem.*, 2014, **2014**, 5514-5521.
148. Q. Yang, Q. Xu, S.-H. Yu and H.-L. Jiang, *Angew. Chem. Int. Ed.*, 2016, **55**, 3685-3689.
149. Q. Luo, L. Chen, B. Duan, Z. Gu, J. Liu, M. Xu and C. Duan, *RSC Adv.*, 2016, **6**, 12467-12471.
150. Y. Su, H. Xu, J. Wang, X. Luo, Z.-l. Xu, K. Wang and W. Wang, *Nano Res.*, 2019, **12**, 625-630.
151. Y. Huang, Y. Zhang, X. Chen, D. Wu, Z. Yi and R. Cao, *Chem. Commun.*, 2014, **50**, 10115-10117.
152. M. Zeng, Z. Chai, X. Deng, Q. Li, S. Feng, J. Wang and D. Xu, *Nano Res.*, 2016, **9**, 2729-2734.
153. L. Wang, Y. F. Yuan, Q. Chen, Y. Q. Zheng, S. M. Yin and S. Y. Guo, *Nanotechnology*, 2019, **30**, 435402.
154. S. El-Hankari, J. Aguilera-Sigalat and D. Bradshaw, *J. Mater. Chem. A*, 2016, **4**, 13509-13518.
155. N. Zhang, Y. Yang, X. Feng, S.-H. Yu, J. Seok, D. A. Muller and H. D. Abruña, *J. Mater. Chem. A*, 2019, **7**, 21128-21139.

156. S. Li, W. Zhang and F. Huo, *Phys. E: Low-Dimens. Syst. Nanostructures*, 2015, **69**, 56-60.
157. P. Hu, J. Zhuang, L.-Y. Chou, H. K. Lee, X. Y. Ling, Y.-C. Chuang and C.-K. Tsung, *J. Am. Chem. Soc*, 2014, **136**, 10561-10564.
158. Q. Liu, N. Wang, J. Caro and A. Huang, *J. Am. Chem. Soc*, 2013, **135**, 17679-17682.
159. J. Zhou, P. Wang, C. Wang, Y. T. Goh, Z. Fang, P. B. Messersmith and H. Duan, *ACS Nano*, 2015, **9**, 6951-6960.
160. S.-L. Cao, H. Xu, L.-H. Lai, W.-M. Gu, P. Xu, J. Xiong, H. Yin, X.-H. Li, Y.-Z. Ma, J. Zhou, M.-H. Zong and W.-Y. Lou, *Bioresour. Bioprocess.*, 2017, **4**, 56.
161. K. Wang, N. Li, X. Hai and F. Dang, *J. Mater. Chem. A*, 2017, **5**, 20765-20770.
162. L. Ning, S. Liao, C. Dong, M. Zhang, W. Gu and X. Liu, *ACS Appl. Mater. Interfaces*, 2020, **12**, 7198-7205.
163. J. Tang, R. R. Salunkhe, J. Liu, N. L. Torad, M. Imura, S. Furukawa and Y. Yamauchi, *J. Am. Chem. Soc*, 2015, **137**, 1572-1580.
164. Z. Hu, Z. Zhang, Z. Li, M. Dou and F. Wang, *ACS Appl. Mater. Interfaces*, 2017, **9**, 16109-16116.
165. M. K. Aslam, S. S. A. Shah, S. Li and C. Chen, *J. Mater. Chem. A*, 2018, **6**, 14083-14090.
166. C. Avci, A. Yazdi, M. Tarrés, E. Bernoud, N. G. Bastús, V. Puntes, I. Imaz, X. Ribas and D. Maspoch, *ACS Appl. Mater. Interfaces*, 2018, **10**, 23952-23960.
167. G. Zhan and H. C. Zeng, *Nat. Commun.*, 2018, **9**, 3778.
168. L. Feng, S. Yuan, J.-L. Li, K.-Y. Wang, G. S. Day, P. Zhang, Y. Wang and H.-C. Zhou, *ACS Cent. Sci.*, 2018, **4**, 1719-1726.
169. Y. Jiang, L. Sun, J. Du, Y. Liu, H. Shi, Z. Liang and J. Li, *Cryst. Growth Des.*, 2017, **17**, 2090-2096.
170. C. Liu, Q. Sun, L. Lin, J. Wang, C. Zhang, C. Xia, T. Bao, J. Wan, R. Huang, J. Zou and C. Yu, *Nat. Commun.*, 2020, **11**, 4971.
171. L. Chai, Z. Hu, X. Wang, Y. Xu, L. Zhang, T.-T. Li, Y. Hu, J. Qian and S. Huang, *Adv. Sci.*, 2020, **7**, 1903195.
172. J. Zhuang, L.-Y. Chou, B. T. Sneed, Y. Cao, P. Hu, L. Feng and C.-K. Tsung, *Small*, 2015, **11**, 5551-5555.
173. J. Yang, H. Ye, F. Zhao and B. Zeng, *ACS Appl. Mater. Interfaces*, 2016, **8**, 20407-20414.
174. F. Wang, H. Wang and T. Li, *Nanoscale*, 2019, **11**, 2121-2125.
175. S. Wang, Y. Fan, J. Teng, Y.-Z. Fan, J.-J. Jiang, H.-P. Wang, H. Grützmacher, D. Wang and C.-Y. Su, *Small*, 2016, **12**, 5702-5709.
176. G. Lu, S. Li, Z. Guo, O. K. Farha, B. G. Hauser, X. Qi, Y. Wang, X. Wang, S. Han, X. Liu, J. S. DuChene, H. Zhang, Q. Zhang, X. Chen, J. Ma, S. C. J. Loo, W. D. Wei, Y. Yang, J. T. Hupp and F. Huo, *Nat. Chem.*, 2012, **4**, 310-316.
177. C.-H. Kuo, Y. Tang, L.-Y. Chou, B. T. Sneed, C. N. Brodsky, Z. Zhao and C.-K. Tsung, *J. Am. Chem. Soc*, 2012, **134**, 14345-14348.
178. F.-L. Li, H.-X. Li and J.-P. Lang, *CrystEngComm*, 2016, **18**, 1760-1767.
179. X. Wang, J. Liu, S. Leong, X. Lin, J. Wei, B. Kong, Y. Xu, Z.-X. Low, J. Yao and H. Wang, *ACS Appl. Mater. Interfaces*, 2016, **8**, 9080-9087.
180. B. Li, J.-G. Ma and P. Cheng, *Angew. Chem. Int. Ed.*, 2018, **57**, 6834-6837.
181. K. Shen, L. Zhang, X. Chen, L. Liu, D. Zhang, Y. Han, J. Chen, J. Long, R. Luque, Y. Li and B. Chen, *Science*, 2018, **359**, 206-210.
182. X. Zhou, L. Chen, W. Zhang, J. Wang, Z. Liu, S. Zeng, R. Xu, Y. Wu, S. Ye, Y. Feng, X. Cheng, Z. Peng, X. Li and Y. Yu, *Nano Lett.*, 2019, **19**, 4965-4973.

183. H. Hong, J. Liu, H. Huang, C. Atangana Etogo, X. Yang, B. Guan and L. Zhang, *J. Am. Chem. Soc*, 2019, **141**, 14764-14771.
184. B. Y. Guan, L. Yu and X. W. Lou, *Adv. Sci.*, 2017, **4**, 1700247.
185. C. Liang, Y. Tang, X. Zhang, H. Chai, Y. Huang and P. Feng, *Environ. Res.*, 2020, **182**, 109059.
186. H. Tian, F. Huang, Y. Zhu, S. Liu, Y. Han, M. Jaroniec, Q. Yang, H. Liu, G. Q. M. Lu and J. Liu, *Adv. Funct. Mater.*, 2018, **28**, 1801737.
187. M. Zhang, C. Wang, R. Luo, W. Zhang, S. Chen, X. Yan, J. Qi, X. Sun, L. Wang and J. Li, *J. Mater. Chem. A*, 2019, **7**, 5173-5178.
188. Y. Chen, S. Ji, S. Zhao, W. Chen, J. Dong, W.-C. Cheong, R. Shen, X. Wen, L. Zheng, A. I. Rykov, S. Cai, H. Tang, Z. Zhuang, C. Chen, Q. Peng, D. Wang and Y. Li, *Nat. Commun.*, 2018, **9**, 5422.
189. V. S. Kale, M. Hwang, H. Chang, J. Kang, S. I. Chae, Y. Jeon, J. Yang, J. Kim, Y.-J. Ko, Y. Piao and T. Hyeon, *Adv. Funct. Mater.*, 2018, **28**, 1803786.
190. Q. Li, M. Wu, J. Zhao, Q. Lü, L. Han and R. Liu, *J. Electron. Mater.*, 2019, **48**, 3050-3058.
191. T. Wang, Y. He, Y. Liu, F. Guo, X. Li, H. Chen, H. Li and Z. Lin, *Nano Energy*, 2021, **79**, 105487.
192. Z. Zhao, T. Lin, W. Liu, L. Hou, F. Ye and S. Zhao, *Spectrochim. Acta A Mol. Biomol. Spectrosc.*, 2019, **219**, 240-247.
193. Z. Chi, Y. Feng, Y. Ma, D. Kong, H. Yin, S. Li, L. Li, Z. Guo and L. Wang, *Chem. Commun.*, 2021, **57**, 11248-11251.
194. M. J. Wang, Z. X. Mao, L. Liu, L. Peng, N. Yang, J. Deng, W. Ding, J. Li and Z. Wei, *Small*, 2018, **14**, 1804183.
195. X. Lv, L. Wang, J. Fu, Y. Li and L. Yu, *New J. Chem.*, 2020, **44**, 15140-15147.
196. X. Ge, C. Li, Z. Li and L. Yin, *Electrochim. Acta*, 2018, **281**, 700-709.
197. M. Wu, C. Li, J. Zhao, Y. Ling and R. Liu, *Dalton Trans.*, 2018, **47**, 7812-7818.
198. H. Yang, X. Chen, W.-T. Chen, Q. Wang, N. C. Cuello, A. Nafady, A. M. Al-Enizi, G. I. N. Waterhouse, G. A. Goenaga, T. A. Zawodzinski, P. E. Kruger, J. E. Clements, J. Zhang, H. Tian, S. G. Telfer and S. Ma, *ACS Nano*, 2019, **13**, 8087-8098.
199. X. Wang, Z. Na, D. Yin, C. Wang, Y. Wu, G. Huang and L. Wang, *ACS Nano*, 2018, **12**, 12238-12246.
200. S. Sun, Y. Tang, C. Wu and C. Wan, *Anal. Chim. Acta*, 2020, **1107**, 55-62.
201. B. Pan, X. Zhu, Y. Wu, T. Liu, X. Bi, K. Feng, N. Han, J. Zhong, J. Lu, Y. Li and Y. Li, *Adv. Sci.*, 2020, **7**, 2001002.
202. Y. Song, N. Wang, L.-y. Yang, Y. g. Wang, D. Yu and X.-k. Ouyang, *Ind. Eng. Chem. Res.*, 2019, **58**, 6394-6401.
203. Y. Han, P. Qi, S. Li, X. Feng, J. Zhou, H. Li, S. Su, X. Li and B. Wang, *Chem. Commun.*, 2014, **50**, 8057-8060.
204. X. Duan, S. Ren, N. Pan, M. Zhang and H. Zheng, *J. Mater. Chem. A*, 2020, **8**, 9355-9363.
205. J. Cai, L. Jiang, H. Wei, C. Wang, L. Yu and L. Zhang, *Microporous Mesoporous Mater.*, 2019, **287**, 9-17.
206. S. S. Sankar, G. Keerthana, K. Manjula, J. H. Sharad and S. Kundu, *Inorg. Chem.*, 2021, **60**, 4034-4046.
207. G. Lee, Y. D. Seo and J. Jang, *Chem. Commun.*, 2017, **53**, 11441-11444.
208. X. Dai, X. Li and X. Wang, *Chem. Eng. J.*, 2018, **338**, 82-91.
209. M. Wen, K. Mori, Y. Futamura, Y. Kuwahara, M. Navlani-García, T. An and H. Yamashita, *Sci. Rep.*, 2019, **9**, 15675.

210. W. Wang, S. Chen, E. Guisasola Cal, M. Martínez Moro, S. Moya, E. Coy, C. Wang, J.-R. Hamon and D. Astruc, *Inorg. Chem. Front.*, 2020, **7**, 3945-3952.
211. Q.-Q. Chang, Y.-W. Cui, H.-H. Zhang, F. Chang, B.-H. Zhu and S.-Y. Yu, *RSC Adv.*, 2019, **9**, 12689-12695.
212. D. D. Tuan and K.-Y. A. Lin, *Chem. Eng. J.*, 2018, **351**, 48-55.
213. Y. Tong, G. Xue, H. Wang, M. Liu, J. Wang, C. Hao, X. Zhang, D. Wang, X. Shi, W. Liu, G. Li and Z. Tang, *Nanoscale*, 2018, **10**, 16425-16430.
214. Z. Xu, W. Zhang, J. Weng, W. Huang, D. Tian and F. Huo, *Nano Res.*, 2016, **9**, 158-164.
215. A. Ayala, C. Carbonell, I. Imaz and D. Maspoch, *Chem. Commun.*, 2016, **52**, 5096-5099.
216. X.-Q. Tan, J.-Y. Liu, J.-R. Niu, J.-Y. Liu and J.-Y. Tian, *Materials (Basel)*, 2018, **11**, 1953.
217. Y.-X. Li, H. Fu, P. Wang, C. Zhao, W. Liu and C.-C. Wang, *Environ. Pollut.*, 2020, **256**, 113417.
218. B.-Y. Song and S. Yao, *Front. Chem.*, 2020, **8**, 314.
219. J. Qiu, X.-F. Zhang, X. Zhang, Y. Feng, Y. Li, L. Yang, H. Lu and J. Yao, *J. Hazard. Mater.*, 2018, **349**, 234-241.
220. C. Prasad, H. Tang, Q. Q. Liu, S. Zulfiqar, S. Shah and I. Bahadur, *J. Mol. Liq.*, 2019, **289**, 111114.
221. S. Saghir, E. Fu and Z. Xiao, *Microporous Mesoporous Mater.*, 2020, **297**, 110010.
222. J. Cao, S. Sun, X. Li, Z. Yang, W. Xiong, Y. Wu, M. Jia, Y. Zhou, C. Zhou and Y. Zhang, *Chem. Eng. J.*, 2020, **382**, 122802.
223. Y. Wang, J. Cao, Z. Yang, W. Xiong, Z. Xu, P. Song, M. Jia, S. Sun, Y. Zhang and W. Li, *J. Solid State Chem.*, 2021, **294**, 121857.
224. M. Luo, M. Li, B. Lü, Q. Liu, Z. Di and L. Guo, *ACS Appl. Nano Mater.*, 2021, **4**, 3734-3741.
225. S. Saghir and Z. Xiao, *Powder Technol.*, 2021, **377**, 453-463.
226. C. Sun, J. Yang, X. Rui, W. Zhang, Q. Yan, P. Chen, F. Huo, W. Huang and X. Dong, *J. Mater. Chem. A*, 2015, **3**, 8483-8488.
227. H. Li, Q. Jin, J. Zhao, B. Wang and X. Guo, *Dalton Trans.*, 2020, **49**, 12686-12694.
228. W. Wang, H. Yan, U. Anand and U. Mirsaidov, *J. Am. Chem. Soc*, 2021, **143**, 1854-1862.
229. A. Hameed, M. Batool, W. Iqbal, S. Abbas, M. Imran, I. A. Khan and M. A. Nadeem, *Front. Chem.*, 2021, **9**, 686968.
230. W. Chen, C. Wang, S. Su, H. Wang and D. Cai, *Chem. Eng. J.*, 2021, **414**, 128784.
231. D. Guo, X. Song, L. Tan, H. Ma, W. Sun, H. Pang, L. Zhang and X. Wang, *Chem. Eng. J.*, 2019, **356**, 955-963.
232. Z. Zhao, H. Duan, H. Pang and R. Zhu, *Chem.: Asian J.*, 2021, **16**, 845-849.
233. X. Chu, C. Wang, L. Zhou, X. Yan, Y. Chi and X. Yang, *RSC Adv.*, 2018, **8**, 39879-39883.
234. D. Wang, S. Li, Y. Du, X. Wu and Y. Chen, *Catalysts*, 2019, **9**, 352.
235. F. Qu, T. Thomas, B. Zhang, X. Zhou, S. Zhang, S. Ruan and M. Yang, *Sens. Actuators B: Chem.*, 2018, **273**, 1202-1210.
236. X. Yang, Z. Wen, Z. Wu and X. Luo, *Inorg. Chem. Front.*, 2018, **5**, 687-693.
237. C.-W. Chang, Y.-H. Kao, P.-H. Shen, P.-C. Kang and C.-Y. Wang, *J. Hazard. Mater.*, 2020, **400**, 122974.
238. X. Zhang, G. Ji, W. Liu, X. Zhang, Q. Gao, Y. Li and Y. Du, *J. Mater. Chem. C*, 2016, **4**, 1860-1870.

239. F. Lyu, Y. Bai, Z. Li, W. Xu, Q. Wang, J. Mao, L. Wang, X. Zhang and Y. Yin, *Adv. Funct. Mater.*, 2017, **27**, 1702324.
240. Z. Li and H. C. Zeng, *J. Am. Chem. Soc*, 2014, **136**, 5631-5639.
241. R. Wu, D. P. Wang, J. Han, H. Liu, K. Zhou, Y. Huang, R. Xu, J. Wei, X. Chen and Z. Chen, *Nanoscale*, 2015, **7**, 965-974.
242. M. Zhang, C. Wang, C. Liu, R. Luo, J. Li, X. Sun, J. Shen, W. Han and L. Wang, *J. Mater. Chem. A*, 2018, **6**, 11226-11235.
243. L. Shang, H. Yu, X. Huang, T. Bian, R. Shi, Y. Zhao, G. I. N. Waterhouse, L.-Z. Wu, C.-H. Tung and T. Zhang, *Adv. Mater.*, 2016, **28**, 1668-1674.
244. J. Zhu, D. Xu, L.-j. Ding and P.-c. Wang, *Chem. Eur. J.*, 2021, **27**, 2707-2716.
245. Z. Li, M. Hu, B. Liu, J. Liu, P. Wang, J. Yao, X. Zhang, M. He and W. Song, *ChemCatChem*, 2021, **13**, 868-873.
246. D. Kim, D. W. Kim, O. Buyukcakir, M.-K. Kim, K. Polychronopoulou and A. Coskun, *Adv. Funct. Mater.*, 2017, **27**, 1700706.
247. L. Sarango, J. Benito, I. Gascón, B. Zornoza and J. Coronas, *Microporous Mesoporous Mater.*, 2018, **272**, 44-52.
248. V. Chernikova, O. Shekhah and M. Eddaoudi, *ACS Appl. Mater. Interfaces*, 2016, **8**, 20459-20464.
249. L. Fan, M. Xue, Z. Kang, H. Li and S. Qiu, *J. Mater. Chem.*, 2012, **22**, 25272-25276.
250. I. Stassen, M. Styles, G. Grenci, Hans V. Gorp, W. Vanderlinden, Steven D. Feyter, P. Falcaro, D. D. Vos, P. Vereecken and R. Ameloot, *Nat. Mater.*, 2016, **15**, 304-310.
251. G. Lu and J. T. Hupp, *J. Am. Chem. Soc*, 2010, **132**, 7832-7833.
252. H. Bux, C. Chmelik, R. Krishna and J. Caro, *J. Membr. Sci.*, 2011, **369**, 284-289.
253. M.-J. Park and J.-S. Lee, *RSC Adv.*, 2017, **7**, 21045-21049.
254. L. Sarango, L. Paseta, M. Navarro, B. Zornoza and J. Coronas, *J. Ind. Eng. Chem.*, 2018, **59**, 8-16.
255. H. T. Kwon, H.-K. Jeong, A. S. Lee, H. S. An and J. S. Lee, *J. Am. Chem. Soc*, 2015, **137**, 12304-12311.
256. O. Shekhah, L. Fu, R. Sougrat, Y. Belmabkhout, A. J. Cairns, E. P. Giannelis and M. Eddaoudi, *Chem. Commun.*, 2012, **48**, 11434-11436.
257. G. Ramu, M. Lee and H.-K. Jeong, *Microporous Mesoporous Mater.*, 2018, **259**, 155-162.
258. X. Wang, S. Zhao, Y. Zhang, Z. Wang, J. Feng, S. Song and H. Zhang, *Chem. Sci.*, 2016, **7**, 1109-1114.
259. D. Wang, B. Yan, Y. Guo, L. Chen, F. Yu and G. Wang, *Sci. Rep.*, 2019, **9**, 5934.
260. Y. Zhang, T. Han, Z. Wang, C. Zhao, J. Li, T. Fei, S. Liu, G. Lu and T. Zhang, *Sens. Actuators B: Chem.*, 2017, **243**, 1231-1239.
261. Y. M. Chen, L. Yu and X. W. Lou, *Angew. Chem. Int. Ed.*, 2016, **55**, 5990-5993.
262. X. Song, S. Chen, L. Guo, Y. Sun, X. Li, X. Cao, Z. Wang, J. Sun, C. Lin and Y. Wang, *Adv. Energy Mater.*, 2018, **8**, 1801101.
263. J. Tao, M.-S. Lee, M. L. Sushko, J. J. De Yoreo, J. Liu, Z. Zhang, D. Banerjee, S. Akkineni, M. E. Bowden, P. K. Thallapally, Y. Shin and M. A. Sinnwell, *Chem. Mater.*, 2020, **32**, 6666-6675.
264. M. Li, J. Meng, Q. Li, M. Huang, X. Liu, K. A. Owusu, Z. Liu and L. Mai, *Adv. Funct. Mater.*, 2018, **28**, 1802016.
265. J. Meng, X. Liu, J. Li, Q. Li, C. Zhao, L. Xu, X. Wang, F. Liu, W. Yang, X. Xu, Z. Liu, C. Niu and L. Mai, *Nano Lett.*, 2017, **17**, 7773-7781.
266. Y. Yue, B. Guo, Z.-A. Qiao, P. F. Fulvio, J. Chen, A. J. Binder, C. Tian and S. Dai, *Microporous Mesoporous Mater.*, 2014, **198**, 139-143.

267. M. Schelling, M. Kim, E. Otal, M. Aguirre and J. P. Hinestroza, *Cellulose*, 2020, **27**, 6399-6410.
268. A. I. Khudiar, A. K. Elttayef, M. K. Khalaf and A. M. Oufi, *Mater. Res. Express*, 2019, **6**, 126450.
269. M. Shah, H. T. Kwon, V. Tran, S. Sachdeva and H.-K. Jeong, *Microporous Mesoporous Mater.*, 2013, **165**, 63-69.
270. F. Yu, Y. Chen, Y. Wang, C. Liu and J. Qin, *J. Mater. Res.*, 2020, **35**, 299-311.
271. Z. Li, M. Shao, L. Zhou, R. Zhang, C. Zhang, M. Wei, D. G. Evans and X. Duan, *Adv. Mater.*, 2016, **28**, 2337-2344.
272. Y. Yang, X. Yan, X. Hu, R. Feng and M. Zhou, *J. Colloid Interface Sci.*, 2017, **505**, 206-212.
273. Y. Qin, *Polym. Int.*, 2008, **57**, 171-180.
274. J. Nana, L. Daohao, H. Guiqing, S. Jin, L. Ping, W. Li, H. Bin, S. Xilin and Z. Xiaoliang, *J. Photonics Energy*, 2020, **10**, 1-10.
275. S. Ma, M. Zhang, J. Nie, J. Tan, S. Song and Y. Luo, *Carbohydr. Polym.*, 2019, **208**, 328-335.
276. M. Wang, J. Zhang, X. Yi, X. Zhao, B. Liu and X. Liu, *Appl. Surf. Sci.*, 2020, **507**, 145166.
277. Y. Li, H. Liu, H. Wang, J. Qiu and X. Zhang, *Chem. Sci.*, 2018, **9**, 4132-4141.
278. Q. Yang, R. Lu, S. Ren, C. Chen, Z. Chen and X. Yang, *Chem. Eng. J.*, 2018, **348**, 202-211.
279. K. Jayaramulu, K. K. R. Datta, C. Rösler, M. Petr, M. Otyepka, R. Zboril and R. A. Fischer, *Angew. Chem. Int. Ed.*, 2016, **55**, 1178-1182.
280. J. E. Ellis, Z. Zeng, S. I. Hwang, S. Li, T.-Y. Luo, S. C. Burkert, David L. White, N. L. Rosi, J. J. Gassensmith and A. Star, *Chem. Sci.*, 2019, **10**, 737-742.
281. Y. Li, Z. Lin, X. Wang, Z. Duan, P. Lu, S. Li, D. Ji, Z. Wang, G. Li, D. Yu and W. Liu, *Sep. Purif. Technol.*, 2021, **270**, 118794.
282. H. Nabipour, S. Nie, X. Wang, L. Song and Y. Hu, *Compos. Part A Appl. Sci. Manuf.*, 2020, **129**, 105720.
283. A. Prabhu, A. Al Shoaibi and C. Srinivasakannan, *Mater. Lett.*, 2015, **146**, 43-46.
284. J. Wen, H. Liu, Y. Zheng, Y. Wu and J. Gao, *Z. Anorg. Allg. Chem.*, 2020, **646**, 444-450.
285. M. Zhao, A. Tesfay Reda and D. Zhang, *ACS Omega*, 2020, **5**, 8012-8022.
286. M. Jiang, H. Li, L. Zhou, R. Xing and J. Zhang, *ACS Appl. Mater. Interfaces*, 2018, **10**, 827-834.
287. L. Zhu, L. Zong, X. Wu, M. Li, H. Wang, J. You and C. Li, *ACS Nano*, 2018, **12**, 4462-4468.
288. Y. Chen, S. Li, X. Pei, J. Zhou, X. Feng, S. Zhang, Y. Cheng, H. Li, R. Han and B. Wang, *Angew. Chem. Int. Ed.*, 2016, **55**, 3419-3423.
289. C. Liu, X. Huang, J. Liu, J. Wang, Z. Chen, R. Luo, C. Wang, J. Li, L. Wang, J. Wan and C. Yu, *Adv. Sci.*, 2020, **7**, 1901480.
290. Y. Liu, G. Li, Z. Chen and X. Peng, *J. Mater. Chem. A*, 2017, **5**, 9775-9784.
291. Y. Zhang, B. Lin, J. Wang, J. Tian, Y. Sun, X. Zhang and H. Yang, *J. Mater. Chem. A*, 2016, **4**, 10282-10293.
292. X. Liu, L. Zhang, X. Gao, C. Guan, Y. Hu and J. Wang, *ACS Appl. Mater. Interfaces*, 2019, **11**, 23236-23243.
293. H. Wang, Y. Wang, A. Jia, C. Wang, L. Wu, Y. Yang and Y. Wang, *Catal. Sci. Technol.*, 2017, **7**, 5572-5584.
294. L. Jiao, Y.-X. Zhou and H.-L. Jiang, *Chem. Sci.*, 2016, **7**, 1690-1695.
295. H. Zhang, W. Zhao, M. Zou, Y. Wang, Y. Chen, L. Xu, H. Wu and A. Cao, *Adv. Energy Mater.*, 2018, **8**, 1800013.

296. S.-K. Park and Y. C. Kang, *ACS Appl. Mater. Interfaces*, 2018, **10**, 17203-17213.
297. S. Tanaka, K. Okubo, K. Kida, M. Sugita and T. Takewaki, *J. Membr. Sci.*, 2017, **544**, 306-311.
298. J. A. Allegretto, A. Iborra, J. M. Giussi, C. von Bilderling, M. Ceolín, S. Moya, O. Azzaroni and M. Rafti, *Chem. Eur. J.*, 2020, **26**, 12388-12396.
299. J. Ma and B. Yan, *New J. Chem.*, 2018, **42**, 15061-15067.
300. A. Huang, W. Dou and J. Caro, *J. Am. Chem. Soc*, 2010, **132**, 15562-15564.
301. Z. Xie, J. Yang, J. Wang, J. Bai, H. Yin, B. Yuan, J. Lu, Y. Zhang, L. Zhou and C. Duan, *Chem. Commun.*, 2012, **48**, 5977-5979.
302. A. Huang, H. Bux, F. Steinbach and J. Caro, *Angew. Chem. Int. Ed.*, 2010, **49**, 4958-4961.
303. Q. Li, S. Gong, H. Zhang, F. Huang, L. Zhang and S. Li, *Chem. Eng. J.*, 2019, **371**, 26-33.
304. S.-L. Jian, L.-Y. Hsiao, M.-H. Yeh and K.-C. Ho, *J. Mater. Chem. A*, 2019, **7**, 1479-1490.
305. D. Wu, X. Zhang, J. Zhu and D. Cheng, *Engineered Science*, 2018, **2**, 49-56.
306. F. Fu, B. Zheng, L.-H. Xie, H. Du, S. Du and Z. Dong, *Crystals*, 2018, **8**, 367.
307. W. Zhang, Z.-Y. Wu, H.-L. Jiang and S.-H. Yu, *J. Am. Chem. Soc*, 2014, **136**, 14385-14388.
308. Y.-n. Wu, M. Zhou, B. Zhang, B. Wu, J. Li, J. Qiao, X. Guan and F. Li, *Nanoscale*, 2014, **6**, 1105-1112.
309. L. Hu, Z. Yan, J. Zhang, X. Peng, X. Mo, A. Wang and L. Chen, *J. Mater. Sci.*, 2019, **54**, 11009-11023.
310. X. Hu, X. Yan, M. Zhou and S. Komarneni, *Microporous Mesoporous Mater.*, 2016, **219**, 311-316.
311. H. Lee, M. Dellatore Shara, M. Miller William and B. Messersmith Phillip, *Science*, 2007, **318**, 426-430.
312. J. Ran, H. Chen, S. Bi, Q. Guo, C. Yan, X. Tang, D. Cheng, G. Cai and X. Wang, *Prog. Org. Coat.*, 2021, **152**, 106123.
313. A. Huang, Q. Liu, N. Wang and J. Caro, *J. Mater. Chem. A*, 2014, **2**, 8246-8251.
314. N. Li, G. Chen, J. Zhao, B. Yan, Z. Cheng, L. Meng and V. Chen, *J. Membr. Sci.*, 2019, **591**, 117341.
315. X.-p. Wang, J. Hou, F.-s. Chen and X.-m. Meng, *Sep. Purif. Technol.*, 2020, **236**, 116239.
316. J. Zhang, W. Zhang, T. Bao and Z. Chen, *J. Chromatogr. A*, 2015, **1388**, 9-16.
317. Z. Lei, Y. Deng and C. Wang, *J. Mater. Chem. A*, 2018, **6**, 3258-3263.
318. A. Huang, Q. Liu, N. Wang, Y. Zhu and J. Caro, *J. Am. Chem. Soc*, 2014, **136**, 14686-14689.
319. R. L. Papurello and J. M. Zamaro, *J. Mater. Sci.*, 2021, **56**, 9065-9078.
320. C. Zhang, Y. Li, H. Wang, S. He, Y. Xu, C. Zhong and T. Li, *Chem. Sci.*, 2018, **9**, 5672-5678.
321. W. Li, P. Su, Z. Li, Z. Xu, F. Wang, H. Ou, J. Zhang, G. Zhang and E. Zeng, *Nat. Commun.*, 2017, **8**, 406.
322. W. Li, W. Wu, Z. Li, J. Shi and Y. Xia, *J. Mater. Chem. A*, 2018, **6**, 16333-16340.
323. Z. Zhong, J. Yao, R. Chen, Z. Low, M. He, J. Z. Liu and H. Wang, *J. Mater. Chem. A*, 2015, **3**, 15715-15722.
324. Y. Luo, W. Cui, Y. Zou, H. Chu, F. Xu and L. Sun, *J. Therm. Anal. Calorim.*, 2020, **142**, 891-898.
325. J. B. James and Y. S. Lin, *J. Phys. Chem. C*, 2016, **120**, 14015-14026.
326. S. Tanaka and Y. Tanaka, *ACS Omega*, 2019, **4**, 19905-19912.

327. Z. Wang, T. Yan, J. Fang, L. Shi and D. Zhang, *J. Mater. Chem. A*, 2016, **4**, 10858-10868.
328. H. Jing, X. Song, S. Ren, Y. Shi, Y. An, Y. Yang, M. Feng, S. Ma and C. Hao, *Electrochim. Acta*, 2016, **213**, 252-259.
329. C. Young, R. R. Salunkhe, J. Tang, C.-C. Hu, M. Shahabuddin, E. Yanmaz, M. S. A. Hossain, J. H. Kim and Y. Yamauchi, *Phys. Chem. Chem. Phys.*, 2016, **18**, 29308-29315.
330. S. Chao, F. Zou, F. Wan, X. Dong, Y. Wang, Y. Wang, Q. Guan, G. Wang and W. Li, *Sci. Rep.*, 2017, **7**, 39789.
331. S. Gadipelli and Z. X. Guo, *ChemSusChem*, 2015, **8**, 2123-2132.
332. B. Chen, G. Ma, Y. Zhu and Y. Xia, *Sci. Rep.*, 2017, **7**, 5266.
333. H. Li, Y. He, T. He, S. Yan, X. Ma and J. Chen, *J. Mater. Sci.: Mater. Electron.*, 2019, **30**, 21388-21397.
334. H. Chen, K. Shen, J. Chen, X. Chen and Y. Li, *J. Mater. Chem. A*, 2017, **5**, 9937-9945.
335. Q. Yang, Z. Li, R. Zhang, L. Zhou, M. Shao and M. Wei, *Nano Energy*, 2017, **41**, 408-416.
336. R. Yang, X. Yan, Y. Li, X. Zhang and J. Chen, *ACS Appl. Mater. Interfaces*, 2017, **9**, 42482-42491.
337. Y. Li, X. Cai, S. Chen, H. Zhang, K. H. L. Zhang, J. Hong, B. Chen, D.-H. Kuo and W. Wang, *ChemSusChem*, 2018, **11**, 1040-1047.
338. G. Srinivas, V. Krungleviciute, Z.-X. Guo and T. Yildirim, *Energy Environ. Sci.*, 2014, **7**, 335-342.
339. Y. Wang, B. Wang, H. Shi, C. Zhang, C. Tao and J. Li, *Inorg. Chem. Front.*, 2018, **5**, 2739-2745.
340. S. Luidold and H. Antrekowitsch, *JOM*, 2007, **59**, 20-26.
341. C. Wang, X. Wang, F. Lai, Z. Liu, R. Dong, W. Li, H. Sun and B. Geng, *ACS Appl. Nano Mater.*, 2020, **3**, 5698-5705.
342. C. Wu, J. Guo, J. Zhang, Y. Zhao, J. Tian, T. T. Isimjan and X. Yang, *Renew. Energ.*, 2019, **136**, 1064-1070.
343. M. J. Behr, E. A. Gaulding, K. A. Mkhoyan and E. S. Aydil, *J. Appl. Phys.*, 2010, **108**, 053303.
344. Y. Li, K. Ji, Y. Duan, G. Meng and Z. Dai, *Coatings*, 2017, **7**, 221.
345. R. N. Othman, A. I. Ismadi and S. N. Tawil, *J. Phys. Conf. Ser.*, 2017, **829**, 012013.
346. N. Gupta, S. M. Gupta and S. K. Sharma, *Carbon Lett.*, 2019, **29**, 419-447.
347. M. H. Rümmeli, A. Bachmatiuk, F. Börrnert, F. Schäffel, I. Ibrahim, K. Cendrowski, G. Simha-Martynkova, D. Plachá, E. Borowiak-Palen, G. Cuniberti and B. Büchner, *Nanoscale Res. Lett.*, 2011, **6**, 303.
348. L. M. Hoyos-Palacio, A. G. García, J. F. Pérez-Robles, J. González and H. V. Martínez-Tejada, *IOP Conf. Ser.: Mater. Sci. Eng.*, 2014, **59**, 012005.
349. Y. Yin, X. Liu, X. Wei, R. Yu and J. Shui, *ACS Appl. Mater. Interfaces*, 2016, **8**, 34686-34698.
350. B. Y. Xia, Y. Yan, N. Li, H. B. Wu, X. W. Lou and X. Wang, *Nat. Energy*, 2016, **1**, 15006.
351. C. L. Mangun, K. R. Benak, J. Economy and K. L. Foster, *Carbon*, 2001, **39**, 1809-1820.
352. B. Stöhr, H. P. Boehm and R. Schlögl, *Carbon*, 1991, **29**, 707-720.
353. P. Vinke, M. van der Eijk, M. Verbree, A. F. Voskamp and H. van Bekkum, *Carbon*, 1994, **32**, 675-686.
354. R. J. J. Jansen and H. van Bekkum, *Carbon*, 1995, **33**, 1021-1027.

355. M. S. Shafeeyan, W. M. A. W. Daud, A. Houshmand and A. Arami-Niya, *Appl. Surf. Sci.*, 2011, **257**, 3936-3942.
356. J. Liu, S. Webster and D. L. Carroll, *J. Phys. Chem. B*, 2005, **109**, 15769-15774.
357. L. Ge, R. Lin, Z. Zhu and H. Wang, *J. Mater. Res.*, 2018, **33**, 538-545.
358. T.-N. Tran, C.-H. Shin, B.-J. Lee, J. S. Samdani, J.-D. Park, T.-H. Kang and J.-S. Yu, *Catal. Sci. Technol.*, 2018, **8**, 5368-5381.
359. Y. Qu, Z. Li, W. Chen, Y. Lin, T. Yuan, Z. Yang, C. Zhao, J. Wang, C. Zhao, X. Wang, F. Zhou, Z. Zhuang, Y. Wu and Y. Li, *Nat. Catal.*, 2018, **1**, 781-786.
360. M. Lan, R.-M. Guo, Y. Dou, J. Zhou, A. Zhou and J.-R. Li, *Nano Energy*, 2017, **33**, 238-246.
361. J. Park, J.-G. Song, T. Choi, S. Sim, H. Choi, S. W. Han, H.-B.-R. Lee, S.-H. Kim and H. Kim, *Curr. Appl. Phys.*, 2016, **16**, 691-695.
362. B. Chen, G. Ma, Y. Zhu, J. Wang, W. Xiong and Y. Xia, *J. Power Sources*, 2016, **334**, 112-119.
363. Z. Huang, Z. Yang, M. Z. Hussain, B. Chen, Q. Jia, Y. Zhu and Y. Xia, *Electrochim. Acta*, 2020, **330**, 135335.
364. Z. Huang, Z. Yang, M. Z. Hussain, Q. Jia, Y. Zhu and Y. Xia, *J. mater. sci. technol.*, 2021, **84**, 76-85.
365. X.-L. Yang, Y.-S. Ye, Z.-M. Wang, Z.-H. Zhang, Y.-L. Zhao, F. Yang, Z.-Y. Zhu and T. Wei, *ACS Omega*, 2020, **5**, 26230-26236.
366. Y. Zhuang, X. Zhang, Q. Chen, S. Li, H. Cao and Y. Huang, *Mater. Sci. Eng. C*, 2019, **94**, 858-866.
367. B. Chen, G. Ma, D. Kong, Y. Zhu and Y. Xia, *Carbon*, 2015, **95**, 113-124.
368. M. Z. Hussain, G. S. Pawar, Z. Huang, A. A. Tahir, R. A. Fischer, Y. Zhu and Y. Xia, *Carbon*, 2019, **146**, 348-363.
369. D. Ding, K. Shen, X. Chen, H. Chen, J. Chen, T. Fan, R. Wu and Y. Li, *ACS Catal.*, 2018, **8**, 7879-7888.
370. Y. Bai, J. Dong, Y. Hou, Y. Guo, Y. Liu, Y. Li, X. Han and Z. Huang, *Chem. Eng. J.*, 2019, **361**, 703-712.
371. D. Esken, H. Noei, Y. Wang, C. Wiktor, S. Turner, G. Van Tendeloo and R. A. Fischer, *J. Mater. Chem.*, 2011, **21**, 5907-5915.
372. Z.-B. Zhai, K.-J. Huang, X. Wu, H. Hu, Y. Xu and R.-M. Chai, *Dalton Trans.*, 2019, **48**, 4712-4718.
373. A. Abdul Razzaq, X. Yuan, Y. Chen, J. Hu, Q. Mu, Y. Ma, X. Zhao, L. Miao, J.-H. Ahn, Y. Peng and Z. Deng, *J. Mater. Chem. A*, 2020, **8**, 1298-1306.
374. P. Zeng, J. Li, M. Ye, K. Zhuo and Z. Fang, *Chem. Eur. J.*, 2017, **23**, 9517-9524.
375. P.-Z. Li, K. Aranishi and Q. Xu, *Chem. Commun.*, 2012, **48**, 3173-3175.
376. S. Feng, H. Zhong, J. Song, C. Zhu, P. Dong, Q. Shi, D. Liu, J. Li, Y.-C. Chang, S. P. Beckman, M.-k. Song, D. Du and Y. Lin, *ACS Appl. Energy Mater.*, 2018, **1**, 7014-7021.
377. C. Zhang, B. An, L. Yang, B. Wu, W. Shi, Y.-C. Wang, L.-S. Long, C. Wang and W. Lin, *J. Mater. Chem. A*, 2016, **4**, 4457-4463.
378. Y. Yi, W. Zhao, Z. Zeng, C. Wei, C. Lu, Y. Shao, W. Guo, S. Dou and J. Sun, *Small*, 2020, **16**, 1906566.
379. H. Hu, J. Zhang, B. Guan and X. W. Lou, *Angew. Chem. Int. Ed.*, 2016, **55**, 9514-9518.
380. H. Liu, Z. Li, L. Zhang, H. Ruan and R. Hu, *Nanoscale Res. Lett.*, 2019, **14**, 237.
381. X. Wang, X. Huang, W. Gao, Y. Tang, P. Jiang, K. Lan, R. Yang, B. Wang and R. Li, *J. Mater. Chem. A*, 2018, **6**, 3684-3691.
382. D. Esken, S. Turner, C. Wiktor, S. B. Kalidindi, G. Van Tendeloo and R. A. Fischer, *J. Am. Chem. Soc*, 2011, **133**, 16370-16373.

383. G. Ye, Q. He, S. Liu, K. Zhao, Y. Su, W. Zhu, R. Huang and Z. He, *J. Mater. Chem. A*, 2019, **7**, 16508-16515.
384. M. Zahmakiran, *Dalton Trans.*, 2012, **41**, 12690-12696.
385. M. Zhang, Y. Gao, C. Li and C. Liang, *Chinese J. Catal.*, 2015, **36**, 588-594.
386. D. Fairen-Jimenez, S. A. Moggach, M. T. Wharmby, P. A. Wright, S. Parsons and T. Düren, *J. Am. Chem. Soc*, 2011, **133**, 8900-8902.
387. D. I. Kolokolov, L. Diestel, J. Caro, D. Freude and A. G. Stepanov, *J. Phys. Chem. C*, 2014, **118**, 12873-12879.
388. G. Kakoulaki, I. Kougias, N. Taylor, F. Dolci, J. Moya and A. Jäger-Waldau, *Energy Convers. and Manag.*, 2021, **228**, 113649.
389. M. Z. Hussain, B. van der Linden, Z. Yang, Q. Jia, H. Chang, R. A. Fischer, F. Kapteijn, Y. Zhu and Y. Xia, *J. Mater. Chem. A*, 2021, **9**, 4103-4116.
390. M. Z. Hussain, Z. Yang, Z. Huang, Q. Jia, Y. Zhu and Y. Xia, *Adv. Sci.*, 2021, **8**, 2100625.
391. M. Z. Hussain, Z. Yang, B. v. d. Linden, Z. Huang, Q. Jia, E. Cerrato, R. A. Fischer, F. Kapteijn, Y. Zhu and Y. Xia, *J. Energy Chem.*, 2021, **57**, 485-495.
392. N. K. Oh, J. Seo, S. Lee, H.-J. Kim, U. Kim, J. Lee, Y.-K. Han and H. Park, *Nat. Commun.*, 2021, **12**, 4606.
393. J. Wang, H. Kong, J. Zhang, Y. Hao, Z. Shao and F. Ciucci, *Prog. Mater. Sci.*, 2021, **116**, 100717.
394. S. Li, X. Hao, A. Abudula and G. Guan, *J. Mater. Chem. A*, 2019, **7**, 18674-18707.
395. C. G. Morales-Guio, L.-A. Stern and X. Hu, *Chem. Soc. Rev.*, 2014, **43**, 6555-6569.
396. H. Jin, C. Guo, X. Liu, J. Liu, A. Vasileff, Y. Jiao, Y. Zheng and S.-Z. Qiao, *Chem. Rev.*, 2018, **118**, 6337-6408.
397. Q. Liang, G. Brocks and A. Bieberle-Hütter, *J. Phys. Energy*, 2021, **3**, 026001.
398. L. Li, P. Wang, Q. Shao and X. Huang, *Adv. Mater.*, 2021, **33**, 2004243.
399. S. Sultan, M. Ha, D. Y. Kim, J. N. Tiwari, C. W. Myung, A. Meena, T. J. Shin, K. H. Chae and K. S. Kim, *Nat. Commun.*, 2019, **10**, 5195.
400. P. Arunkumar, S. Gayathri and J. H. Han, *ACS Appl. Energy Mater.*, 2022, **5**, 2975-2992.
401. J. Sun, J. Li, Z. Li, X. Hu, H. Bai and X. Meng, *ACS Sustain. Chem. Eng.*, 2022, **10**, 4022-4030.
402. M. Wu, J. Zhao, C. Li and R. Liu, *J. Mater. Chem. A*, 2022, **10**, 4791-4799.
403. L. Fan, T. Meng, M. Yan, D. Wang, Y. Chen, Z. Xing, E. Wang and X. Yang, *Small*, 2021, **17**, 2100998.
404. H.-b. Zheng, Y.-l. Li, Y.-l. Wang, F. Ma, P.-z. Gao, W.-m. Guo, H. Qin, X.-p. Liu and H.-n. Xiao, *J. Alloys Compd.*, 2022, **894**, 162411.
405. W. Li, J. Liu, P. Guo, H. Li, B. Fei, Y. Guo, H. Pan, D. Sun, F. Fang and R. Wu, *Adv. Energy Mater.*, 2021, **11**, 2102134.
406. S. Li, C. Xu, Q. Zhou, Z. Liu, Z. Yang, Y. Gu, Y. Ma and W. Xu, *J. Alloys Compd.*, 2022, **902**, 163627.
407. J. Li, Y. Xu, L. Liang, R. Ge, J. Yang, B. Liu, J. Feng, Y. Li, J. Zhang, M. Zhu, S. Li and W. Li, *Sustain. Mater. Technol.*, 2022, **32**, e00421.
408. M. Guo, F. Qiu, Y. Yuan, T. Yu, C. Yuan and Z.-H. Lu, *Inorg. Chem.*, 2021, **60**, 16761-16768.
409. M. Li, M. Wang, D. Liu, Y. Pan, S. Liu, K. Sun, Y. Chen, H. Zhu, W. Guo, Y. Li, Z. Cui, B. Liu, Y. Liu and C. Liu, *J. Mater. Chem. A*, 2022, **10**, 6007-6015.
410. T. Rodenas, S. Beeg, I. Spanos, S. Neugebauer, F. Girgsdies, G. Algara-Siller, P. P. M. Schleker, P. Jakes, N. Pfänder, M. Willinger, M. Greiner, G. Prieto, R. Schlögl and S. Heumann, *Adv. Energy Mater.*, 2018, **8**, 1802404.

411. Z. Chen, H. Xu, Y. Ha, X. Li, M. Liu and R. Wu, *Appl. Catal. B: Environ.*, 2019, **250**, 213-223.
412. H. Chu, P. Feng, B. Jin, G. Ye, S. Cui, M. Zheng, G.-X. Zhang and M. Yang, *Chem. Eng. J.*, 2022, **433**, 133523.
413. A. Muthurasu, B. Dahal, T. Mukhiya, K. Chhetri and H. Y. Kim, *ACS Appl. Mater. Interfaces*, 2020, **12**, 41704-41717.
414. L. Zhang, Y. Chen, G. Liu, Z. Li, S. Liu, S. K. Tiwari, O. Ola, B. Pang, N. Wang and Y. Zhu, *ACS Omega*, 2022, **7**, 12846-12855.
415. X.-Z. Song, Y.-H. Zhao, W.-B. Yang, Y.-L. Meng, X. Chen, Z.-Y. Niu, X.-F. Wang and Z. Tan, *ACS Appl. Nano Mater.*, 2021, **4**, 13450-13458.
416. Y. Mei, Y. Cong, S. Huang, J. Qian, J. Ye and T.-T. Li, *Inorg. Chem.*, 2022, **61**, 1159-1168.
417. Y.-L. Wu, X. Li, Y.-S. Wei, Z. Fu, W. Wei, X.-T. Wu, Q.-L. Zhu and Q. Xu, *Adv. Mater.*, 2021, **33**, 2006965.
418. J. Hong, S. Hyun, M. Tsipoaka, J. S. Samdani and S. Shanmugam, *ACS Catal.*, 2022, **12**, 1718-1731.
419. X. Gu, Y.-G. Ji, J. Tian, X. Wu and L. Feng, *Chem. Eng. J.*, 2022, **427**, 131576.
420. Z. Wang, W. Xu, X. Chen, Y. Peng, Y. Song, C. Lv, H. Liu, J. Sun, D. Yuan, X. Li, X. Guo, D. Yang and L. Zhang, *Adv. Funct. Mater.*, 2019, **29**, 1902875.
421. H. Zhou, M. Zheng, H. Tang, B. Xu, Y. Tang and H. Pang, *Small*, 2020, **16**, 1904252.
422. F. Tang, X. Gao and Z. Jin, *Electrochim. Acta*, 2020, **337**, 135807.
423. D. Yin, M.-L. Wang, Y.-D. Cao, X. Yang, S.-Y. Ji, H.-P. Hao, G.-G. Gao, L.-L. Fan and H. Liu, *ACS Appl. Energy Mater.*, 2021, **4**, 6892-6902.
424. A. A. Lourenço, V. D. Silva, R. B. da Silva, U. C. Silva, C. Chesman, C. Salvador, T. A. Simões, D. A. Macedo and F. F. da Silva, *J. Colloid Interface Sci.*, 2021, **582**, 124-136.
425. Y. Wang, R. Dong, P. Tan, H. Liu, H. Liao, M. Jiang, Y. Liu, L. Yang and J. Pan, *J. Colloid Interface Sci.*, 2022, **609**, 617-626.
426. J. Zhou, H. Zheng, Q. Luan, X. Huang, Y. Li, Z. Xi, G. Lu, L. Xing and Y. Li, *Sustain. Energy Fuels*, 2019, **3**, 3201-3207.
427. Y. Li, T. Zhao, M. Lu, Y. Wu, Y. Xie, H. Xu, J. Gao, J. Yao, G. Qian and Q. Zhang, *Small*, 2019, **15**, 1901940.
428. S. Chen, X. Liu, H. Sun, Z. Cao, J. Xiong and Y. Li, *J. Alloys Compd.*, 2022, **897**, 163203.
429. Y. Wang, M. Xie, F. Dai, J. Liu, L. Zhang, R. Zhang, Z. Zhang and W. Hu, *J. Colloid Interface Sci.*, 2022, **615**, 725-731.
430. L. Gao, X. Cui, C. D. Sewell, J. Li and Z. Lin, *Chem. Soc. Rev.*, 2021, **50**, 8428-8469.
431. M. H. Naveen, T. L. Bui, L. Lee, R. Khan, W. Chung, R. Thota, S.-W. Joo and J. H. Bang, *ACS Appl. Mater. Interfaces*, 2022, **14**, 15165-15175.
432. Y. Zhang, W. Ye, J. Fan, V. Cecen, P. Shi, Y. Min and Q. Xu, *ACS Sustain. Chem. Eng.*, 2021, **9**, 11052-11061.
433. Y. Zhang, P. Wang, J. Yang, S. Lu, K. Li, G. Liu, Y. Duan and J. Qiu, *Carbon*, 2021, **177**, 344-356.
434. Y. Li, Z. Zhang, M. Xie, C. Li, Z. Shi and S. Feng, *Appl. Surf. Sci.*, 2022, **583**, 152402.
435. S. Huang, Z. Jin, Y. Ding, P. Ning, Q. Chen, J. Fu, Q. Zhang, J. Zhang, P. Xin, Y. Jiang and Z. Hu, *Small*, 2021, **17**, 2103178.
436. H. B. Wu, B. Y. Guan, P. He and X.-Y. Yu, *J. Mater. Chem. A*, 2018, **6**, 19338-19341.

437. A. A. Bunaciu, E. G. Udriştioiu and H. Y. Aboul-Enein, *Crit. Rev. Anal. Chem.*, 2015, **45**, 289-299.
438. W. Zhou, R. Apkarian, Z. L. Wang and D. Joy, in *Scanning microscopy for nanotechnology*, eds. W. Zhou and Z. L. Wang, Springer, 2006, ch. 1, pp. 1-40.
439. B. J. Inkson, in *Materials Characterization Using Nondestructive Evaluation (NDE) Methods*, eds. G. Hübschen, I. Altpeter, R. Tschuncky and H.-G. Herrmann, Woodhead Publishing, 2016, ch. 2, pp. 17-43.
440. N. Tanaka, in *Electron Nano-Imaging: Basics of Imaging and Diffraction for TEM and STEM*, ed. N. Tanaka, Springer Japan, 2017, pp. 17-28.
441. M. Abd Mutalib, M. A. Rahman, M. H. D. Othman, A. F. Ismail and J. Jaafar, in *Membrane Characterization*, eds. N. Hilal, A. F. Ismail, T. Matsuura and D. Oatley-Radcliffe, Elsevier, 2017, ch. 9, pp. 161-179.
442. D. C. Bell and A. J. Garratt-Reed, *Energy Dispersive X-ray Analysis in the Electron Microscope*, Taylor & Francis, 2003.
443. J. S. Gaffney, N. A. Marley and D. E. Jones, in *Characterization of Materials*, Wiley, 2012, pp. 1-33.
444. P. Colomban and G. Gouadec, in *Raman Spectroscopy for Soft Matter Applications*, ed. M. S. Amer, Wiley, 2009, ch. 2, pp. 11-29.
445. K. N. Kudin, B. Ozbas, H. C. Schniepp, R. K. Prud'homme, I. A. Aksay and R. Car, *Nano Lett.*, 2008, **8**, 36-41.
446. A. C. Ferrari and J. Robertson, *Phys. Rev. B*, 2000, **61**, 14095-14107.
447. D. B. Schuepfer, F. Badaczewski, J. M. Guerra-Castro, D. M. Hofmann, C. Heiliger, B. Smarsly and P. J. Klar, *Carbon*, 2020, **161**, 359-372.
448. L. Zou and H.-C. Zhou, in *Nanostructured Materials for Next-Generation Energy Storage and Conversion: Hydrogen Production, Storage, and Utilization*, eds. Y.-P. Chen, S. Bashir and J. L. Liu, Springer, 2017, pp. 143-170.
449. P. van der Heide, *X-ray Photoelectron Spectroscopy: An introduction to Principles and Practices*, Wiley, 2011.
450. A. J. Bard, L. R. Faulkner and H. S. White, in *Electrochemical Methods: Fundamentals and Applications*, ed. D. Harris, Wiley New York, 2 edn., 2001, ch. 14, pp. 580-632.
451. M. Jahan, Z. Liu and K. P. Loh, *Adv. Funct. Mater.*, 2013, **23**, 5363-5372.
452. M. Bouroushian, *Electrochemistry of metal chalcogenides*, Springer, 1 edn., 2010.
453. X. Chia, A. Y. Eng, A. Ambrosi, S. M. Tan and M. Pumera, *Chem. Rev.*, 2015, **115**, 11941-11966.
454. D. Voiry, H. Yamaguchi, J. Li, R. Silva, D. C. Alves, T. Fujita, M. Chen, T. Asefa, V. B. Shenoy, G. Eda and M. Chhowalla, *Nat. Mater.*, 2013, **12**, 850-855.
455. G. Ye, Y. Gong, J. Lin, B. Li, Y. He, S. T. Pantelides, W. Zhou, R. Vajtai and P. M. Ajayan, *Nano Lett.*, 2016, **16**, 1097-1103.
456. S. Peng, L. Li, J. Zhang, T. L. Tan, T. Zhang, D. Ji, X. Han, F. Cheng and S. Ramakrishna, *J. Mater. Chem. A*, 2017, **5**, 23361-23368.
457. L. Tao, X. Duan, C. Wang, X. Duan and S. Wang, *Chem. Commun.*, 2015, **51**, 7470-7473.
458. G. B. de-Mello, L. Smith, S. J. Rowley-Neale, J. Gruber, S. J. Hutton and C. E. Banks, *RSC Adv.*, 2017, **7**, 36208-36213.
459. D. Voiry, M. Salehi, R. Silva, T. Fujita, M. Chen, T. Asefa, V. B. Shenoy, G. Eda and M. Chhowalla, *Nano Lett.*, 2013, **13**, 6222-6227.
460. X. Li, G. Zhu, Q. Kang, Z.-D. Huang, X. Feng, Y. Li, R. Liu and Y. Ma, *RSC Adv.*, 2015, **5**, 55396-55400.
461. P. Ganesan, M. Prabu, J. Sanetuntikul and S. Shanmugam, *ACS Catal.*, 2015, **5**, 3625-3637.

462. X. Zhou, X. Yang, H. Li, M. N. Hedhili, K.-W. Huang, L.-J. Li and W. Zhang, *J. Mater. Chem. A*, 2017, **5**, 15552-15558.
463. X. Shang, J.-Q. Chi, S.-S. Lu, B. Dong, X. Li, Y.-R. Liu, K.-L. Yan, W.-K. Gao, Y.-M. Chai and C.-G. Liu, *Int. J. Hydrog. Energy*, 2017, **42**, 4165-4173.
464. Y. R. Liu, W. H. Hu, X. Li, B. Dong, X. Shang, G. Q. Han, Y. M. Chai, Y. Q. Liu and C. G. Liu, *Appl. Surf. Sci.*, 2016, **384**, 51-57.
465. E. L. First and C. A. Floudas, *Microporous Mesoporous Mater.*, 2013, **165**, 32-39.
466. J. J. Walsh, A. M. Bond, R. J. Forster and T. E. Keyes, *Coord. Chem. Rev.*, 2016, **306**, 217-234.
467. D. Y. Du, J. S. Qin, S. L. Li, Z. M. Su and Y. Q. Lan, *Chem. Soc. Rev.*, 2014, **43**, 4615-4632.
468. J. S. Qin, D. Y. Du, W. Guan, X. J. Bo, Y. F. Li, L. P. Guo, Z. M. Su, Y. Y. Wang, Y. Q. Lan and H. C. Zhou, *J. Am. Chem. Soc.*, 2015, **137**, 7169-7177.
469. H. B. Wu, B. Y. Xia, L. Yu, X. Y. Yu and X. W. Lou, *Nat. Commun.*, 2015, **6**, 6512.
470. Y. J. Tang, M. R. Gao, C. H. Liu, S. L. Li, H. L. Jiang, Y. Q. Lan, M. Han and S. H. Yu, *Angew. Chem. Int. Ed.*, 2015, **54**, 12928-12932.
471. Q. Lan, Z. M. Zhang, C. Qin, X. L. Wang, Y. G. Li, H. Q. Tan and E. B. Wang, *Chem. Eur. J.*, 2016, **22**, 15513-15520.
472. J. S. Li, Y. J. Tang, C. H. Liu, S. L. Li, R. H. Li, L. Z. Dong, Z. H. Dai, J. C. Bao and Y. Q. Lan, *J. Mater. Chem. A*, 2016, **4**, 1202-1207.
473. Z. P. Shi, Y. X. Wang, H. L. Lin, H. B. Zhang, M. K. Shen, S. H. Xie, Y. H. Zhang, Q. S. Gao and Y. Tang, *J. Mater. Chem. A*, 2016, **4**, 6006-6013.
474. L. Zhang, T. Mi, M. A. Ziaee, L. Liang and R. Wang, *J. Mater. Chem. A*, 2018, **6**, 1639-1647.
475. J. Qian, F. Sun and L. Qin, *Mater Lett*, 2012, **82**, 220-223.
476. L. Lan, G. Xie, T. Wu, D. Feng and X. Ma, *RSC Adv.*, 2016, **6**, 55894-55902.
477. Z. Zuhra, H. Lei, Z. Zhao, Y. Zhou, L. Zhang and L. Qin, *New J. Chem.*, 2017, **41**, 8382-8389.
478. S. Farhadi, M. M. Amini and F. Mahmoudi, *RSC Adv.*, 2016, **6**, 102984-102996.
479. F. Xu, T. P. Almeida, H. Chang, Y. Xia, M. L. Wears and Y. Zhu, *Nanoscale*, 2013, **5**, 10504-10510.
480. B. Chen, R. Li, G. Ma, X. Gou, Y. Zhu and Y. Xia, *Nanoscale*, 2015, **7**, 20674-20684.
481. Y. Feldman, E. Wasserman, D. J. Srolovitz and R. Tenne, *Science*, 1995, **267**, 222-225.
482. H. Yang, S. Liu, J. Li, M. Li, G. Peng and G. Zou, *Nanotechnology*, 2006, **17**, 1512.
483. M. Domínguez, E. Taboada, H. Idriss, E. Molins and J. Llorca, *J. Mater. Chem.*, 2010, **20**, 4875-4883.
484. X. Li, C. Zeng, J. Jiang and L. Ai, *J. Mater. Chem. A*, 2016, **4**, 7476-7482.
485. P. D. Tran, S. Y. Chiam, P. P. Boix, Y. Ren, S. S. Pramana, J. Fize, V. Artero and J. Barber, *Energy Environ. Sci.*, 2013, **6**, 2452-2459.
486. J. R. Regalbuto, T. H. Fleisch and E. E. Wolf, *J. Catal.*, 1987, **107**, 114-128.
487. K. Nishiyama, R. Matsuo, J. Sasano, S. Yokoyama and M. Izaki, *AIP Adv.*, 2017, **7**, 035004.
488. C. Liu, Y. Qiu, Y. Xia, F. Wang, X. Liu, X. Sun, Q. Liang and Z. Chen, *Nanotechnology*, 2017, **28**, 445403.
489. T. A. J. Loh, D. H. C. Chua and A. T. S. Wee, *Sci. Rep.*, 2015, **5**, 18116.

490. J. Huang, X. Wang, J. Li, L. Cao, Z. Xu and H. Wei, *J. Alloys Compd.*, 2016, **673**, 60-66.
491. J. Wang, R. Ma, Z. Zhou, G. Liu and Q. Liu, *Sci. Rep.*, 2015, **5**, 9304.
492. G. Li, J. Sun, W. Hou, S. Jiang, Y. Huang and J. Geng, *Nat. Commun.*, 2016, **7**, 10601.
493. A. Dychalska, P. Popielarski, W. Frankow, K. Fabisiak, K. Paprocki and M. Szybowicz, *Mater. Sci.*, 2015, **33**, 799-805.
494. H. Jiang, J. X. Gu, X. S. Zheng, M. Liu, X. Q. Qiu, L. B. Wang, W. Z. Li, Z. F. Chen, X. B. Ji and J. Li, *Energy Environ. Sci.*, 2019, **12**, 322-333.
495. J. D. Benck, T. R. Hellstern, J. Kibsgaard, P. Chakthranont and T. F. Jaramillo, *ACS Catal.*, 2014, **4**, 3957-3971.
496. Y. H. Li, P. F. Liu, L. F. Pan, H. F. Wang, Z. Z. Yang, L. R. Zheng, P. Hu, H. J. Zhao, L. Gu and H. G. Yang, *Nat. Commun.*, 2015, **6**, 8064.
497. T. Zheng, W. Sang, Z. He, Q. Wei, B. Chen, H. Li, C. Cao, R. Huang, X. Yan, B. Pan, S. Zhou and J. Zeng, *Nano Lett.*, 2017, **17**, 7968-7973.
498. M. Jahan, Z. Liu and K. P. Loh, *Adv. Funct. Mater.*, 2013, **23**, 5363-5372.
499. L. Wang, X. Wu, S. Guo, M. Han, Y. Zhou, Y. Sun, H. Huang, Y. Liu and Z. Kang, *J. Mater. Chem. A*, 2017, **5**, 2717-2723.
500. J. Huang, D. Hou, Y. Zhou, W. Zhou, G. Li, Z. Tang, L. Li and S. Chen, *J. Mater. Chem. A*, 2015, **3**, 22886-22891.
501. T. A. Shifa, F. Wang, Z. Cheng, X. Zhan, Z. Wang, K. Liu, M. Safdar, L. Sun and J. He, *Nanoscale*, 2015, **7**, 14760-14765.
502. M. Cai, J. Han, Y. Lin, W. Liu, X. Luo, H. Zhang and M. Zhong, *Electrochim. Acta*, 2018, **287**, 1-9.
503. X. Shang, J. Q. Chi, S. S. Lu, B. Dong, X. Li, Y. R. Liu, K. L. Yan, W. K. Gao, Y. M. Chai and C. G. Liu, *Int. J. Hydrogen Energy*, 2017, **42**, 4165-4173.
504. L. Yang, X. Wu, X. Zhu, C. He, M. Meng, Z. Gan and P. K. Chu, *Appl. Surf. Sci.*, 2015, **341**, 149-156.
505. Y. Jia, L. Z. Zhang, A. J. Du, G. P. Gao, J. Chen, X. C. Yan, C. L. Brown and X. D. Yao, *Adv. Mater.*, 2016, **28**, 9532-9538.
506. L. Wu, K. Zhang, T. Wang, X. Xu, Y. Zhao, Y. Sun, W. Zhong and Y. Du, *ACS Appl. Nano Mater.*, 2018, **1**, 1083-1093.
507. I. S. Amiinu, X. Liu, Z. Pu, W. Li, Q. Li, J. Zhang, H. Tang, H. Zhang and S. Mu, *Adv. Funct. Mater.*, 2017, **28**, 1704638.
508. J. Long, Y. Gong and J. Lin, *J. Mater. Chem. A*, 2017, **5**, 10495-10509.
509. X. Zhang, S. Liu, Y. Zang, R. Liu, G. Liu, G. Wang, Y. Zhang, H. Zhang and H. Zhao, *Nano Energy*, 2016, **30**, 93-102.
510. J. Wang, H.-x. Zhong, Z.-l. Wang, F.-l. Meng and X.-b. Zhang, *ACS Nano*, 2016, **10**, 2342-2348.
511. P. Guo, Y.-X. Wu, W.-M. Lau, H. Liu and L.-M. Liu, *J. Alloys Compd.*, 2017, **723**, 772-778.
512. I. S. Amiinu, Z. Pu, X. Liu, K. A. Owusu, H. G. R. Monestel, F. O. Boakye, H. Zhang and S. Mu, *Adv. Funct. Mater.*, 2017, **27**, 1702300.
513. X. Chia, A. Y. S. Eng, A. Ambrosi, S. M. Tan and M. Pumera, *Chem. Rev.*, 2015, **115**, 11941-11966.
514. X. Wu, H. Zhang, J. Zhang and X. W. Lou, *Adv. Mater.*, 2021, **33**, 2008376.
515. P. Zhuang, Y. Sun, P. Dong, W. Smith, Z. Sun, Y. Ge, Y. Pei, Z. Cao, P. M. Ajayan, J. Shen and M. Ye, *Adv. Funct. Mater.*, 2019, **29**, 1901290.
516. X. Zhang, F. Zhou, S. Zhang, Y. Liang and R. Wang, *Adv. Sci.*, 2019, **6**, 1900090.
517. E. German and R. Gebauer, *Appl. Surf. Sci.*, 2020, **528**, 146591.

518. Y. Li, Z. Yin, M. Cui, X. Liu, J. Xiong, S. Chen and T. Ma, *J. Mater. Chem. A*, 2021, **9**, 2070-2092.
519. H. Wang, W. Zhang, X. Zhang, S. Hu, Z. Zhang, W. Zhou and H. Liu, *Nano Res.*, 2021, **14**, 4857-4864.
520. W.-H. Huang, X.-M. Li, X.-F. Yang, H.-B. Zhang, F. Wang and J. Zhang, *Chem. Commun.*, 2021, **57**, 4847-4850.
521. V. Ganesan and J. Kim, *Int. J. Hydrog. Energy*, 2020, **45**, 13290-13299.
522. Y. Guo, J. Tang, Z. Wang, Y.-M. Kang, Y. Bando and Y. Yamauchi, *Nano Energy*, 2018, **47**, 494-502.
523. C.-A. Chen, C.-L. Lee, P.-K. Yang, D.-S. Tsai and C.-P. Lee, *Catalysts*, 2021, **11**, 151.
524. R. Abinaya, J. Archana, S. Harish, M. Navaneethan, S. Ponnusamy, C. Muthamizhchelvan, M. Shimomura and Y. Hayakawa, *RSC Adv.*, 2018, **8**, 26664-26675.
525. H. Wang, Z. Xu, Z. Zhang, S. Hu, M. Ma, Z. Zhang, W. Zhou and H. Liu, *Nanoscale*, 2020, **12**, 22541-22550.
526. L. Wang, L. Wang, X. Meng and F.-S. Xiao, *Adv. Mater.*, 2019, **31**, 1901905.
527. Y. Jazaa, T. Lan, S. Padalkar and S. Sundararajan, *Lubricants*, 2018, **6**, 106.
528. Z. Huang, Z. Yang, M. Z. Hussain, Q. Jia, Y. Zhu and Y. Xia, *J. Mater. Sci. Technol.*, 2021, **84**, 76-85.
529. X. Zheng, J. Xu, K. Yan, H. Wang, Z. Wang and S. Yang, *Chem. Mater.*, 2014, **26**, 2344-2353.
530. H. Li, K. Yu, C. Li, Z. Tang, B. Guo, X. Lei, H. Fu and Z. Zhu, *Sci. Rep.*, 2015, **5**, 18730.
531. X. Yu, M. Zhang, J. Chen, Y. Li and G. Shi, *Adv. Energy Mater.*, 2016, **6**, 1501492.
532. Z. Huang, Z. Yang, M. Z. Hussain, B. Chen, Q. Jia, Y. Zhu and Y. Xia, *Electrochim. Acta*, 2020, **330**, 135335.
533. S. Gao, J. Hou, Z. Deng, T. Wang, S. Beyer, A. G. Buzanich, J. J. Richardson, A. Rawal, R. Seidel, M. Y. Zulkifli, W. Li, T. D. Bennett, A. K. Cheetham, K. Liang and V. Chen, *Chem*, 2019, **5**, 1597-1608.
534. J. Javidi, M. Esmaeilpour, Z. Rahiminezhad and F. N. Dodeji, *J Clust Sci*, 2014, **25**, 1511-1524.
535. H. Wei, J. Ren, B. Han, L. Xu, L. Han and L. Jia, *Colloids Surf. B*, 2013, **110**, 22-28.
536. P. Zhou, J. Cheng, Y. Yan, S. Xu and C. Zhou, *Sep. Purif. Technol.*, 2021, **272**, 118871.
537. Z. Zhu, R. Tain and C. Rhodes, *Can. J. Chem.*, 2003, **81**, 1044-1050.
538. A. Patel, N. Narkhede and A. Patel, *Catal. Surv. from Asia*, 2019, **23**, 257-264.
539. K. M. Im, T.-W. Kim and J.-R. Jeon, *ACS Biomater. Sci. Eng.*, 2017, **3**, 628-636.
540. L. Sun, C. Wang, X. Wang and L. Wang, *Small*, 2018, **14**, 1800090.
541. J. Ran, L. Xiao, W. Wu, Y. Liu, W. Qiu and J. Wu, *Nanotechnology*, 2016, **28**, 055604.
542. J. Qin, S. Wang and X. Wang, *Appl. Catal. B: Environ.*, 2017, **209**, 476-482.
543. W. Kong, J. Li, Y. Chen, Y. Ren, Y. Guo, S. Niu and Y. Yang, *Appl. Surf. Sci.*, 2018, **437**, 161-168.
544. M. Zhang, C. Wang, R. Luo, W. Zhang, S. Chen, X. Yan, J. Qi, X. Sun, L. Wang and J. Li, *J. Mater. Chem. A*, 2019, **7**, 5173-5178.
545. P. Muhammed Shafi and A. Chandra Bose, *AIP Adv.*, 2015, **5**, 057137.
546. K. N. Kudin, B. Ozbas, H. C. Schniepp, R. K. Prud'homme, I. A. Aksay and R. Car, *Nano Lett.*, 2008, **8**, 36-41.
547. A. C. Ferrari and J. Robertson, *Phys. Rev. B*, 2000, **61**, 14095-14107.

548. L. Deng, Z. Yang, R. Li, B. Chen, Q. Jia, Y. Zhu and Y. Xia, *Front. Chem. Sci. Eng.*, 2021, **15**, 1487-1499.
549. D. H. Kweon, M. S. Okyay, S.-J. Kim, J.-P. Jeon, H.-J. Noh, N. Park, J. Mahmood and J.-B. Baek, *Nat. Commun.*, 2020, **11**, 1278.
550. H. Han, Z. Bai, T. Zhang, X. Wang, X. Yang, X. Ma, Y. Zhang, L. Yang and J. Lu, *Nano Energy*, 2019, **56**, 724-732.
551. F. Yang, P. Zhao, X. Hua, W. Luo, G. Cheng, W. Xing and S. Chen, *J. Mater. Chem. A*, 2016, **4**, 16057-16063.
552. Y. Zhong, Y. Zhang, G. Zhang, R. Li and X. Sun, *Appl. Surf. Sci.*, 2012, **263**, 410-415.
553. P. Mallet, H. Guyot, J. Y. Veuillen and N. Motta, *Phys. Rev. B*, 2001, **63**, 165428.
554. Z. Chen, A. Liao, Z. Guo, F. Yu, T. Mei, Z. Zhang, M. S. Irshad, C. Liu, L. Yu and X. Wang, *Electrochim. Acta*, 2020, **353**, 136561.
555. S. H. Yang, S.-K. Park, J. K. Kim and Y. C. Kang, *J. Mater. Chem. A*, 2019, **7**, 13751-13761.
556. R. Wei, K. Zhang, P. Zhao, Y. An, C. Tang, C. Chen, X. Li, X. Ma, Y. Ma and X. Hao, *Appl. Surf. Sci.*, 2021, **549**, 149327.
557. J. Xie, X. Yang and Y. Xie, *Nanoscale*, 2020, **12**, 4283-4294.
558. W. Hong, M. Kitta and Q. Xu, *Small Methods*, 2018, **2**, 1800214.
559. F. Bu, W. Chen, M. F. Aly Aboud, I. Shakir, J. Gu and Y. Xu, *J. Mater. Chem. A*, 2019, **7**, 14526-14535.
560. Y. Sun, J. Wang, B. Zhao, R. Cai, R. Ran and Z. Shao, *J. Mater. Chem. A*, 2013, **1**, 4736-4746.
561. J.-W. Shi, Y. Zou, D. Ma, Z. Fan, L. Cheng, D. Sun, Z. Wang, C. Niu and L. Wang, *Nanoscale*, 2018, **10**, 9292-9303.
562. C. Ray, S. C. Lee, K. V. Sankar, B. Jin, J. Lee, J. H. Park and S. C. Jun, *ACS Appl. Mater. Interfaces*, 2017, **9**, 37739-37749.
563. X. Ma, W. Chen, Q. Li, L. Xue and C. Peng, *Energy Environ. Mater.*, 2021, **4**, 658-663.
564. J. Zhang, D. Meng, H. Huang, H. Cai, Q. Huang, J. Wang, Y. Yang, X. Zhai, Z. Fu and Y. Lu, *AIP Adv.*, 2018, **8**, 025322.
565. X. Cui, W. Li, K. Junge, Z. Fei, M. Beller and P. J. Dyson, *Angew. Chem. Int. Ed.*, 2020, **59**, 7501-7507.
566. A. Macedo Andrade, Z. Liu, S. Grewal, A. J. Nelson, Z. Nasef, G. Diaz and M. H. Lee, *Dalton Trans.*, 2021, **50**, 5473-5482.
567. B. Chen, X. He, F. Yin, H. Wang, D.-J. Liu, R. Shi, J. Chen and H. Yin, *Adv. Funct. Mater.*, 2017, **27**, 1700795.
568. J. Cui, Y. Qiu, H. Zhang, Z. Yao, W. Zhao, Y. Liu and J. Sun, *Solid State Ion.*, 2021, **361**, 115548.
569. A. Abdul Razzaq, Y. Yao, R. Shah, P. Qi, L. Miao, M. Chen, X. Zhao, Y. Peng and Z. Deng, *Energy Stor. Mater.*, 2019, **16**, 194-202.
570. G. Li, J. Sun, W. Hou, S. Jiang, Y. Huang and J. Geng, *Nat. Commun.*, 2016, **7**, 10601.
571. Y. Ling, Z. Yang, Q. Zhang, Y. Zhang, W. Cai and H. Cheng, *Chem. Commun.*, 2018, **54**, 2631-2634.
572. L. Liu and A. Corma, *Chem. Rev.*, 2018, **118**, 4981-5079.
573. Y. Huang, Y. Sun, X. Zheng, T. Aoki, B. Pattengale, J. Huang, X. He, W. Bian, S. Younan, N. Williams, J. Hu, J. Ge, N. Pu, X. Yan, X. Pan, L. Zhang, Y. Wei and J. Gu, *Nat. Commun.*, 2019, **10**, 982.
574. T. Li and G. Galli, *J. Phys. Chem. C*, 2007, **111**, 16192-16196.

575. T. F. Jaramillo, K. P. Jørgensen, J. Bonde, J. H. Nielsen, S. Horch and I. Chorkendorff, *Science*, 2007, **317**, 100-102.
576. B. Hinnemann, P. G. Moses, J. Bonde, K. P. Jørgensen, J. H. Nielsen, S. Horch, I. Chorkendorff and J. K. Nørskov, *J. Am. Chem. Soc.*, 2005, **127**, 5308-5309.
577. D. Merki, H. Vrubel, L. Rovelli, S. Fierro and X. Hu, *Chem. Sci.*, 2012, **3**, 2515-2525.
578. J. Deng, H. Li, S. Wang, D. Ding, M. Chen, C. Liu, Z. Tian, K. S. Novoselov, C. Ma, D. Deng and X. Bao, *Nat. Commun.*, 2017, **8**, 14430.
579. Y. Shi, Y. Zhou, D.-R. Yang, W.-X. Xu, C. Wang, F.-B. Wang, J.-J. Xu, X.-H. Xia and H.-Y. Chen, *J. Am. Chem. Soc.*, 2017, **139**, 15479-15485.
580. M. Hakala, R. Kronberg and K. Laasonen, *Sci. Rep.*, 2017, **7**, 15243.
581. C. Di Giovanni, W.-A. Wang, S. Nowak, J.-M. Grenèche, H. Lecoq, L. Mouton, M. Giraud and C. Tard, *ACS Catal.*, 2014, **4**, 681-687.
582. C. D. Giovanni, Á. Reyes-Carmona, A. Coursier, S. Nowak, J. M. Grenèche, H. Lecoq, L. Mouton, J. Rozière, D. Jones, J. Peron, M. Giraud and C. Tard, *ACS Catal.*, 2016, **6**, 2626-2631.
583. S. Chen, Z. Kang, X. Zhang, J. Xie, H. Wang, W. Shao, X. Zheng, W. Yan, B. Pan and Y. Xie, *ACS Cent. Sci.*, 2017, **3**, 1221-1227.
584. Y. Guo, C. Shang, X. Zhang and E. Wang, *Chem. Commun.*, 2016, **52**, 11795-11798.
585. H. Wang, C. Tsai, D. Kong, K. Chan, F. Abild-Pedersen, J. K. Nørskov and Y. Cui, *Nano Res.*, 2015, **8**, 566-575.
586. X. Zhao, X. Ma, Q. Lu, Q. Li, C. Han, Z. Xing and X. Yang, *Electrochim. Acta*, 2017, **249**, 72-78.
587. S. Chen, S. Huang, J. Hu, S. Fan, Y. Shang, M. E. Pam, X. Li, Y. Wang, T. Xu, Y. Shi and H. Y. Yang, *Nano-Micro Lett.*, 2019, **11**, 80.
588. Y. Guo, Z. Yao, B. J. J. Timmer, X. Sheng, L. Fan, Y. Li, F. Zhang and L. Sun, *Nano Energy*, 2019, **62**, 282-288.
589. P. Horcajada, S. Surblé, C. Serre, D.-Y. Hong, Y.-K. Seo, J.-S. Chang, J.-M. Grenèche, I. Margiolaki and G. Férey, *Chem. Commun.*, 2007, 2820-2822.
590. R. Liang, R. Chen, F. Jing, N. Qin and L. Wu, *Dalton Trans.*, 2015, **44**, 18227-18236.
591. W. Sun, Y. Si, H. Jing, Z. Dong, C. Wang, Y. Zhang, L. Zhao, W. Feng and Y. Yan, *Chem. Res. Chin. Uni.*, 2018, **34**, 464-469.
592. W. Chen, X. Zhang, L. Mi, C. Liu, J. Zhang, S. Cui, X. Feng, Y. Cao and C. Shen, *Adv. Mater.*, 2019, **31**, 1806664.
593. J. Yang, X. Wang, B. Li, L. Ma, L. Shi, Y. Xiong and H. Xu, *Adv. Funct. Mater.*, 2017, **27**, 1606497.
594. Y. Ding, Y. Niu, J. Yang, L. Ma, J. Liu, Y. Xiong and H. Xu, *Small*, 2016, **12**, 5414-5421.
595. T. Szatkowski, M. Wysokowski, G. Lota, D. Pęziak, V. V. Bazhenov, G. Nowaczyk, J. Walter, S. L. Molodtsov, H. Stöcker, C. Himcinschi, I. Petrenko, A. L. Stelling, S. Jurga, T. Jesionowski and H. Ehrlich, *RSC Adv.*, 2015, **5**, 79031-79040.
596. P. M. Hallam, M. Gómez-Mingot, D. K. Kampouris and C. E. Banks, *RSC Adv.*, 2012, **2**, 6672-6679.
597. A. C. Domask, R. L. Gurunathan and S. E. Mohney, *J. Electron. Mater.*, 2015, **44**, 4065-4079.
598. Y.-J. Tang, A. M. Zhang, H.-J. Zhu, L.-Z. Dong, X.-L. Wang, S.-L. Li, M. Han, X.-X. Xu and Y.-Q. Lan, *Nanoscale*, 2018, **10**, 8404-8412.

599. Q. Zhang, J. Liao, M. Liao, J. Dai, H. Ge, T. Duan and W. Yao, *Appl. Surf. Sci.*, 2019, **473**, 799-806.
600. D. Zhang, B. Li, S. Wang and S. Yang, *ACS Appl. Mater. Interfaces*, 2017, **9**, 40265-40272.
601. Z. Liu, F. Wang, M. Li and Z.-H. Ni, *RSC Adv.*, 2016, **6**, 37500-37505.
602. Y. Zhou, Y. Leng, W. Zhou, J. Huang, M. Zhao, J. Zhan, C. Feng, Z. Tang, S. Chen and H. Liu, *Nano Energy*, 2015, **16**, 357-366.
603. Y. Tian, Z. Wei, X. Wang, S. Peng, X. Zhang and W.-m. Liu, *Int. J. Hydrog. Energy*, 2017, **42**, 4184-4192.
604. G. Tai, T. Zeng, J. Yu, J. Zhou, Y. You, X. Wang, H. Wu, X. Sun, T. Hu and W. Guo, *Nanoscale*, 2016, **8**, 2234-2241.
605. P. Qin, G. Fang, W. Ke, F. Cheng, Q. Zheng, J. Wan, H. Lei and X. Zhao, *J. Mater. Chem. A*, 2014, **2**, 2742-2756.
606. M.-L. Grutza, A. Rajagopal, C. Streb and P. Kurz, *Sustain. Energy Fuels*, 2018, **2**, 1893-1904.
607. L. Ma, L. R. L. Ting, V. Molinari, C. Giordano and B. S. Yeo, *J. Mater. Chem. A*, 2015, **3**, 8361-8368.
608. X. Xiao, D. Huang, Y. Fu, M. Wen, X. Jiang, X. Lv, M. Li, L. Gao, S. Liu, M. Wang, C. Zhao and Y. Shen, *ACS Appl. Mater. Interfaces*, 2018, **10**, 4689-4696.
609. G. Dong, M. Fang, H. Wang, S. Yip, H.-Y. Cheung, F. Wang, C.-Y. Wong, S. T. Chu and J. C. Ho, *J. Mater. Chem. A*, 2015, **3**, 13080-13086.
610. S. H. Yu and D. H. C. Chua, *ACS Appl. Mater. Interfaces*, 2018, **10**, 14777-14785.
611. J. Zhang, F. Meng, R. I. Todd and Z. Fu, *Scr. Mater.*, 2010, **62**, 658-661.
612. A. C. Garcia, M. T. Koper, ACS Catal., 2018, **8**, 9359-9363.